



DOTTORATO DI RICERCA IN CHIMICA

Convenzione tra
UNIVERSITÀ DEGLI STUDI DI TRIESTE
e
UNIVERSITÀ CA' FOSCARI DI VENEZIA

CICLO XXXVII

**VALORIZATION OF PYROLYSIS PRODUCTS
DERIVED FROM WASTE**

Settore scientifico-disciplinare: 03/CHEM-04

**DOTTORANDA
LONGO LILIA**

**COORDINATORE
PROF. ENZO ALESSIO**

**SUPERVISORE DI TESI
PROF. MICHELA SIGNORETTO**

**CO-SUPERVISORE DI TESI
DR. NICOLA VECCHINI**

ANNO ACCADEMICO 2023/2024

Abstract

The demand for sustainable energy and circular resource management is driving research into bio-based and waste-derived materials. In this context, pyrolysis is emerging as an efficient and versatile technology, converting waste into oil, gas, and char fractions that can serve as raw materials for fuels, chemicals, and smart materials. This thesis focuses on valorizing pyrolysis-derived fractions from both lignocellulosic and non-lignocellulosic biomass, as well as plastic waste. Specifically, the first part of the research explores the use of the solid fraction (biochar) obtained by slow pyrolysis of biomass sources like hazelnut shells, rice husks, rice grains, and tannery leather shavings. These biochars were transformed into activated carbons to support Pd- and Co-based catalysts. Pd-supported catalysts were applied in benzaldehyde hydrogenation as model reaction to investigate the influence of biochar feedstock on catalytic performance. Activated rice husk biochar (A-RH) emerged as the optimal support. Additionally, co-pyrolyzing rice husk with leather shavings produced a new hybrid material with enhanced catalytic properties and selectivity. Leveraging these insights, Co-based catalysts were synthesized and applied in the hydrodeoxygenation (HDO) of isoeugenol and furfural. These compounds represent the phenolic and furanic fractions of bio-oil, that could be used as alternative source of fuels, especially in the aviation sector. Co/A-RH demonstrated superior activity, attributed to its intrinsic properties and strong interaction with the metal phase, facilitating synergy between Co^0 and Co^{2+} species. Lastly, part of this research targeted plastic-derived chars. These chars were not suitable to be used as supports for catalytic materials, therefore gasification was considered for the valorization of this byproduct of plastic recycling. By successfully converting them into carbon monoxide via the Boudouard reaction, the carbon balance in chemical recycling of plastics was improved. This approach contributed to carbon capture and reutilization. Overall, this thesis highlights the transformative potential of waste-derived materials in catalysis, supporting sustainable fuel production and offering viable strategies for enhanced circular resource utilization.

Index

List of abbreviations	III
1. Introduction	1
1.1 Waste as source	4
1.1.1 Biomass	4
1.1.2 Plastic	8
1.2 Pyrolysis	10
1.3 References	13
2. Aim of the thesis	17
3. Valorization of biomass <i>via</i> pyrolysis	19
3.1 General introduction	19
3.2 Biochar as support for heterogeneous catalysts	26
3.2.1 Introduction	26
3.2.2. Experimental.....	32
3.2.3 Results and discussion	36
3.2.4 Co-pyrolysis of LS and RH for the preparation of Pd-based catalyst	53
3.2.5 Conclusions.....	70
3.2.6 Appendix.....	71
3.2.7. References	75
3.3 Hydrodeoxygenation of bio-oil model compounds using biochar-based catalysts	92
3.3.1 Introduction	92
3.3.2 Experimental.....	105
3.3.3 Results and discussion	108
3.3.4. Conclusions.....	136
3.3.5 Appendix.....	137
3.3.3 References	141
4. Recovery of char from pyrolysis of mixed plastics	148
4.1 Introduction	148
4.1.1 Plastic pyrolysis	148
4.1.2 Plastic recycling and industries: an overview.....	152
4.1.3 Boudouard Equilibrium	156

4.2 Experimental	162
4.3 Results and discussion	166
4.4 Conclusions	178
4.5 Appendix	179
4.6 References	184
5. Concluding remarks	190

List of abbreviations

AC	Activated carbon (commercial)
ACs	Activated biochars
A-HS	Activated biochar derived from hazelnut shells
AI	Alkali Index
A-LS	Activated biochar derived from leather shaving waste
A-RG	Activated biochar derived from rice grains
A-RH	Activated biochar derived from rice husk
A-RL	Activated biochar derived from the co-pyrolysis of rice husk and leather shaving waste
BAL	Benzaldehyde
BALOH	Benzyl alcohol
BCs	Biochars
BET	Brunauer-Emmett-Teller
B-HS	Biochar derived from hazelnut shells
B-LS	Biochar derived from leather shaving waste
BP	Byproducts
B-RG	Biochar derived from rice grains
B-RH	Biochar derived from rice husk
B-RL	Biochar derived from the co-pyrolysis of rice husk and leather shaving waste
CB	Carbon black
CNT	Carbon nanotubes
CommChar	Commercial char derived from the pyrolysis of a different <i>plasmix</i>
DHE	Dihydroeugenol
E _a	Activation energy
EDX	Energy Dispersive X-ray analysis
EU	Eugenol
FC	Fixed carbon
FF	Furfural
FID	Flame Ignition Detector
FT-IR	Fourier Transform Infrared Spectroscopy
GC	Gas Chromatograph
GHG	Greenhouse Gas Emissions
HDO	Hydrodeoxygenation
HDPE	High Density Polyethylene
HS	Hazelnut shells
IE	Isoeugenol
LDPE	Low Density Polyethylene
LBM	Lignocellulosic Biomass
LS	Leather shaving waste
MF	2-methylfuran
MP-AES	Microwave Plasma Atomic Emission Spectroscopy
MSW	Municipal Solid Waste
MWCNT	Multiwalled carbon nanotubes
NC	N-doped carbon
NH ₃ -TPD	Temperature Programmed Desorption of ammonia
NLBM	Non-lignocellulosic Biomass
PA	Polyamide
PC	Polycarbonate
PCH	Propylcyclohexane
PCOL	Propylcyclohexanol
PCONE	Propylcyclohexanone
PE	Polyethylene
PET	Polyethylene terephthalate

pH _{PZC}	pH at the point zero charge
Plasmix	Mixed plastic waste
PMMA	Polymethyl metacrylate
PP	Polypropylene
PPHOL	4-propylphenol
PS	Polystyrene
PUR	Polyurethane
PVC	Polyvinyl chloride
RG	Rice grain
RH	Rice husk
RPM	Random Pore Model
SAF	Sustainable Aviation Fuels
SCM	Shrinking Core Model
SEM	Scanning Electron Microscopy
TCD	Thermal Conductivity Detector
TEM	Transmission Electron Microscopy
TGA	Thermogravimetric Analysis
TOF	Turnover Frequency
TOL	Toluene
TPD	Temperature Programmed Desorption
TPR	Temperature Programmed Reduction
UN	United Nations
UV	Ultra Violet radiation
VerChar	Char derived from the Versalis pyrolysis of <i>plasmix</i>
VerK	Char derived from the Versalis pyrolysis of <i>plasmix</i> , added with K ₂ CO ₃
VerOx	Char derived from the Versalis pyrolysis of <i>plasmix</i> , added with PET
VM	Volatile Matter
VRM	Volume Reaction Model
X	Conversion
XPS	X-ray Photoemission Spectroscopy
XRD	X-ray diffraction
ΔG	Gibbs free energy change
ΔH	Enthalpy change
ΔS	Entropy change

1. Introduction

Concerns over climate change, particularly global warming driven by increased greenhouse gas emissions from the consumption of non-renewable resources, have prompted research into alternative solutions to meet energy demands¹. Despite this, petroleum-derived liquid fuels continue to be the dominant source of energy². The continuous exploitation of fossil fuels generates side effects for the environment. As a result of their combustion, approximately 37 billion tons per year of CO₂, along with other harmful gases, are released into the atmosphere globally, causing the greenhouse effect³.

The reliance on fossil fuels (coal, oil, and natural gas) not only poses significant environmental risks but also raises political and security concerns, as these resources are unevenly distributed, and often located far from areas of high demand (Figure 1.1, Table 1.1).

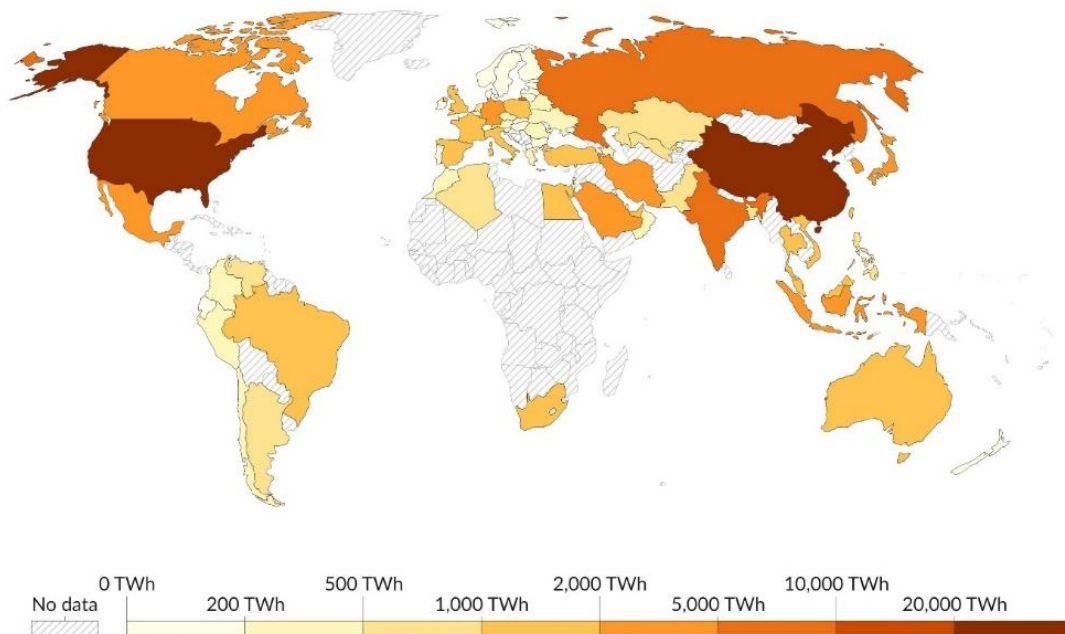


Figure 1.1. Fossil fuel consumption in 2023. Source <https://ourworldindata.org/fossil-fuels>

1. Introduction

Table 1.1. Top 10 producer countries of fossil sources. Source https://www.visualcapitalist.com/visualizing-the-scale-of-global-fossil-fuel-production/#google_vignette.

Top 10 coal-producing countries				Top 10 oil-producing countries			Top 10 gas-producing countries		
Rank	Country	Million tonnes	%	Country	Million tonnes	%	Country	Million tonnes	%
1	China	4126.0	50	U.S.A.	711.1	17	U.S.A.	934.2	23
2	India	811.3	10	Russia	536.4	13	Russia	701.7	17
3	Indonesia	614.0	8	Saudi Arabia	515.0	12	Iran	256.7	6
4	U.S.A.	524.4	6	Canada	267.1	6	China	209.2	5
5	Australia	478.6	6	Iraq	200.8	5	Qatar	117.0	4
6	Russia	433.7	5	China	198.9	5	Canada	172.3	4
7	South Africa	234.5	3	Iran	167.7	4	Australia	147.2	4
8	Germany	126.0	2	U.A.E.	164.4	4	Saudi Arabia	117.3	3
9	Kazakhstan	115.7	1	Brazil	156.8	4	Norway	114.3	3
10	Poland	107.6	1	Kwait	131.1	3	Algeria	100.8	2

Over the past 50 years, interest in sustainable technologies has surged, motivated by the need to transition towards a more sustainable energy landscape. The concept of sustainable development, first defined in the UN's *Our Common Future* report in 1987⁴ emphasized the need for balanced resource use. In 1992, the connection between energy, greenhouse gas emissions, and climate was formally acknowledged in the UN's Framework Convention on Climate Change, with further emphasis in the 1997 Kyoto Protocol, which stressed the urgency of sustainable energy development. The UN's Millennium Declaration in 2000 reinforced the importance of diversifying energy resources. By 2015, the 2030 Agenda for Sustainable Development was ratified, featuring 17 goals, of which 7 directly address environmental protection (Goals 6, 13, 14, 15), energy (Goal 7), and sustainable consumption (Goal 12), as reported in Figure 1.2⁵.



Figure 1.2. Sustainable development goals of the 2030 Agenda.

1. Introduction

In 2020, the European Commission approved the *European Green Deal*, a comprehensive policy framework aimed at achieving climate neutrality in the European Union by 2050. Central to this initiative is the promotion of a circular economy, a model that challenges the traditional linear economic approach of "make, use, dispose"⁶. A circular economy strives to minimize waste by transforming end-of-life products into new resources, effectively "closing the loop" in industrial ecosystems. The principles of "reduce, reuse, recycle" underline this model, where reducing waste, reusing materials, and recycling non-reusable products are prioritized. Adopting this model could potentially reduce greenhouse gas emissions by up to 70%.

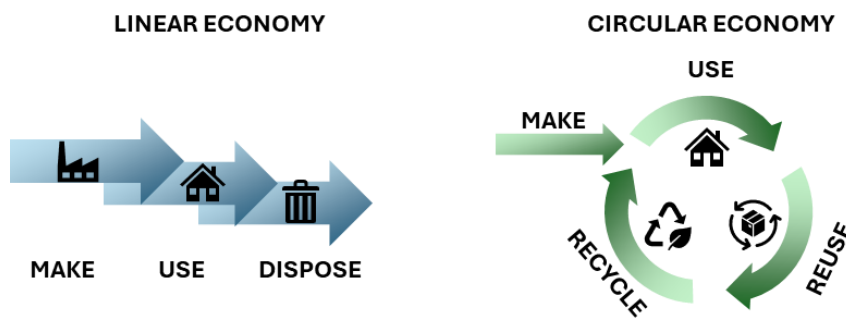


Figure 1.3. Linear economy vs circular economy.

In this context, the reuse of waste as an alternative to fossil fuels offers a promising pathway to lower greenhouse gas emissions while adhering to circular economy principles. This approach can facilitate a reduction in fossil fuel dependency and provide sustainable sources of both energy and raw materials. Furthermore, with the global population and consumption patterns continually increasing, waste generation is expected to rise by millions of tons annually over the next 20 to 30 years (Figure 1.4). Therefore, leveraging waste as a resource presents a dual advantage: it utilizes renewable materials and aids in managing the environmental impact of waste, particularly in reducing landfill pollution.

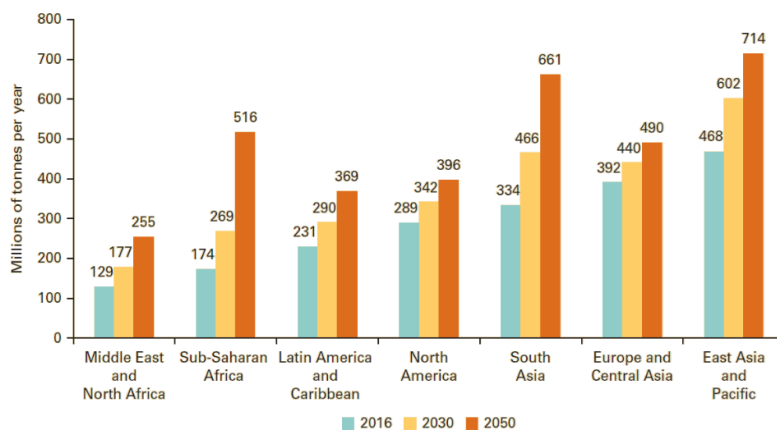


Figure 1.4. Projected waste generation, by region (millions of tonnes/year) in the next 30 years. Source <https://www.iea.org/search>

1.1 Waste as source

Global waste generation is projected to rise to 3.40 billion tons by 2050⁷, with high-income nations expecting a 19% increase by the same year. Various types of waste can be considered valuable sources of chemicals and energy, with particular attention given to biomass as a renewable resource. Indeed, the production of agricultural waste has been escalating globally, driven by a combination of factors including population growth, rapid urbanization, and economic development⁸.

In addition to biomass, other waste types, particularly plastic waste, must be addressed to reduce reliance on fossil fuels and mitigate environmental contamination. Despite plastic not being renewable, effective recycling processes can substantially extend its lifecycle. By recovering the organic content of plastic waste and transforming it into new chemicals or energy sources, plastic recycling aligns with the principles of a circular economy, contributing to waste reduction and resource recovery.

Biomass and waste are unique among renewable energy sources, such as solar power⁹, hydroelectricity¹⁰, geothermal¹¹, and tidal energy¹², because they serve as a source of carbon⁴. Unlike other renewables, which primarily produce energy, biomass and waste can be converted into a wide range of valuable products, including fuels, plastics, and various chemical compounds, making them crucial in both energy generation and chemical industries.

In the following chapters, the key characteristics of biomass waste (Chapter 1.1.1) and plastic waste (Chapter 1.1.2) are reviewed, along with the most employed strategies for their valorization and utilization as alternative sources of energy and chemicals, with a particular focus on the use of pyrolysis (Chapter 1.2). These discussions highlight the advantages and challenges associated with each waste type, as well as the technological approaches used to enhance their potential within the framework of a circular economy.

1.1.1 Biomass

Biomass refers to the entirety of organic material directly or indirectly derived from the photosynthesis process¹³, including residues from agriculture, forestry, aquatic crops, industry, animals and households, as well as byproducts from the processing of these materials¹⁴. It is classified as renewable because the CO₂ released during its processing or thermal conversion is fixed back into organic matter within relatively short cycles (years), thereby maintaining a closed carbon loop. Plants reabsorb the CO₂ released through the degradation of other biomass, making the process carbon neutral. In contrast, the CO₂ emitted from fossil fuel combustion is part of a carbon cycle that spans millions of years, far

1. Introduction

exceeding human timeframes for renewability. Biomass also presents advantages in terms of cost-effectiveness, local availability, and large-scale production.

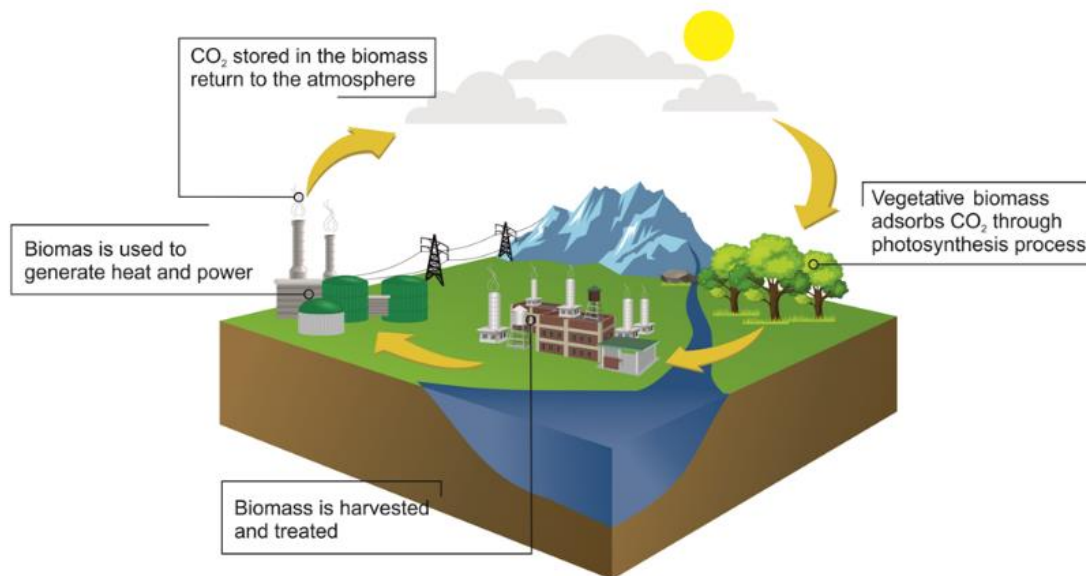


Figure 1.1.1.1. CO₂ closed loop in the production and utilization of biomass. Source: *Biofuel Research Journal* 22 (2019) 962-979¹³.

The world's total biomass reserves are estimated at approximately 1.8 trillion tons of land-based biomass and 4 billion tons of aquatic biomass. These reserves correspond to an estimated energy potential of around 33,000 EJ¹⁵ which is more than 80 times the current annual global energy consumption. However, despite this vast potential, renewable energies contribute to only about 14% of the world's primary energy supply. This underexploitation highlights the significant opportunity for expanding biomass use as a renewable energy source to meet growing global energy demands while reducing reliance on fossil fuels to harness the full potential of biomass, and biorefineries play a critical role. A biorefinery is an integrated network of facilities that converts biomass into biofuels, energy, and chemicals through multi-step processes¹⁶. Following the selection of feedstock, the biomass typically undergoes a pretreatment phase, which is essential for preparing it for subsequent biological and chemical transformations. By efficiently converting biomass into energy, biofuels, and high-value products such as fine chemicals, cosmetics, and pharmaceuticals, biorefineries can contribute to both large-scale energy production and the generation of specialized products. Additionally, biorefineries produce materials like bioplastics, along with food and animal feed sources, offering a versatile approach to sustainable development.

1. Introduction

The composition of biomass is highly diverse and can be primarily divided into lignocellulosic biomass (LBM), comprising woody and herbaceous biomass, and non-lignocellulosic biomass, comprising aquatic, animal, and human waste (NLBM). LBM primarily consists of cellulose, lignin, and hemicellulose, while NLBM have a more varied composition depending on the type of waste. Animal and human biomass contain high levels of proteins^{17,18}, algae and oily biomasses are abundant in lipids¹³.

When considering biomass for fuel production, it is also categorized into four generations based on its source and processing technologies¹⁹:

- I. First generation biomass includes edible oil seeds, food crops, and animal fats, primarily used for biodiesel production. The use of agricultural land for biofuel production competes directly with food production, potentially driving up food prices. Due to this food-fuel conflict, the reliance on first-generation biomass has declined.
- II. Second generation biomass are comprised of non-edible oil seeds, waste cooking oil, and lignocellulosic materials from non-food or dedicated energy crops (e.g., miscanthus, switchgrass). By utilizing non-food feedstocks, second-generation biomass reduces food competition and optimizes land use. However, it requires extensive pre-treatment and processing to convert these materials into viable energy sources or chemicals and their exploitation to date is not enough to cover global need.
- III. Third generation biomass mainly consists of aquatic plants and algae, which grow rapidly and can be cultivated in marine environments, thereby avoiding competition with food crops. Algae, with their high lipid content, are particularly suited for biodiesel production. However, the widespread use of third-generation biomass is limited by the high costs associated with bioreactors and cultivation systems, and as for second generation biomass, their utilization is still too scarce to be employed as single alternative to fossil sources.
- IV. Fourth generation biomass refers to genetically engineered organisms designed to enhance the production of specific components (e.g., lipids from algae). While fourth-generation biomass offers significant potential for sustainable biofuel production, it remains in the early stages of research and development, and its large-scale exploitation is still limited.

Unlike crude oil, which is primarily composed of hydrocarbons, biomass-derived materials are often highly oxygenated. This higher oxygen content in biomass introduces challenges for its direct use as fuel or chemical feedstock. However, the more diverse and flexible composition of biomass presents significant opportunities for producing a wide range of chemicals²⁰.

1. Introduction

To enable the use of biomass in sectors traditionally dominated by fossil fuels, such as in biorefineries, various treatments are necessary. These treatments primarily focus on reducing the oxygen content, often through processes like hydrodeoxygenation, which involves the addition of hydrogen to remove oxygen. This allows biomass-derived products to achieve properties similar to those of fossil fuel-derived products, making them viable alternatives in energy and chemical industries.

Biomass can be converted into fuels or high-value products via distinct pathways, divided into physical, chemical, thermochemical and biological processes^{21,22}, schematized in Figure 1.1.1.2. Thermochemical methods, including pyrolysis, gasification, carbonization, and liquefaction, use heat to break down biomass, resulting in a range of valuable products. These processes can be distinguished based on the target products. For example, hydrothermal and conventional gasification convert biomass into syngas (a mixture of carbon monoxide, hydrogen, and carbon dioxide) through controlled oxidation at high temperatures. Liquefaction involves the conversion of biomass into liquid fuels under conditions of high pressure and moderate temperatures, providing a viable alternative for biofuel production. In carbonization, biomass is heated in a low-oxygen environment, producing biochar, a stable, carbon-rich material with various applications. Among these thermochemical technologies, pyrolysis plays a particularly important role. It is the thermal decomposition of organic matter in the absence of oxygen, and it can yield a solid, liquid, and gaseous phase. By adjusting process parameters such as temperature, heating rate, and residence time, the product distribution between biochar, bio-oil, and biogas can be controlled to suit specific applications. This flexibility makes pyrolysis a highly versatile and adaptable technology for biomass valorization.

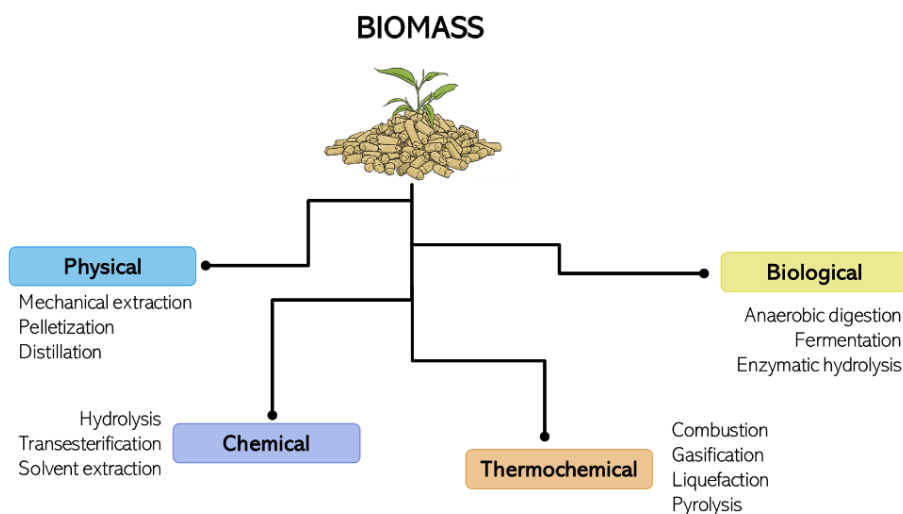


Figure 1.1.1.2. Methods for biomass valorization

In this work, special attention is given to pyrolysis due to its capacity to simultaneously produce multiple products. This multifunctionality enhances its potential as an efficient and sustainable method for transforming biomass into valuable fuels and materials, offering both environmental and economic benefits.

1.1.2 Plastic

Plastic is a versatile, lightweight, cheap and widely used material, deriving from synthetic polymers, primarily from petrochemicals. Its use has revolutionized modern life, resulting indispensable in several applications, such as packaging, construction, medical equipment, electronics etc.²³. Plastics are categorized into two primary subtypes based on their thermal response: thermoplastic and thermosetting polymers. Thermoplastic polymers soften upon heating without undergoing chemical alterations, allowing them to be melted and reshaped multiple times. In contrast, thermosetting polymers undergo irreversible chemical reactions during their initial curing process, resulting in a rigid structure that cannot be remelted or reformed upon subsequent heating²⁴. The industrial production of plastics started in the second half of the 20th century, and it has increased year by year, reaching 400.3 Mt of plastic produced in 2022²⁵. In Europe, the predominant application of plastic is packaging, accounting for 40% of usage, followed by building and construction (20%), automotive (10%), electrical and electronics (6%) etc.²⁶. The packaging market primarily utilizes thermoplastic polymers such as polyethylene (PE), polypropylene (PP), polyethylene terephthalate (PET) and polystyrene (PS). PS, along with polyvinyl chloride (PVC) and polyurethane (PUR) (the latter being a thermosetting polymer) are instead mainly employed in the building and construction sector²⁷.

The inherent chemical stability, durability, and inertness of plastics, while advantageous for many applications, simultaneously present significant challenges in terms of waste management. The predominantly non-biodegradable nature of most plastics, coupled with inadequate waste disposal practices, has led to severe environmental consequences²⁸. Moreover, due to the variable nature of plastic polymers, and the presence of high amounts of additives, which can comprise up to 40-50 wt.% of the final material, the disposal and recycling of these materials is particularly challenging. Compared to other commonly used materials such as paper, glass, and metals, plastic recycling remains significantly underdeveloped. According to a report by the United Nations Centre for Regional Development (UNCRD), Southeast Asian countries exhibit the highest levels of plastic waste mismanagement, with approximately 88% of plastic waste ultimately entering aquatic environments. In contrast, the European Union, often regarded as a leader in plastic recycling, manages to recycle only 32% of its plastic waste²⁹.

1. Introduction

Approximately 42% of this waste is either utilized as refuse-derived fuel or incinerated for energy recovery, while the remaining 25% is relegated to municipal solid waste disposal. Despite these efforts, significant waste management challenges persist. The durability and extensive use of plastics contribute to serious environmental issues, from the association of chlorinated plastics with dioxin formation in waste incinerators to the pervasive "plastic soup" in the oceans. The accumulation of plastic in natural environments is increasingly leading to soil and water contamination. Plastic waste serves as a vector for organic pollutants, heavy metals, and pathogens, and the release of toxic compounds through abiotic degradation contributes to soil degradation²⁹ and water contamination³⁰. Microplastics can infiltrate fish tissues and, through bioaccumulation in the food chain, present significant health risks to humans^{31,32}. These problems are exacerbated not only by consumer behavior and inadequate regulations but also by technological and economic constraints that make recycling less economically viable compared to landfill disposal. Consequently, significant efforts are being invested in advancing recycling technologies and improving waste management practices for these critical materials.

The strategies to accomplish plastic recycling can be divided into four categories: primary, secondary, tertiary and quaternary³³. Primary recycling consists in re-extrusion, not being applicable to plastic mixtures (PM) or municipal solid waste (MSW). Secondary recycling consists in the separation of plastics from contaminants and melting and remolding of the polymers into new products. However, the obtained recycled materials display lower quality and performances compared to the original products^{34,35}. Tertiary recycling refers to chemical recycling, which involves the breakdown of plastics into their chemical constituents to produce new materials or chemicals. The common approaches include solvolysis, pyrolysis and gasification^{34,36}. This approach allows to obtain virgin polymers with the same characteristics as the starting materials. Quaternary recycling pertains to energy recovery through incineration, where plastics are burned to generate energy. It results the easiest and most scalable strategy, but it has several drawbacks such as air pollution, with the emission of VOCs, NO_x, SO_x, chlorinated compounds and dioxins^{37,38}.

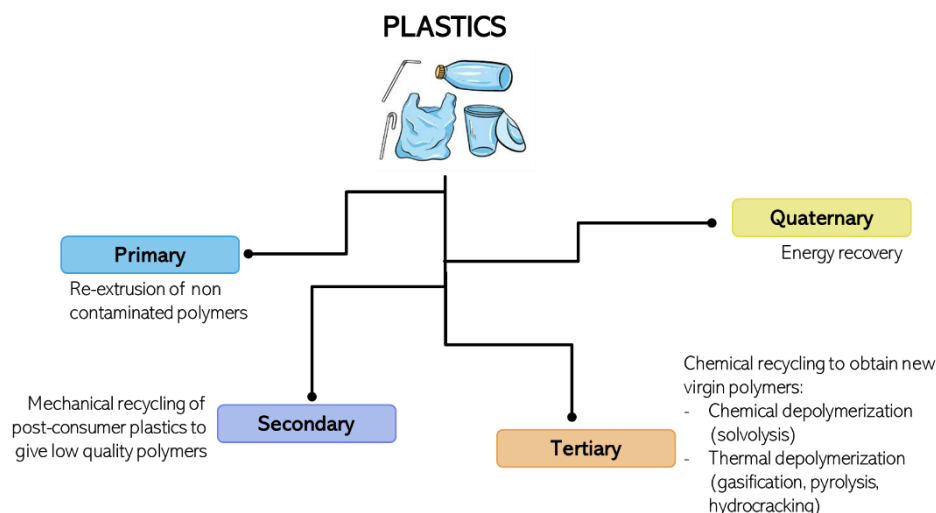


Figure 1.1.2.1. Types of plastic recycling.

The advantages of the employment of chemical recycling, in particular thought pyrolysis, are several: it can be used for plastics that cannot be recovered mechanically because of its properties (i.e. thermosetting polymers) or due to the low degree of purity, meaning the presence of additives, multilayered plastics, composites with other materials or more in general a mix of plastic deriving from urban wastes.

1.2 Pyrolysis

Pyrolysis is a versatile, cost-effective, and robust thermochemical process for transforming a wide range of organic materials, including biomass, municipal waste, and plastics. In this process, organic matter is decomposed at elevated temperatures (400–700°C) in the absence of oxygen, yielding three primary products: a liquid fraction (oil or bio-oil, if derived from biomass), a solid fraction (char or biochar), and gases (syngas or biogas)²⁷. The ratio and composition of the three products are highly dependent on the starting feedstock. Consequently, the pyrolysis process can be tailored to produce specific target products based on the characteristics of the initial material.

The flexibility of pyrolysis technology enables its integration with existing agricultural, forestry, and industrial systems for waste treatment, producing valuable outputs for various applications. The liquid fraction can be upgraded for use as fuel or chemicals³⁹, while the solid char can serve as a substitute for fossil-based coal in energy production, as a soil amendment⁴⁰ that improves carbon sequestration and reduces greenhouse gases, and can also be utilized in several other fields, such as catalysis, energy storage (batteries), and as an adsorbent for pollutant removal⁴¹. The gas fraction can be utilized as a fuel or as renewable source of syngas⁴².

1. Introduction

Pyrolysis equipment ranges from small-scale laboratory devices capable of processing a few milligrams of material to large industrial systems handling several tons per hour. The largest pyrolysis units in North America can process 250–200 dry tons of biomass per day.

The composition and yields of the three pyrolysis products are highly dependent on the feedstock (which will be discussed in detail in the following chapters) and the operational conditions, such as temperature, heating rate, residence time, and total flow rate. Pyrolysis can be classified into four general types: slow pyrolysis, fast pyrolysis, flash pyrolysis, and catalytic pyrolysis⁴³.

- Slow pyrolysis: it is carried out at a slow heating rate (°C/min) and long residence time (minutes to hours). The main target is the production of char⁴⁴. For lignocellulosic biomass, slow pyrolysis typically yields 35 % biochar, 30 % bio-oil, and 35 % biogas⁴⁵.
- Fast pyrolysis: it has a higher heating rate (°C/s) and shorter residence time (few seconds).
- Flash pyrolysis: the heating rates are even higher (10^3 – 10^4 °C/s) with residence times under a second. Both for fast and flash pyrolysis the target product is the liquid fraction, which can reach 50–70 %^{46,47}.
- Catalytic pyrolysis: it involves the use of a catalyst during the pyrolysis process^{48–50}. It is mainly used for improving oil characteristics, facilitating the removal of oxygenated compounds⁵¹ and enhancing the stability of the mixture, and to reduce coke formation^{52,53}. The most used catalysts include solid acids such as zeolites, silica–alumina, silicalite, fluid catalytic cracking (FCC) catalysts, alumina, and molecular sieves. Additionally, metal oxides such as zinc oxide, zirconia, ceria, and copper chromite are also employed. Notably, char produced during pyrolysis can itself function as a catalyst, promoting secondary reactions that further refine the product composition^{54,55}.

During pyrolysis, several chemical reactions are initiated by the high-energy input, which can be classified into primary and secondary reactions⁵⁶. Primary reactions include depolymerization, fragmentation, and char formation⁵⁷. Depolymerization, which begins at around 250 °C and continues up to 500 °C, breaks the chemical bonds of the macromolecules present in the feedstock (such as lignin, cellulose, and hemicellulose in biomass, proteins in animal waste, or polymer chains in plastics), producing volatile and condensable fractions. Fragmentation reactions become dominant at higher temperatures (>550 °C), increasing gas yields. Char formation involves the condensation of aromatic rings into macro polycyclic structures⁵⁸. The primary products formed during pyrolysis can undergo secondary reactions, such as cracking, dehydration, isomerization, aromatization, decarboxylation, and recombination.

1. Introduction

The type of reactor has an important impact in the final pyrolysis results, acting on the mixing of the matter, heat transfer and residence time. Pyrolysis can be carried out in batch, semi-batch or continuous flow reactors both with fluidized or fixed bed, and there are also some innovative solutions such as plasma, microwave⁵⁹ or solar reactors. Batch and semi-batch reactors, due to the simple design, are useful to investigate pyrolysis conditions. Based on literature results, batch or semi-batch reactors are preferable to conduct thermal pyrolysis, because the reaction parameters can be easily controlled. Catalytic pyrolysis is instead favored in continuous system, to improve selectivity toward liquid products, because it is easier to control the contact time between feed and catalyst, lowering char formation.

1.3 References

- (1) Singh, S. Energy Crisis and Climate Change, *Energy*; **2021**, 1–17. <https://doi.org/10.1002/9781119741503.ch1>.
- (2) Chu, S.; Majumdar, A. Opportunities and Challenges for a Sustainable Energy Future. *Nature* **2012**, *488* (7411), 294–303. <https://doi.org/10.1038/nature11475>.
- (3) *Global CO2 emissions rose less than initially feared in 2022 as clean energy growth offset much of the impact of greater coal and oil use - News*. IEA. <https://www.iea.org/news/global-co2-emissions-rose-less-than-initially-feared-in-2022-as-clean-energy-growth-offset-much-of-the-impact-of-greater-coal-and-oil-use> (accessed 2024-10-27).
- (4) Gunnarsdottir, I.; Davidsdottir, B.; Worrell, E.; Sigurgeirsdottir, S. Sustainable Energy Development: History of the Concept and Emerging Themes. *Renewable and Sustainable Energy Reviews* **2021**, *141*, 110770. <https://doi.org/10.1016/j.rser.2021.110770>.
- (5) *THE 17 GOALS | Sustainable Development*. <https://sdgs.un.org/goals> (accessed 2024-10-27).
- (6) Stahel, W. R. The Circular Economy. *Nature* **2016**, *531* (7595), 435–438. <https://doi.org/10.1038/531435a>.
- (7) Chandrappa, R.; Das, D. B. Waste Quantities and Characteristics, *Solid Waste Management: Principles and Practice*; **2024**, 47–87. https://doi.org/10.1007/978-3-031-50442-6_2.
- (8) Xu, M.; Yang, M.; Sun, H.; Gao, M.; Wang, Q.; Wu, C. Bioconversion of Biowaste into Renewable Energy and Resources: A Sustainable Strategy. *Environmental Research* **2022**, *214*, 113929. <https://doi.org/10.1016/j.envres.2022.113929>.
- (9) Rabaia, M. K. H.; Abdelkareem, M. A.; Sayed, E. T.; Elsaid, K.; Chae, K.-J.; Wilberforce, T.; Olabi, A. G. Environmental Impacts of Solar Energy Systems: A Review. *Science of The Total Environment* **2021**, *754*, 141989. <https://doi.org/10.1016/j.scitotenv.2020.141989>.
- (10) Darmawi; Sipahutar, R.; Bernas, S. M.; Imanuddin, M. S. Renewable Energy and Hydropower Utilization Tendency Worldwide. *Renewable and Sustainable Energy Reviews* **2013**, *17*, 213–215. <https://doi.org/10.1016/j.rser.2012.09.010>.
- (11) Glassley, W. E. *Geothermal Energy: Renewable Energy and the Environment, Second Edition*; CRC Press, 2014.
- (12) Kadiri, M.; Ahmadian, R.; Bockelmann-Evans, B.; Rauen, W.; Falconer, R. A Review of the Potential Water Quality Impacts of Tidal Renewable Energy Systems. *Renewable and Sustainable Energy Reviews* **2012**, *16* (1), 329–341. <https://doi.org/10.1016/j.rser.2011.07.160>.
- (13) Tursi, A. A Review on Biomass: Importance, Chemistry, Classification, and Conversion. *Biofuel Research Journal* **2019**, *6* (2), 962–979. <https://doi.org/10.18331/BRJ2019.6.2.3>.
- (14) Sadh, P. K.; Chawla, P.; Kumar, S.; Das, A.; Kumar, R.; Bains, A.; Sridhar, K.; Duhan, J. S.; Sharma, M. Recovery of Agricultural Waste Biomass: A Path for Circular Bioeconomy. *Science of The Total Environment* **2023**, *870*, 161904. <https://doi.org/10.1016/j.scitotenv.2023.161904>.
- (15) Kalak, T. Potential Use of Industrial Biomass Waste as a Sustainable Energy Source in the Future. *Energies* **2023**, *16* (4), 1783. <https://doi.org/10.3390/en16041783>.
- (16) Moncada B., J.; Aristizábal M., V.; Cardona A., C. A. Design Strategies for Sustainable Biorefineries. *Biochemical Engineering Journal* **2016**, *116*, 122–134. <https://doi.org/10.1016/j.bej.2016.06.009>.
- (17) Lü, F.; Shao, L.-M.; Zhang, H.; Fu, W.-D.; Feng, S.-J.; Zhan, L.-T.; Chen, Y.-M.; He, P.-J. Application of Advanced Techniques for the Assessment of Bio-Stability of Biowaste-Derived Residues: A Minireview. *Bioresource Technology* **2018**, *248*, 122–133. <https://doi.org/10.1016/j.biortech.2017.06.045>.

1. Introduction

- (18) Swain, A. A.; Oraon, R.; Baudh, K.; Kumar, M. Biowaste Valorization for Production of Bacterial Cellulose and Its Multifarious Applications Contributing to Environmental Sustainability. *Environmental Sustainability* **2022**, *5* (1), 51–63. <https://doi.org/10.1007/s42398-022-00221-0>.
- (19) Jacobsson, S.; Johnson, A. The Diffusion of Renewable Energy Technology: An Analytical Framework and Key Issues for Research. *Energy Policy* **2000**, *28* (9), 625–640. [https://doi.org/10.1016/S0301-4215\(00\)00041-0](https://doi.org/10.1016/S0301-4215(00)00041-0).
- (20) Bozell, J. J. Chemicals and Materials from Renewable Resources. In *Chemicals and Materials from Renewable Resources*; ACS Symposium Series; American Chemical Society, 2001; Vol. 784, pp 1–9. <https://doi.org/10.1021/bk-2001-0784.ch001>.
- (21) Bhatia, S. K.; Joo, H.-S.; Yang, Y.-H. Biowaste-to-Bioenergy Using Biological Methods – A Mini-Review. *Energy Conversion and Management* **2018**, *177*, 640–660. <https://doi.org/10.1016/j.enconman.2018.09.090>.
- (22) Okolie, J. A.; Epelle, E. I.; Tabat, M. E.; Orivri, U.; Amenaghawon, A. N.; Okoye, P. U.; Gunes, B. Waste Biomass Valorization for the Production of Biofuels and Value-Added Products: A Comprehensive Review of Thermochemical, Biological and Integrated Processes. *Process Safety and Environmental Protection* **2022**, *159*, 323–344. <https://doi.org/10.1016/j.psep.2021.12.049>.
- (23) Rahimi, A.; García, J. M. Chemical Recycling of Waste Plastics for New Materials Production. *Nature Review Chemistry* **2017**, *1* (6), 1–11. <https://doi.org/10.1038/s41570-017-0046>.
- (24) Pascualt, J.-P.; Williams, R. J. J. Thermosetting Polymers. In *Handbook of Polymer Synthesis, Characterization, and Processing*; John Wiley & Sons, Ltd, 2013; pp 519–533. <https://doi.org/10.1002/9781118480793.ch28>.
- (25) Li, T.; Theodosopoulos, G.; Lovell, C.; Loukodimou, A.; Maniam, K. K.; Paul, S. Progress in Solvent-Based Recycling of Polymers from Multilayer Packaging. *Polymers* **2024**, *16* (12), 1670. <https://doi.org/10.3390/polym16121670>.
- (26) *Plastics - the Facts 2021 • Plastics Europe*. Plastics Europe. <https://plasticseurope.org/knowledge-hub/plastics-the-facts-2021/> (accessed 2024-10-27).
- (27) Shen, L.; Worrell, E. Chapter 31 - Plastic Recycling. In *Handbook of Recycling (Second Edition)*; Meskers, C., Worrell, E., Reuter, M. A., Eds.; Elsevier, 2024; pp 497–510. <https://doi.org/10.1016/B978-0-323-85514-3.00014-2>.
- (28) Ali, S. S.; Elsamahy, T.; Koutra, E.; Kornaros, M.; El-Sheekh, M.; Abdelkarim, E. A.; Zhu, D.; Sun, J. Degradation of Conventional Plastic Wastes in the Environment: A Review on Current Status of Knowledge and Future Perspectives of Disposal. *Science of The Total Environment* **2021**, *771*, 144719. <https://doi.org/10.1016/j.scitotenv.2020.144719>.
- (29) Tumu, K.; Vorst, K.; Curtzwiler, G. Global Plastic Waste Recycling and Extended Producer Responsibility Laws. *Journal of Environmental Management* **2023**, *348*, 119242. <https://doi.org/10.1016/j.jenvman.2023.119242>.
- (30) Chamas, A.; Moon, H.; Zheng, J.; Qiu, Y.; Tabassum, T.; Jang, J. H.; Abu-Omar, M.; Scott, S. L.; Suh, S. Degradation Rates of Plastics in the Environment. *ACS Sustainable Chemistry & Engineering Journal* **2020**, *8* (9), 3494–3511. <https://doi.org/10.1021/acssuschemeng.9b06635>.
- (31) Webb, H. K.; Arnott, J.; Crawford, R. J.; Ivanova, E. P. Plastic Degradation and Its Environmental Implications with Special Reference to Poly(Ethylene Terephthalate). *Polymers* **2013**, *5* (1), 1–18. <https://doi.org/10.3390/polym5010001>.
- (32) Dai, L.; Zhou, N.; Lv, Y.; Cheng, Y.; Wang, Y.; Liu, Y.; Cobb, K.; Chen, P.; Lei, H.; Ruan, R. Pyrolysis Technology for Plastic Waste Recycling: A State-of-the-Art Review. *Progress in Energy and Combustion Science* **2022**, *93*, 101021. <https://doi.org/10.1016/j.pecs.2022.101021>.
- (33) Singh, N.; Hui, D.; Singh, R.; Ahuja, I. P. S.; Feo, L.; Fraternali, F. Recycling of Plastic Solid Waste: A State of Art Review and Future Applications. *Composites Part B: Engineering* **2017**, *115*, 409–422. <https://doi.org/10.1016/j.compositesb.2016.09.013>.
- (34) Ciuffi, B.; Chiaramonti, D.; Rizzo, A. M.; Frediani, M.; Rosi, L. A Critical Review of SCWG in the Context of Available Gasification Technologies for Plastic Waste. *Applied Sciences* **2020**, *10* (18), 6307. <https://doi.org/10.3390/app10186307>.

1. Introduction

- (35) Li, J.; Burra, K. G.; Wang, Z.; Liu, X.; Kerdsuwan, S.; Gupta, A. K. Energy Recovery From Composite Acetate Polymer-Biomass Wastes via Pyrolysis and CO₂-Assisted Gasification. *Journal of Energy Resources Technology* **2020**, *143* (042305). <https://doi.org/10.1115/1.4048245>.
- (36) Barredo, A.; Asueta, A.; Amundarain, I.; Leivar, J.; Miguel-Fernández, R.; Arnaiz, S.; Epelde, E.; López-Fonseca, R.; Gutiérrez-Ortiz, J. I. Chemical Recycling of Monolayer PET Tray Waste by Alkaline Hydrolysis. *Journal of Environmental Chemical Engineering* **2023**, *11* (3), 109823. <https://doi.org/10.1016/j.jece.2023.109823>.
- (37) Al-Salem, S. M.; Lettieri, P.; Baeyens, J. Recycling and Recovery Routes of Plastic Solid Waste (PSW): A Review. *Waste Management* **2009**, *29* (10), 2625–2643. <https://doi.org/10.1016/j.wasman.2009.06.004>.
- (38) Nagy, Á.; Kuti, R. The Environmental Impact of Plastic Waste Incineration. *Academic and Applied Research in Military and Public Management Science* **2016**, *15*, 231–237. <https://doi.org/10.32565/aarms.2016.3.3>.
- (39) Gollakota, A. R. K.; Reddy, M.; Subramanyam, M. D.; Kishore, N. A Review on the Upgradation Techniques of Pyrolysis Oil. *Renewable and Sustainable Energy Reviews* **2016**, *58*, 1543–1568. <https://doi.org/10.1016/j.rser.2015.12.180>.
- (40) European Commission. Joint Research Centre. Institute for Environment and Sustainability. *Biochar Application to Soils: A Critical Scientific Review of Effects on Soil Properties, Processes and Functions.*; Publications Office: LU, 2010.
- (41) Bartoli, M.; Giorcelli, M.; Jagdale, P.; Rovere, M.; Tagliaferro, A. A Review of Non-Soil Biochar Applications. *Materials* **2020**, *13* (2), 261. <https://doi.org/10.3390/ma13020261>.
- (42) Zhang, Y.; Liang, Y.; Li, S.; Yuan, Y.; Zhang, D.; Wu, Y.; Xie, H.; Brindhadevi, K.; Pugazhendhi, A.; Xia, C. A Review of Biomass Pyrolysis Gas: Forming Mechanisms, Influencing Parameters, and Product Application Upgrades. *Fuel* **2023**, *347*, 128461. <https://doi.org/10.1016/j.fuel.2023.128461>.
- (43) Al-Rumaihi, A.; Shahbaz, M.; McKay, G.; Mackey, H.; Al-Ansari, T. A Review of Pyrolysis Technologies and Feedstock: A Blending Approach for Plastic and Biomass towards Optimum Biochar Yield. *Renewable and Sustainable Energy Reviews* **2022**, *167*, 112715. <https://doi.org/10.1016/j.rser.2022.112715>.
- (44) Demirbas, A.; Arin, G. An Overview of Biomass Pyrolysis. *Energy Sources* **2002**, *24* (5), 471–482. <https://doi.org/10.1080/00908310252889979>.
- (45) Goyal, H. B.; Seal, D.; Saxena, R. C. Bio-Fuels from Thermochemical Conversion of Renewable Resources: A Review. *Renewable and Sustainable Energy Reviews* **2008**, *12* (2), 504–517. <https://doi.org/10.1016/j.rser.2006.07.014>.
- (46) Amutio, M.; Lopez, G.; Aguado, R.; Bilbao, J.; Olazar, M. Biomass Oxidative Flash Pyrolysis: Autothermal Operation, Yields and Product Properties. *Energy Fuels* **2012**, *26* (2), 1353–1362. <https://doi.org/10.1021/ef201662x>.
- (47) Jahirul, M. I.; Rasul, M. G.; Chowdhury, A. A.; Ashwath, N. Biofuels Production through Biomass Pyrolysis —A Technological Review. *Energies* **2012**, *5* (12), 4952–5001. <https://doi.org/10.3390/en5124952>.
- (48) Norouzi, O.; Taghavi, S.; Arku, P.; Jafarian, S.; Signoreto, M.; Dutta, A. What Is the Best Catalyst for Biomass Pyrolysis? *Journal of Analytical and Applied Pyrolysis* **2021**, *158*, 105280. <https://doi.org/10.1016/j.jaap.2021.105280>.
- (49) Grams, J.; Jankowska, A.; Goscianska, J. Advances in Design of Heterogeneous Catalysts for Pyrolysis of Lignocellulosic Biomass and Bio-Oil Upgrading. *Microporous and Mesoporous Materials* **2023**, *362*, 112761. <https://doi.org/10.1016/j.micromeso.2023.112761>.
- (50) Hubble, A. H.; Ryan, E. M.; Goldfarb, J. L. Enhancing Pyrolysis Gas and Bio-Oil Formation through Transition Metals as *in Situ* Catalysts. *Fuel* **2022**, *308*, 121900. <https://doi.org/10.1016/j.fuel.2021.121900>.
- (51) Dickerson, T.; Soria, J. Catalytic Fast Pyrolysis: A Review. *Energies* **2013**, *6* (1), 514–538. <https://doi.org/10.3390/en6010514>.
- (52) Whyte, H. E.; Loubar, K.; Awad, S.; Tazerout, M. Pyrolytic Oil Production by Catalytic Pyrolysis of Refuse-Derived Fuels: Investigation of Low Cost Catalysts. *Fuel Processing Technology* **2015**, *140*, 32–38. <https://doi.org/10.1016/j.fuproc.2015.08.022>.

1. Introduction

- (53) Stelmachowski, M. Thermal Conversion of Waste Polyolefins to the Mixture of Hydrocarbons in the Reactor with Molten Metal Bed. *Energy Conversion and Management* **2010**, *51* (10), 2016–2024. <https://doi.org/10.1016/j.enconman.2010.02.035>.
- (54) Morf, P.; Hasler, P.; Nussbaumer, T. Mechanisms and Kinetics of Homogeneous Secondary Reactions of Tar from Continuous Pyrolysis of Wood Chips. *Fuel* **2002**, *81* (7), 843–853. [https://doi.org/10.1016/S0016-2361\(01\)00216-2](https://doi.org/10.1016/S0016-2361(01)00216-2).
- (55) Zhang, L.; Hu, X.; Hu, K.; Hu, C.; Zhang, Z.; Liu, Q.; Hu, S.; Xiang, J.; Wang, Y.; Zhang, S. Progress in the Reforming of Bio-Oil Derived Carboxylic Acids for Hydrogen Generation. *Journal of Power Sources* **2018**, *403*, 137–156. <https://doi.org/10.1016/j.jpowsour.2018.09.097>.
- (56) Hu, X.; Gholizadeh, M. Biomass Pyrolysis: A Review of the Process Development and Challenges from Initial Researches up to the Commercialisation Stage. *Journal of Energy Chemistry* **2019**, *39*, 109–143. <https://doi.org/10.1016/j.jechem.2019.01.024>.
- (57) Collard, F.-X.; Blin, J. A Review on Pyrolysis of Biomass Constituents: Mechanisms and Composition of the Products Obtained from the Conversion of Cellulose, Hemicelluloses and Lignin. *Renewable and Sustainable Energy Reviews* **2014**, *38*, 594–608. <https://doi.org/10.1016/j.rser.2014.06.013>.
- (58) Van de Velden, M.; Baeyens, J.; Brems, A.; Janssens, B.; Dewil, R. Fundamentals, Kinetics and Endothermicity of the Biomass Pyrolysis Reaction. *Renewable Energy* **2010**, *35* (1), 232–242. <https://doi.org/10.1016/j.renene.2009.04.019>.
- (59) Lam, S. S.; Chase, H. A. A Review on Waste to Energy Processes Using Microwave Pyrolysis. *Energies* **2012**, *5* (10), 4209–4232. <https://doi.org/10.3390/en5104209>.

2. Aim of the thesis

The aim of this PhD thesis is to advance the valorization of waste materials through pyrolysis, supporting circular economy and sustainability objectives. Specifically, the thesis explores transforming lignocellulosic biomass and complex industrial byproducts, such as tannery waste and plastics, into higher-value products that can serve as alternatives to conventional fossil-derived materials. This research focuses on the valorization of both biomass and plastic waste, structured across three core topics:

1. **Biomass valorization for biochar production:** this part of the thesis examines the pyrolysis of biomass to produce biochar, intended for use as a support material in heterogeneous catalyst preparation.
2. **Catalytic upgrading of bio-oil:** this part of the thesis involves utilizing the biochar-based catalysts to upgrade the liquid fraction (bio-oil) obtained from biomass pyrolysis, specifically through hydrodeoxygenation (HDO) reactions.
3. **Plastic char valorization:** finally, this part of the thesis investigates the valorization of char obtained from plastic pyrolysis by gasification via the Boudouard reaction, with the goal of producing carbon monoxide for reintegration into plastic production processes.

Thesis Structure Overview:

Chapter 1: Introduction

This chapter addresses the environmental challenges of biomass and plastic waste, explores the concept of circular economy to transform waste into resources, and presents pyrolysis as a strategic method for converting waste into valuable products such as bio-oil, biochar, and syngas.

Chapter 2: Aim of the thesis

Chapter 3: Biomass Valorization via Pyrolysis

Section 3.1. Introduction: an introduction to the primary pyrolysis products (bio-oil, biochar, and biogas) and pathways for valorizing bio-oil and biochar.

Section 3.2. Biochar as support for heterogeneous catalyst: a detailed study of lignocellulosic and non-lignocellulosic biomass for biochar synthesis, focusing on biochar characteristics as catalytic supports, with practical examples in catalysis.

Section 3.3. Hydrodeoxygenation of bio-oil model compounds using biochar-based catalysts: application of selected biochars as support for catalysts in the hydrodeoxygenation of bio-oil model compounds, namely isoeugenol and furfural.

Chapter 4: Recovery of Char from Pyrolysis of Mixed Plastics

After a brief overview of plastic pyrolysis processes and industry trends toward adopting this technology for plastic recycling, this section discusses the Boudouard reaction application in valorizing char derived from mixed plastic pyrolysis, with the specific aim of producing carbon monoxide—a valuable input for plastic production.

Chapter 5: General Conclusions

This chapter summarizes the key findings of the research, highlighting the major goals achieved and their contributions to the understanding of biomass and plastic valorization through pyrolysis. It reflects on how these investigations have advanced knowledge in these fields and their implications for sustainable waste management.

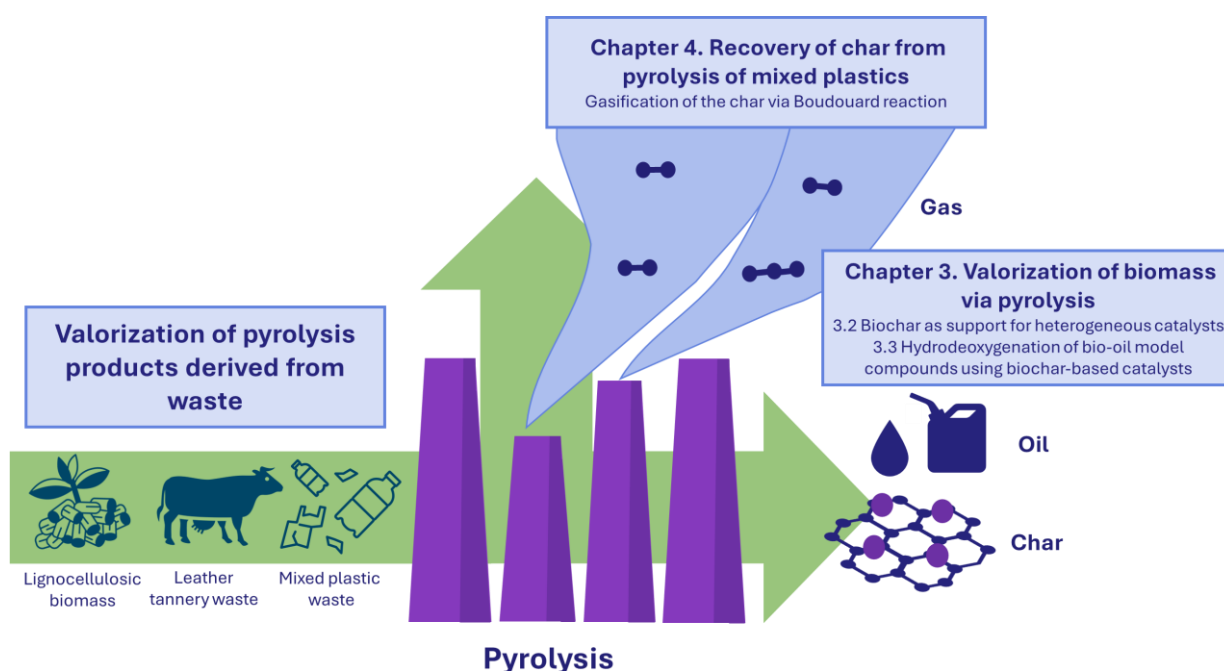


Figure 2.1. Schematic representation of the developed topics of the thesis.

3. Valorization of biomass *via* pyrolysis

3.1 General introduction

Lignocellulosic biomass pyrolysis

Among the various types of biomasses, lignocellulosic biomass is the most extensively studied and utilized. These materials comprise three primary components: lignin, cellulose, and hemicellulose (Figure 3.1.1). Cellulose is a linear polysaccharide made up of glucose monomers linked by β -glycosidic bonds, while hemicellulose is a heteropolysaccharide composed of a variety of sugars, including glucose, galactose, mannose, xylose, arabinose, and glucuronic acid. Lignin, the structural component of the biomass cell wall, consists of phenylpropane polymers. During pyrolysis, each component undergoes distinct reactions, resulting in the production of bio-oil, biogas, and biochar. Cellulose and hemicellulose decompose at lower temperatures (below 400 °C), producing furans, ketones, and aldehydes in the liquid phase, as well as gases such as CO, CH₄, CO₂, and H₂, alongside char resulting from the repolymerization of these products. In contrast, lignin decomposes at higher temperatures (>400 °C), generating a range of gaseous products, including H₂, CH₄, C₂H₄, C₂H₆, C₃H₄, formaldehyde, and acetaldehyde, along with phenolic liquid compounds. The majority of the produced char originates from the lignin fraction, due to the condensation of aromatic rings during its decomposition¹⁻⁴.

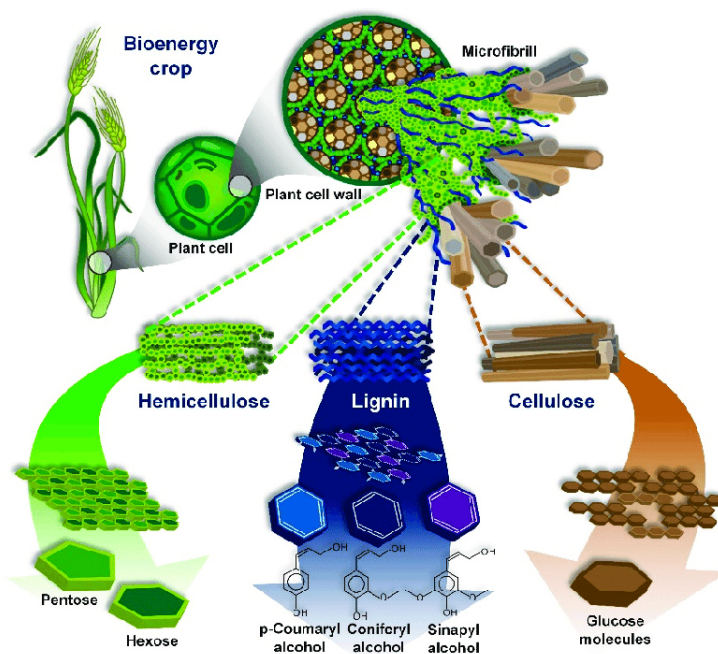


Figure 3.1.1. Structure of lignocellulosic biomass. Source: Applied Science 2019, 9, 3721⁵.

3. Valorization of biomass *via* pyrolysis

Several types of biomasses have been explored as feedstock for pyrolysis, including agricultural residues such as waste wood, nutshells, wheat straw, and husks. The most studied biomass types are presented in Table 3.1.1. The selection of biomass and the pyrolysis conditions are typically tailored to the desired primary product.

Table 3.1.1. Key lignocellulosic biomass types used in pyrolysis and their respective compositions adapted from Garba et al.⁶.

Feedstock	Cellulose (wt%)	Hemicellulose (wt%)	Lignin (wt%)	Reference
Pinewood	49	16	25	[7]
Rice straw	38	27	13	[8]
Rice Husk	29	16	7	[8]
Switch grass	23	19	20	[8]
Pine sawdust	35–45	25–30	10–30	[8]
Palm shell	28	22	27	[9]
Palm tree fibers	28	30	27	[9]
Empty fruit bunches	51	21	23	[9]
Beach wood	42	31	12	[10]
Empty Fruit bunches	43	20	22	[10]
Sawdust	32	20	30	[10]
Wheat shell	11	21	26	[10]
Palm kernel shell	31	31	32	[11]
Wheat straw	37–41	27–32	13–15	[12]

Non-lignocellulosic biomass pyrolysis

In addition to lignocellulosic biomass, various non-lignocellulosic biomasses (NLBM) have been utilized for pyrolysis, including algae, hair, bones, sewage sludge, meat, manure, feathers, leather, and other animal-derived byproducts¹³. These biomasses have a fundamentally different composition compared to lignocellulosic biomass and can vary significantly among themselves. Generally, their primary components include proteins, lipids, and carbohydrates. During pyrolysis, the weaker bonds, such as hydrogen bonds in proteins, begin to break down at around 200 °C, with the main decomposition of organic materials occurring between 300–600 °C. Unlike lignocellulosic biomass, NLBM contains significant amounts of nitrogen, sulfur, and phosphorus, leading to more complex pyrolysis reactions¹⁴.

The properties of products deriving from NLBM can vary depending on the feedstock, so that the desired requirements can be addressed by selecting biomass sources. For instance, algae are typically used to produce gas (such as hydrogen)^{15,16} or bio-oil¹⁷ due to their high lipid content, while animal-derived biomasses are often targeted for char production, as the presence of proteins enables natural nitrogen doping^{18,19}.

This thesis is focused on the valorization of both lignocellulosic biomass and animal-derived waste - specifically leather shaving waste generated from the tannery process²⁰ - via pyrolysis. The application of pyrolysis for the valorization of this waste is still scarce²¹. The first to study the kinetics of thermal decomposition of tannery waste were Cabellero *et al.* in 1998²², and most of the studies were focused on char production²³⁻²⁷, with only a few on the valorization of this waste for bio-oil production²⁸⁻³⁰. As already mentioned, three distinct fractions can be obtained from biomass pyrolysis, namely biogas, biochar and bio-oil. As all three fractions can be exploited to produce high added value chemicals, materials and fuels, therefore their main characteristics and applications are discussed below.

Biogas

The biogas produced from biomass pyrolysis primarily consists of H₂ and CO, along with CH₄, CO₂ and several low molecular weight organic compounds, such as short chain hydrocarbons³¹. Although biogas has a significantly lower heating value compared to natural gas (6 MJ/kg vs. 54 MJ/kg), it is commonly used as an energy source, particularly for sustaining pyrolysis^{14,32}. Moreover, biogas can serve as a sustainable source for syngas production, which can then be converted into hydrogen or other fuels and chemicals³³.

Biochar

Biochar is the solid byproduct of pyrolysis, primarily composed of carbon (65-90%)³⁴ along with smaller amounts of hydrogen, oxygen, and trace quantities of nitrogen, phosphorus, sulfur, and inorganic species (ash), including K, Na, Ca, Mg, Si, Al^{35,36}. By sequestering carbon in its structure for extended periods, biochar can serve as a carbon sink, contributing to the reduction of greenhouse gas (GHG) emissions and potentially becoming a carbon-negative material^{37,38}.

Biochar structure consists of condensed aromatic rings, varying between amorphous, turbostratic, and graphitic forms, depending on pyrolysis conditions, particularly temperature³⁹. Pyrolysis temperature also has a significant impact on biochar physicochemical properties, such as surface area, pH, and surface functional groups⁴⁰. Moreover, also the nature of the feedstock strongly influences the final properties of biochar^{41,42}.

In terms of chemical composition, heteroatoms present in the biomass can be retained in the biochar matrix, or as surface functional groups, including carboxyl, hydroxyl, amino, and lactone groups. The presence of functional groups on biochar surface is an important characteristic for several biochar applications, such as soil amendment, adsorbent and catalyst⁴³.

The starting raw material also has influence on biochar's porosity and texture. The selection of feedstock with hierarchical structures, such as wood, grasses, and nut shells, can result in hierarchical porosity of the final biochar^{44,45}. In lignocellulosic biomass, the decomposition of cellulose and hemicellulose leads to the formation of channels and pores, while a higher lignin content results in a biochar with a greater surface area^{46,47}. Biochars derived from non-lignocellulosic biomass tend to have higher inorganic content, although certain lignocellulosic feedstocks, such as rice husk, naturally contain high silica content that is retained in the biochar¹³. Ash content plays a significant role in biochar's final structure, as it can act as an intrinsic catalyst during pyrolysis, promoting oxidation and increasing surface area, or during subsequent activation processes.

The textural properties of biochar can be modified by proper activation steps. Activation is a thermal treatment occurring in presence of both chemical (KOH, ZnCl₂, K₂CO₃, H₂SO₄, H₃PO₄) or physical (CO₂, steam, ozone) agents that lead to oxidation and devolatilization of part of the carbonaceous structure in form of CO and CO₂, generating new porosity and enhancing the surface area. An example of the reactions occurring during physical activation is reported in Eq. 3.1.1, and Eq. 3.1.2. Physical activation occurs at high temperatures (800-900 °C)^{48,49} and maximize the formation of micropores^{33,50}. The chemical activation allows the formation of chars with modulable porosity, ranging from micro to mesopores, and to work at lower temperatures, but it requires corrosive compounds that complicate the scalability of the process and can lead to damages of the plants^{34,51} (Figure 3.1.2).



Due to its high carbon content, electrical conductivity, thermal stability, and potential for large surface areas, biochar has attracted attention as a sustainable alternative to other carbon-based materials. Its chemical, textural, and morphological properties can be finely tuned for specific applications through treatments such as activation and doping⁵². Biochar has been applied in diverse fields, including soil amendment⁵³⁻⁵⁷, abatement of pollutants and water treatment^{36,39,46,56,58}, energy production^{59,60}, and catalysis^{35,61-64}.

The valorization of biochar as support for the preparation of heterogeneous catalysts has been part of this work of thesis, and it is discussed in detail in Chapter 3.2.

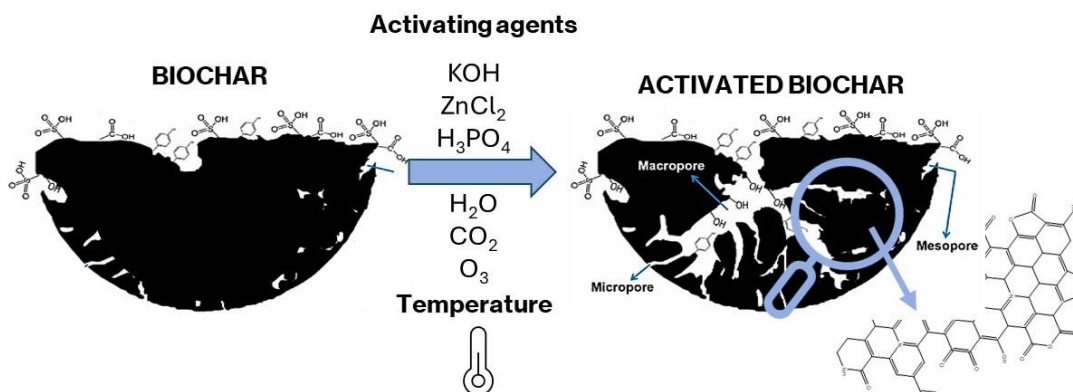


Figure 3.1.2. Biochar structure and modification after activation.

Bio-oil

Bio-oil is the condensable fraction obtained from the pyrolysis of biomass. The composition of bio-oil is strongly influenced by the original biomass feedstock, and the pyrolysis conditions. The most exploited biomass for bio-oil production is lignocellulosic biomass, deriving from agriculture and forestry residues. Bio-oil is a complex liquid, containing more than 250 distinct compounds, characterized by a high oxygen content. It also has a high amount of water, comprising up to 25 wt. %^{65,65}, which originates from the moisture of biomass and from the condensation reactions occurring during pyrolysis. The organic major components are acids (3-5 %), aldehydes and ketones (3-4,5 %), anhydrosugars (1-5 %), alcohols (~1 %), furans (1-3 %), cyclopentenones and phenolic compounds (1-5 %)⁶⁶. Lyu *et al.*, investigated the bio-oil composition of four different lignocellulosic biomasses (bagasse, corncob, spruce, and pine) and recognized the molecules represented in Figure 3.1.3 as main components of bio-oil⁶⁶.

Due to the high oxygen content (15-60 %), bio-oil exhibits high viscosity, instability, and corrosiveness. It is prone to polymerization and polycondensation during storage or heating, leading to changes in its chemical and physical properties⁶⁷. The high oxygen content also causes a low calorific value, with bio-oil yielding about 17 MJ kg⁻¹, compared to 40 MJ kg⁻¹ for conventional petroleum fuels^{29,68}. Furthermore, the presence of polar oxygenated compounds renders bio-oil immiscible with traditional hydrocarbons, precluding direct use through blending. Consequently, bio-oil cannot be used as an alternative biofuel without further upgrading⁶⁹⁻⁷¹.

3. Valorization of biomass *via* pyrolysis

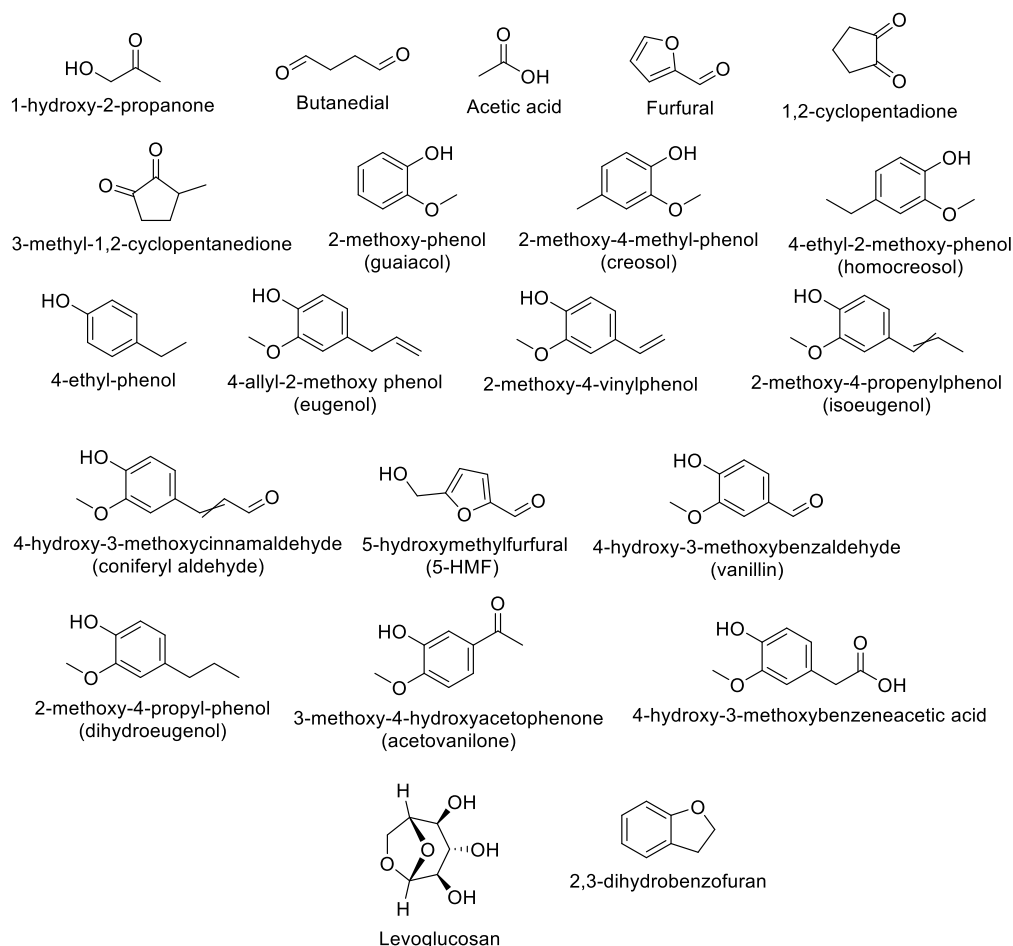


Figure 3.1.3. Principal compounds of bio-oil.

Significant research has been devoted to improving bio-oil quality. The most widely studied upgrading methodologies include emulsification, steam reforming⁷², hydrocracking^{73,74}, catalytic cracking^{75,76}, and hydrodeoxygenation (HDO)⁷⁷. Emulsification⁷⁸, the simplest method, involves mixing bio-oil with hydrocarbon using surfactants to stabilize the mixture. While this method improves bio-oil's stability and viscosity, it does not mitigate its corrosivity, nor substantially enhance its calorific value.

Catalytic upgrading, including hydrocracking, steam reforming, and HDO offers more promising routes for bio-oil enhancement. However, steam reforming of bio-oil primarily aims to produce H₂, making this strategy unsuitable for generating liquid biofuels. Hydrocracking, in contrast, employs hydrogen to break down larger molecules into smaller ones, while HDO focuses on removing oxygen functionalities without cleaving carbon chains. The HDO process is particularly advantageous for producing diesel, gasoline and kerosene-grade hydrocarbons^{79,80}.

The valorization of bio-oil model compounds through HDO to produce biofuels has been one of the key topics in this PhD thesis, and it is addressed in detail in Chapter 3.3.

3. Valorization of biomass *via* pyrolysis

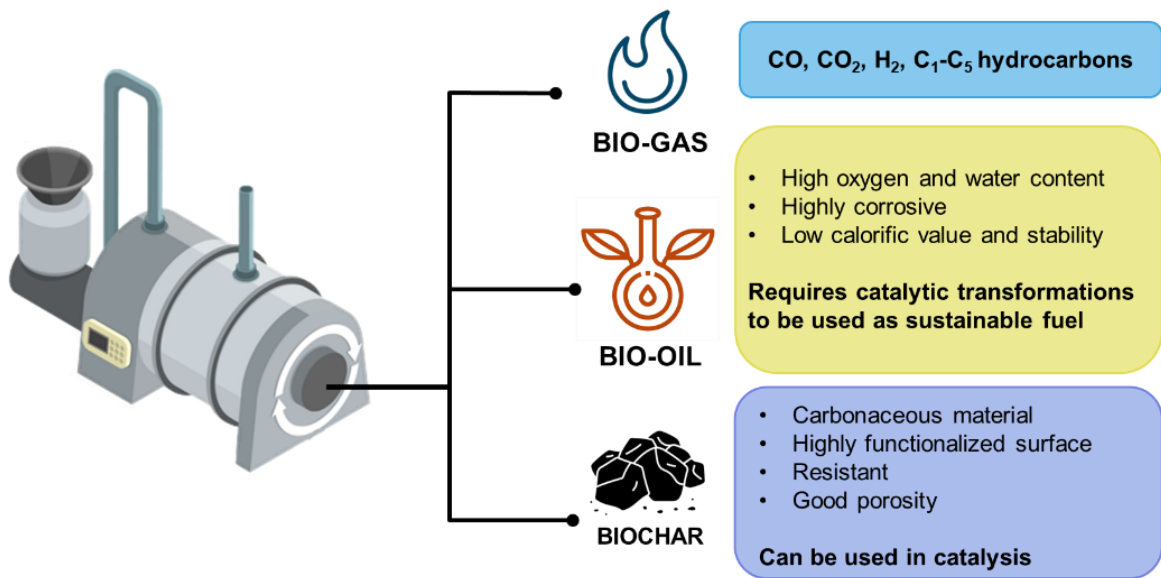
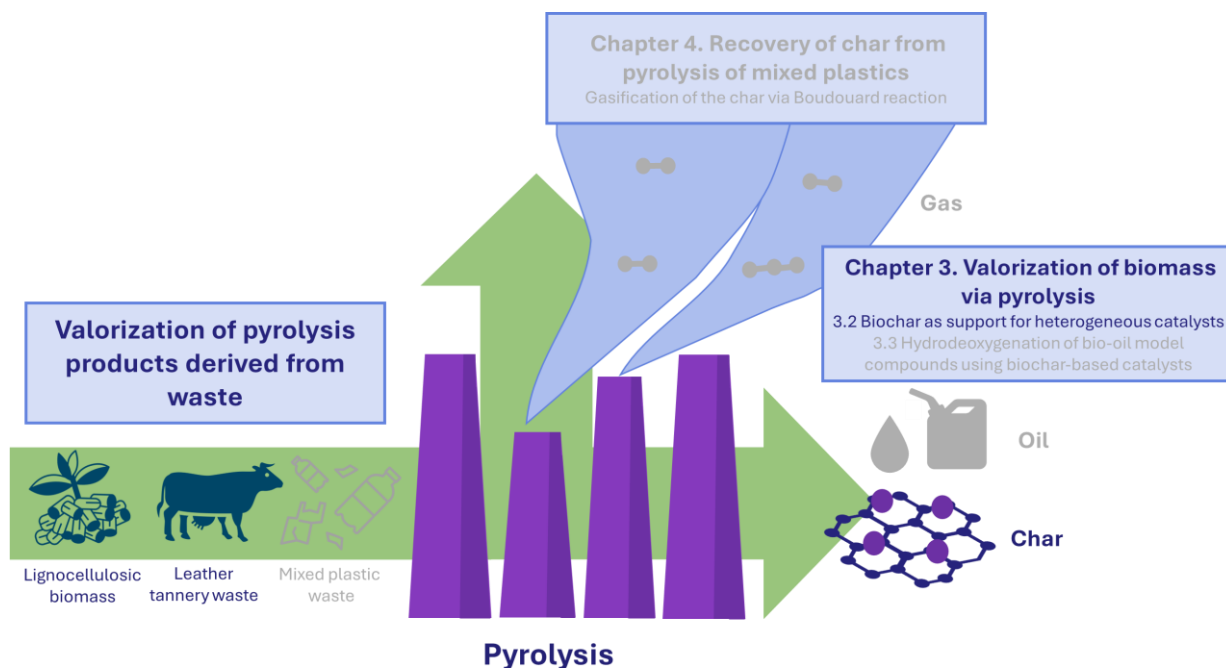


Figure 3.1.4. The three fractions obtained from biomass pyrolysis.

3.2 Biochar as support for heterogeneous catalysts



3.2.1 Introduction

In the context of a circular economy, the reutilization of materials traditionally considered waste is a critical strategy. While the valorization of lignocellulosic biomass is a major focus, other types of waste — such as those from industrial sectors — present greater challenges for reuse and require deeper investigation. One such sector is the leather industry, which encompasses the global processing, production, and distribution of leather. Due to growing demand for leather goods⁸¹, this industry is expanding, with Italy holding a leading position in European leather production⁸².

The tannery process involves several stages, including rawhide collection, tanning, finishing, and the manufacture of leather goods. This industry plays a significant role in both the agricultural and fashion sectors, though it is also associated with considerable environmental impacts due to chemical usage and waste generation. Leather tanning refers to the process of treating hides to make them durable and resistant to decomposition, involving steps such as cleaning, fleshing, splitting, tanning, shaving, and buffing⁸³. However, the process is notorious for producing large volumes of toxic solid and liquid waste, with an estimated 700 kg of solid waste generated per 1000 kg of wet salted leather⁸⁴. Sustainability initiatives, including the use of Cr-free tanning agents (such as vegetable tannins or organic polymers) and the valorization of byproducts like tannery residues, are increasingly gaining importance in modern leather production.

Among tannery waste, shaving residues account for about 35-40% of the total, representing a significant environmental and economic challenge due to the impact related to their disposal impact.

Pyrolysis, being a versatile and cross-cutting technology, has been explored as a treatment method for leather waste. The pyrolysis of leather wastes has been investigated over the years²¹, especially for char production and use in several applications, such as solid fuel⁸³, pollutants absorption and abatement^{85,86}, supercapacitors⁸⁷, and fertilizers^{84,88}. Under European legislation, the use of materials derived from animal transformations in some fields, particularly in soil amendments, cosmetics, and the food industry, is prohibited⁸⁹. Consequently, alternative applications for these materials must be explored. Recently, our research group explored the potential of an activated biochar derived from metal-free leather shaving waste (LS) prepared using *Life GOAST* (Green Organic Agents for Sustainable Tanneries) technology. The pyrolysis of this material has been shown to produce high yields of biochar and its performances as anode material for Li and Li-free batteries have been investigated²⁷. In this work of thesis, particular attention is given to the use of biochar derived by leather shaving waste as support for heterogeneous catalysts, to be used in hydrogenation reactions.

Carbon-materials have long been employed in heterogeneous catalysis, both as active catalysts and as support for active phases⁹⁰. It is well established that the role of support extends beyond merely providing a carrier for the active phase to enhance dispersion and prevent leaching or sintering, and they can actively contribute to the catalytic process. This occurs either through direct interactions with the active phase, modifying its catalytic properties, or through interactions with reactants, enhancing chemisorption. For instance, carbon atoms located at the edges of graphitic planes are unsaturated, with a high density of unpaired electrons that serve as active sites for the chemisorption of reactant.

Biochars and activated biochars possess a highly disordered structure with a significant number of edge carbon atoms. In addition, key features such as high surface area and modifiable porous structure, the presence of heteroatoms in the structure (i.e. N-doping) or on the surface, (hydroxyl, carboxylic, lactone, amino groups), have an important role in its catalytic applications. High surface area allows to achieve high dispersion of the metal phase, increasing the available active sites for the reaction to occur⁹¹. Furthermore, a hierarchical network of interconnected meso- and micropores facilitates reactant diffusion to the active sites. The presence of heteroatoms in the carbon lattice, (such as N-doping) can modify its electronic properties, by promoting charge delocalization and disrupting the inert sp² carbon network⁹². Recently, N-doped carbons have attracted considerable attention due to their ability to enhance catalytic performance^{93,94}. Nitrogen doping induces lattice deformation in the carbon structure, creating defects that enrich the surface with protons, thereby enhancing the hydrogenation capability of non-noble metals. N-doping can be achieved through the pyrolysis of nitrogen-containing

compounds, such as melamine, combined with organic substances like glucose⁹⁵. Alternatively, N can be naturally present in the biomass used for carbon production, such as in leather shaving waste, which is rich in proteins⁹⁶, or in shrimp shells, which contain chitin⁹⁷. Surface functionalities, in turn, contribute to catalyst performance by enhancing the anchoring of active metals, stabilizing the catalyst against leaching and sintering^{98,99}, reducing biochar hydrophobicity to improve wettability in aqueous environments, and influencing surface acidity to boost reactions such as acid-catalyzed transesterification⁶². Moreover, biochar exhibits high thermal stability, resistance to acidic and basic environments, and moderate mechanical strength. The structural flexibility of carbon-based materials allows for the customization of catalytic properties to meet specific requirements. These attributes make biochar a highly suitable material for catalytic applications, either as a catalyst itself or as a support for active phases.

Unlike other carbonaceous materials, such as activated carbon, graphite, or carbon nanotubes, which can only be derived from specific precursors, biochar can be produced from virtually any biomass through pyrolysis. Nevertheless, the properties of the resulting biochar are heavily influenced by the type of feedstock used. Biochars derived from both LBM and NLBM have been employed as catalyst or support in various catalytic fields, such as contaminant degradation^{58,85,100}, fine chemical synthesis^{62,101-103}, biomass and bio-oil upgrading^{64,104}, bio-oil upgrading¹⁰⁵⁻¹⁰⁸, and reforming processes^{35,63,109-111}. Buentello-Montoya, *et al.*¹¹² utilized hardwood biochar and activated biochar as catalyst for the steam reforming of tar. Guo *et al.*¹¹³ explored the catalytic activity of Fe-group metals supported on biochar for the catalytic microwave pyrolysis. Biochar has also been used for the preparation of heterogeneous catalysts for the upgrading of bioderived platform chemicals, such as vanillin¹¹⁴⁻¹¹⁶, guaiacol¹¹⁷, and 5-hydroxymethyl furfural^{96,118}, and it has also found applications in photocatalysis³⁹.

The choice of biomass feedstock is well known to play a pivotal role in shaping the properties of biochar, which subsequently impact the performance of the resulting catalyst. In this study, alongside leather shaving waste (LS), additional second-generation biomass sources, particularly lignocellulosic materials, were carefully selected. These included hazelnut shells, rice husks, and rice grains, chosen due to their local abundance in Italy, aligning with sustainability and circular economy goals. The study had multiple objectives: to highlight the fundamental influence of biomass feedstock on biochar characteristics and to optimize these properties for enhanced valorization of diverse biomass types.

The selected second-generation biomasses are described above:

- a) Leather tannery shaving waste (LS), derived from a chromium-free tanning process. It is a solid waste, mainly consisting of collagen fibers, proteins and tanning agents (organic green polymers)¹¹⁹.
- b) Hazelnut shells (HS), a lignocellulosic biomass, composed mainly of lignin, cellulose and hemicellulose. This byproduct is highly abundant in Italy, which ranks as the second-largest producer of hazelnut in the world^{92,120}.
- c) Rice husks (RH), another LBM, which, in addition to its lignocellulosic components, contains a significant amount of silica (approximately 30 %)¹²¹.
- d) Broken rice grains (RG) are an industrial byproduct obtained from the whitening and polishing process of rice. It is rich in starch, protein, vitamins, and minerals. Both RH and RG, byproducts of rice production, represent a globally highly abundant biomass resource, as rice is one of the most widely consumed foods worldwide¹²².

In addition to examining individual pyrolysis processes, the study explored the co-pyrolysis of two different feedstocks (leather shaving waste and rice husks) to investigate how this approach could further modify the properties of both biochar and catalysts, potentially offering new avenues for performance optimization. The findings related to co-pyrolysis will be addressed in detail in Chapter 3.2.4.

The biomasses underwent slow pyrolysis to maximize biochar yield. The resulting biochars were characterized by (CHNS, ash content, N₂ physisorption, SEM) and to further enhance their suitability as catalyst supports, they were physically activated using steam. To evaluate their catalytic potential, the biochar-based materials were used to prepare Pd-supported catalysts for hydrogenation reactions. Pd/C remains one of the most widely used hydrogenation catalysts in industry, and finding alternative sources for activated carbon is a critical topic in catalysis. In this study, the hydrogenation of benzaldehyde was selected as a model reaction to test the performance of the Pd/C catalysts, with potential industrial applications in aldehyde hydrogenation processes, such as the hydrogenation of 4-carboxybenzaldehyde (4-CBA) during terephthalic acid¹²³⁻¹²⁶, and bio-oil upgrading^{127,128}.

The main and side reaction pathways for hydrogenation of benzaldehyde are schematized in Figure 3.2.1.1. Typically, the main reaction is consecutive, consisting of two steps: in the first step, the reduction of the aldehyde group occurs with the formation of the benzyl alcohol (II) as the intermediate. Benzyl alcohol, in the presence of hydrogen and the hydrogenation metal-based catalyst, goes through the hydrogenolysis of the C-O bond, leading to the formation of toluene (III)¹²⁶. When using ethanol as

the solvent and in the presence of acidity, acetal (IV) and ethoxy methylbenzene (V) can be produced through side reaction pathways^{129,130}.

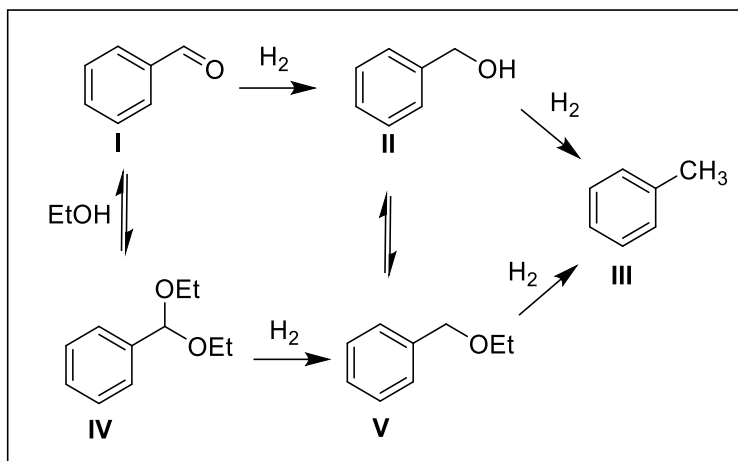


Figure 3.2.1.1. Reaction pathway from benzaldehyde to toluene.

Benzyl alcohol and its derivatives are important intermediates in the synthesis of vitamins, drugs, pesticides, fragrances, and various ethers used in the cosmetic and flavoring industries. It is also used as a solvent for inks, paints, and lacquers. On the other hand, toluene is an excellent organic solvent being widely used in the production of benzene derivatives, caprolactam, saccharin, an intermediate in the synthesis of dyes, perfumes, polyurethane resins, and furthermore as an additive in gasolines to increase the octane number^{131,132}.

Since the hydrogenation of the aldehydic group, and the hydrogenolysis of the hydroxyl group to toluene are consecutive reactions, it is possible to modulate the conditions to selectively conduct the reaction to the desired product. Nevertheless, the study of this tandem reaction is useful to understand and compare the activity of different catalysts and to explore the potentiality of biochars as catalytic supports.

In the hydrogenation of benzaldehyde, different types of catalysts have been used and tested mostly based on noble metals such as Pd¹²³, Pt¹³³, Ru¹³⁴, Rh¹³⁵, which are still the most efficient ones and also non noble metals such as Ni¹³⁶, Co¹³⁷, and Cu¹³⁸. In addition, various supports based on oxides such as alumina, silica zirconia, titania, ceria, and carbon have been applied for the reaction¹³⁸⁻¹⁴¹. Up to now, biochar obtained from different classes of biomasses has been used as the support of metal-based catalysts for different hydrogenation reactions^{96,142}. For benzaldehyde hydrogenation, only one study has been reported in which the carbon support was obtained from pyrolysis of lignin model component and magnetic Fe₂O₃ was loaded on the support to be used as the catalyst of the reaction. The reaction resulted in 95% yield of benzyl alcohol at full conversion of benzaldehyde with the use of non-green solvent (THF), harsh reaction conditions (120 °C, 35 bar H₂) and a very long reaction time (18 h)¹⁴³.

Hence, the aim of the present study is to investigate and optimize a proper biochar support from actual waste biomasses for Pd based catalysts to be used in targeted hydrogenation. To achieve this, after formulation of Pd/activated biochar catalysts, all supports and catalysts were characterized in depth and they were then tested in benzaldehyde hydrogenation, while comparing the result with a Pd catalyst prepared by the same technique on a commercial active carbon.

3.2.2. Experimental

Hazelnut shells (HS) from cultivar Tonda Gentile Romana were supplied by Fattoria Lucciano Soc. Agr. S.s., Civita Castellana, Viterbo, Italy; metal-free leather tannery shaving waste (LS) supplied from PASUBIO S.p.A. tannery, Arzignano, Italy, through the European project of GOAST technology, Green Organic Agents for Sustainable Tanneries; broken rice grains (RG) and rice husks (RH) were supplied by Riseria delle Abbadesse, Grumolo delle Abbadesse, Vicenza, Italy.

Pyrolysis and activation

The pyrolysis process was carried out in a laboratory-scale prototype plant (Carbolite custom model EVT 12 / 450B) consisting of a fixed bed quartz tube fixed inside a vertical tubular oven equipped with the lines and Brooks mass flow controllers for passing nitrogen inert gas and the steam activation agent. In addition, the temperature was adjusted and controlled using electrical heating system, thermocouples, and a PID temperature controller. The system is schematized in Figure 3.2.2.1.

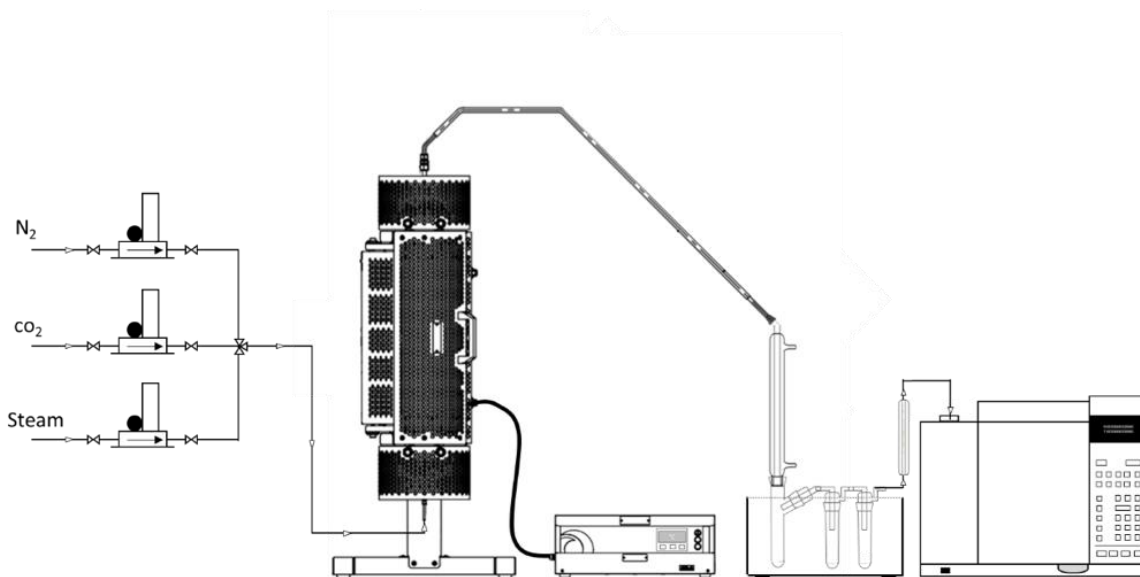


Figure 3.2.2.1. Schematic representation of the pyrolysis plant.

About 40 g of biomass was loaded inside the quartz reactor. The pyrolysis was carried out in the presence of a nitrogen flow of 100 mL/min and the system was heated up to a 700 °C, with a ramp of 5 °C/min and it was maintained at this temperature for 30 min. The biochars obtained by pyrolysis were labeled as B-HS, B-RH, B-RG, and B-LS, according to the feedstock. After pyrolysis, the biochar was subjected to the physical activation process by steam in the same oven at temperature of 850 °C, with a rate of 10 °C/min, in the presence of a H₂O/N₂ mixture at 50 vol. % with a total gas flow of 100 mL/min, for 90 minutes. The activated biochars were washed with a 1M HCl solution, in a ratio of 1 g activated

biochar: 20 mL HCl solution. The suspension was left in ultrasound for 1 h to eliminate most of the inorganic components, that can be found in variable amounts in natural feedstocks, and then it was filtered, washed with deionized water until reaching a neutral pH²⁷. The sample was dried in an oven at 110 °C for 16 h and finally, it was ground and sieved to obtain a powder with the fraction between 105-63 µm. The final samples were labelled A-LS, A-HS, A-RH, A-RG, respectively. A commercial activated carbon (AC) was used as a reference to compare the catalytic properties of the selected materials.

Catalyst preparation

The Pd catalysts were synthesized using wet impregnation technique. First, 1 g of activated biochar or commercial active carbon was mixed with a predetermined amount of aqueous solution of H₂PdCl₄ as Pd precursor to obtain nominal Pd content of 0.6 wt.% in the final catalyst. The palladium was reduced with a sodium formate solution at 80 °C. The final suspension was filtered and washed with deionized water until the complete elimination of the chlorides, and the catalysts was then dried at 110 °C for 18 hours.

Biomass, biochar, support and catalyst characterizations

The CHNS elemental analyses of biomasses, biochars and activated biochars were performed using UNICUBE organic elemental analyzer (Elementar). The percentage of ash was calculated following the thermos-gravimetric analysis (TGA 8000 PerkinElmer) according to the ASTM-D7582 protocol and the oxygen percentage was calculated by difference of the two analyses, as given by the following equation (Eq.3.2.2.1):

$$O\% = 100 - (C\% + H\% + N\% + S\% + \text{ash}\%) \quad (\text{Eq.3.2.2.1})$$

Fourier transform infrared (FT-IR) analyses were performed by Perkin Elmer Spectrum, one spectrometer with a wave number range of 400 – 4000 cm⁻¹ and resolution of 4 cm⁻¹ at room temperature. To evaluate the surface area and pore volume, N₂ physisorption analyses were carried out at -196 °C using Tristar II Plus Micromeritics (MICROMERITICS USA). Samples (ca. 50 mg) were previously degassed at 200 °C for 2 hours using a vacuum degasser system. The surface area was calculated by the Brunauer Emmett Teller (BET) and Langmuir and T-Plot equations and the total pore volume V_{tot} was measured according to the adsorbed amount of N₂ and p/p₀ (absolute pressure/saturation vapor pressure) values near 0.98. Pd effective amount was analyzed by Microwave Plasma – Atomic Emission Spectrometry (Agilent Technology 4210 MP-AES). About 50 mg of the catalyst was digested with a mixture containing 5 mL of HCl (37 %): HNO₃ (65 %) = 3:1 and 5 mL of deionized water for 5 hours.

X-ray powder diffraction (XRD) analyses were carried out by a Bruker D8 Advance Da Vinci diffractometer equipped with LynxEye detector and a sealed tube providing CuK α radiation at an accelerated voltage of 40 kV and an applied current of 30 mA.

Scanning electron microscopies (SEM) were carried out using a FE-SEM LEO 1525 ZEISS (Jena, DE). The acceleration potential voltage was maintained at 15 keV and measurements were carried out using AsB detector (Angle selective Backscattered detector) and In-lens detector. Samples were deposited on conductive carbon adhesive tape and metallized by sputtering with chromium (8 nm). Elemental composition and chemical mapping were determined using a Bruker Quantax EDX.

TEM images were obtained using a Philips 208 Transmission Electron Microscope. The samples were prepared by putting one drop of an ethanol dispersion of the catalyst powder on a copper grid pre-coated with a Formvar film and dried in air.

Temperature Programed Reductions (TPR) of catalysts were carried out with a lab-made instrument under 5 vol % H₂ in Ar flow, heating from 25 °C to 800 °C with a ramp of 10 °C min⁻¹. The effluent gases were analyzed by a Micrometrics TPDTPR 2900 analyzer equipped with a TCD detector (Gow-Mac 24-550 TCD instrument CO, Bethlehem, PA, USA).

Catalyst testing

Benzaldehyde hydrogenation was carried out in a semi-batch reactor, consisting of a jacketed three-necked flask. A hydrogen bubbler was inserted to flow the gas into the solution at atmospheric pressure. The flask was equipped with an external jacket, which was connected to a thermostat (Haake DC 30) allowing the reactor temperature to be kept constant throughout the reaction time.

Preliminary tests were carried out to verify that during the reaction, the conversion of benzaldehyde to the respective products was not affected from mass transfer phenomena (diffusion). The chosen reaction conditions were the following. Solvent: ethanol (20 mL), temperature: 25 °C, pressure: 1 bar, benzaldehyde/Pd: 260 w/w, benzaldehyde concentration: 0.1 M, stirring speed: 1500 rpm, H₂ flow: 33 mL/min, catalyst particle size: between 105-63 μm ¹²³. In a typical catalytic test, 160 mg of catalyst and 20 mL of ethanol (>99.9% J.T. Baker) as the solvent were loaded in the reactor, which was saturated with H₂ under stirring. The temperature was increased to 80 °C to activate the catalyst and these conditions were maintained for 1 h. At the end of this first phase, the temperature was decreased to 25 °C, and the benzaldehyde (>99% Aldrich) and internal standard (n-octane, > 99 % Fluka) were added. The reaction solution was taken at certain time intervals, and it was analyzed using an Agilent Technologies 7820 gas chromatograph equipped with an HP-5 column (L=30 m, \varnothing = 0.32 mm and film made of polysiloxane = 0.25 μm) with FID detector.

In addition, the types of products were confirmed using a GC/MS (EI, 70 eV) with a HP5-MS capillary column (L= 30 m; Ø= 0.32 mm; film= 0.25 µm). The relative error of repeating reactivity test for each catalyst was less than 5 %. For the catalyst recycling, the same conditions were employed. Between the cycles, the catalysts were filtered and washed with ethanol, and dried in the oven at 110°C.

The benzaldehyde conversion and products selectivity were calculated according to the following equations (Eq. 3.2.2.2, 3.2.2.3):

$$\text{Conversion (\%)} = \frac{\text{moles of reacted benzaldehyde at a certain time}}{\text{initial moles of benzaldehyde}} * 100 \quad (\text{Eq. 3.2.2.2})$$

$$\text{Selectivity (i) (\%)} = \frac{\text{moles of product (i) at a certain time}}{\text{moles of product (i)+moles of other products}} * 100 \quad (\text{Eq. 3.2.2.3})$$

3.2.3 Results and discussion

Characterization of biomass, biochars and activated biochars

The chemical composition of the biomasses (HS, LS, RG, RH), biochars (BCs) (B-HS, B-LS, B-RG, B-RH) and the corresponding activated biochars (ACs) (A-HS, A-LS, A-RG, A-RH), as well as the commercial activated carbon (AC) was estimated by elemental analysis and determination of the ash content. The yield of BCs after pyrolysis and ACs after activation are also reported. The results are reported in Table 3.2.3.1.

Table 3.2.3.1. CHNS elemental analysis of biomasses, biochars, activated biochars and commercial carbon. The amount of elements is reported in mass percentage.

Samples	Yield (%)	C [%]	N [%]	H [%]	S [%]	O [%]	Ash [%]	H/C	O/C
HS	/	49.1	0.3	5.7	0.5	42.9	0.9	0.12	0.87
B-HS	30	86.1	0.3	2.2	0.1	9.4	1.8	0.03	0.11
A-HS	57.6	94.3	0.2	0.8	0.1	4.0	0.5	0.01	0.04
LS	/	46.9	11.5	6.1	3.4	28.6	3.4	0.13	0.61
B-LS	33	74.1	10.3	1.6	1.1	4.8	8.0	0.02	0.06
A-LS	55.0	81.5	6.0	1.8	0.5	7.1	3.0	0.02	0.09
RG	/	44.7	1.7	7.0	0.5	46.2	0.7	0.16	1.03
B-RG	27	85.2	26	1.9	0.2	5.6	4.5	0.02	0.07
A-RG	67.9	87.7	1.8	1.0	0.1	8.3	1.0	0.01	0.09
RH	/	37.7	0.6	5.1	1.0	55.7	18.1	0.13	1.48
B-RH	38	50.9	0.4	1.2	0.2	2.4	44.5	0.03	0.05
A-RH	70.7	39.4	0.2	0.5	0.1	3.2	56.6	0.01	0.08
AC	/	92.5	0.2	0.5	0.1	6.4	0.2	0.005	0.07

After pyrolysis, the biochar yield for all samples was approximately 30%, aligning with values reported in literature as 31% yield for HS under comparable conditions¹⁴⁴. Yilmaz and coworkers²¹ reported a 44% yield of biochar from vegetable-tanned leather at 600°C. The lower biochar yield observed in our study is attributed to the higher pyrolysis temperature, which promotes further decomposition of the biomass into liquid and gaseous products. The higher yield noted for B-RH, compared to the other biochars is linked to its elevated inorganic content (ash), which is not involved in the pyrolysis process and remains in the solid fraction.

The activation process resulted in burn-off values ranging from 30% to 70%, corresponding to an increase in porosity. The highest burn-off values were observed in samples that experienced the greatest surface area expansion during activation, as confirmed by N₂ physisorption measurements (Figure 3.2.3.2, Table 3.2.3.2).

Elemental distribution varied significantly across the different feedstocks, strongly influenced by the nature of the starting materials. These differences are attributable to the complexity of biomass structures, composed of various components (cellulose, hemicellulose, and lignin in HS and RH, starch in RG, and proteins and vegetable tanning agents in LS) that differ in their thermal decomposition behavior at elevated temperatures¹⁴⁵.

Samples A-HS, A-RG, and AC exhibited notably high carbon contents (94.3%, 87.7%, and 92.5%, respectively)¹²³. A-LS, derived from animal residues primarily composed of proteins, showed a high nitrogen content (6.0%), making A-LS a natural oxygen- and nitrogen-doped carbon material. This dual doping imparts distinct characteristics to A-LS compared to biochars derived from lignocellulosic biomass. On the other hand, A-RH displayed significantly lower carbon content due to the high inorganic content, predominantly silica (confirmed also by the EDX measurement, reported in Appendix, Figure 3.2.6.1)¹⁴⁶. Activation generally led to a reduction in heteroatom content and a decrease in the H/C and O/C ratios, indicative of increased aromaticity and enhanced structural stability of the biochars^{146,147}. As shown in Table 3.2.3.1, samples AC and A-HS presented the lowest H/C ratios, suggesting a high degree of carbonization, resulting in a highly condensed and stable structure¹⁴⁹.

Despite the activation process, all biochars retained a notable amount of oxygen, likely in the form of surface oxygen-containing functional groups. Interestingly, sulfur was present in small amounts across all samples. This feature could be advantageous for catalytic applications, as sulfur is known to act as a poison for noble metals⁹⁶. The presence of surface functionalities and aromatic structures was confirmed by FT-IR spectroscopy (Figure 3.2.3.1a). Key signals included the stretching vibrations of C=C ($\sim 1548\text{ cm}^{-1}$), C-H (800 cm^{-1}), -OH (3455 cm^{-1}), and C-O ($\sim 1400\text{ cm}^{-1}$), indicating the presence of oxygenated functional groups such as ketones, aldehydes, lactones, carboxyls, alcohols, phenols, and ethers. Additional evidence of these functionalities came from Temperature Programmed Desorption (TPD) measurements³⁴ (Figure 3.2.3.1b). In this type of analysis, the functional groups are thermally decomposed releasing CO, CO₂, and H₂O at different temperatures depending on the thermal stability of the considered functional groups³⁵. In all samples, the band at temperature range of 100-400 °C is associated with the CO₂ released by the decomposition of the carboxyl groups. Moreover, the band between 800-900 °C is related to the release of CO from the decomposition of the carbonyl and quinone groups. In the TPD graphs of A-HS and A-RG samples, an additional band at 700 °C can be observed which is due to generation of CO from thermal decomposition of quinones, ethers and phenols^{150,151}. The presence of silica in A-RH was further confirmed by FT-IR, with the detection of Si-OH groups, which could enhance metal phase anchoring and dispersion within the pores of the A-RH support.

The presence of nitrogen in A-LS was also confirmed by FT-IR, with a characteristic stretching vibration of the N-H bond in alkyl or arylamines¹⁵². Prado-Burguete *et al.*¹⁵³ observed that increasing oxygen-based functional groups on carbonaceous supports with similar porosity improved the dispersion of the metal phase. Although A-RH had the lowest overall oxygen content (3.2%), its O/C ratio was comparable to those of A-RG and A-LS, due to the relatively lower carbon content in the sample. This suggests that the carbon fraction in A-RH possesses a highly oxygenated surface.

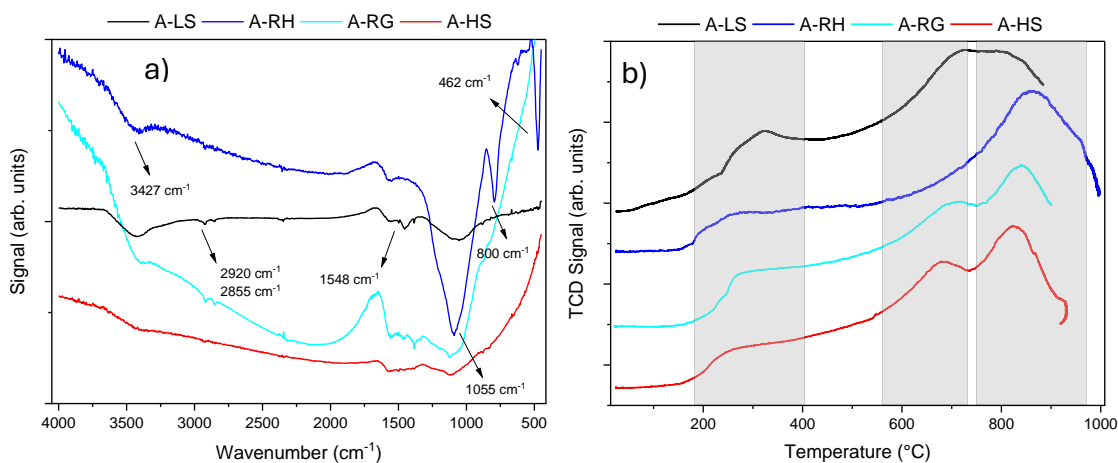


Figure 3.2.3.1. a) FT-IR spectra and b) He-TPD curves of the activated biochars A-LS (black), A-RH (blue), A-RG (cyan), A-HS (red).

The adsorption-desorption isotherms of BCs and ACs samples are shown in Fig.3.2.3.2, and the textural properties are reported in Table 3.2.3.2. The nature of the initial biomass influenced the final texture of the biochars: B-LS and B-RG biochars show type III isotherm related to non-porous materials according to the IUPAC classification, and these materials did not show any surface area. On the contrary, B-RH and B-HS biochars exhibit type I adsorption isotherms confirming the characteristic of microporous materials. These types of materials indicate surface area values greater than the previous samples. A higher porosity and surface area of B-HS and B-RH were related to the lignocellulosic origin of biomass¹⁵⁴. Indeed, during the pyrolysis, the pore structure is preserved by the stability of the lignin, which decomposition occurs at high pyrolysis temperature (above 500°C, up to 900°C)¹⁵⁵. This did not occur in the case of B-L and B-RG, that are mainly made of protein and starch¹⁵⁶. These components decompose at lower temperature, releasing a higher amount of volatiles, and resulting in a lower yield of char¹⁴⁹. To increase the porosity and surface area of all the biochars to be used as catalyst supports, a physical activation process in the presence of steam was carried out after pyrolysis. As can be seen in Fig. 3.2.3.2b, A-HS and A-RH displayed the combination of a type I and IV isotherm belonging to materials with the coexistence of both micropores and mesopores, according to the IUPAC classification.

In particular, the sharp increase of absorbed gas volume in the lower relative pressure is the characteristics of Type I isotherm and microporous materials, while the hysteresis loop in the pressure range of $0.4 < p/p_0 < 0.99$ is due to the presences of meso and macropores in the samples. In the case of A-LS, A-RG, and AC, isotherm Type I and mainly microporous texture can be observed. As can be seen in Table 3.2.3.2, the surface area of activated materials followed the order of $A-RH < A-RG < A-LS < A-HS < AC$. The high surface area of the commercial sample AC can be probably ascribable to a physical activation performed at a higher temperature compared to activated biochars prepared in this work¹⁵⁷. All activated biochars showed promising textural properties for catalytic application.

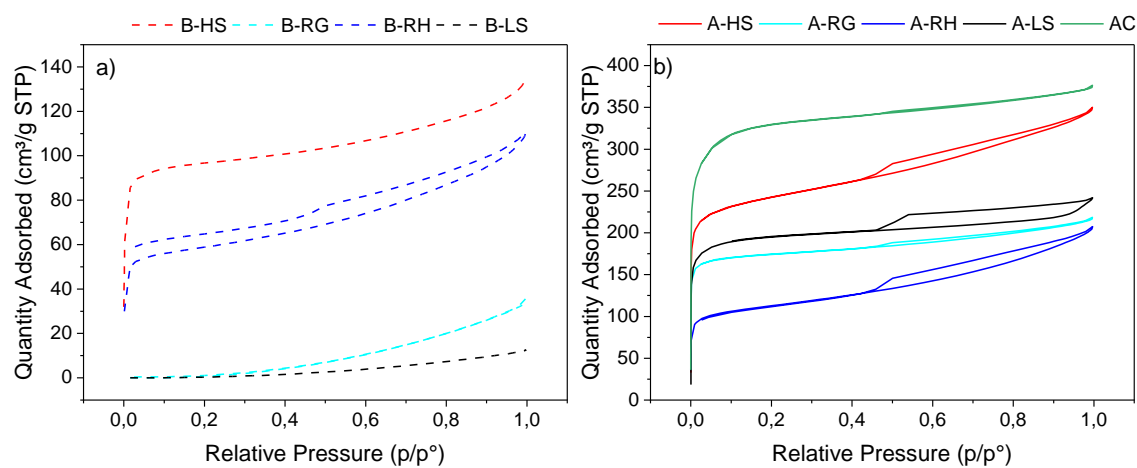


Figure 3.2.3.2. N_2 adsorption-desorption isotherms of a) biochars B-HS (dotted red), B-RG (dotted cyan), B-RH (dotted blue), and B-LS (dotted black); b) activated biochars A-HS (solid red), A-RG (solid cyan), A-RH (solid blue), A-LS (solid black), and AC (solid green).

Table 3.2.3.2. Textural properties of biochars and activated biochars measured by N_2 physisorption analyses.

Samples	S_{BET}^2 (m^2/g) ^a	S_{micro}^2 (m^2/g) ^b	V_{tot}^3 (cm^3/g) ^c	V_{micro}^3 (cm^3/g) ^d
B-HS	313	226	0,20	0,11
A-HS	794	1000	0,31	0,24
B-LS	/	/	/	/
A-LS	633	783	0,25	0,23
B-RG	/	/	/	/
A-RG	565	707	0,24	0,21
B-RH	199	270	0,15	0,06
A-RH	367	543	0,14	0,10
AC	1059	1064	0,40	0,27

^aSurface area calculated by BET method. ^bMicropore surface area calculated by t-plot method. ^cTotal pore volume calculated according to the adsorbed amount of N_2 and P/P_0 values near 0.98. ^dMicropore volume calculated by t-plot method.

3. Valorization of biomass *via* pyrolysis – 3.2 Biochar as support for heterogeneous catalysts

The lowest surface area of A-RH could be explained by the high percentage of Si in this sample¹⁵⁸, which was not altered by the activation treatment. Indeed, the activating agent can interact only with the carbon, oxygen, nitrogen and sulfur atoms in the precursor, mainly oxidizing carbon to CO and CO₂ and consequently leading to the formation of pores.

The surface morphologies of biochars, activated biochars, and AC were analyzed using scanning electron microscopy (SEM), with the corresponding images presented in Fig. 3.2.3.3 (and additional images in the Appendix, Figure 3.2.6.2).

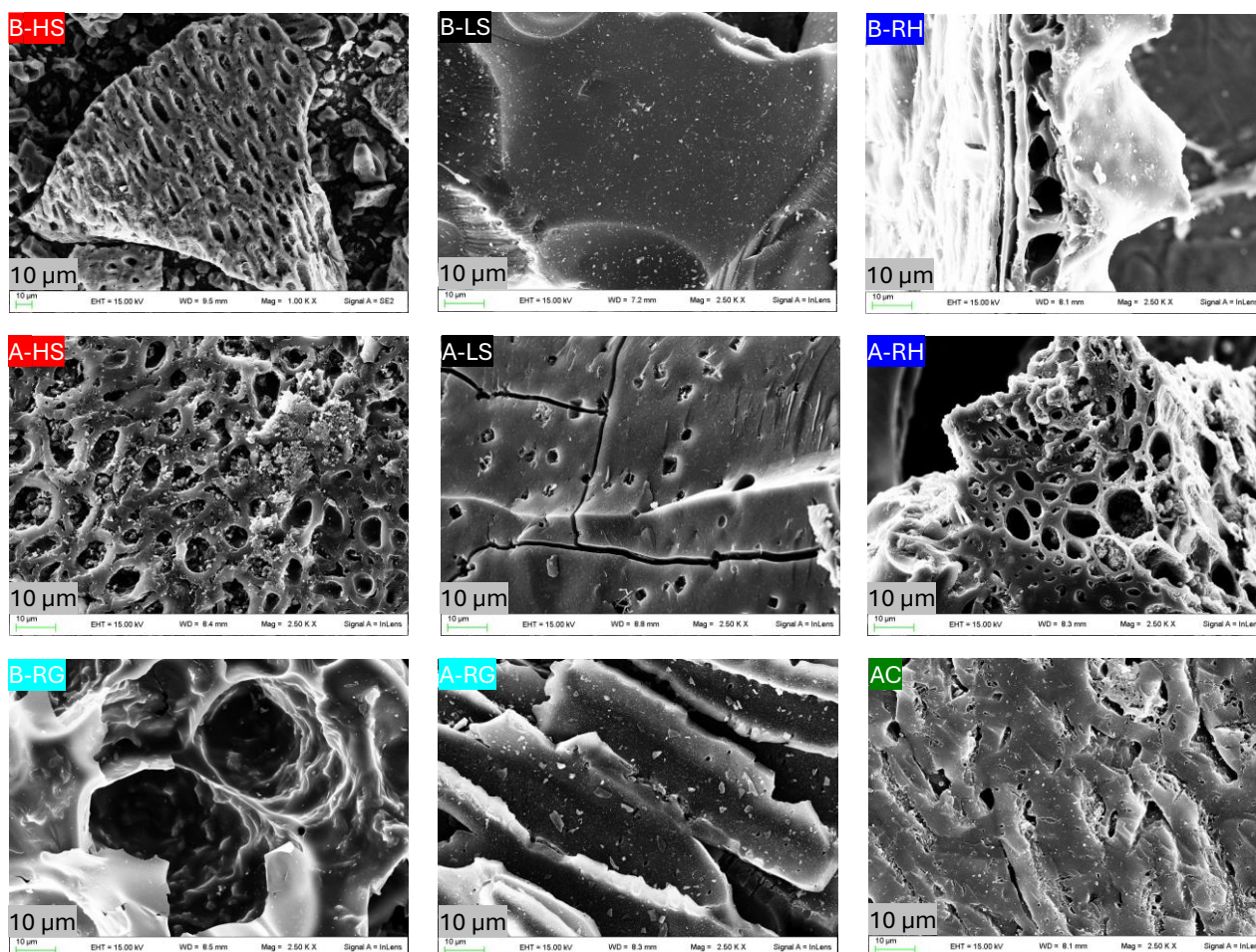


Figure 3.2.3.3. SEM images of biochars, activated biochars and commercial AC with 1.00 and 2.50 K X magnifications.

The AC exhibited a surface characterized by small, homogeneously distributed cavities. In contrast, A-HS and A-RH displayed a sponge-like structure with rounded and elliptical cavities, as well as internal channels¹⁴⁶. The physical activation process led to the development of additional pores, depressions, and channels in the biochars, as also observed by Alvarez *et al.*^{159,160}. These internal features enhance the potential of trapping metallic nanoparticles and improve resistance to leaching.

Lignocellulosic biomasses, such as HS and RH, are known to retain the structural integrity of plant cell walls, composed mainly of cellulose, lignin, and hemicellulose¹⁶¹, which accounts for their distinct morphology post-activation. Furthermore, a comparison of the SEM images of B-RH and A-RH in Figure 3.2.3.3 (and in the Appendix, Figure 3.2.6.2) reveals that the corrugated structure of B-RH, characteristic of this biomass, remains preserved after activation. This corrugated structure is attributed to the hybrid nature of the biochar, with a high silica content (confirmed by EDX analysis in the Appendix Figure 3.2.6.1), which is uniformly dispersed throughout the material, forming a sandwich-like double layer with the carbonaceous fraction.

The SEM image of biochar from leather shavings (B-LS) displays a flat surface with no visible pores²⁷. After activation, however, the activated leather shaving biochar (A-LS) exhibits superficial pores with diameters in the micrometer range. N₂ physisorption data confirms that these samples are predominantly microporous (pores < 2 nm), which are beyond the resolution of SEM⁹⁶. The distinct morphology of leather shaving biochar is likely due to its collagen fiber-rich composition, combined with fibroblasts and tanning agents¹⁶², which differs significantly from lignocellulosic biomass. The soft matter of the leather does not maintain its structure post-pyrolysis. Both B-RG and A-RG exhibit a jagged surface with large, irregular depressions.

The different characterizations conducted on the carbonaceous materials evidenced that their chemical composition, textural and morphological properties differ among the samples, due to the nature of the feedstock. Therefore, the aim of this work was to evaluate if the intrinsic properties of the chars could influence the final properties of the catalysts, by modulating the quantity and dispersion of the deposited metal phase, and therefore influencing the catalytic performance of the resulting heterogeneous catalysts, particularly with respect to activity and selectivity. Consequently, following the deposition of Pd onto the carbonaceous supports, the physicochemical properties of the prepared catalysts were thoroughly investigated, and the results are presented in the subsequent section.

Characterization of the catalysts

According to the results of MP-AES analyses reported in Table 3.2.3.3, the actual Pd loading of all catalysts was different, and not always coherent with the nominal value (0.6 wt. %). Among all catalysts, Pd/A-RH and Pd/A-HS showed the highest metal loading, while Pd/A-LS showed the lowest loading value. It was assumed that the chemical, structural and morphological properties of the carbonaceous supports had strong influences on the anchorage of Pd nanoparticles, affecting the leaching during final washing procedure of the catalyst.

Table 3.2.3.3. Pd loading determined by MP-AES analyses and Pd particle size (nm) measured by TEM.

Sample	Nominal Pd loading (wt. %)	Effective Pd loading (wt. %)	Average Pd particle size (nm)
Pd/A-HS	0.6	0.5	4.8
Pd/A-LS	0.6	0.2	5.9
Pd/A-RG	0.6	0.3	5.2
Pd/A-RH	0.6	0.6	3.8
Pd/AC	0.6	0.4	3.9

As observed by N₂ physisorption results in Table 3.2.3.2 and Fig. 3.2.3.2, both A-HS and A-RH showed the coexistence of micro and mesopores, which could promote a greater entrapment of the metal phase. Moreover, the SEM images in Fig. 3.2.3.3 showed a different and typical morphology of A-HS and A-RH compared to other carbonaceous supports. These two samples displayed inner pores, channels and cavities that could help with a better trapping and anchoring of the Pd nanoparticles and increase their resistance to leaching, especially during washing step of the catalyst preparation process⁹⁶.

On the other hand, according to the results of the elemental analysis of activated biochars, and the FT-IR spectra reported in Figure 3.2.3.2 and Table 3.2.3.2, A-RH showed a rather high O/C ratio and a high presence of oxygen-based functional groups. In contrast, A-HS showed lower O/C ratio and oxygen-based functionality. Oxygenated groups could help with a better interaction between the support and the Pd precursor, leading to a lower leaching of Pd during final washing of the catalyst. Anyways, the surface functional groups could not be ascribed as the principal feature to ensure good anchorage and loading of the metal. Indeed, the improper texture and morphology of A-LS, with superficial and mainly micropores, led to the weak trapping and anchorage of metal nanoparticles in the support, and hence the lowest loading of Pd even though this support showed a high surface area, and high N,O-based functional groups. A-RG and AC, with a rather high O/C ratio, showed an intermediate behavior in terms of metal loading, that could be referred to their textural and morphological properties. The materials have a microporous texture, but from SEM images it is possible to observe a more corrugated surface, with respect to A-LS.

Further characterizations were carried out to investigate the influence of the different carbonaceous supports on the final properties of the catalysts and their catalytic activity in the benzaldehyde hydrogenation. The TEM images and the Pd particle size distribution of the catalysts are shown in Figure 3.2.3.4. In general, by XRD pattern we can obtain the size of single crystals, but in TEM image, it is possible to see the nanoparticles which come from agglomeration of single crystals. In this study, we assume that single crystals are smaller than 4 nm which made it impossible to see in XRD pattern (Figure 3.2.6.3 in Appendix).

However, the nanoparticles from agglomeration of single crystals had obviously a mean size superior to single crystals. Larger nanoparticles can confirm an eraser movement of Pd single crystals in the support texture and their higher agglomeration^{96,116}.

In particular, Pd/A-HS and Pd/AC showed uniformly distributed Pd nanoparticles with the mean size slightly larger than 4 nm. Also Pd/A-RH displays a high dispersion of metallic phase over the entire surface of the support and no active phase agglomerations are observed. A-RH is a hybrid material made of two cross-linked structures of silica and carbon; the presence of silica can increase the dispersion of the metal phase, thanks to the presence of hydroxyl groups (Si-OH), and allowing the improvement of the hydrophilic nature of this material¹⁶³. On the contrary, in Pd/A-LS and Pd/A-RG catalysts, the dispersion of the Pd particle is not homogeneous and some evident agglomerates can be observed. Indeed, the larger Pd average particle size is estimated for these two catalysts with approximately around 5.2 nm for Pd/A-RG and 5.9 nm for Pd/A-LS. It can be hypothesized that A-LS and A-RG supports, with superficial depressions and pores, and A-LS with a minor stacking disorder of the layers (Figure 3.2.3.3) can mainly disperse the metal particles on the external surface, and not inside the pores¹⁶⁴. Finally, it can be concluded that a combination of chemical, textural, and more importantly morphological properties favored a better trapping and anchoring of the Pd and a higher loading for A-HS and A-RH.

3. Valorization of biomass *via* pyrolysis – 3.2 Biochar as support for heterogeneous catalysts

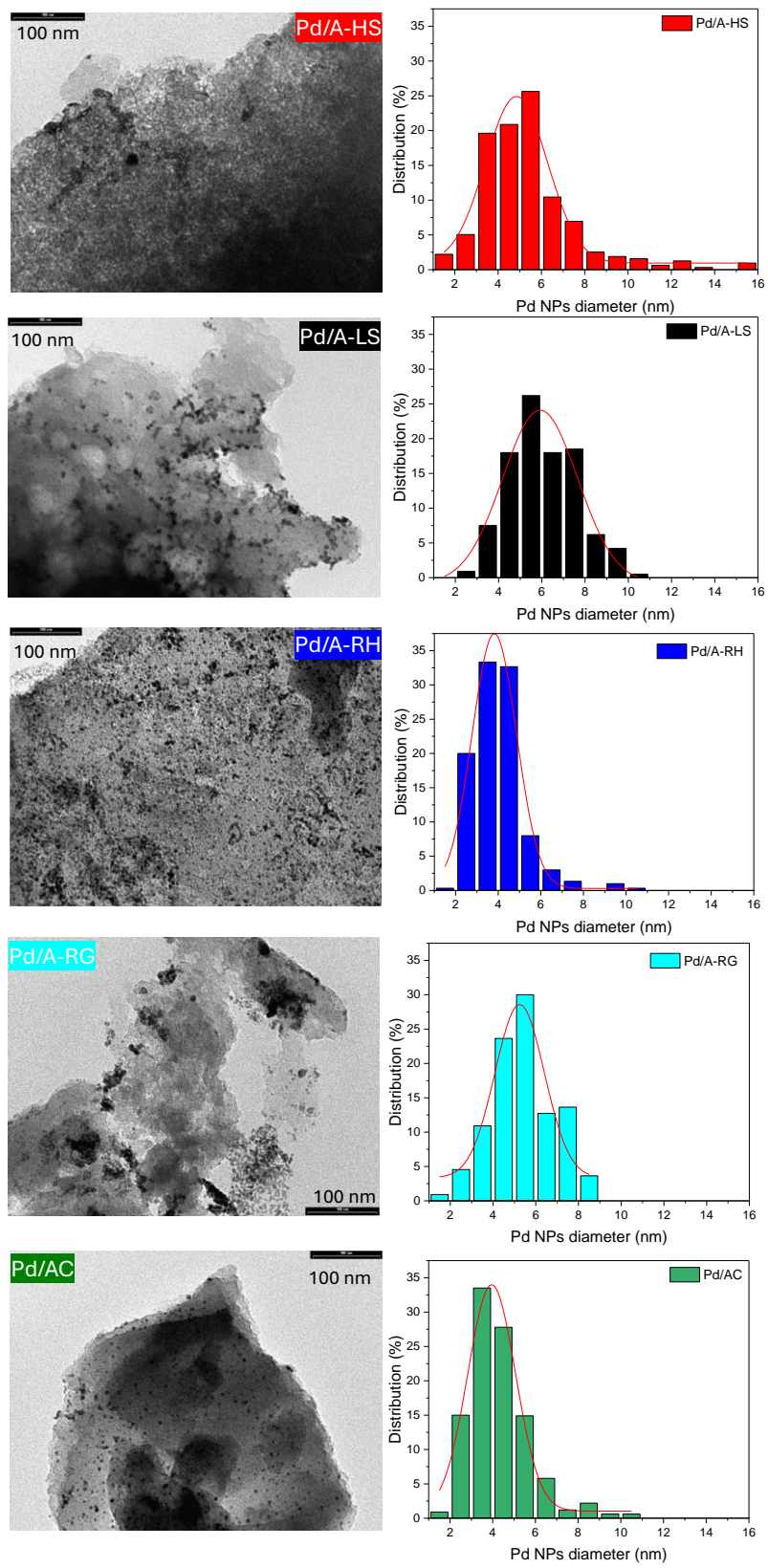


Figure 3.2.3.4. TEM images and Pd particle size distribution histograms of reduced Pd/A-HS (red), Pd/A-LS (black), Pd/A-RG (cyan), Pd/A-RH (blue), and Pd/AC (green).

TPR measurements of reduced catalysts were carried out to derive useful information on the metal phases and to observe whether all the palladium hydroxide has been reduced to the metallic state. TPR profiles in Figure 3.2.3.5 show a negative peak at about 70 °C due to the decomposition of β -palladium hydride¹⁶⁵. Indeed, metallic palladium can adsorb hydrogen on its surface at room temperature, leading to the formation of hydrides which are unstable at temperatures above 60 °C. In addition, all samples indicate a very large peak at temperatures above 400 °C which is related to the methanation of activated biochars or to the interaction between the surface carbon atoms with hydrogen¹⁶⁶. The Pd/A-LS catalyst shows a more intense peak compared to the other samples, which explains a higher consumption of hydrogen. In fact, as was observed from the FT-IR and TPD results (Figure 3.2.3.1a,b), A-LS showed a remarkable surface functionality. Furthermore, this peak for Pd/A-RH is not very intense that could be correlated to the fact that A-RH is a hybrid material consisting of a carbonaceous structure and silica presenting though a lower carbon content than the other activated biochars. For Pd/A-RG and Pd/A-LS, there is a positive peak in the temperature range 230-250 °C which is associated with the decomposition of species such as palladium oxychlorides¹⁶⁶. This can confirm that the metal precursor was not completely reduced to the metallic state by sodium formate. Indeed, A-LS and A-RG showed a higher quantity of nitrogen according to the elemental analysis results in Table 3.2.3.1 which could exist as self-doped and functional groups in these supports. Bulushev *et al.*¹⁶⁷, noted that doped nitrogen in carbonaceous support can favor the stabilization of these Pd²⁺-based species, thus preventing the reduction of palladium to the metallic state¹⁶⁸.

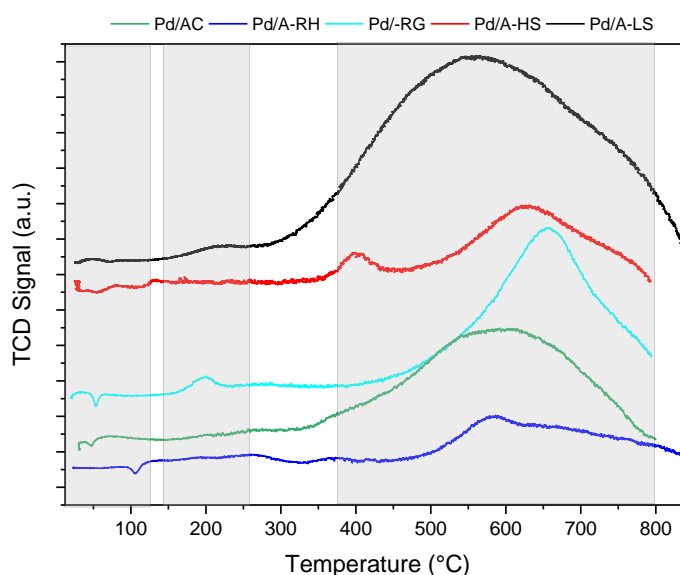


Figure 3.2.3.5. TPR profiles of all reduced catalysts

After full characterizations of all catalysts, they were tested in the hydrogenation of benzaldehyde.

Catalytic tests

The synthesized catalysts were tested in the benzaldehyde hydrogenation, and the benzaldehyde conversion and products selectivity are reported in Figure 3.2.3.6.

As can be seen in Figure 3.2.3.6, the best activity was obtained for Pd/A-RH and Pd/A-HS where the conversion increased rapidly over time and reached full conversion after 40 min. On the contrary, the conversion over Pd/AC, Pd/A-RG, Pd/A-LS increased slightly and reached a maximum of 97%, 80% and 45%, respectively after 200 min of reaction. Looking at the selectivity of benzyl alcohol and toluene products, Pd/A-HS and Pd/A-RH exhibit a most rapid increase of benzaldehyde selectivity during the first 40 min of the reaction and then its gradual decrease after 40 min. This can suggest that for these two catalysts, toluene started to be produced from hydrogenation of benzyl alcohol after 40 min of the reaction which can also be observed from selectivity of toluene. The final benzyl alcohol and toluene selectivity for Pd/A-HS and Pd/A-RH were 21%, 78% and 3%, 97%, respectively. However, Pd/AC showed a different trend in which the formation of benzyl alcohol gradually increased throughout the reaction time, reaching up to 80% selectivity after 200 min. For this catalyst the formation of toluene was inhibited, and it was able to achieve only 8% of toluene selectivity. Pd/A-RG and Pd/A-LS produced benzyl alcohol with low final selectivity of 30% and 12%, respectively and the producibility of toluene was negligible. The low selectivity obtained from the Pd/AC, Pd/A-RG and Pd/A-LS catalysts was attributed to the formation of by-products, which have been identified as diethoxy methylbenzene and ethoxy methylbenzene by GC/MS analysis. For Pd/A-RG and Pd/A-LS catalysts, the selectivity to by-products increased very rapidly in the first 10 minutes of the reaction up to a value of about 74% for both samples and then showed a slight decrease for Pd/A-RG. On the contrary, a very low amount of by-products was detected in the reactions over Pd/A-HS and Pd/A-RH. For these catalysts, the selectivity towards ethoxy methylbenzene and diethoxy methylbenzene increased significantly in the first 10-20 minutes and subsequently decreased and then disappeared during the reaction. Instead, a similar trend was observed for Pd/AC but with a higher selectivity to by-products and not their complete disappearance after 200 min of the reaction. For Pd/A-HS, Pd/A-RH and Pd/AC, the subsequent reduction of diethoxy methylbenzene and ethoxy methylbenzene selectivity might be due to the conversion of these intermediates into toluene and benzyl alcohol, respectively (Figure 3.2.1.1). Overall, two synthesized catalysts meaning Pd/A-RH and Pd/A-HS showed the highest activity and selectivity especially compared to Pd/AC with commercial support. The variable activity and selectivity of the catalysts was primarily related to the different metal loading.

Pd/A-RH and Pd/A-HS, which exhibited the highest metal loading, close to the nominal value, displayed the highest activity and good selectivity, because the side reactions, not catalyzed by the active metal phase, were suppressed in favor of the hydrogenation pathways. On the other hand, Pd/A-LS and Pd/A-RG, with a low Pd loading, did not favor the hydrogenation route, and the acetalization could occur more easily. Pd/AC, with an intermediate value of Pd wt. %, displayed intermediate behavior, maintaining a good selectivity toward BALOH, but resulting in low activity and therefore slow formation of TOL. The effective loading value of Pd and NPs size dispersion (Table 3.2.3.3) were influenced by the properties of the supports, and that influenced the catalytic behavior of the materials. Indeed, Pd/A-RH and Pd/A-HS catalysts displayed a micro-mesoporous structure, and a morphology made of cavities and holes, as well as a proper amount of surface functionalities, and resulted in higher effective Pd loading, smaller Pd nano particle size and higher dispersion, therefore being more selective to desired products. The other chars being mainly microporous had a lower effective Pd loading and with more evident agglomerations, which favored the reaction towards higher by-products formation.

As discussed in the previous section, chemical, textural and morphological properties of the biochar-based supports were fundamental parameters that strongly affected the performance and characteristics of the catalysts, since it could modulate and determine the dimensions, form, dispersion, and availability of the metallic active centers. Therefore, it can be concluded that the origin of initial biomass has a fundamental role in reaching a final biochar-based support with proper feature for desired catalytic application.

3. Valorization of biomass via pyrolysis – 3.2 Biochar as support for heterogeneous catalysts

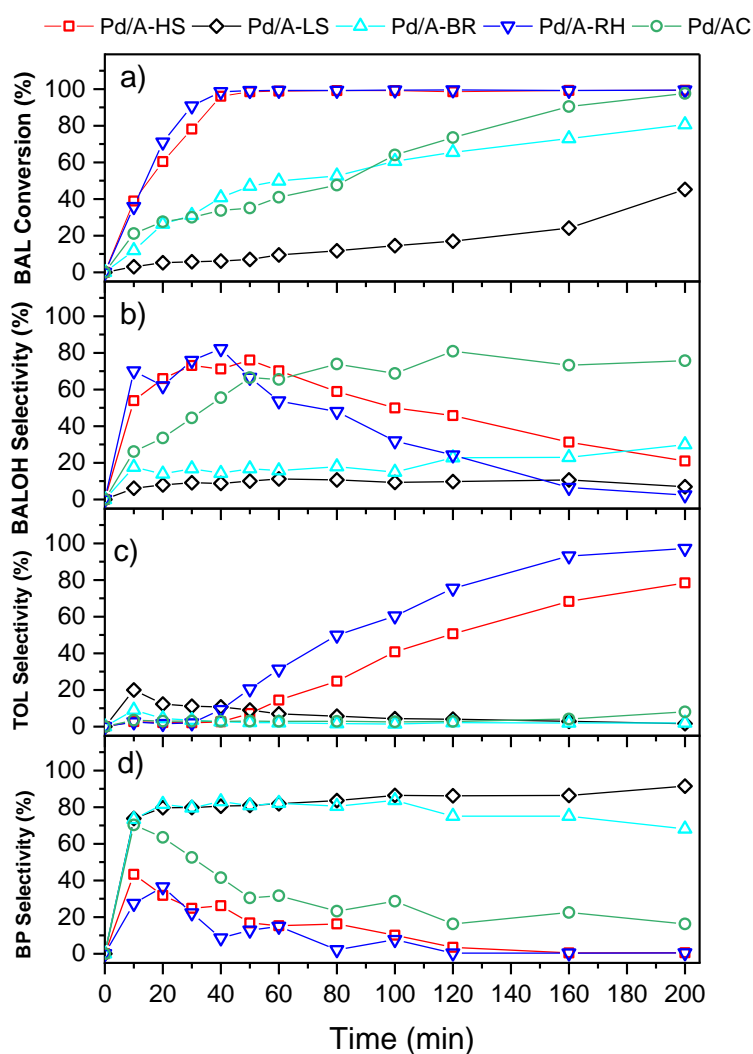


Figure 3.2.3.6. Hydrogenation of benzaldehyde over all prepared catalysts Pd/A-HS (red), Pd/A-LS (black), Pd/A-RG (cyan), Pd/A-RH (blue), Pd/AC (green): a) benzaldehyde (BAL) conversion (%), b) benzyl alcohol (BALOH) selectivity (%), c) toluene (TOL) selectivity (%), d) by-products (BP) selectivity (%) as a function of reaction time (min). Reaction conditions: ethanol: 20 mL, temperature: 25 °C, pressure: 1 bar, H₂ flow: 33 mL/min, benzaldehyde concentration: 0.1 M, catalyst: 160 mg, stirring speed: 1500 rpm.

Since the conversion of benzaldehyde is considered as a model reaction for production of fuels from valorization of biomass, wide variety of studies were carried out on hydrodeoxygenation of benzaldehyde to toluene in the literature. In particular, various noble, non-noble metals, and oxide, carbonaceous supports were used in the formulation of the heterogeneous catalysts for this model reaction. The most important examples are reported in Table 3.2.3.4.

Table 3.2.3.4. Comparison of results obtained with different reported heterogeneous catalysts

Catalyst	Benzaldehyde conversion (%)	Products	Reaction conditions	Ref.
Pd/A-RH	>99	Toluene selectivity: 97%	Ethanol solvent, 25 °C, 1 bar H ₂ and flow of 33 mL/min, 200 min, Pd: 0.6 wt.%	This work
Pd/Al ₂ O ₃	100	Benzyl alcohol concentration: 0.06 mol/L	Cyclohexane solvent, 40 °C, H ₂ flow of 20 mL/min, 60 min, Pd: 5 wt.%	[169]
Pd/FER zeolite	~100	Toluene yield: 100 %	80 °C, 40 bar H ₂ , 120 min	[170]
Pt/C, Rh/C as the best Pd/C Ni/C	100	Benzyl alcohol yield: 100%	Acetate buffer at pH 5, room temperature, 1 bar of H ₂ flow, 120 min, metal: 5 wt.%	[171]
Pd-Ru/CNTs	31	Benzyl alcohol selectivity:	Ethanol solvent, 40 °C, total gas pressure of 50 bar, 60 min, total metal: 1.5 wt.%	[141]
Pd-Ru/NGC	43	44% and 82%		
Pd/C	100	Toluene selectivity: 100%	p-xylene solvent, 50°C, 2 bar H ₂ , 180 min, Pd: 1 wt.%	[172]

Even if it is always difficult to compare catalytic tests performed under different reactions conditions, it is possible to see for instance, that alumina and FER zeolite were used as the supports of noble Pd metal-based catalyst in two studies. Pd/Al₂O₃ was selective to benzyl alcohol (0.06 mol/L)¹⁶⁹. On the contrary, Pd/FER zeolite was selective to toluene (100 % yield) at different reaction conditions¹⁷⁰. Moreover, carbonaceous supports have been widely used for the preparation of hydrogenation catalysts. Song *et al*, investigated carbon supported Ru, Rh, Pd, and Cu catalysts loading a higher percentage of metals (5wt.%) compared to our study. Among all the catalysts investigated, Pd/C and Rh/C were the most active and selective to benzyl alcohol. They reported 100% benzaldehyde conversion and benzyl alcohol yield for Rh/C at room temperature¹⁷¹. In addition, when using bimetallic Ru-Pd/C (C: NGC, CNT) catalysts, the reaction was more selective to benzyl alcohol and lower toluene was produced compared to the catalyst of current study¹⁴¹. In the work reported by Stucchi and co-workers, Pd supported on commercial carbon was completely selective to toluene in full benzaldehyde conversion at mild reaction conditions¹⁷². In current study, for the first time we investigated activated biochar obtained from different biomasses as innovative and sustainable supports of Pd based catalyst for proposed reaction, which could be fundamental from the point of view of the circular economy. In addition, when Pd/A-RH was employed, it was possible to obtain high selectivity of both benzyl alcohol and toluene subsequently, at milder reaction conditions using non-toxic solvent compared to the ones reported in literature.

Recycling tests and catalyst stability

Among all the formulated catalysts of this study, the best catalytic performance was achieved by Pd/A-RH, reaching 99% conversion in 40 min, 82% selectivity toward benzyl alcohol in 40 min, and 98 % selectivity toward toluene in 200 min. Therefore, the recyclability and stability of this catalyst was investigated, and compared to Pd/AC, as a reference (Figure 3.2.3.7).

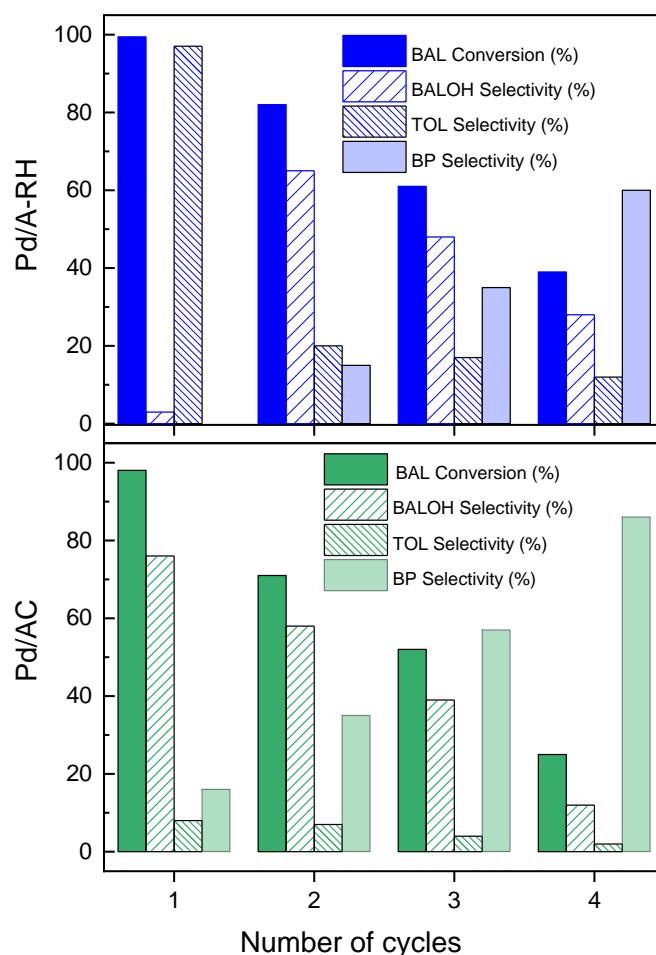


Figure 3.2.3.7. Recycling tests over Pd/A-RH (blue) and Pd/AC (green) at 200 min. Reaction conditions: ethanol: 20 mL, temperature: 25 °C, pressure: 1 bar, H₂ flow: 33 mL/min, benzaldehyde concentration: 0.1 M, stirring speed: 1500 rpm.

As can be seen in Figure 3.2.3.7, the conversion decreased from the first to the fourth cycle, reaching 39% and 25% for Pd/A-RH and Pd/AC, respectively. During the cycles, the products distribution meaning the selectivity to different products was also altered. For Pd/A-RH, the selectivity toward toluene rapidly decreased from the first to second cycle and benzyl alcohol instead increased, denoting a slowing on the kinetic of the reaction. Moreover, a constant increase in the selectivity of by-products was observed. The same trend was followed by Pd/AC, in which after 4 cycles the selectivity to by-products reached 86%. From these results, the deactivation of both catalysts is clearly visible, even if more marked in the case of Pd/AC. To understand the reasons for deactivation, further

characterizations were conducted on the spent catalysts. First, MP-AES measurements were performed for the spent catalysts after four cycles of reaction (Table 3.2.3.5). As can be seen, the Pd content of both catalysts was decreased after four cycles compared to the fresh catalysts, suggesting that metal leaching happened. Pd/A-RH lost 33% of Pd, while Pd/AC lost a higher metal content, up to 75%.

Table 3.2.3.5 Pd loading determined by MP-AES analysis, and average Pd particle size of fresh and spent catalysts

Sample	Pd loading on fresh catalyst (wt. %)	Pd loading on spent catalyst (wt. %)	Average Pd particle size on fresh catalyst (nm)	Average Pd particle size on spent catalyst (nm)
Pd/A-RH	0.6	0.4	3.8	4.5
Pd/AC	0.4	0.1	3.9	8.8

In addition, as is shown in TEM images of Figure 3.2.3.8, for both spent catalysts the increment of Pd particle size and agglomeration occurred. This effect was slightly observed in Pd/A-RH, with a medium particle size of 4.5 nm vs 3.8 nm of the fresh catalyst, while it was much more pronounced on Pd/AC, that showed a medium particle size of 8,8 nm vs 4.3 nm. Both leaching and sintering can be assumed as the causes of deactivation of the catalysts, thus leading to a decrease in terms of conversion and selectivity toward the desired products. The reduction of active phase leads to the concurrence of side reactions, such as the acetalization of benzaldehyde (Figure 3.2.1.1).

3. Valorization of biomass *via* pyrolysis – 3.2 Biochar as support for heterogeneous catalysts

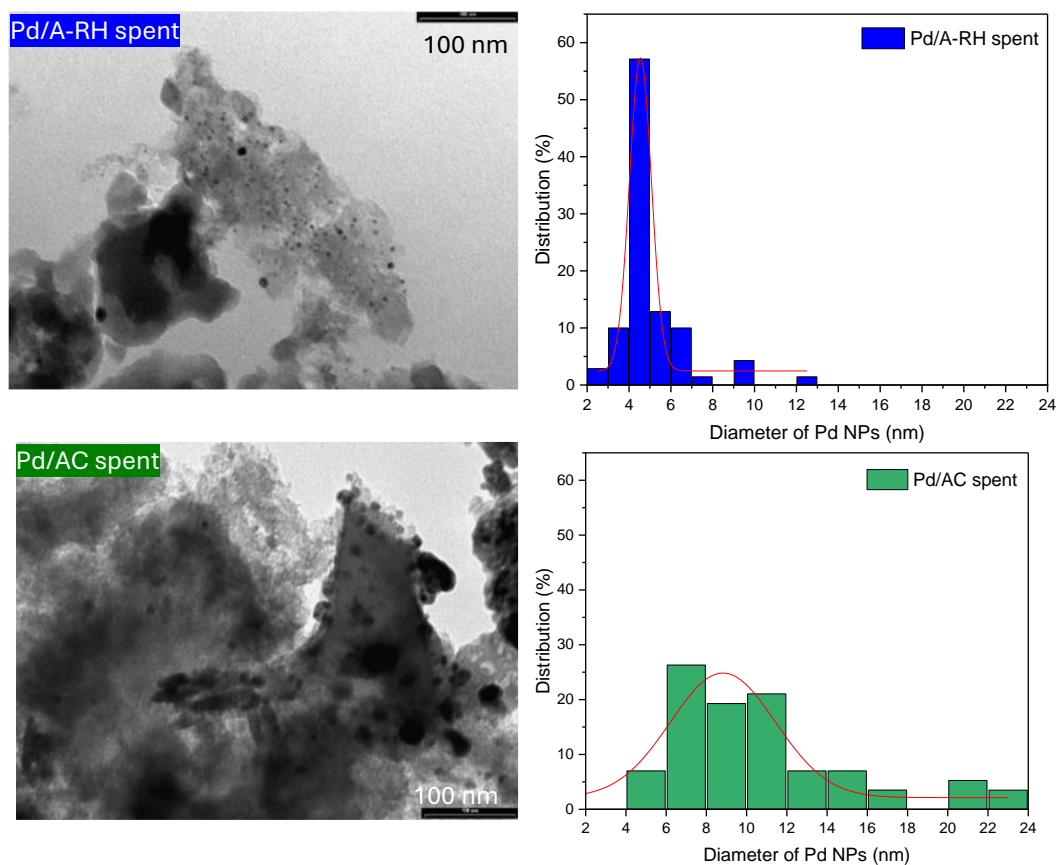


Figure 3.2.3.8. TEM images and Pd particle size distribution histograms fresh Pd/A-RH spent (blue, top) and Pd/AC spent (green, bottom).

In conclusion, it can be affirmed that support played an important role in the stability of the catalyst. Indeed, A-RH was able to better anchor Pd, leading to less leaching and sintering effects. These features can be attributed to the peculiar hybrid organic/inorganic nature and the valuable content of oxygenated functionalities. More importantly, the morphology of this material, made of channels, inner cavities, meso and micropores, could better entrap the metal phase, compared to the commercial activated carbon, made of superficial microporous structure.

One of the key objectives of this work was to valorize complex waste materials, such as leather shaving (LS), with the ultimate goal of utilizing them as support for heterogeneous catalysts. LS offers unique properties, including natural nitrogen doping and a high surface area, which make it a promising candidate. However, the activated leather shaving (A-LS) demonstrated poor catalytic performance compared to biochars derived from lignocellulosic sources. This was attributed to its low metal anchoring capacity and flat morphology, which negatively impacted the efficiency of mass transfer to the active sites within its internal cavities. Consequently, an alternative approach was adopted to enhance the utility of this biomass: co-pyrolysis with rice husk (RH).

3.2.4 Co-pyrolysis of LS and RH for the preparation of Pd-based catalyst

3.2.4.1 Introduction

As discussed in the previous chapters, among the various biomasses used for heterogeneous catalyst fabrication, rice husk-derived activated biochar (A-RH) demonstrated superior performance as a support for Pd-based catalysts. This enhanced activity is attributed to its hierarchical porous structure, which promotes efficient internal mass transfer, and the strong interaction and dispersion of metal active sites on its surface. Additionally, its hybrid composition of carbon and silica further tailors its catalytic properties. As a result, co-pyrolysis of rice husk with leather shaving (LS) from the tannery industry has been adopted as a novel strategy to transform this complex waste into a high-value material for catalytic applications.

This approach has been previously reported for the co-valorization of lignocellulosic biomass with coal, plastics or tire wastes¹⁷³ for optimization of the biochar features and physicochemical properties towards specific applications¹⁷⁴. Co-pyrolysis can indeed tune the porosity, surface functionality, point zero charge (PZC), and surface charge of the final biochar, as the key factors in targeted applications¹⁷⁵. The co-pyrolysis of rice husk with different biomasses or non-biomass wastes has already been investigated in literature, targeting bio-oil¹⁷⁶, and biochar^{53,177,178} production. For instance, the addition of rice husk to oily sludge was found to improve bio-oil quality due to the synergistic effect of the alkali ashes of the biomasses, which significantly reduced the oxygenated compounds¹⁷⁹. In this regard, Zhang *et al.*¹⁸⁰ reported that the addition of rice husk to sewage sludge pyrolysis enhanced the interactions with heavy metals, thereby improving the removal efficiency. The co-pyrolysis of different types of leather wastes has been also reported¹⁸¹. For example, the co-pyrolysis of tanned buffing dust, chrome shavings and tanning sludges led to higher yields of light tar, and increased surface area in the biochar. This improvement was attributed to the synergistic action of various metal compounds (like CaCO_3 and Fe_2O_3) in the residues³⁰. However, the combination of rice husk and leather tannery wastes for char production has not been reported yet.

In this work, the co-pyrolysis and activation of leather shaving (LS) and rice husk (RH) were investigated to prepare a new hybrid activated biochar, named A-RL, which was subsequently employed for the development of Pd-based heterogeneous catalysts. Building on the insights from previous studies (Chapter 3.2.2, 3.2.3), the catalyst synthesis was optimized by considering the point of zero charge (PZC) of the supports and adopting the deposition method, by controlling the pH of the precursor solution to enhance the anchoring and deposition of the active phase¹⁸².

3. Valorization of biomass via pyrolysis - 3.2 Biochar as support for heterogeneous catalysts – 3.2.4 Co-pyrolysis of LS and RH for the preparation of Pd based catalysts

The catalytic performance of the newly developed catalysts—Pd/A-RH2, Pd/A-LS2, and Pd/A-RL—was evaluated using the model reaction of consecutive hydrogenation of benzaldehyde to benzyl alcohol and toluene. Comprehensive characterization of both the supports and the catalysts was performed to elucidate the synergistic effects of the original biomasses on the observed catalytic activity.

3.2.4.2 Experimental

Biochars synthesis and activation

The synthesis of B-RH and B-LS, and the subsequent activation is described in Chapter 3.2.2, Experimental. For co-pyrolysis, RH and LS were ground to a mesh size lower than 100 μm , mixed in a 1:1 ratio (w/w) to give a homogeneous powder (RL), which was then subjected to the same pyrolysis and activation process and acidic washing as for the single biomasses, and labelled B-RL, and A-RL, respectively.

Preparation of the catalysts

The activated biochars were ground to a fraction of 105-63 μm . Pd/A-RH2, Pd/A-LS2, and Pd/A-RL were prepared by the deposition precipitation method of H_2PdCl_4 (nominal 0.6 wt.%) with a controlled pH of 10.5, which was adjusted over time with a NaOH solution. The mixture was stirred at an ambient temperature for 2 hours and then heated to 80 °C. At this temperature, a solution of sodium formate (2:1 with respect to Pd) was added, and the mixture was kept under stirring for 1 hour to allow the Pd reduction to the metallic form. The catalyst was then filtered and washed with deionized water until no chlorides are found through a negative AgNO_3 test, then dried in oven at 110 °C for 18 hours.

Biochars, activated biochars, and catalysts characterization

CHNS elemental analysis, Scanning Electron Microscopy (SEM), metal content determination, Transmission Electron Microscopy (TEM), N_2 physisorption, and Temperature Programmed Desorption (TPR) were performed on the samples derived from the co-pyrolysis. These analyses complemented the characterizations already conducted on other materials using the same techniques (for further details, see Chapter 3.2.2). In addition to these methods, further insights were gathered using additional techniques. The point zero charge of the ACs was determined by the pH drift method¹⁸³. In brief, 150 mg of char was suspended in a series of solutions (50 mL) with varying initial pH values, modified by addition of HCl or NaOH (from 2 to 12), and stirred for 48 h, allowing the system to reach equilibrium. After equilibration, the final pH is measured. The measured pH was plotted vs. the initial pH. The pH_{pzc} is the point where the curve pH_{final} vs. $\text{pH}_{\text{initial}}$ crosses the line $\text{pH}_{\text{initial}} = \text{pH}_{\text{final}}$. Raman spectra were recorded using a micro-Raman system (Senterra Bruker Optik GmbH, Massachusetts, USA), $\lambda = 532$ nm, and a laser power of 10 mW. The visible spectra were obtained using the Ocean Optics spectrophotometer (USB 2000), equipped with optical fiber, tungsten-halogen source, and silicon (350–720 nm) and germanium (720–1050 nm) detectors. X-ray powder diffraction (XRD) analysis was performed by a Bruker D8 Advance Da Vinci diffractometer equipped with LynxEye detector and a sealed tube providing $\text{CuK}\alpha$ radiation at an accelerated voltage of 40 kV and an applied current of 30 mA.

XPS measurements were carried out with a PHI Genesis instrument from Physical Electronics (Chanhassen, MN, USA), equipped with a monochromatic Al K α X-ray source. The samples were supported on a copper conductive tape compatible with UHV for charge compensation. Dual charge neutralization was used to neutralize charge accumulation during analysis. The binding energy was calibrated based on the C 1s peak at 284.6 eV. CO chemisorption was carried out in a lab-made equipment coupled with a Micromeritics TPRTPD 2900 analyzer equipped with a Gow-Mac 24-550 TCD Detector (Bethlehem, PA, USA). For CO pulse chemisorption, 500 mg of the sample powders was placed in the same U-shaped quartz reactor, pre-treated in H₂ at 25 °C for 1 hour (40 mL/min) and then purged in He for 2 hours at 25 °C (40 mL/min). The system was then kept at 25 °C to inject 0.21 mL of CO through a loop until saturation.

Catalytic tests

In a typical experiment, 200 mg of catalyst (63-105 μ m) was placed in the reactor with 75 mL of ethanol (Sigma Aldrich). H₂ was bubbled in the solution with the flow rate of 30 mL/min at atmospheric pressure and the system was heated at 80 °C for 1 h to ensure the reduction of Pd. The system was then cooled down to 25 °C and benzaldehyde was added to a final concentration 0.1. The system was stirred at 1400 rpm and the reaction was monitored over time sampling a small aliquot every 10 min. N-octane (Sigma Aldrich) was used as internal standard.

In addition, the kinetics constants and TOF values were also found using Eq. 3.2.4.2.1, and Eq. 3.2.4.2.2.

$$k_{Benzaldehyde} = \frac{dC_{Benzaldehyde}}{dt} \quad (\text{Eq. 3.2.4.2.1})$$

$$TOF = \frac{n_t \text{ products}}{D_{Pd} * t} \quad (\text{Eq. 3.2.4.2.2})$$

Where D_{Pd} corresponds to the Pd dispersion, calculated by CO chemisorption as (Eq. 3.2.4.2.3):

$$D = \frac{N_S}{N_T} \quad (\text{Eq. 3.2.4.2.3})$$

(N_S is the total number of metal atoms at the surface and N_T is the total number of metal atoms (surface and bulk)¹⁸⁵. The time considered for TOF calculation is 600 seconds.

3.2.4.3 Results and discussion

Biochar and supports characterizations

To confirm that co-pyrolysis was an effective method for producing a hybrid and homogeneous material with combined properties from both starting biomasses, a range of structural and chemical characterizations were conducted on the three biochars — B-RH, B-LS, and B-RL — as well as their corresponding activated forms. These analyses aimed to assess the integration of characteristics from each biomass and verify the success of the co-pyrolysis process.

Table 3.2.4.3.1 presents the elemental analysis of A-RL, including ash and oxygen content, along with the H/C and O/C ratios. For comparison, A-RH and A-LS are also included. A-RL exhibited an intermediate carbon content of 53.7%, reflecting the contributions from both biomasses. All samples showed low H/C values (0.01-0.02), indicating a high degree of aromatization. A-RL had a lower nitrogen content compared to A-LS, though it was still notable (1.6%). Interestingly, A-RL displayed a lower oxygen content than the other two materials, likely due to enhanced oxygen removal during co-pyrolysis¹⁸⁶. Literature suggests that co-pyrolysis of different materials (e.g., industrial sludges and biomass) can lead to synergistic effects, such as the formation of oxygen-containing intermediates, free radical release, and the catalytic role of different ashes. These factors promote reactions like deacetylation and decarbonylation, resulting in higher oxygenated volatile releases and lower oxygen content in the resulting char¹⁸⁷. The O/C ratio, linked to the hydrophilicity of chars, was also evaluated. However, for A-RH and A-RL, the high silica content (41.3% ash in A-RL, predominantly silica, as confirmed by EDX in Figure 3.2.6.1 and 3.2.6.4, in Appendix) plays a major role in influencing hydrophilicity compared to A-LS, which, despite its highest O/C ratio, lacks the significant ash content¹⁸⁸.

Table 3.2.4.3.1. Proximate analysis of the activated biochars.

Sample	C [%]	N [%]	H [%]	S [%]	O [%]	Ash [%]	H/C	O/C
ARL	53.7	1.6	1.2	0.8	1.4	41.3	0.02	0.02
ALS	81.5	6.0	1.8	0.5	7.1	3.0	0.02	0.09
ARH	39.4	0.2	0.5	0.1	3.2	56.6	0.01	0.08

The structural features of the chars were investigated by Raman and XRD spectroscopy. In the Raman spectra of the biochars (Figure 3.2.6.5 in Appendix) and the activated biochars (Figure 3.2.4.3.1), two characteristic bands are present at around 1333 and 1590 cm^{-1} , which correspond to the sp^2 bonded carbon with structural defects (D) and sp^2 bonded graphitic carbon (G), respectively¹⁸⁹.

The peaks position and values are given in Table 3.2.4.3.2. Some minor bands are also observed at 1180 and 1500 cm^{-1} , which can be due to some aromatics tarry compounds that could still be present in the char structure¹⁹⁰.

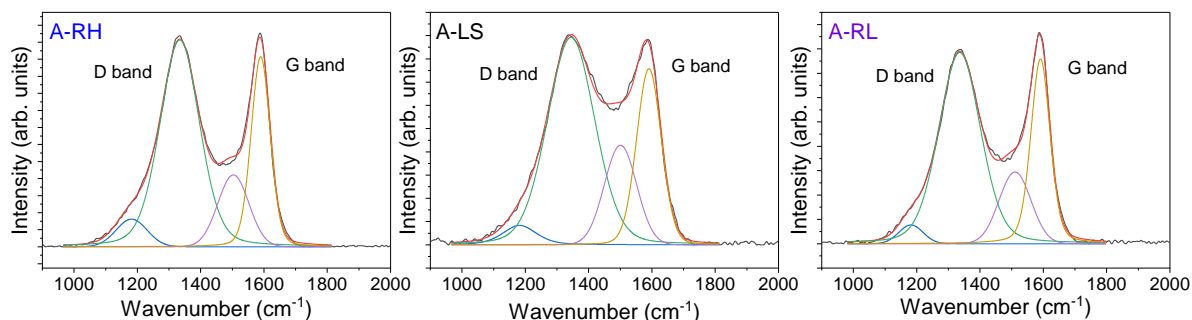


Figure 3.2.4.3.1. Raman Spectra of A-RH, A-LS, and A-RL.

Considering the position of the D and G bands of the BCs and ACs from the same starting feedstocks (Table 3.2.4.3.2), a shift toward low wavenumber in the position of the D band and to high wavenumber in the G band could be evidenced for all cases. This could be related to an increase in the order degree of the carbon structure after activation, due to a higher temperature treatment and a decrease in volatiles content¹⁸⁹. The ratio I_D/I_G provides useful information about the order degree of the materials (Table 3.2.4.3.2). As can be seen, B-RH showed a higher degree of order with respect to B-LS and B-RL (0.90, 0.98, and 1.93, respectively). However, after activation, the biochars obtained from the single pyrolysis displayed an increase in the structural defects, due to the high temperature and oxidizing treatment given by steam as activating agent¹⁹¹ while the I_D/I_G value for A-RL were maintained almost constant. The presence of heteroatoms can cause many defects in the carbon structure. Therefore, considering the ultimate analyses (Table 3.2.4.3.1), the Raman results are consistent with the O and N content in the ACs. Moreover, the D and G peaks position for B-RL and A-RL is closer to B-RH and A-RH respectively, than to B-LS and A-LS. This analogy could be positive for the purpose of this work, being A-RH the best catalytic support tested so far.

Table 3.2.4.3.2. Raman Spectroscopy Analysis: D and G Band positions, I_D/I_G ratios, and Full Width at Half Maximum (FWHM) for BCs and ACs.

Sample	D position	G position	I_D/I_G	FWHM D	FWHM G
B-RH	1340	1588	0.90	148.6	88.2
A-RH	1335	1589	1.09	148.6	70.5
B-LS	1350	1580	0.98	186.4	110.8
A-LS	1345	1590	1.18	176.4	93.2
B-RL	1340	1588	1.03	148.6	78.1
A-RL	1336	1592	1.03	156.2	73.1

In the XRD patterns of all the ACs, Figure 3.2.4.3.2, two broad peaks at $2\theta = 22-25^\circ$ (002) and 43° (110), are associated with the carbonaceous structure, based on the hexagonal graphite 2H model. These peaks correspond to the stacking of aromatic ring layers and the in-plane extension of aromatic molecules, respectively⁹⁶. Compared to ordered graphite, where $d(002)=3.354 \text{ \AA}$, the ACs exhibit a higher degree of disorder. Also, the results of XRD confirmed the presence of SiO_2 in various forms. In A-LS quartz is the most abundant phase. In A-RH cristobalite was typically as the prevalent form¹⁹². Notably, A-RL shows a relative higher abundance of SiO_2 compared to carbon, with the predominance of the cristobalite phase, but also the presence of quartz, confirming the coexistence of the two starting materials in the same char. The relative high abundance of SiO_2 with respect to carbon, evidenced once again shows that there are synergistic effects during co-pyrolysis, enabling them to promote some specific reactions. Wang *et al.*¹⁹³ for example, found that the activation energy of co-pyrolysis of sludge and rice husk was lower than that of individual pyrolysis steps, allowing the reaction to proceed under milder conditions. This was attributed to the synergistic effects of alkali metals present in the biomasses¹⁸⁶. Similar effects are likely to occur in the co-pyrolysis of RH and LS, influencing the reorganization of the silica crystal phase in the material and achieving a higher degree of order at an activation temperature of $850 \text{ }^\circ\text{C}$.

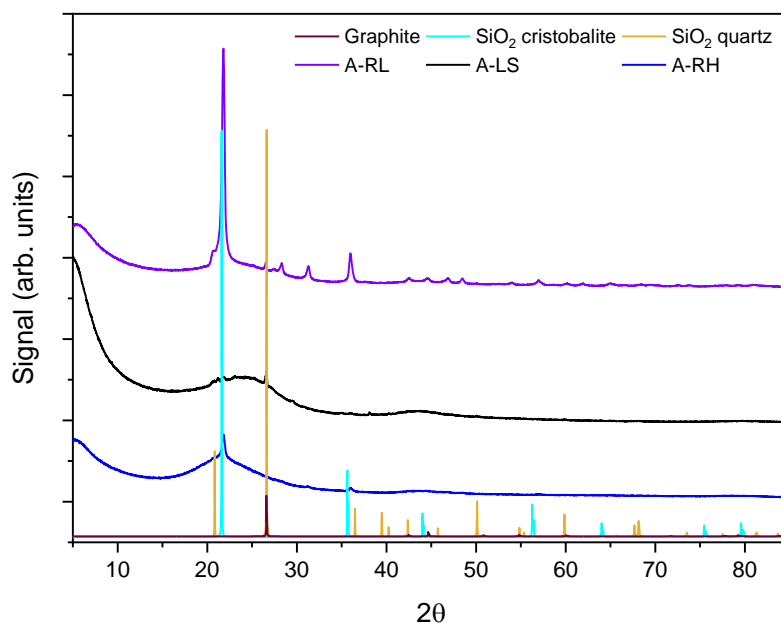


Figure 3.2.4.3.22. XRD patterns of A-RH, A-LS and A-RL

From a morphological point of view, highlighted by SEM micrographs, (B-RH and B-LS in Figure 3.2.3.3, A-RH, A-LS, and A-RL in Figure 3.2.4.3.3) it is visible that as in A-RH, also in A-RL, the cellular structure of the rice husk is somehow preserved.

3. Valorization of biomass via pyrolysis - 3.2 Biochar as support for heterogeneous catalysts – 3.2.4 Co-pyrolysis of LS and RH for the preparation of Pd based catalysts

It has been hypothesized that RH could act as a hard template for LS, that instead is completely decomposed under the pyrolysis conditions, forming a layer on the top of the rice husk biochar structure. According to the previous works, the use of biopolymers like cellulose and starch, and hard/soft templates like block co-polymers or mesoporous ordered silica or microporous alumina, results in the interconnected structures consisting of micro, meso, and macro pores^{194–196}. In this case, the natural hierarchical structure of lignocellulosic biomass is retained in A-RL, confirming also the similarity of Raman signals with A-RH, and acts as hard template for LS.

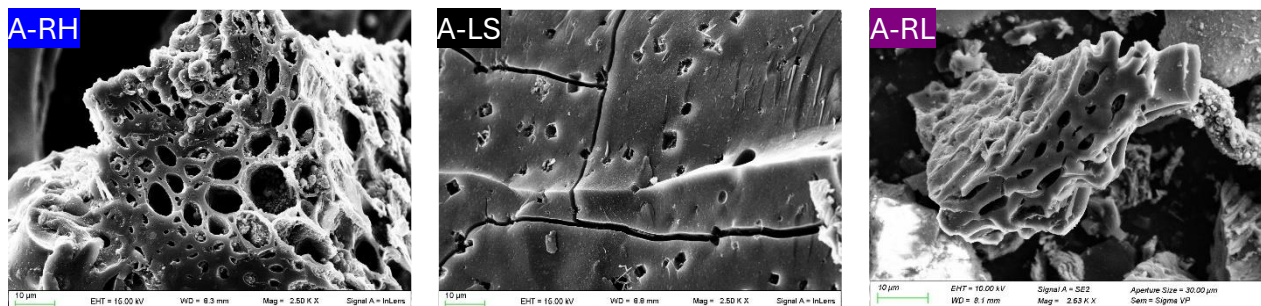


Figure 3.2.4.3.3. SEM images of A-RH, A-LS, and A-RL.

The analogies between RH and RL derived materials were also confirmed by N_2 physisorption analyses (Figure 3.2.3.4.4, Table 3.2.3.4.3). B-RL exhibited a porous structure similar to B-RH, with the highest surface area among the biochars ($S_{BET} = 345 \text{ m}^2/\text{g}$). This further supports the idea that the reactions occurring during co-pyrolysis influenced the final properties of the char, particularly its porous structure¹⁹³. After activation, A-RL, like A-RH, demonstrated a combination of type I and type IV isotherms, indicating the presence of interconnected micro- and mesopores. The textural properties of the co-pyrolysis char confirmed that rice husk played a major role in determining the structural and textural properties. The textural properties of the co-pyrolysis-derived char confirmed that rice husk played a significant role in shaping the structural and textural characteristics. While A-LS had a higher surface area, the interconnected micro- and mesopores in A-RH and A-RL are particularly important for catalysis, as they facilitate the diffusion of reactants to active sites and minimize diffusive resistance, which is beneficial for catalytic performance⁴⁵.

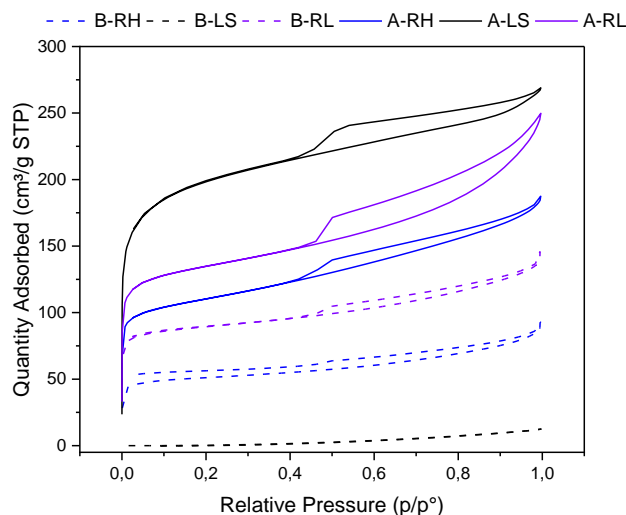


Figure 3.2.3.4.4. N₂ adsorption-desorption of BCs (B-RH, dotted blue, B-LS, dotted black, B-RL dotted purple) and ACs (A-RH solid blue, A-LS solid black, A-RL solid purple).

Table 3.2.3.4.3. Textural properties of BCs and ACs

Samples	S _{BET} ^a	S _{micro}	V _{tot}	V _{micro}
B-RH	199	270	0.15	0.06
B-LS	/	/	/	/
B-RL	345	271	0.13	0.10
A-RH	367	543	0.14	0.10
A-LS	633	789	0.25	0.23
A-RL	445	463	0.17	0.12

^aSurface area calculated by BET method. ^bMicropore surface area calculated by t-plot method. ^cTotal pore volume calculated according to the adsorbed amount of N₂ and P/P₀ values near 0.98. ^dMicropore volume calculated by t-plot method.

As previously discussed, surface functionalities are a key aspect that influences catalytic activity through controlling the total charge and nucleation sites for metal nanoparticles growth. Table 3.2.4.3.4 illustrates the surface chemical composition of the materials measured by XPS. The presence of C, N, O, Si on the surface of the samples was confirmed by XPS analyses, with some traces of inorganics like Ca, Na and Cl. The high value of O atomic % reported for A-RH and A-RL (22 and 20.6%, respectively) is mainly referred to the oxygen of SiO₂. N was evidenced in both in A-LS and A-RL, even if in higher % on the surface of A-LS, in line with CHNS measurements. From XPS spectra reported in Figure 3.2.4.3.5 the C1s core level spectra for A-RH and A-RL are deconvoluted into six contributions, while that of A-LS gave five contributions evidently. The main difference was related to the presence of the peak at 283 eV, attributed to C-Si bonds¹⁹⁷. The other components, at 284.5 eV, 285.0 eV, 286.6 eV, 288.8 eV and 291.0 eV are assigned to sp² hybridization (C=C) of the graphitic and aromatic bonds, sp³ C-C bonds, C-O or C-N, C=O, and π-plasmon excitations, respectively¹⁹⁸. According to the atomic % of each contribution, as reported in Table 3.2.4.3.5, A-LS has the highest amount of surface functionalities which can act as

3. Valorization of biomass via pyrolysis - 3.2 Biochar as support for heterogeneous catalysts – 3.2.4 Co-pyrolysis of LS and RH for the preparation of Pd based catalysts

anchoring sites for metal NPs, with 10% of C-O/C-N species and 5.5 % of C=O species, in line with the chemical bulk composition reported by CHNS (Table 3.2.4.3.1). However, A-RH and A-RL also have a considerable amount of oxygen related to SiO₂, that can be found in form of -OH free functionalities on the surface. N 1s core level spectra of A-LS (reported in Appendix, Table 3.2.6.1, Figure 3.2.6.6) showed the presence of three main contributions at 398.2 eV and 400.6 eV, and 404.0 eV, that were attributed to pyridinic, pyrrolic and N-oxidized functionalities, respectively¹⁹⁹⁻²⁰¹. N1s spectra of A-RL showed instead only two peaks, at 397.9 eV and 400.9 eV, corresponding to pyridinic and pyrrolic functionalities. It is reported that pyridinic sites are the major contributors to the dispersion of metals NPs²⁰¹, followed by pyrrolic. However, the presence of N-oxide groups, and C=O functionalities like carboxylic or carbonylic can also play an important role in modify the charge of the material, increasing the overall acidity .

Table 3.2.4.3.4. XPS atomic concentration of A-LS, A-RH, and A-RL.

Sample	XPS Atomic concentration [%]						
	C	O	N	Si	Ca	Cl	Na
A-LS	85.0	7.0	6.0	-	0.1	0.4	1.5
A-RH	70.0	22.0	-	8.0	-	-	-
A-RL	71.0	20.6	1.0-	7.2	-	0.5	0.5

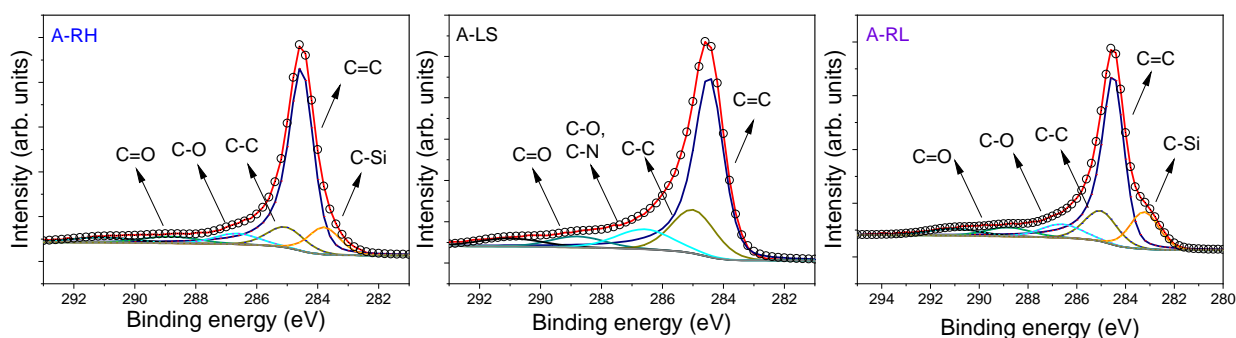


Figure 3.2.4.3.5. C 1s XPS Spectra of the activated biochars A-RH, A-LS, and A-RL.

Table 3.2.4.3.5. C 1s XPS binding energies and atomic % of the activated biochars A-RH, A-LS, and A-RL.

Sample	C1s (eV) (atomic %)					
	C-Si	C=C	C-C	C-O, C-N	C=O	π
A-RH	283.79	284.55	285.05	286.65	288.85	291.05
	(9.9)	(67.5)	(8.9)	(5.5)	(4.4)	(3.8)
A-LS	-	284.49	284.99	286.59	288.79	290.99
		(62.0)	(17.4)	(10.3)	(5.5)	(4.8)
A-RL	283.24	284.52	285.02	286.62	288.82	291.02
	(13.1)	(58.5)	(12.2)	(6.8)	(4.9)	(4.3)

An enhanced acidity of A-LS compared to the other biochars aspect was supported by pH_{PZC} measurements, reported in Table 3.2.4.3.6 (the curve is reported in Figure 3.2.6.7, in Appendix), that evidenced a low point zero charge (around 4.1) for A-LS, compared to A-RH and A-RL, which display a neutral pH_{PZC} . The absence of N-oxidized functionalities on the surface of A-RL also reduced its acidity.

Table 3.2.4.3.6. pH_{PZC} of the activated biochars A-RH, A-LS, and A-RL.

Sample	pH_{PZC}
A-RH	7.1
A-LS	4.1
A-RL	7.6

This important difference may explain the low interaction between A-LS and the Pd precursor, as discussed in Chapter 3.2.3. A-LS exhibited a pH_{PZC} of 4.1, indicating that at neutral pH in water, its surface was fully deprotonated and carried a negative net charge. As a result, during the impregnation step, interaction with the Pd precursor (PdCl_4^{2-}) was hindered, leading to low metal loading. Moreover, the impregnation method for Pd/C catalyst synthesis led to the formation of Pd^{2+} species, likely as oxychlorides, which affected the system's acidity and promoted side reactions like acetalization

(Chapter 3.2.3). On the other hand, the neutral pH_{PZC} of A-RH resulted in a neutral surface that could better adsorb the metal complex^{182,202}.

Catalysts synthesis, characterizations and activity

Based on the considerations outlined in the previous section, deposition-precipitation using H_2PdCl_4 as a precursor was selected as an alternative synthesis method to impregnation, for catalyst preparation, aimed at valorizing LS. This approach was chosen to avoid electrostatic repulsion between the char and the precursor, thereby promoting the deposition of neutral $\text{Pd}(\text{OH})_2$ species on the carbon surface. The char was suspended in a basic solution, and the pH was adjusted to 10.5 using NaOH. The metal

precursor was then added dropwise while carefully monitoring the pH to facilitate the precipitation of Pd(OH)₂.

After reduction, the resulting catalysts were labeled Pd/A-RH2, Pd/A-LS2, and Pd/A-RL, and they were fully characterized. The absence of oxychlorides species was confirmed by TPR analysis (Figure 3.2.4.3.6), by the absence of a peak indicating H₂ consumption at around 250 °C.

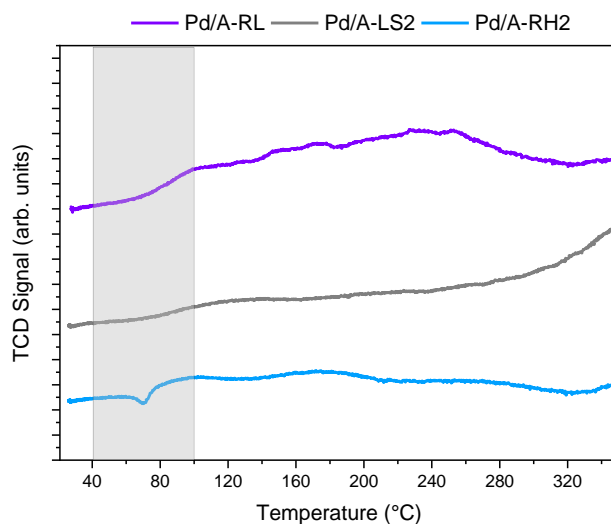


Figure 3.2.4.3.6. TPR profiles of Pd/A-RH2 (light blue), Pd/A-LS2 (gray), and Pd/A-RL (purple).

MP-AES measurements were conducted on the final catalysts to determine the actual Pd loading (Table 3.2.4.3.7). Despite the use of a different Pd loading method, the analysis revealed a lower Pd content for Pd/A-LS2 compared to Pd/A-RH2 and Pd/A-RL (0.44 wt.% vs. 0.64 wt.% and 0.67 wt.% for Pd/A-RH2 and Pd/A-RL, respectively), although it was an improvement over the impregnation method (Pd/A-LS, that reported 0.2 wt. %). Evidently, the distinct characteristics of this material, such as its morphology and microporous structure, had in any case an influence on the deposition of Pd on the A-LS surface. It is worth noting that Pd/A-RL resulted in the catalyst with the higher metal loading.

Table 3.2.4.3.7. Pd effective wt. % determined by MP-AES measurements, average Pd particle size determined by TEM and CO chemisorption, Pd dispersion, and Pd 3d_{5/2} XPS binding energies and atomic % of the three catalysts.

Sample	Pd effective wt. %	Average Pd particle size (nm)		Pd dispersion (D) %	Pd 3d _{5/2} (eV)	Pd 3d _{5/2} (atomic %)	
		TEM	CO chemisorption				
Pd/A-RH2	0.64	1.2	4.1	26	334.20 (33)	335.96 (46)	337.74 (21)
Pd/A-LS2	0.44	1.8	2.3	47	-	335.78 (58)	337.59 (42)
Pd/A-RL	0.67	1.5	2.1	53	-	335.70 (69)	337.52 (31)

Nevertheless, the precipitation method improved the dispersion of Pd NPs on the surface of all the ACs, with respect to the impregnation method. TEM images (Figure 3.2.4.3.7, Table 3.2.4.3.7) revealed the formation of well dispersed spherical Pd NPs on the surface of all the catalysts, with an average diameter of <2 nm. It is noteworthy that using the deposition-precipitation method, Pd/A-RH2 (Figure 3.2.6.7b, Appendix) exhibited also some larger and less uniform agglomerations with an average size of 22 nm. This observation was corroborated by CO chemisorption measurements (Table 3.2.4.3.7), which indicated an average Pd NP size of 4.1 nm for Pd/ARH, in contrast to 2.3 and 2.1 nm for Pd/ALS and Pd/ARL, respectively (Table 3.2.4.3.7). The TPR profile of Pd/A-RH (Figure 3.2.4.3.6) displayed a negative peak at 80 °C, associated with the decomposition of β -hydride species^{123,165}, further confirming the presence of larger particles on the surface of this catalyst. In contrast, the smaller Pd NPs (around 2 nm in diameter) on Pd/A-LS and Pd/A-RL were not capable of forming the β -hydride^{203,204}. Notably, Pd/A-RL showed the best Pd dispersion 53 %, followed by Pd/A-LS (47 %), and Pd/A-RH (26 %), and smallest NP size, making it the most promising candidate for applications requiring high Pd surface availability.

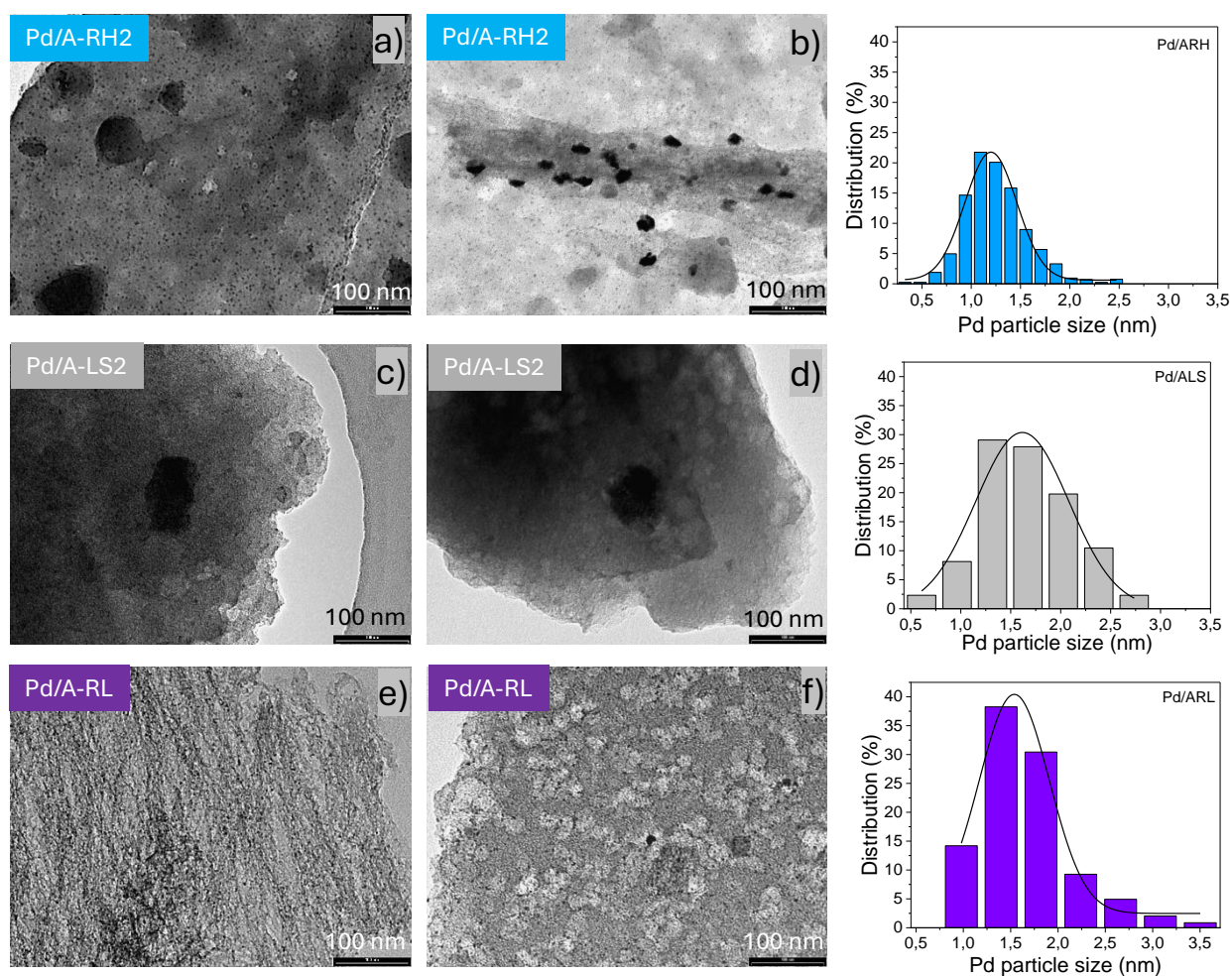


Figure 3.2.4.3.7 TEM images: a,b = Pd/A-RH2, c,d = Pd/A-LS2, e,f = Pd/A-RL, and Pd NPs size distribution of the three catalysts.

For the comparison of the catalytic tests results, the concentrations of the reactant and products were normalized by the gram of Pd effectively present in the reaction media. Figure 3.2.4.3.8 depicts the kinetic profiles for the consecutive hydrogenation of benzaldehyde to benzyl alcohol followed by the hydrodeoxygenation to toluene across the three catalytic systems. Zero-order plots were compared to evaluate the kinetics of Pd over the different supports, and the resulting kinetic constants for benzaldehyde conversion are reported in Table 3.2.4.3.8.

The catalytic activity of the systems, compared in terms of Turnover Frequency (TOF)²⁰⁵, as detailed in Table 3.2.4.3.8, revealed that Pd/A-RH2 and Pd/A-RL exhibited tenfold higher activity compared to Pd/A-LS2 (0.37 and 0.31 s⁻¹ vs. 0.04 s⁻¹). The linear trend observed for the disappearance of benzaldehyde over time indicated a zero-order kinetic, suggesting that the reaction rate is independent of BAL concentration, and in line with previous works that reported similar zero-order kinetics for palladium-based catalysts¹⁸⁴. The rate constant (k) was determined using Eq. 3.2.4.2.2. This independence from BAL concentration is likely due to the saturation of the catalyst's active sites, where the reaction rate is governed by the surface availability for hydrogenation and product desorption. Although the TOF and k_{ald} values of Pd/A-RL were slightly lower than those of Pd/A-RH2 (k_{ald} = 33 vs. 42 mol L⁻¹s⁻¹gPd⁻¹), Pd/A-RL demonstrated higher yields of the desired products (BALOH and TOL). Consequently, selectivity was also superior for Pd/A-RL. At 30 minutes, the yield of BALOH was 77% for Pd/A-RL, compared to 76% for Pd/A-RH2, with Pd/A-RL also achieving a higher selectivity (94%). After 60 minutes, the combined yields of BALOH and TOL were 84% and 12%, respectively, for Pd/A-RL, compared to 59% and 22% for Pd/A-RH2. The byproducts formed, especially with Pd/A-RH2, were identified as ethoxy and diethoxy methylbenzene, resulting from acetalization with ethanol used as the solvent. In contrast, Pd/A-LS2 showed significantly lower activity, with a TOF of only 0.04 s⁻¹ and poor BAL conversion (9% after 30 minutes). Despite the synthesis approach improving the characteristics of Pd/A-LS2 in terms of metal loading, oxidation state, and dispersion, the low activity of this catalyst was still evident, confirming that the chemical-physical properties of the support influenced catalytic performances, reducing the interaction with the reactants. Overall, these results demonstrate that while Pd/A-RH2 and Pd/A-RL exhibited comparable activity, Pd/A-RL achieved superior selectivity and product yields.

3. Valorization of biomass via pyrolysis - 3.2 Biochar as support for heterogeneous catalysts – 3.2.4 Co-pyrolysis of LS and RH for the preparation of Pd based catalysts

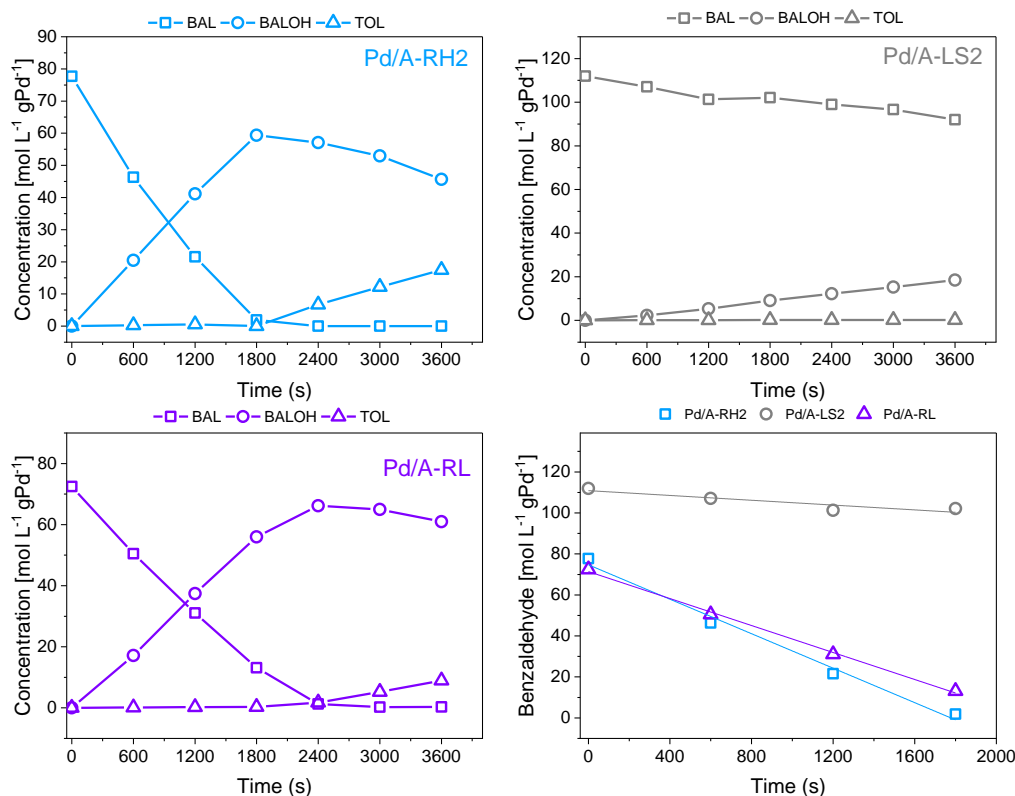


Figure 3.2.4.3.8. Kinetic profiles and zero order plots of benzaldehyde hydrogenation over Pd/A-RH2, Pd/A-LS2, Pd/A-RL. Reaction conditions: ethanol 100 mL, BAL 0.1 M, catalyst 200 mg, temperature: 25 °C, pressure: 1 bar, H₂ 30 mL/min stirring speed: 1400 rpm

Table 3.2.4.3.8. Results of benzaldehyde hydrogenation over the three catalysts.

Sample	TOF (s ⁻¹)	$k_{ald} \times 10^3$ (mol L ⁻¹ s ⁻¹ gPd ⁻¹)	Benzaldehyde conversion (%) at 30 min	BALOH yield (%) at 30 min	BALOH selectivity (%) at 30 min	BALOH + TOL yield (%) at 60 min
Pd/A-RH	0.37	42	97	76	78	59 + 22
Pd/A-LS	0.04	6	9	8	92	17 + 1
Pd/A-RL	0.31	33	82	77	94	84 + 12

Apart from Pd size and distribution, it is well known that for hydrogenation reactions, Pd⁰ is the most active phase²⁰⁶. Therefore, Pd 3d XPS measurements were performed to assess the amount of Pd⁰ and Pd²⁺ on the surface of the catalysts (Figure 3.2.4.3.9). For Pd/A-LS2 and Pd/A-RL (Figure 3.2.4.3.9b, 3.2.4.3.9c), the doublets corresponding to Pd 3d_{5/2} and Pd 3d_{3/2} were resolved into four distinct components, whereas six components were identified for Pd/A-RH2 (Figure 3.2.4.3.9a). Regarding Pd 3d_{5/2}, the predominant peak at 335.7 ± 0.2 eV was attributed to the metallic Pd⁰, while the shoulder at 337.6 ± 0.2 eV implies the presence of Pd²⁺ on the surface, likely in the form of PdO. The component at 334.20 eV observed for Pd/A-RH was associated with metallic Pd⁰ existing as larger nanoparticles, consistent with the previous characterization findings.

It is known that the 3d binding energy of Pd⁰ shifts towards higher values with decreasing cluster size¹⁹⁸. The atomic surface concentration of the Pd species is summarized in Table 3.2.4.3.7. Notably, considering the double contribution of Pd⁰ for Pd/A-RH2, this sample exhibits the highest proportion of reduced species (approximately 80%), followed by Pd/A-RL (around 70%) and Pd/A-LS (about 60%), confirming a positive relation between the oxidation states of the metal and the activity. The higher selectivity of Pd/A-RL is therefore to be referred to as the more homogeneous distribution and higher dispersion of Pd.

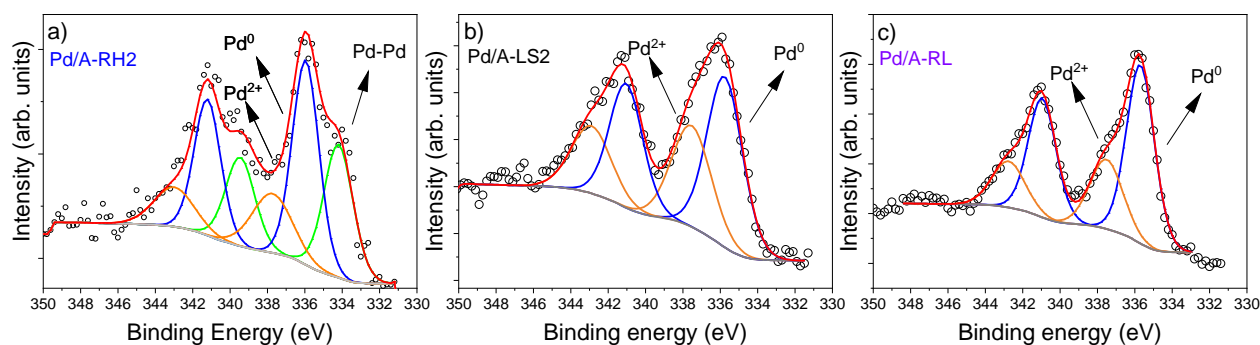


Figure 3.2.4.3.9. Pd 3dXPS spectra of a) Pd/A-RH2, b) Pd/A-LS2, c) Pd/A-RL

The high percentage of Pd²⁺ in Pd/A-LS2 could be assigned to several factors. For instance, a greater presence of micropores on ALS can hinder the reduction of Pd species by limiting the accessibility and diffusion of the reducing agent to the active sites where Pd precursor species are adsorbed²⁰⁷. Another reason could be found in the role of the surface functionalities: recently, Stucchi *et al.*, reported that the oxygen functionalities on the surface of carbon can also influence the catalytic activity of Pd/C catalysts²⁰⁶. The researchers found that the main interaction between benzaldehyde and the catalyst occurs in the aromatic ring. Therefore, the presence of a high amount of oxygen functionalities, especially highly polarized such as C=O, can hinder the absorption of benzaldehyde on the surface and decrease the catalytic activity. Pd/A-LS2 indeed resulted in the sample with the highest oxygen (and nitrogen) functionalities. This feature, together with the Pd oxidation state, the lower amount of metal anchored, the highly microporosity and the flat morphology, well explain the modest catalytic activity.

On the other hand, combining the leather shaving waste biomass with the lignocellulosic rice husk biomass in the co-pyrolysis process, followed by the activation step in steam, resulted in a new material with enhanced characteristics, that allowed to obtain a catalyst with very highly dispersed Pd NPs and with good catalytic activity, and enhanced selectivity toward hydrogenation/hydrogenolysis reactions.

3. Valorization of biomass via pyrolysis - 3.2 Biochar as support for heterogeneous catalysts – 3.2.4 Co-pyrolysis of LS and RH for the preparation of Pd based catalysts

Considering the promising results, Pd/A-RL was subjected to recycling to assess stability. The recyclability was investigated at less than 50% conversion for three cycles (Figure 3.2.4.3.10). After one cycle, the catalyst showed constant conversion and an increase in selectivity for both products (from 78 to 87% for BALOH and from 0.9 to 1.8% for toluene). Despite a slight decrease of conversion after the third cycle (from 33% to 26%), the selectivity further increased, up to 99% for BALOH, indicating that no side reactions were occurring and that only the reaction rate was influenced.

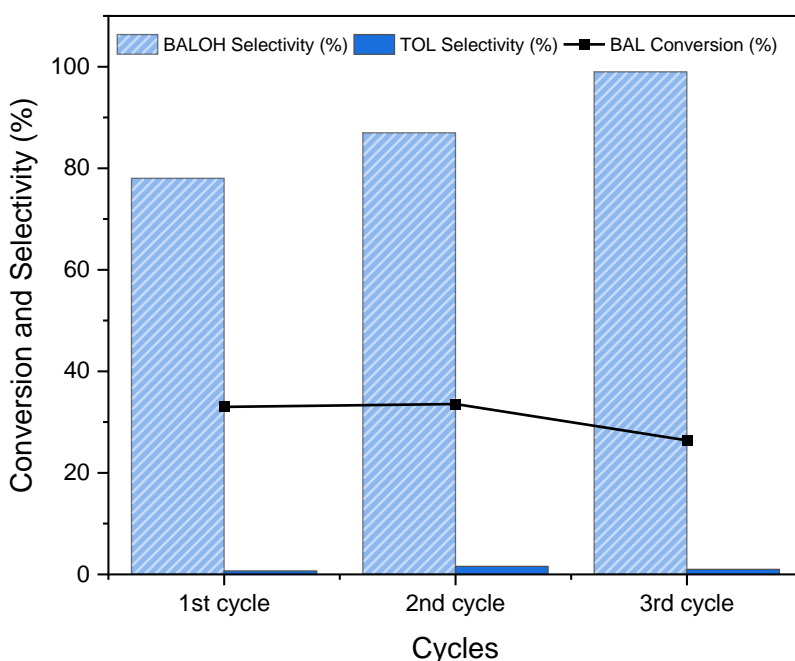


Figure 3.2.4.3.10. Pd/A-RL recycling tests. Reaction conditions: Reaction conditions: ethanol 100 mL, BAL 0.1 M, catalyst 200 mg, temperature: 25 °C, pressure: 1 bar, H₂ 30 mL/min stirring speed: 1400 rpm

3.2.5 Conclusions

In this work, the potentials of activated biochars derived from different waste biomasses as support for the preparation of Pd-based catalysts were investigated. The catalytic properties were compared in the hydrogenation of benzaldehyde. Pd/A-RH achieved nearly complete benzaldehyde conversion after 40 minutes, demonstrating high selectivity to benzyl alcohol (82%) and toluene (97%) after 200 minutes, under mild reaction conditions (25 °C, 1 bar, H₂ flow of 33 mL/min). In contrast, A-RG and A-LS showed weaker Pd trapping and anchorage, resulting in fewer active sites insufficient for converting benzaldehyde under the proposed reaction conditions. A-LS, even after optimization of the synthetic approach to enhance metal anchoring and improve dispersion, exhibited low catalytic activity, with a TOF tenfold lower than the corresponding A-RH-based catalyst (0.04 vs 0.37 s⁻¹). Characterization results confirmed that the final chemical, textural, and morphological properties of the activated biochars were significantly affected by the origin of the initial biomasses, which in turn influenced the properties and efficiency of the Pd-based catalysts. The presence of inner channels and cavities with a micro-mesoporous texture, along with oxygenated functionalities and a hybrid organic/inorganic structure, made A-RH an optimal support for Pd, facilitating efficient trapping and anchorage of the nanoparticles, achieving great dispersion, and enhancing the material's stability compared to the other studied catalysts.

The co-pyrolysis of LS and RH proved to be an effective method for tuning the characteristics of the two materials, successfully combining their properties. The sponge-like morphology and micro-mesoporous texture of A-RH were preserved, and the addition of LS resulted in an increase of total surface area. Furthermore, A-RL displayed a more functionalized surface, increasing the nucleation sites for the support and achieving a higher, more homogeneous distribution of the metal active phase. Consequently, Pd/A-RL demonstrated superior selectivity towards the desired products (96 % vs 81 % Pd/A-RH₂), effectively suppressing side reactions such as the acetalization of benzaldehyde with ethanol. Therefore, co-pyrolysis allowed for the valorization of a complex waste like LS, rendering it suitable for catalysis. In conclusion, both biomass-derived catalysts (Pd/A-RH and Pd/A-RL) exhibited superior performance in terms of activity, selectivity, and stability during the target reaction compared to those prepared with commercial carbon (AC).

3.2.6 Appendix

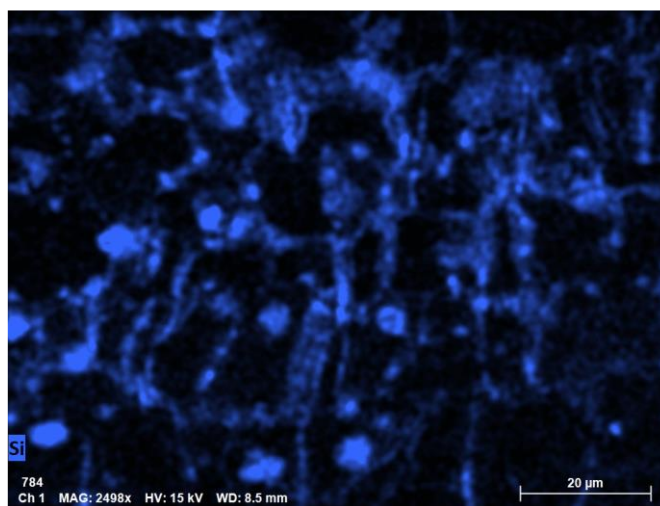
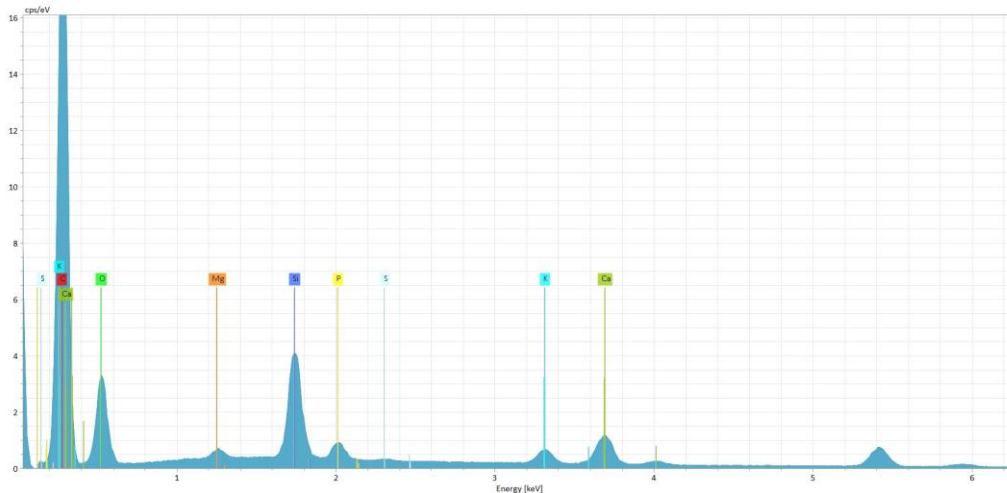


Figure 3.2.6.1. EDX spectra and map of Si element distribution of A-RH

3. Valorization of biomass via pyrolysis - 3.2 Biochar as support for heterogeneous catalysts – 3.2.4 Co-pyrolysis of LS and RH for the preparation of Pd based catalysts

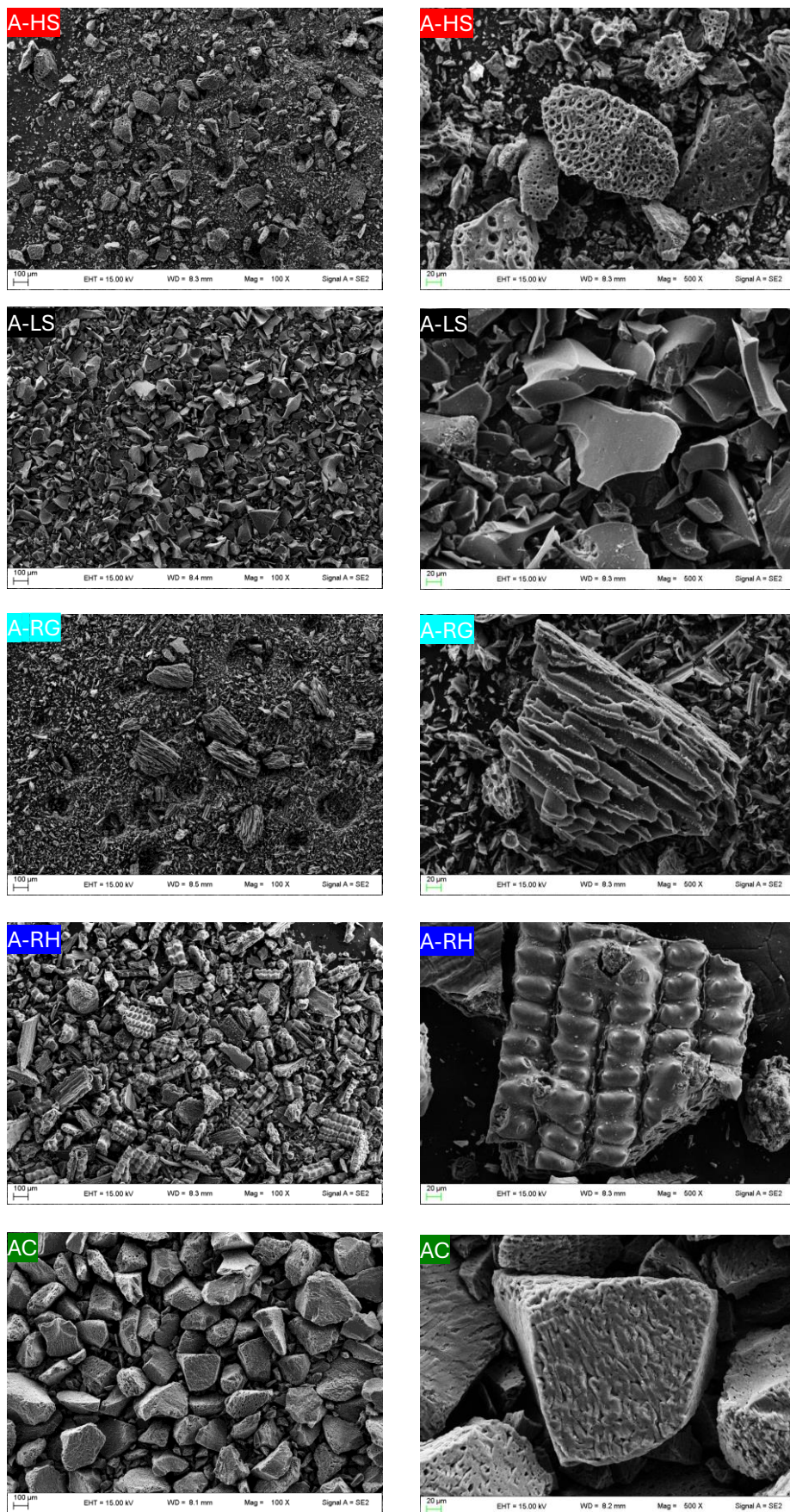


Figure 3.2.6.2. SEM images of ACs.

3. Valorization of biomass via pyrolysis - 3.2 Biochar as support for heterogeneous catalysts – 3.2.4 Co-pyrolysis of LS and RH for the preparation of Pd based catalysts

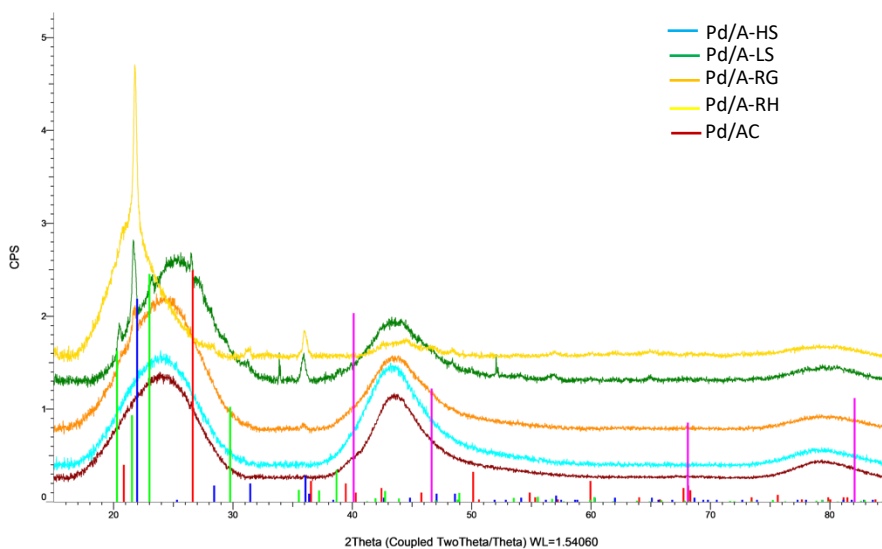


Figure 3.2.6.3. XRD patterns of Pd/A-HS (light blue), Pd/A-LS (green), Pd/A-RG (orange), and Pd/A-RH (yellow) and Pd/AC (dark red).

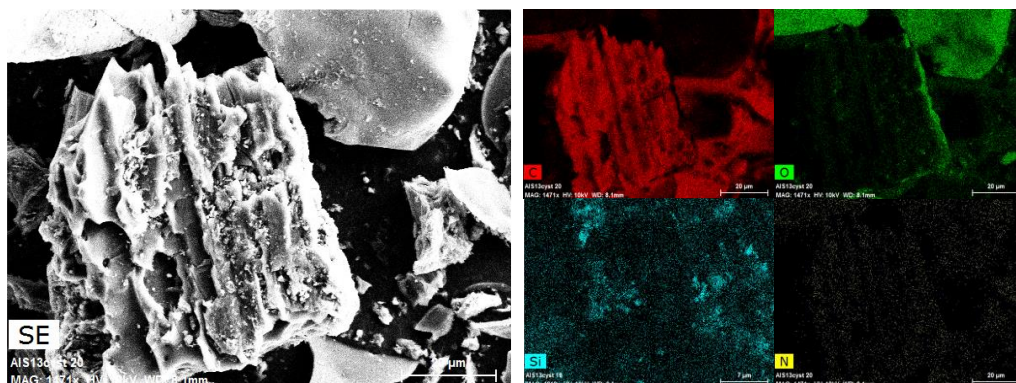


Figure 3.2.6.4. SEM-EDX and mapping of C, O, Si, N elements of A-RL

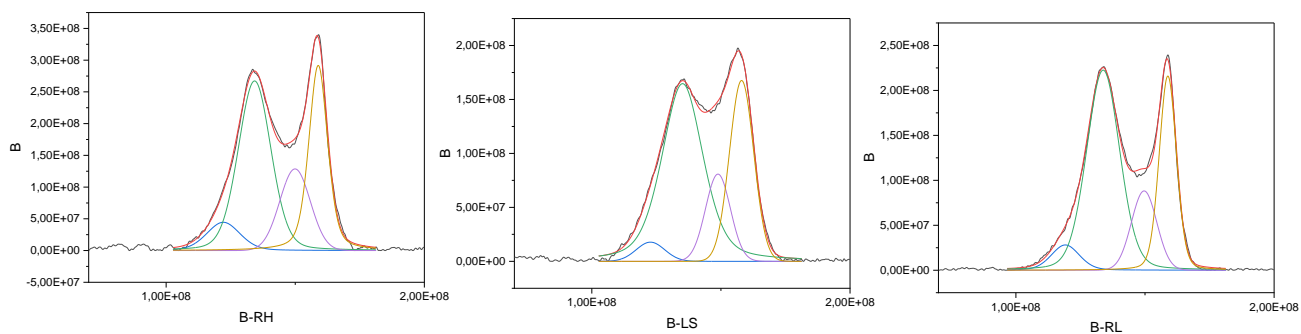


Figure 3.2.6.5. Raman spectra of biochars B-RH, B-LS, and B-RL.

3. Valorization of biomass via pyrolysis - 3.2 Biochar as support for heterogeneous catalysts – 3.2.4 Co-pyrolysis of LS and RH for the preparation of Pd based catalysts

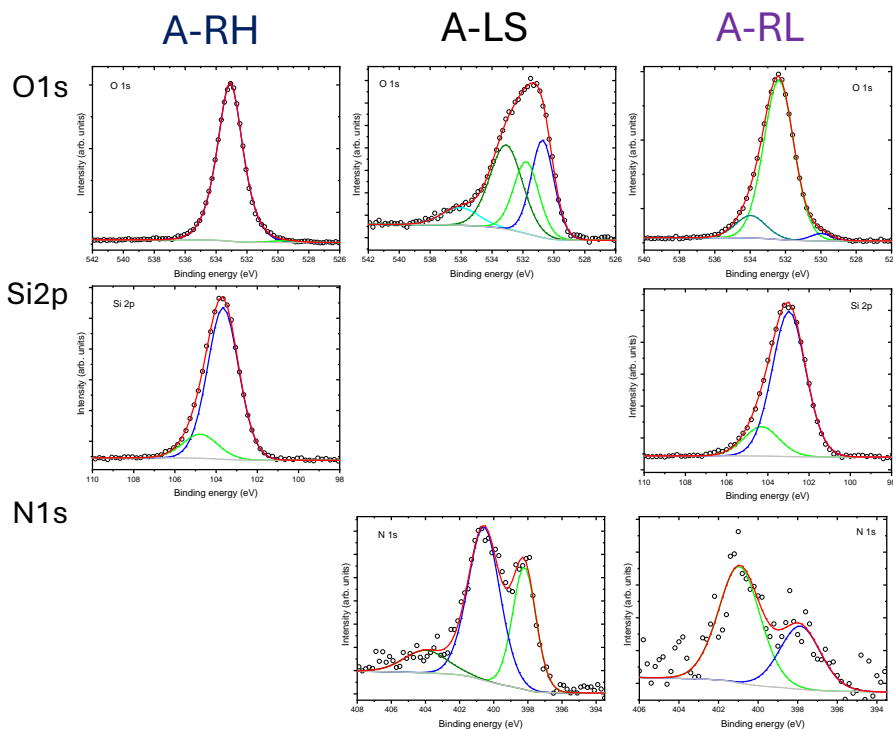


Figure 3.2.6.6. O1s, Si2p and N1s XPS spectra of A-RH, A-LS, and A-RL.

Table 3.2.6.1 N 1s XPS binding energies and atomic % of A-LS and A-RL.

Sample	N1s (eV) (atomic %)		
	Pyridinic	Pyrrolic	N-oxides
A-LS	398.21 (32.8)	400.57 (56.0)	403.99 (11.2)
A-RL	397.(34.6)	400.9 (65.4)	/

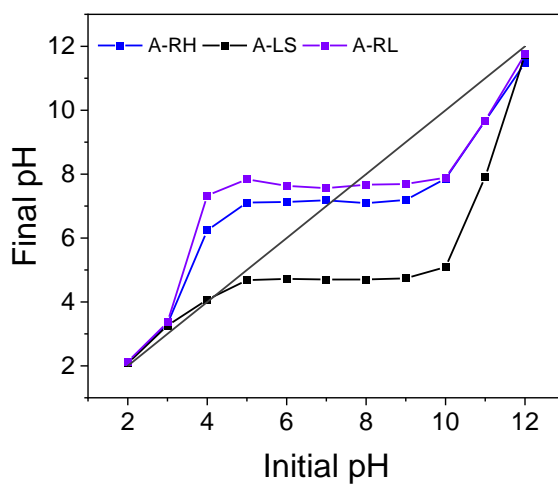


Figure 3.2.6.7. Plot of $pH_{initial}$ vs pH_{final} for the measurement of pH_{PZC} via the pH drift method, for A-RH (blue), A-LS (black), and A-RL (purple)

3.2.7. References

- (1) Zou, R.; Qian, M.; Wang, C.; Mateo, W.; Wang, Y.; Dai, L.; Lin, X.; Zhao, Y.; Huo, E.; Wang, L.; Zhang, X.; Kong, X.; Ruan, R.; Lei, H. Biochar: From by-Products of Agro-Industrial Lignocellulosic Waste to Tailored Carbon-Based Catalysts for Biomass Thermochemical Conversions. *Chemical Engineering Journal* **2022**, *441*, 135972. <https://doi.org/10.1016/j.cej.2022.135972>.
- (2) Varhegyi, G.; Antal, M. J. Jr.; Szekely, T.; Szabo, P. Kinetics of the Thermal Decomposition of Cellulose, Hemicellulose, and Sugarcane Bagasse. *Energy Fuels* **1989**, *3* (3), 329–335. <https://doi.org/10.1021/ef00015a012>.
- (3) Stefanidis, S. D.; Kalogiannis, K. G.; Iliopoulou, E. F.; Michailof, C. M.; Pilavachi, P. A.; Lappas, A. A. A Study of Lignocellulosic Biomass Pyrolysis via the Pyrolysis of Cellulose, Hemicellulose and Lignin. *Journal of Analytical and Applied Pyrolysis* **2014**, *105*, 143–150. <https://doi.org/10.1016/j.jaap.2013.10.013>.
- (4) Pasangulapati, V.; Ramachandriya, K. D.; Kumar, A.; Wilkins, M. R.; Jones, C. L.; Huhnke, R. L. Effects of Cellulose, Hemicellulose and Lignin on Thermochemical Conversion Characteristics of the Selected Biomass. *Bioresource Technology* **2012**, *114*, 663–669. <https://doi.org/10.1016/j.biortech.2012.03.036>.
- (5) Hernández-Beltrán, J. U.; Hernández-De Lira, I. O.; Cruz-Santos, M. M.; Saucedo-Luevanos, A.; Hernández-Terán, F.; Balagurusamy, N. Insight into Pretreatment Methods of Lignocellulosic Biomass to Increase Biogas Yield: Current State, Challenges, and Opportunities. *Applied Sciences* **2019**, *9* (18), 3721. <https://doi.org/10.3390/app9183721>.
- (6) Kabir, G., Hameed, B.H. Recent Progress on Catalytic Pyrolysis of Lignocellulosic Biomass to High-Grade Bio-Oil and Bio-Chemicals. *Renewable and Sustainable Energy Reviews* **2017**, *70*, 945–967. <https://doi.org/10.1016/j.rser.2016.12.001>.
- (7) Shi, X.; Wang, J. A Comparative Investigation into the Formation Behaviors of Char, Liquids and Gases during Pyrolysis of Pinewood and Lignocellulosic Components. *Bioresource Technology* **2014**, *170*, 262–269. <https://doi.org/10.1016/j.biortech.2014.07.110>.
- (8) Phan, B.; Duong, T. L.; Nguyen, V.; Tran, T.; Nguyen, M.; Nguyen, H. L.; Nguyen, D.; Luu, L. Evaluation of the Production Potential of Bio-Oil from Vietnamese Biomass Resources by Fast Pyrolysis. *Biomass and Bioenergy* **2014**, *62*. <https://doi.org/10.1016/j.biombioe.2014.01.012>.
- (9) Abnisa, F.; Arami Niya, A.; Daud, W.; Sahu, J.; Noor, I. Utilization of Oil Palm Tree Residues to Produce Bio-Oil and Bio-Char via Pyrolysis. *Energy Conversion and Management* **2013**, *76*, 1073–1082. <https://doi.org/10.1016/j.enconman.2013.08.038>.
- (10) Zhang, H.; Xiao, R.; Wang, D.; He, G.; Shao, S.; Zhang, J.; Zhong, Z. Biomass Fast Pyrolysis in a Fluidized Bed Reactor under N-2, CO₂, CO, CH₄ and H-2 Atmospheres. *Bioresource technology* **2011**, *102*, 4258–4264. <https://doi.org/10.1016/j.biortech.2010.12.075>.
- (11) Kim, S.; Koo, B.; Ryu, J.; Lee, J.; Kim, C.; Lee, D. H.; Kim, G.; Choi, S. Bio-Oil from the Pyrolysis of Palm and Jatropha Wastes in a Fluidized Bed. *Fuel Processing Technology* **2013**, *108*, 118–124. <https://doi.org/10.1016/j.fuproc.2012.05.002>.
- (12) Butler, E.; Devlin, G.; Meier, D.; McDonnell, K. Characterisation of Spruce, Salix, Miscanthus and Wheat Straw for Pyrolysis Applications. *Bioresource technology* **2012**, *131C*, 202–209. <https://doi.org/10.1016/j.biortech.2012.12.013>.

3. Valorization of biomass via pyrolysis - 3.2 Biochar as support for heterogeneous catalysts – 3.2.4 Co-pyrolysis of LS and RH for the preparation of Pd based catalysts

- (13) Li, D.-C.; Jiang, H. The Thermochemical Conversion of Non-Lignocellulosic Biomass to Form Biochar: A Review on Characterizations and Mechanism Elucidation. *Bioresource Technology* **2017**, *246*. <https://doi.org/10.1016/j.biortech.2017.07.029>.
- (14) Fahmy, T.; Fahmy, Y.; Mobarak, F.; El-Sakhawy, M.; Abouzeid, R. Biomass Pyrolysis: Past, Present, and Future. *Environment Development and Sustainability* **2020**, *22*, 17–32. <https://doi.org/10.1007/s10668-018-0200-5>.
- (15) Demirbas, A. Hydrogen from Mosses and Algae via Pyrolysis and Steam Gasification. *Energy Sources, Part A: Recovery, Utilization, and Environmental Effects* **2009**, *32* (2), 172–179. <https://doi.org/10.1080/15567030802464388>.
- (16) Mishra, K.; Siwal, S.; Saini, A.; Thakur, V. Recent Update on Gasification and Pyrolysis Processes of Lignocellulosic and Algal Biomass for Hydrogen Production. *Fuel* **2023**, *332*, 126169. <https://doi.org/10.1016/j.fuel.2022.126169>.
- (17) Saber, M.; Nakhshinie, B.; Yoshikawa, K. A Review of Production and Upgrading of Algal Bio-Oil. *Renewable and Sustainable Energy Reviews* **2016**, *58*, 918–930. <https://doi.org/10.1016/j.rser.2015.12.342>.
- (18) Ro, K.; Cantrell, K.; Hunt, P. G. High-Temperature Pyrolysis of Blended Animal Manures for Producing Renewable Energy and Value-Added Biochar. *Industrial & Engineering Chemistry Research* **2010**, *49*. <https://doi.org/10.1021/ie101155m>.
- (19) Si, W.; Zhou, J.; Zhang, S.; Li, S.; Xing, W.; Zhuo, S. Tunable N-Doped or Dual N, S-Doped Activated Hydrothermal Carbons Derived from Human Hair and Glucose for Supercapacitor Applications. *Electrochimica Acta* **2013**, *107*, 397–405. <https://doi.org/10.1016/j.electacta.2013.06.065>.
- (20) *Lifegoast*. <https://www.lifegoast.eu/> (accessed 2024-10-23).
- (21) Yılmaz, O.; Kantarli, I.; Yuksel, M.; Saglam, M.; Yanik, J. Conversion of Leather Wastes to Useful Products. *Resources, Conservation and Recycling* **2007**, *49*, 436–448. <https://doi.org/10.1016/j.resconrec.2006.05.006>.
- (22) Caballero, J.; Font, R.; Esperanza, M. Kinetics of the Thermal Decomposition of Tannery Waste. *Journal of Analytical and Applied Pyrolysis* **1998**, *47*, 165–181. [https://doi.org/10.1016/S0165-2370\(98\)00081-3](https://doi.org/10.1016/S0165-2370(98)00081-3).
- (23) Tôrres Filho, A.; Lange, L. C.; de Melo, G. C. B.; Praes, G. E. Pyrolysis of Chromium Rich Tanning Industrial Wastes and Utilization of Carbonized Wastes in Metallurgical Process. *Waste Management* **2016**, *48*, 448–456. <https://doi.org/10.1016/j.wasman.2015.11.046>.
- (24) Gil, R. R.; Girón, R. P.; Lozano, M. S.; Ruiz, B.; Fuente, E. Pyrolysis of Biocollagenic Wastes of Vegetable Tanning. Optimization and Kinetic Study. *Journal of Analytical and Applied Pyrolysis* **2012**, *98*, 129–136. <https://doi.org/10.1016/j.jaap.2012.08.010>.
- (25) Marcilla, A.; García, A. N.; León, M.; Martínez, P.; Bañón, E. Analytical Pyrolysis As a Method to Characterize Tannery Wastes. *Industrial & Engineering Chemistry Research* **2011**, *50* (15), 8994–9002. <https://doi.org/10.1021/ie200582k>.
- (26) Kantarli, I. C.; Yanik, J. Activated Carbon from Leather Shaving Wastes and Its Application in Removal of Toxic Materials. *Journal of Hazardous Materials* **2010**, *179* (1), 348–356. <https://doi.org/10.1016/j.jhazmat.2010.03.012>.
- (27) Salimi, P.; Tieuli, S.; Taghavi, S.; Venezia, E.; Fugattini, S.; Lauciello, S.; Prato, M.; Marras, S.; Li, T.; Signoretto, M.; Costamagna, P.; Zaccaria, R. P. Sustainable Lithium-Ion Batteries Based on Metal-Free Tannery Waste Biochar. *Green Chemistry* **2022**, *24* (10), 4119–4129. <https://doi.org/10.1039/D1GC04772H>.

3. Valorization of biomass via pyrolysis - 3.2 Biochar as support for heterogeneous catalysts – 3.2.4 Co-pyrolysis of LS and RH for the preparation of Pd based catalysts

- (28) Amdouni, S.; Ben Hassen Trabelsi, A.; Mabrouk Elasm, A.; Chagtm, R.; Haddad, K.; Jamaoui, F.; Khedhira, H.; Chérif, C. Tannery Fleshing Wastes Conversion into High Value-Added Biofuels and Biochars Using Pyrolysis Process. *Fuel* **2021**, *294*, 120423. <https://doi.org/10.1016/j.fuel.2021.120423>.
- (29) Lin, Y.-Y.; Chen, W.-H.; Liu, H.-C. Aging and Emulsification Analyses of Hydrothermal Liquefaction Bio-Oil Derived from Sewage Sludge and Swine Leather Residue. *Journal of Cleaner Production* **2020**, *266*, 122050. <https://doi.org/10.1016/j.jclepro.2020.122050>.
- (30) Zhang, J.; Yang, H.; Kang, G.; Yu, J.; Gao, S.; Liu, Z.; Li, C.; Zeng, X.; Lu, S. The Synergistic Effect on the Product Distribution for the Co-Pyrolysis of Tannery Wastes. *Fuel* **2022**, *322*, 124080. <https://doi.org/10.1016/j.fuel.2022.124080>.
- (31) Hu, X.; Gholizadeh, M. Biomass Pyrolysis: A Review of the Process Development and Challenges from Initial Researches up to the Commercialisation Stage. *Journal of Energy Chemistry* **2019**, *39*, 109–143. <https://doi.org/10.1016/j.jechem.2019.01.024>.
- (32) Kalak, T. Potential Use of Industrial Biomass Waste as a Sustainable Energy Source in the Future. *Energies* **2023**, *16* (4), 1783. <https://doi.org/10.3390/en16041783>.
- (33) Zhou, N.; Zhou, J.; Dai, L.; Guo, F.; Wang, Y.; Li, H.; Deng, W.; Lei, H.; Chen, P.; Liu, Y.; Ruan, R. Syngas Production from Biomass Pyrolysis in a Continuous Microwave Assisted Pyrolysis System. *Bioresource Technology* **2020**, *314*, 123756. <https://doi.org/10.1016/j.biortech.2020.123756>.
- (34) Cheng, F.; Li, X. Preparation and Application of Biochar-Based Catalysts for Biofuel Production. *Catalysts* **2018**, *8* (9), 346. <https://doi.org/10.3390/catal8090346>.
- (35) Pereira Lopes, R.; Astruc, D. Biochar as a Support for Nanocatalysts and Other Reagents: Recent Advances and Applications. *Coordination Chemistry Reviews* **2021**, *426*, 213585. <https://doi.org/10.1016/j.ccr.2020.213585>.
- (36) Saravanan, A.; Kumar, P. S. Biochar Derived Carbonaceous Material for Various Environmental Applications: Systematic Review. *Environmental Research* **2022**, *214*, 113857. <https://doi.org/10.1016/j.envres.2022.113857>.
- (37) Matuščík, J.; Pohořelý, M.; Kočí, V. Is Application of Biochar to Soil Really Carbon Negative? The Effect of Methodological Decisions in Life Cycle Assessment. *Science of The Total Environment* **2022**, *807*, 151058. <https://doi.org/10.1016/j.scitotenv.2021.151058>.
- (38) Low, Y. W.; Yee, K. F. A Review on Lignocellulosic Biomass Waste into Biochar-Derived Catalyst: Current Conversion Techniques, Sustainable Applications and Challenges. *Biomass and Bioenergy* **2021**, *154*, 106245. <https://doi.org/10.1016/j.biombioe.2021.106245>.
- (39) Bhavani, P.; Praveen Kumar, D.; Hussain, M.; Aminabhavi, T. M.; Park, Y.-K. Eco-Friendly Rice Husk Derived Biochar as a Highly Efficient Noble Metal-Free Cocatalyst for High Production of H₂ Using Solar Light Irradiation. *Chemical Engineering Journal* **2022**, *434*, 134743. <https://doi.org/10.1016/j.cej.2022.134743>.
- (40) Ding, W.; Dong, X.; Ime, I. M.; Gao, B.; Ma, L. Q. Pyrolytic Temperatures Impact Lead Sorption Mechanisms by Bagasse Biochars. *Chemosphere* **2014**, *105*, 68–74. <https://doi.org/10.1016/j.chemosphere.2013.12.042>.

3. Valorization of biomass via pyrolysis - 3.2 Biochar as support for heterogeneous catalysts – 3.2.4 Co-pyrolysis of LS and RH for the preparation of Pd based catalysts

- (41) Parthasarathy, P.; Al-Ansari, T.; Mackey, H. R.; Sheeba Narayanan, K.; McKay, G. A Review on Prominent Animal and Municipal Wastes as Potential Feedstocks for Solar Pyrolysis for Biochar Production. *Fuel* **2022**, *316*, 123378. <https://doi.org/10.1016/j.fuel.2022.123378>.
- (42) Liu, Z.; Zhang, F.-S.; Wu, J. Characterization and Application of Chars Produced from Pinewood Pyrolysis and Hydrothermal Treatment. *Fuel* **2010**, *89* (2), 510–514. <https://doi.org/10.1016/j.fuel.2009.08.042>.
- (43) Tang, S.; Shao, N.; Zheng, C.; Yan, F.; Zhang, Z. Amino-Functionalized Sewage Sludge-Derived Biochar as Sustainable Efficient Adsorbent for Cu(II) Removal. *Waste Management* **2019**, *90*, 17–28. <https://doi.org/10.1016/j.wasman.2019.04.042>.
- (44) Zhou, X.-L.; Zhang, H.; Shao, L.-M.; Lü, F.; He, P.-J. Preparation and Application of Hierarchical Porous Carbon Materials from Waste and Biomass: A Review. *Waste Biomass Valor* **2021**, *12* (4), 1699–1724. <https://doi.org/10.1007/s12649-020-01109-y>.
- (45) Dutta, S.; Bhaumik, A.; C.-W. Wu, K. Hierarchically Porous Carbon Derived from Polymers and Biomass: Effect of Interconnected Pores on Energy Applications. *Energy & Environmental Science* **2014**, *7* (11), 3574–3592. <https://doi.org/10.1039/C4EE01075B>.
- (46) Raveendran, K.; Ganesh, A. Adsorption Characteristics and Pore-Development of Biomass-Pyrolysis Char. *Fuel* **1998**, *77* (7), 769–781. [https://doi.org/10.1016/S0016-2361\(97\)00246-9](https://doi.org/10.1016/S0016-2361(97)00246-9).
- (47) Ahmad, M.; Lee, S. S.; Dou, X.; Mohan, D.; Sung, J.-K.; Yang, J. E.; Ok, Y. S. Effects of Pyrolysis Temperature on Soybean Stover- and Peanut Shell-Derived Biochar Properties and TCE Adsorption in Water. *Bioresource Technology* **2012**, *118*, 536–544. <https://doi.org/10.1016/j.biortech.2012.05.042>.
- (48) Oginni, O.; Singh, K.; Oporto, G.; Dawson-Andoh, B.; McDonald, L.; Sabolsky, E. Influence of One-Step and Two-Step KOH Activation on Activated Carbon Characteristics. *Bioresource Technology Reports* **2019**, *7*, 100266. <https://doi.org/10.1016/j.biteb.2019.100266>.
- (49) Benedetti, V.; Cordioli, E.; Patuzzi, F.; Baratieri, M. CO₂ Adsorption Study on Pure and Chemically Activated Chars Derived from Commercial Biomass Gasifiers. *Journal of CO₂ Utilization* **2019**, *33*, 46–54. <https://doi.org/10.1016/j.jcou.2019.05.008>.
- (50) Fuertes, A. B.; Ferrero, G. A.; Diez, N.; Sevilla, M. A Green Route to High-Surface Area Carbons by Chemical Activation of Biomass-Based Products with Sodium Thiosulfate. *ACS Sustainable Chem. Eng.* **2018**, *6* (12), 16323–16331. <https://doi.org/10.1021/acssuschemeng.8b03264>.
- (51) Leng, L.; Xiong, Q.; Yang, L.; Li, H.; Zhou, Y.; Zhang, W.; Jiang, S.; Li, H.; Huang, H. An Overview on Engineering the Surface Area and Porosity of Biochar. *Science of The Total Environment* **2021**, *763*, 144204. <https://doi.org/10.1016/j.scitotenv.2020.144204>.
- (52) Singh, E.; Mishra, R.; Kumar, A.; Shukla, S. K.; Lo, S.-L.; Kumar, S. Circular Economy-Based Environmental Management Using Biochar: Driving towards Sustainability. *Process Safety and Environmental Protection* **2022**, *163*, 585–600. <https://doi.org/10.1016/j.psep.2022.05.056>.

3. Valorization of biomass via pyrolysis - 3.2 Biochar as support for heterogeneous catalysts – 3.2.4 Co-pyrolysis of LS and RH for the preparation of Pd based catalysts

- (53) Wang, L.; Ok, Y. S.; Tsang, D. C. W.; Alessi, D. S.; Rinklebe, J.; Wang, H.; Mašek, O.; Hou, R.; O'Connor, D.; Hou, D. New Trends in Biochar Pyrolysis and Modification Strategies: Feedstock, Pyrolysis Conditions, Sustainability Concerns and Implications for Soil Amendment. *Soil Use and Management* **2020**, *36* (3), 358–386. <https://doi.org/10.1111/sum.12592>.
- (54) Qian, K.; Kumar, A.; Zhang, H.; Bellmer, D.; Huhnke, R. Recent Advances in Utilization of Biochar. *Renewable and Sustainable Energy Reviews* **2015**, *42*, 1055–1064. <https://doi.org/10.1016/j.rser.2014.10.074>.
- (55) Wu, S.; He, H.; Inthapanya, X.; Yang, C.; Lu, L.; Zeng, G.; Han, Z. Role of Biochar on Composting of Organic Wastes and Remediation of Contaminated Soils—a Review. *Environ Sci Pollut Res* **2017**, *24* (20), 16560–16577. <https://doi.org/10.1007/s11356-017-9168-1>.
- (56) Liu, S.; Li, M.; Liu, Y.; Liu, N.; Tan, X.; Jiang, L.; Wen, J.; Hu, X.; Yin, Z. Removal of 17 β -Estradiol from Aqueous Solution by Graphene Oxide Supported Activated Magnetic Biochar: Adsorption Behavior and Mechanism. *Journal of the Taiwan Institute of Chemical Engineers* **2019**, *102*, 330–339. <https://doi.org/10.1016/j.jtice.2019.05.002>.
- (57) Wang, R.-Z.; Huang, D.-L.; Liu, Y.-G.; Zhang, C.; Lai, C.; Wang, X.; Zeng, G.-M.; Gong, X.-M.; Duan, A.; Zhang, Q.; Xu, P. Recent Advances in Biochar-Based Catalysts: Properties, Applications and Mechanisms for Pollution Remediation. *Chemical Engineering Journal* **2019**, *371*, 380–403. <https://doi.org/10.1016/j.cej.2019.04.071>.
- (58) Do Minh, T.; Song, J.; Deb, A.; Cha, L.; Srivastava, V.; Sillanpää, M. Biochar Based Catalysts for the Abatement of Emerging Pollutants: A Review. *Chemical Engineering Journal* **2020**, *394*, 124856. <https://doi.org/10.1016/j.cej.2020.124856>.
- (59) Bagheri, A.; Taghavi, S.; Bellani, S.; Salimi, P.; Beydaghi, H.; Panda, J.; Isabella Zappia, M.; Mastronardi, V.; Gamberini, A.; Balkrishna Thorat, S.; Abruzzese, M.; Pasquale, L.; Prato, M.; Signoretto, M.; Feng, X.; Bonaccorso, F. Venice's Macroalgae-Derived Active Material for Aqueous, Organic, and Solid-State Supercapacitors. *Chemical Engineering Journal* **2024**, *496*, 153529. <https://doi.org/10.1016/j.cej.2024.153529>.
- (60) Parsimehr, H.; Ehsani, A.; Payam, S. A. Electrochemical Energy Storage Electrodes from Rice Biochar. *Biomass Conv. Bioref.* **2023**, *13* (14), 12413–12429. <https://doi.org/10.1007/s13399-021-02089-2>.
- (61) Vuppaladadiyam, A. K.; Vuppaladadiyam, S. S. V.; Sahoo, A.; Murugavelh, S.; Anthony, E.; Bhaskar, T.; Zheng, Y.; Zhao, M.; Duan, H.; Zhao, Y.; Antunes, E.; Sarmah, A. K.; Leu, S.-Y. Bio-Oil and Biochar from the Pyrolytic Conversion of Biomass: A Current and Future Perspective on the Trade-off between Economic, Environmental, and Technical Indicators. *Science of The Total Environment* **2023**, *857*, 159155. <https://doi.org/10.1016/j.scitotenv.2022.159155>.
- (62) Lee, J.; Kim, K.-H.; Kwon, E. E. Biochar as a Catalyst. *Renewable and Sustainable Energy Reviews* **2017**, *77*, 70–79. <https://doi.org/10.1016/j.rser.2017.04.002>.
- (63) Frainetti, A. J.; Klinghoffer, N. B. Recent Experimental Advances on the Utilization of Biochar as a Tar Reforming Catalyst: A Review. *International Journal of Hydrogen Energy* **2023**, *48* (22), 8022–8044. <https://doi.org/10.1016/j.ijhydene.2022.11.127>.
- (64) Guo, F.; Peng, K.; Liang, S.; Jia, X.; Jiang, X.; Qian, L. Evaluation of the Catalytic Performance of Different Activated Biochar Catalysts for Removal of Tar from Biomass Pyrolysis. *Fuel* **2019**, *258*, 116204. <https://doi.org/10.1016/j.fuel.2019.116204>.

3. Valorization of biomass via pyrolysis - 3.2 Biochar as support for heterogeneous catalysts – 3.2.4 Co-pyrolysis of LS and RH for the preparation of Pd based catalysts

- (65) Prabhudesai, V. S.; Gurrata, L.; Vinu, R. Catalytic Hydrodeoxygenation of Lignin-Derived Oxygenates: Catalysis, Mechanism, and Effect of Process Conditions. *Energy Fuels* **2022**, *36* (3), 1155–1188. <https://doi.org/10.1021/acs.energyfuels.1c02640>.
- (66) Lyu, G.; Wu, S.; Zhang, H. Estimation and Comparison of Bio-Oil Components from Different Pyrolysis Conditions. *Front. Energy Res.* **2015**, *3*. <https://doi.org/10.3389/fenrg.2015.00028>.
- (67) Luo, Z.; Wang, S.; Liao, Y.; Zhou, J.; Gu, Y.; Cen, K. Research on Biomass Fast Pyrolysis for Liquid Fuel. *Biomass and Bioenergy* **2004**, *26* (5), 455–462. <https://doi.org/10.1016/j.biombioe.2003.04.001>.
- (68) Hiromi Ariyaratne, W. K.; Asgautsen, Ø.; Melaaen, M. C.; Eine, K.; Tokheim, L.-A. Determination of Fossil Fraction of Refuse Derived Fuel by the Selective Dissolution Method in Calorific Value Basis: Development of Simplified Method. *Fuel* **2012**, *98*, 41–47. <https://doi.org/10.1016/j.fuel.2012.03.035>.
- (69) Valle, B.; Remiro, A.; Aramburu, B.; Bilbao, J.; Gayubo, A. G. Strategies for Maximizing the Bio-Oil Valorization by Catalytic Transformation. *Journal of Cleaner Production* **2015**, *88*, 345–348. <https://doi.org/10.1016/j.jclepro.2014.06.017>.
- (70) Pinheiro Pires, A. P.; Arauzo, J.; Fonts, I.; Domine, M. E.; Fernández Arroyo, A.; Garcia-Perez, M. E.; Montoya, J.; Chejne, F.; Pfromm, P.; Garcia-Perez, M. Challenges and Opportunities for Bio-Oil Refining: A Review. *Energy Fuels* **2019**, *33* (6), 4683–4720. <https://doi.org/10.1021/acs.energyfuels.9b00039>.
- (71) Abou Rjeily, M.; Gennequin, C.; Pron, H.; Abi-Aad, E.; Randrianalisoa, J. H. Pyrolysis-Catalytic Upgrading of Bio-Oil and Pyrolysis-Catalytic Steam Reforming of Biogas: A Review. *Environmental Chemistry Letters* **2021**, *19* (4), 2825–2872. <https://doi.org/10.1007/s10311-021-01190-2>.
- (72) Santamaria, L.; Lopez, G.; Arregi, A.; Artetxe, M.; Amutio, M.; Bilbao, J.; Olazar, M. Catalytic Steam Reforming of Biomass Fast Pyrolysis Volatiles over Ni–Co Bimetallic Catalysts. *Journal of Industrial and Engineering Chemistry* **2020**, *91*, 167–181. <https://doi.org/10.1016/j.jiec.2020.07.050>.
- (73) Tanneru, S. K.; Steele, P. H. Direct Hydrocracking of Oxidized Bio-Oil to Hydrocarbons. *Fuel* **2015**, *154*, 268–274. <https://doi.org/10.1016/j.fuel.2015.03.080>.
- (74) Alvarez-Majmutov, A.; Badoga, S.; Chen, J.; Monnier, J.; Zhang, Y. Co-Processing of Deoxygenated Pyrolysis Bio-Oil with Vacuum Gas Oil through Hydrocracking. *Energy Fuels* **2021**, *35* (12), 9983–9993. <https://doi.org/10.1021/acs.energyfuels.1c00822>.
- (75) Stefanidis, S. D.; Kalogiannis, K. G.; Lappas, A. A. Co-Processing Bio-Oil in the Refinery for Drop-in Biofuels via Fluid Catalytic Cracking. *WIREs Energy and Environment* **2018**, *7* (3), e281. <https://doi.org/10.1002/wene.281>.
- (76) Qiu, B.; Yang, C.; Shao, Q.; Liu, Y.; Chu, H. Recent Advances on Industrial Solid Waste Catalysts for Improving the Quality of Bio-Oil from Biomass Catalytic Cracking: A Review. *Fuel* **2022**, *315*, 123218. <https://doi.org/10.1016/j.fuel.2022.123218>.
- (77) Carrasco Díaz, A.; Abdelouahed, L.; Brodu, N.; Montes-Jiménez, V.; Taouk, B. Upgrading of Pyrolysis Bio-Oil by Catalytic Hydrodeoxygenation, a Review Focused on Catalysts, Model Molecules, Deactivation, and Reaction Routes. *Molecules* **2024**, *29* (18), 4325. <https://doi.org/10.3390/molecules29184325>.

3. Valorization of biomass via pyrolysis - 3.2 Biochar as support for heterogeneous catalysts – 3.2.4 Co-pyrolysis of LS and RH for the preparation of Pd based catalysts

- (78) Leng, L.; Li, H.; Yuan, X.; Zhou, W.; Huang, H. Bio-Oil Upgrading by Emulsification/Microemulsification: A Review. *Energy* **2018**, *161*, 214–232. <https://doi.org/10.1016/j.energy.2018.07.117>.
- (79) Sharma, V.; Getahun, T.; Verma, M.; Villa, A.; Gupta, N. Carbon Based Catalysts for the Hydrodeoxygenation of Lignin and Related Molecules: A Powerful Tool for the Generation of Non-Petroleum Chemical Products Including Hydrocarbons. *Renewable and Sustainable Energy Reviews* **2020**, *133*, 110280. <https://doi.org/10.1016/j.rser.2020.110280>.
- (80) Cordero-Lanzac, T.; Palos, R.; Hita, I.; Arandes, J. M.; Rodríguez-Mirasol, J.; Cordero, T.; Bilbao, J.; Castaño, P. Revealing the Pathways of Catalyst Deactivation by Coke during the Hydrodeoxygenation of Raw Bio-Oil. *Applied Catalysis B: Environmental* **2018**, *239*, 513–524. <https://doi.org/10.1016/j.apcatb.2018.07.073>.
- (81) Mahmood Ali, A.; Khan, A.; Shahbaz, M.; Imtiaz Rashid, M.; Imran, M.; Shahzad, K.; Binti Mahpudz, A. A Renewable and Sustainable Framework for Clean Fuel towards Circular Economy for Solid Waste Generation in Leather Tanneries. *Fuel* **2023**, *351*, 128962. <https://doi.org/10.1016/j.fuel.2023.128962>.
- (82) Tieuli, S.; Signoretto, M.; Ghedini, E.; Carlesso, A.; Costantini, A.; Bortolati, C.; Pasquale, R.; Silvestri, M.; Frighetto, L. IL PROGETTO LIFE GOAST. *La Chimica e l'Industria* **2020**, *102* (3), 36. <https://doi.org/10.17374/CI.2020.102.3.36>.
- (83) Onukak, I. E.; Mohammed-Dabo, I. A.; Ameh, A. O.; Okoduwa, S. I. R.; Fasanya, O. O. Production and Characterization of Biomass Briquettes from Tannery Solid Waste. *Recycling* **2017**, *2* (4), 17. <https://doi.org/10.3390/recycling2040017>.
- (84) Kuligowski, K.; Cenian, A.; Konkol, I.; Świerczek, L.; Chojnacka, K.; Izydorczyk, G.; Skrzypczak, D.; Bandrów, P. Application of Leather Waste Fractions and Their Biochars as Organic Fertilisers for Ryegrass Growth: Agri-Environmental Aspects and Plants Response Modelling. *Energies* **2023**, *16* (9), 3883. <https://doi.org/10.3390/en16093883>.
- (85) Herrera, K.; Morales, L. F.; López, J. E.; Montoya-Ruiz, C.; Muñoz, S.; Zapata, D.; Saldarriaga, J. F. Biochar Production from Tannery Waste Pyrolysis as a Circular Economy Strategy for the Removal of Emerging Compounds in Polluted Waters. *Biomass Conversion and Biorefinery* **2024**, *14* (18), 22867–22880. <https://doi.org/10.1007/s13399-023-04261-2>.
- (86) Li, Q.; Tang, Y.; Zhou, B.; Zhou, J.; Shi, B. Resource Utilization of Tannery Sludge to Prepare Biochar as Persulfate Activators for Highly Efficient Degradation of Tetracycline. *Bioresource Technology* **2022**, *358*, 127417. <https://doi.org/10.1016/j.biortech.2022.127417>.
- (87) Grycová, B.; Klemencová, K.; Leštinský, P.; Stejskal, J.; Sába, T.; Trchová, M.; Prokeš, J. Conductivity of Carbonized and Activated Leather Waste. *Sustainable Chemistry and Pharmacy* **2023**, *35*, 101172. <https://doi.org/10.1016/j.scp.2023.101172>.
- (88) Skrzypczak, D.; Szopa, D.; Mikula, K.; Izydorczyk, G.; Baśladyńska, S.; Hoppe, V.; Pstrowska, K.; Wzorek, Z.; Kominko, H.; Kuźażyński, M.; Moustakas, K.; Chojnacka, K.; Witek – Krowiak, A. Tannery Waste-Derived Biochar as a Carrier of Micronutrients Essential to Plants. *Chemosphere* **2022**, *294*, 133720. <https://doi.org/10.1016/j.chemosphere.2022.133720>.
- (89) *L_2021427IT.01014001.xml*. <https://eur-lex.europa.eu/legal-content/IT/TXT/HTML/?uri=CELEX%3A32021R2088> (accessed 2024-10-24).
- (90) Rodríguez-reinoso, F. The Role of Carbon Materials in Heterogeneous Catalysis. *Carbon* **1998**, *36* (3), 159–175. [https://doi.org/10.1016/S0008-6223\(97\)00173-5](https://doi.org/10.1016/S0008-6223(97)00173-5).

3. Valorization of biomass via pyrolysis - 3.2 Biochar as support for heterogeneous catalysts – 3.2.4 Co-pyrolysis of LS and RH for the preparation of Pd based catalysts

- (91) Yang, H.; Chen, Z.; Chen, W.; Chen, Y.; Wang, X.; Chen, H. Role of Porous Structure and Active O-Containing Groups of Activated Biochar Catalyst during Biomass Catalytic Pyrolysis. *Energy* **2020**, *210*, 118646. <https://doi.org/10.1016/j.energy.2020.118646>.
- (92) Ye, S.; Zeng, G.; Tan, X.; Wu, H.; Liang, J.; Song, B.; Tang, N.; Zhang, P.; Yang, Y.; Chen, Q.; Li, X. Nitrogen-Doped Biochar Fiber with Graphitization from *Boehmeria Nivea* for Promoted Peroxymonosulfate Activation and Non-Radical Degradation Pathways with Enhancing Electron Transfer. *Applied Catalysis B: Environmental* **2020**, *269*, 118850. <https://doi.org/10.1016/j.apcatb.2020.118850>.
- (93) Wu, J.; Jin, M.; Li, Y.; Zhao, J.; Wang, T.; Xie, Y.; Liu, L.; Wang, C.; Li, F. Earth-Abundant Co Nanoparticles Encapsulated in N-Doped Hollow Carbon Sphere for Highly Selective Hydrodeoxygenation of Biomass-Derived Vanillin. *Chemical Engineering Journal* **2023**, *463*, 142472. <https://doi.org/10.1016/j.cej.2023.142472>.
- (94) Peng, Q.; Jiang, X.; Cao, G.; Xie, T.; Jin, Z.; Xie, L.; Gan, F.; Ma, S.; Peng, M. Selective Production of High-Value Fuel via Catalytic Upgrading of Bio-Oil over Nitrogen-Doped Carbon-Alumina Hybrid Supported Cobalt Catalysts. *Bioresource Technology* **2024**, *406*, 131059. <https://doi.org/10.1016/j.biortech.2024.131059>.
- (95) Yang, H.; Nie, R.; Xia, W.; Yu, X.; Jin, D.; Lu, X.; Zhou, D.; Xia, Q. Co Embedded within Biomass-Derived Mesoporous N-Doped Carbon as an Acid-Resistant and Chemoselective Catalyst for Transfer Hydrodeoxygenation of Biomass with Formic Acid. *Green Chemistry* **2017**, *19* (23), 5714–5722. <https://doi.org/10.1039/C7GC02648J>.
- (96) Longo, L.; Taghavi, S.; Ghedini, E.; Menegazzo, F.; Di Michele, A.; Cruciani, G.; Signoretto, M. Selective Hydrogenation of 5-Hydroxymethylfurfural to 1-Hydroxy-2,5-Hexanedione by Biochar-Supported Ru Catalysts. *ChemSusChem* **2022**, *15* (13), e202200437. <https://doi.org/10.1002/cssc.202200437>.
- (97) Polidoro, D.; Perosa, A.; Rodríguez-Castellón, E.; Canton, P.; Castoldi, L.; Rodríguez-Padrón, D.; Selva, M. Metal-Free N-Doped Carbons for Solvent-Less CO₂ Fixation Reactions: A Shrimp Shell Valorization Opportunity. *ACS Sustainable Chemistry & Engineering Journal* **2022**, *10* (41), 13835–13848. <https://doi.org/10.1021/acssuschemeng.2c04443>.
- (98) Qin, L.; Wu, Y.; Hou, Z.; Jiang, E. Influence of Biomass Components, Temperature and Pressure on the Pyrolysis Behavior and Biochar Properties of Pine Nut Shells. *Bioresource Technology* **2020**, *313*, 123682. <https://doi.org/10.1016/j.biortech.2020.123682>.
- (99) de la Puente, G.; Gil, A.; Pis, J. J.; Grange, P. Effects of Support Surface Chemistry in Hydrodeoxygenation Reactions over CoMo/Activated Carbon Sulfided Catalysts. *Langmuir* **1999**, *15* (18), 5800–5806. <https://doi.org/10.1021/la981225e>.
- (100) Wu, H.; Feng, Q.; Lu, P.; Chen, M.; Yang, H. Degradation Mechanisms of Cefotaxime Using Biochar Supported Co/Fe Bimetallic Nanoparticles. *Environmental Science: Water Research & Technology* **2018**, *4* (7), 964–975. <https://doi.org/10.1039/C8EW00163D>.
- (101) Chen, Z.; Li, Q.; Xiao, Y.; Zhang, C.; Fu, Z.; Liu, Y.; Yi, X.; Zheng, A.; Li, C.; Yin, D. Acid–Base Synergistic Catalysis of Biochar Sulfonic Acid Bearing Polyamide for Microwave-Assisted Hydrolysis of Cellulose in Water. *Cellulose* **2019**, *26* (2), 751–762. <https://doi.org/10.1007/s10570-018-2098-3>.
- (102) Fuente-Hernández, A.; Lee, R.; Béland, N.; Zamboni, I.; Lavoie, J.-M. Reduction of Furfural to Furfuryl Alcohol in Liquid Phase over a Biochar-Supported Platinum Catalyst. *Energies* **2017**, *10* (3), 286. <https://doi.org/10.3390/en10030286>.

3. Valorization of biomass via pyrolysis - 3.2 Biochar as support for heterogeneous catalysts – 3.2.4 Co-pyrolysis of LS and RH for the preparation of Pd based catalysts

- (103) Lee, Y.; Lee, S. W.; Tsang, Y. F.; Kim, Y. T.; Lee, J. Engineered Rice-Straw Biochar Catalysts for the Production of Value-Added Chemicals from Furan. *Chemical Engineering Journal* **2020**, *387*, 124194. <https://doi.org/10.1016/j.cej.2020.124194>.
- (104) Wang, S.; Li, H.; Wu, M. Advances in Metal/ Biochar Catalysts for Biomass Hydro-Upgrading: A Review. *Journal of Cleaner Production* **2021**, *303*, 126825. <https://doi.org/10.1016/j.jclepro.2021.126825>.
- (105) Chen, W.; Fang, Y.; Li, K.; Chen, Z.; Xia, M.; Gong, M.; Chen, Y.; Yang, H.; Tu, X.; Chen, H. Bamboo Wastes Catalytic Pyrolysis with N-Doped Biochar Catalyst for Phenols Products. *Applied Energy* **2020**, *260*, 114242. <https://doi.org/10.1016/j.apenergy.2019.114242>.
- (106) Chen, W.; Li, K.; Xia, M.; Yang, H.; Chen, Y.; Chen, X.; Che, Q.; Chen, H. Catalytic Deoxygenation Co-Pyrolysis of Bamboo Wastes and Microalgae with Biochar Catalyst. *Energy* **2018**, *157*, 472–482. <https://doi.org/10.1016/j.energy.2018.05.149>.
- (107) Li, P.; Wan, K.; Chen, H.; Zheng, F.; Zhang, Z.; Niu, B.; Zhang, Y.; Long, D. Value-Added Products from Catalytic Pyrolysis of Lignocellulosic Biomass and Waste Plastics over Biochar-Based Catalyst: A State-of-the-Art Review. *Catalysts* **2022**, *12* (9), 1067. <https://doi.org/10.3390/catal12091067>.
- (108) Cao, X.; Sun, S.; Sun, R. Application of Biochar-Based Catalysts in Biomass Upgrading: A Review. *RSC Advances* **2017**, *7* (77), 48793–48805. <https://doi.org/10.1039/C7RA09307A>.
- (109) Wang, Y.; Huang, L.; Zhang, T.; Wang, Q. Hydrogen-Rich Syngas Production from Biomass Pyrolysis and Catalytic Reforming Using Biochar-Based Catalysts. *Fuel* **2022**, *313*, 123006. <https://doi.org/10.1016/j.fuel.2021.123006>.
- (110) Du, Z.-Y.; Zhang, Z.-H.; Xu, C.; Wang, X.-B.; Li, W.-Y. Low-Temperature Steam Reforming of Toluene and Biomass Tar over Biochar-Supported Ni Nanoparticles. *ACS Sustainable Chemistry & Engineering* **2019**, *7* (3), 3111–3119. <https://doi.org/10.1021/acssuschemeng.8b04872>.
- (111) Yao, D.; Hu, Q.; Wang, D.; Yang, H.; Wu, C.; Wang, X.; Chen, H. Hydrogen Production from Biomass Gasification Using Biochar as a Catalyst/Support. *Bioresource Technology* **2016**, *216*, 159–164. <https://doi.org/10.1016/j.biortech.2016.05.011>.
- (112) Buentello-Montoya, D.; Zhang, X.; Li, J.; Ranade, V.; Marques, S.; Geron, M. Performance of Biochar as a Catalyst for Tar Steam Reforming: Effect of the Porous Structure. *Applied Energy* **2020**, *259*, 114176. <https://doi.org/10.1016/j.apenergy.2019.114176>.
- (113) Guo, F.; Dong, Y.; Dong, K.; Xu, L.; Liu, S.; Qiao, Q.; Wei, H.; Wang, Y. Role of Biochar-Based Catalysts in Microwave-Induced Biomass Pyrolysis: Structural Properties and Modification with Fe-Series Metals. *Fuel* **2023**, *341*, 127769. <https://doi.org/10.1016/j.fuel.2023.127769>.
- (114) Mudi, I.; Hart, A.; Ingram, A.; Wood, J. Catalytic Hydrodeoxygenation of Vanillin, a Bio-Oil Model Compound over Renewable Ni/Biochar Catalyst. *Catalysts* **2023**, *13* (1), 171. <https://doi.org/10.3390/catal13010171>.
- (115) Santos, J. L.; Mäki-Arvela, P.; Monzón, A.; Murzin, D. Y.; Centeno, M. Á. Metal Catalysts Supported on Biochars: Part I Synthesis and Characterization. *Applied Catalysis B: Environmental* **2020**, *268*, 118423. <https://doi.org/10.1016/j.apcatb.2019.118423>.

3. Valorization of biomass via pyrolysis - 3.2 Biochar as support for heterogeneous catalysts – 3.2.4 Co-pyrolysis of LS and RH for the preparation of Pd based catalysts

- (116) Santos, J. L.; Mäki-Arvela, P.; Wärnå, J.; Monzón, A.; Centeno, M. A.; Murzin, D. Yu. Hydrodeoxygenation of Vanillin over Noble Metal Catalyst Supported on Biochars: Part II: Catalytic Behaviour. *Applied Catalysis B: Environmental* **2020**, *268*, 118425. <https://doi.org/10.1016/j.apcatb.2019.118425>.
- (117) Adilina, I. B.; Widjaya, R. R.; Hidayati, L. N.; Supriadi, E.; Safaat, M.; Oemry, F.; Restiawaty, E.; Bindar, Y.; Parker, S. F. Understanding the Surface Characteristics of Biochar and Its Catalytic Activity for the Hydrodeoxygenation of Guaiacol. *Catalysts* **2021**, *11* (12), 1434. <https://doi.org/10.3390/catal11121434>.
- (118) Zhu, C.; Wang, H.; Li, H.; Cai, B.; Lv, W.; Cai, C.; Wang, C.; Yan, L.; Liu, Q.; Ma, L. Selective Hydrodeoxygenation of 5-Hydroxymethylfurfural to 2,5-Dimethylfuran over Alloyed Cu–Ni Encapsulated in Biochar Catalysts. *ACS Sustainable Chemistry & Engineering* **2019**, *7* (24), 19556–19569. <https://doi.org/10.1021/acssuschemeng.9b04645>.
- (119) Chiampo, F.; Shanthakumar, S.; Ricky, R.; Pattukandan Ganapathy, G. Tannery: Environmental Impacts and Sustainable Technologies. *Materials Today: Proceedings* **2023**. <https://doi.org/10.1016/j.matpr.2023.02.025>.
- (120) Pütün, A. E.; Özcan, A.; Pütün, E. Pyrolysis of Hazelnut Shells in a Fixed-Bed Tubular Reactor: Yields and Structural Analysis of Bio-Oil. *Journal of Analytical and Applied Pyrolysis* **1999**, *52* (1), 33–49. [https://doi.org/10.1016/S0165-2370\(99\)00044-3](https://doi.org/10.1016/S0165-2370(99)00044-3).
- (121) Shen, Y.; Zhao, P.; Shao, Q. Porous Silica and Carbon Derived Materials from Rice Husk Pyrolysis Char. *Microporous and Mesoporous Materials* **2014**, *188*, 46–76. <https://doi.org/10.1016/j.micromeso.2014.01.005>.
- (122) Kubo, M. Purevdorj, M. The Future of Rice Production and Consumption. *Journal of Food Distribution Research* **2004**, *35*(1), 128-142. <https://doi.org/10.22004/ag.econ.27145>.
- (123) Pinna, F.; Menegazzo, F.; Signoretto, M.; Canton, P.; Fagherazzi, G.; Pernicone, N. Consecutive Hydrogenation of Benzaldehyde over Pd Catalysts: Influence of Supports and Sulfur Poisoning. *Applied Catalysis A: General* **2001**, *219* (1), 195–200. [https://doi.org/10.1016/S0926-860X\(01\)00685-8](https://doi.org/10.1016/S0926-860X(01)00685-8).
- (124) Barnard, E.; Arias, J. J. R.; Thielemans, W. Chemolytic Depolymerisation of PET: A Review. *Green Chemistry* **2021**, *23* (11), 3765–3789. <https://doi.org/10.1039/D1GC00887K>.
- (125) De Vos, L.; Van de Voorde, B.; Van Daele, L.; Dubruel, P.; Van Vlierberghe, S. Poly(Alkylene Terephthalate)s: From Current Developments in Synthetic Strategies towards Applications. *European Polymer Journal* **2021**, *161*, 110840. <https://doi.org/10.1016/j.eurpolymj.2021.110840>.
- (126) Perret, N.; Cárdenas-Lizana, F.; Keane, M. A. Selective Hydrogenation of Benzaldehyde to Benzyl Alcohol over Au/Al₂O₃. *Catalysis Communications* **2011**, *16* (1), 159–164. <https://doi.org/10.1016/j.catcom.2011.09.017>.
- (127) Gunawan, R.; Li, X.; Lievens, C.; Gholizadeh, M.; Chaiwat, W.; Hu, X.; Mourant, D.; Bromly, J.; Li, C.-Z. Upgrading of Bio-Oil into Advanced Biofuels and Chemicals. Part I. Transformation of GC-Detectable Light Species during the Hydrotreatment of Bio-Oil Using Pd/C Catalyst. *Fuel* **2013**, *111*, 709–717. <https://doi.org/10.1016/j.fuel.2013.04.002>.
- (128) Andrews, E.; Lopez-Ruiz, J. A.; Egbert, J. D.; Koh, K.; Sanyal, U.; Song, M.; Li, D.; Karkamkar, A. J.; Derewinski, M. A.; Holladay, J.; Gutiérrez, O. Y.; Holladay, J. D. Performance of Base and Noble Metals for Electrocatalytic Hydrogenation of Bio-Oil-Derived Oxygenated Compounds. *ACS Sustainable Chemistry & Engineering* **2020**, *8* (11), 4407–4418. <https://doi.org/10.1021/acssuschemeng.9b07041>.

3. Valorization of biomass via pyrolysis - 3.2 Biochar as support for heterogeneous catalysts – 3.2.4 Co-pyrolysis of LS and RH for the preparation of Pd based catalysts

- (129) Rorrer, J. E.; Bell, A. T.; Toste, F. D. Synthesis of Biomass-Derived Ethers for Use as Fuels and Lubricants. *ChemSusChem* **2019**, *12* (13), 2835–2858. <https://doi.org/10.1002/cssc.201900535>.
- (130) Pandarus, V.; Ciriminna, R.; Gingras, G.; Béland, F.; Pagliaro, M.; Kaliaguine, S. Hydrogenolysis of C–O Chemical Bonds of Broad Scope Mediated by a New Spherical Sol–Gel Catalyst. *ChemistryOpen* **2018**, *7* (1), 80–91. <https://doi.org/10.1002/open.201700185>.
- (131) Clough, S. R. Toluene. In *Encyclopedia of Toxicology (Third Edition)*; Wexler, P., Ed.; Academic Press: Oxford, 2014; pp 595–598. <https://doi.org/10.1016/B978-0-12-386454-3.00438-3>.
- (132) Corcoran, G. B.; Ray, S. D. Benzyl Alcohol. In *Encyclopedia of Toxicology*; Elsevier, 2014; pp 429–432. <https://doi.org/10.1016/B978-0-12-386454-3.00251-7>.
- (133) Han, M.; Zhang, H.; Du, Y.; Yang, P.; Deng, Z. Catalytic Hydrogenation of Benzaldehydes over Platinum Nanoparticles Immobilized on Magnesium Aluminate Spinel under Mild Conditions. **2010**. <https://doi.org/10.1007/s11144-010-0266-z>.
- (134) Červený, L.; Bělohav, Z.; Hamed, M. N. H. Catalytic Hydrogenation of Aromatic Aldehydes and Ketones over Ruthenium Catalysts. *Research on Chemical Intermediates* **1996**, *22* (1), 15–22. <https://doi.org/10.1163/156856796X00331>.
- (135) Bhanushali, J. T.; Kainthla, I.; Keri, R. S.; Nagaraja, B. M. Catalytic Hydrogenation of Benzaldehyde for Selective Synthesis of Benzyl Alcohol: A Review. *ChemistrySelect* **2016**, *1* (13), 3839–3853. <https://doi.org/10.1002/slct.201600712>.
- (136) Nijhuis, T. A.; Kreutzer, M. T.; Romijn, A. C. J.; Kapteijn, F.; Moulijn, J. A. Monolithic Catalysts as More Efficient Three-Phase Reactors. *Catalysis Today* **2001**, *66* (2), 157–165. [https://doi.org/10.1016/S0920-5861\(00\)00621-0](https://doi.org/10.1016/S0920-5861(00)00621-0).
- (137) Kong, X.; Chen, L. Chemoselective Hydrogenation of Aromatic Aldehydes over SiO₂ Modified Co/γ-Al₂O₃. *Applied Catalysis A: General* **2014**, *476*, 34–38. <https://doi.org/10.1016/j.apcata.2014.02.011>.
- (138) Saadi, A.; Rassoul, Z.; Bettahar, M. M. Gas Phase Hydrogenation of Benzaldehyde over Supported Copper Catalysts. *Journal of Molecular Catalysis A: Chemical* **2000**, *164* (1), 205–216. [https://doi.org/10.1016/S1381-1169\(00\)00199-0](https://doi.org/10.1016/S1381-1169(00)00199-0).
- (139) Hao, Y.; Pischetola, C.; Cárdenas-Lizana, F.; Keane, M. A. Selective Liquid Phase Hydrogenation of Benzaldehyde to Benzyl Alcohol Over Alumina Supported Gold. *Catalysis Letters* **2020**, *150* (3), 881–887. <https://doi.org/10.1007/s10562-019-02944-y>.
- (140) Zhang, Y.; Zhou, J. Pt Nanoparticles Anchored on Rare Metal Oxide Coated on SBA-15: A Highly Active Catalyst for Synergistic Catalytic Hydrogenation of Benzaldehyde. *Nanotechnology* **2020**, *31* (29), 295703. <https://doi.org/10.1088/1361-6528/ab81c4>.
- (141) Mironenko, R. M.; Belskaya, O. B.; Likholobov, V. A. Approaches to the Synthesis of Pd/C Catalysts with Controllable Activity and Selectivity in Hydrogenation Reactions. *Catalysis Today* **2020**, *357*, 152–165. <https://doi.org/10.1016/j.cattod.2019.03.023>.
- (142) Zou, L.; Liu, Q.; Zhu, D.; Huang, Y.; Mao, Y.; Luo, X.; Liang, Z. Experimental and Theoretical Studies of Ultrafine Pd-Based Biochar Catalyst for Dehydrogenation of Formic Acid and Application of In Situ Hydrogenation. *ACS Applied Materials & Interfaces* **2022**, *14* (15), 17282–17295. <https://doi.org/10.1021/acsami.2c00343>.

3. Valorization of biomass via pyrolysis - 3.2 Biochar as support for heterogeneous catalysts – 3.2.4 Co-pyrolysis of LS and RH for the preparation of Pd based catalysts

- (143) Sarki, N.; Kumar, R.; Singh, B.; Ray, A.; Naik, G.; Natte, K.; Narani, A. Lignin Residue-Derived Carbon-Supported Nanoscale Iron Catalyst for the Selective Hydrogenation of Nitroarenes and Aromatic Aldehydes. *ACS Omega* **2022**, *7* (23), 19804–19815. <https://doi.org/10.1021/acsomega.2c01566>.
- (144) Zhao, C.; Liu, X.; Chen, A.; Chen, J.; Lv, W.; Liu, X. Characteristics Evaluation of Bio-Char Produced by Pyrolysis from Waste Hazelnut Shell at Various Temperatures. *Energy Sources, Part A: Recovery, Utilization, and Environmental Effects* **2024**, *46* (1), 7403–7413. <https://doi.org/10.1080/15567036.2020.1754530>.
- (145) Wang, S.; Dai, G.; Yang, H.; Luo, Z. Lignocellulosic Biomass Pyrolysis Mechanism: A State-of-the-Art Review. *Progress in Energy and Combustion Science* **2017**, *62*, 33–86. <https://doi.org/10.1016/j.pecs.2017.05.004>.
- (146) Hossain, S. S.; Mathur, L.; Roy, P. K. Rice Husk/Rice Husk Ash as an Alternative Source of Silica in Ceramics: A Review. *Journal of Asian Ceramic Societies* **2018**, *6* (4), 299–313. <https://doi.org/10.1080/21870764.2018.1539210>.
- (147) Angin, D. Effect of Pyrolysis Temperature and Heating Rate on Biochar Obtained from Pyrolysis of Safflower Seed Press Cake. *Bioresource Technology* **2013**, *128*, 593–597. <https://doi.org/10.1016/j.biortech.2012.10.150>.
- (148) Shafizadeh, F.; Sekiguchi, Y. Development of Aromaticity in Cellulosic Chars. *Carbon* **1983**, *21* (5), 511–516. [https://doi.org/10.1016/0008-6223\(83\)90144-6](https://doi.org/10.1016/0008-6223(83)90144-6).
- (149) Zhao, S.-X.; Ta, N.; Wang, X.-D. Effect of Temperature on the Structural and Physicochemical Properties of Biochar with Apple Tree Branches as Feedstock Material. *Energies* **2017**, *10* (9), 1293. <https://doi.org/10.3390/en10091293>.
- (150) Ghedini, E.; Taghavi, S.; Menegazzo, F.; Signoreto, M. A Review on the Efficient Catalysts for Algae Transesterification to Biodiesel. *Sustainability* **2021**, *13* (18), 10479. <https://doi.org/10.3390/su131810479>.
- (151) Figueiredo, J. L.; Pereira, M. F. R.; Freitas, M. M. A.; Órfão, J. J. M. Modification of the Surface Chemistry of Activated Carbons. *Carbon* **1999**, *37* (9), 1379–1389. [https://doi.org/10.1016/S0008-6223\(98\)00333-9](https://doi.org/10.1016/S0008-6223(98)00333-9).
- (152) El-Hendawy, A.-N. A. Variation in the FTIR Spectra of a Biomass under Impregnation, Carbonization and Oxidation Conditions. *Journal of Analytical and Applied Pyrolysis* **2006**, *75* (2), 159–166. <https://doi.org/10.1016/j.jaap.2005.05.004>.
- (153) Prado-Burguete, C.; Linares-Solano, A.; Rodríguez-Reinoso, F.; de Lecea, C. S.-M. The Effect of Oxygen Surface Groups of the Support on Platinum Dispersion in Pt/Carbon Catalysts. *Journal of Catalysis* **1989**, *115* (1), 98–106. [https://doi.org/10.1016/0021-9517\(89\)90010-9](https://doi.org/10.1016/0021-9517(89)90010-9).
- (154) Barana, D.; Salanti, A.; Orlandi, M.; Ali, D. S.; Zoia, L. Biorefinery Process for the Simultaneous Recovery of Lignin, Hemicelluloses, Cellulose Nanocrystals and Silica from Rice Husk and *Arundo Donax*. *Industrial Crops and Products* **2016**, *86*, 31–39. <https://doi.org/10.1016/j.indcrop.2016.03.029>.
- (155) Leng, L.; Xiong, Q.; Yang, L.; Li, H.; Zhou, Y.; Zhang, W.; Jiang, S.; Li, H.; Huang, H. An Overview on Engineering the Surface Area and Porosity of Biochar. *Science of The Total Environment* **2021**, *763*, 144204. <https://doi.org/10.1016/j.scitotenv.2020.144204>.
- (156) Zhou, Z.; Robards, K.; Helliwell, S.; Blanchard, C. Composition and Functional Properties of Rice. *International Journal of Food Science & Technology* **2002**, *37* (8), 849–868. <https://doi.org/10.1046/j.1365-2621.2002.00625.x>.

3. Valorization of biomass via pyrolysis - 3.2 Biochar as support for heterogeneous catalysts – 3.2.4 Co-pyrolysis of LS and RH for the preparation of Pd based catalysts

- (157) Fu, J.; Zhang, J.; Jin, C.; Wang, Z.; Wang, T.; Cheng, X.; Ma, C. Effects of Temperature, Oxygen and Steam on Pore Structure Characteristics of Coconut Husk Activated Carbon Powders Prepared by One-Step Rapid Pyrolysis Activation Process. *Bioresource Technology* **2020**, *310*, 123413. <https://doi.org/10.1016/j.biortech.2020.123413>.
- (158) Liou, T.-H.; Wu, S.-J. Characteristics of Microporous/Mesoporous Carbons Prepared from Rice Husk under Base- and Acid-Treated Conditions. *Journal of Hazardous Materials* **2009**, *171* (1), 693–703. <https://doi.org/10.1016/j.jhazmat.2009.06.056>.
- (159) Alvarez, J.; Lopez, G.; Amutio, M.; Bilbao, J.; Olazar, M. Physical Activation of Rice Husk Pyrolysis Char for the Production of High Surface Area Activated Carbons. *Industrial & Engineering Chemistry Research* **2015**, *54* (29), 7241–7250. <https://doi.org/10.1021/acs.iecr.5b01589>.
- (160) Kwiatkowski, M.; Broniek, E. An Analysis of the Porous Structure of Activated Carbons Obtained from Hazelnut Shells by Various Physical and Chemical Methods of Activation. *Colloids and Surfaces A: Physicochemical and Engineering Aspects* **2017**, *529*, 443–453. <https://doi.org/10.1016/j.colsurfa.2017.06.028>.
- (161) Pang, C. H.; Lester, E.; Wu, T. Influence of Lignocellulose and Plant Cell Walls on Biomass Char Morphology and Combustion Reactivity. *Biomass and Bioenergy* **2018**, *119*, 480–491. <https://doi.org/10.1016/j.biombioe.2018.10.011>.
- (162) Niu, J.; Shao, R.; Liu, M.; Zan, Y.; Dou, M.; Liu, J.; Zhang, Z.; Huang, Y.; Wang, F. Porous Carbons Derived from Collagen-Enriched Biomass: Tailored Design, Synthesis, and Application in Electrochemical Energy Storage and Conversion. *Advanced Functional Materials* **2019**, *29* (46), 1905095. <https://doi.org/10.1002/adfm.201905095>.
- (163) Ghadermazi, M.; Moradi, S.; Mozafari, R. Rice Husk-SiO₂ Supported Bimetallic Fe–Ni Nanoparticles: As a New, Powerful Magnetic Nanocomposite for the Aqueous Reduction of Nitro Compounds to Amines. *RSC Advances* **2020**, *10* (55), 33389–33400. <https://doi.org/10.1039/D0RA05381C>.
- (164) Shukla, S. S.; Chava, R.; Appari, S.; A, B.; Kuncharam, B. V. R. Sustainable Use of Rice Husk for the Cleaner Production of Value-Added Products. *Journal of Environmental Chemical Engineering* **2022**, *10* (1), 106899. <https://doi.org/10.1016/j.jece.2021.106899>.
- (165) Belskaya, O. B.; Mironenko, R. M.; Likholobov, V. A. Effect of Carbon Support Nature and Palladium Content on the Properties of Pd/C Catalysts in Hydrogenation of Benzaldehyde. *Theoretical and Experimental Chemistry* **2013**, *48* (6), 381–385. <https://doi.org/10.1007/s11237-013-9285-y>.
- (166) Oliveira, L. C. A.; Silva, C. N.; Yoshida, M. I.; Lago, R. M. The Effect of H₂ Treatment on the Activity of Activated Carbon for the Oxidation of Organic Contaminants in Water and the H₂O₂ Decomposition. *Carbon* **2004**, *42* (11), 2279–2284. <https://doi.org/10.1016/j.carbon.2004.05.003>.
- (167) Bulushev, D. A.; Zacharska, M.; Lisitsyn, A. S.; Podyacheva, O. Yu.; Hage, F. S.; Ramasse, Q. M.; Bangert, U.; Bulusheva, L. G. Single Atoms of Pt-Group Metals Stabilized by N-Doped Carbon Nanofibers for Efficient Hydrogen Production from Formic Acid. *ACS Catalysis* **2016**, *6* (6), 3442–3451. <https://doi.org/10.1021/acscatal.6b00476>.
- (168) Arrigo, R.; Schuster, M. E.; Xie, Z.; Yi, Y.; Wowsnick, G.; Sun, L. L.; Hermann, K. E.; Friedrich, M.; Kast, P.; Hävecker, M.; Knop-Gericke, A.; Schlögl, R. Nature of the N–Pd Interaction in Nitrogen-Doped Carbon Nanotube Catalysts. *ACS Catalysis* **2015**, *5* (5), 2740–2753. <https://doi.org/10.1021/acscatal.5b00094>.

3. Valorization of biomass via pyrolysis - 3.2 Biochar as support for heterogeneous catalysts – 3.2.4 Co-pyrolysis of LS and RH for the preparation of Pd based catalysts

- (169) Boulho, C.; Gibson, E. K.; McAllister, M. I.; Moss, R.; Lennon, D. The Application of Attenuated Total Reflection Infrared Spectroscopy to Investigate the Liquid Phase Hydrogenation of Benzaldehyde Over an Alumina-Supported Palladium Catalyst. *Topics in Catalysis* **2020**, 63 (3), 386–393. <https://doi.org/10.1007/s11244-020-01323-x>.
- (170) Zhao, Z.; Li, Y.; Feyen, M.; McGuire, R.; Müller, U.; Zhang, W. Pd Nanoparticles Encapsulated in FER Zeolite through a Layer Reassembling Strategy as Shape-Selective Hydrogenation Catalyst. *ChemCatChem* **2018**, 10 (10), 2254–2259. <https://doi.org/10.1002/cctc.201800040>.
- (171) Song, Y.; Sanyal, U.; Pangotra, D.; Holladay, J. D.; Camaioni, D. M.; Gutiérrez, O. Y.; Lercher, J. A. Hydrogenation of Benzaldehyde via Electrocatalysis and Thermal Catalysis on Carbon-Supported Metals. *Journal of Catalysis* **2018**, 359, 68–75. <https://doi.org/10.1016/j.jcat.2017.12.026>.
- (172) Stucchi, M.; Vasile, F.; Cattaneo, S.; Villa, A.; Chieragato, A.; Vandegheuchte, B. D.; Prati, L. An Insight into the Role of Reactant Structure Effect in Pd/C Catalysed Aldehyde Hydrogenation. *Nanomaterials* **2022**, 12 (6), 908. <https://doi.org/10.3390/nano12060908>.
- (173) Hassan, H.; Lim, J. K.; Hameed, B. H. Recent Progress on Biomass Co-Pyrolysis Conversion into High-Quality Bio-Oil. *Bioresource Technology* **2016**, 221, 645–655. <https://doi.org/10.1016/j.biortech.2016.09.026>.
- (174) Al-Rumaihi, A.; Shahbaz, M.; Mckay, G.; Mackey, H.; Al-Ansari, T. A Review of Pyrolysis Technologies and Feedstock: A Blending Approach for Plastic and Biomass towards Optimum Biochar Yield. *Renewable and Sustainable Energy Reviews* **2022**, 167, 112715. <https://doi.org/10.1016/j.rser.2022.112715>.
- (175) Ahmed, M. J.; Hameed, B. H. Insight into the Co-Pyrolysis of Different Blended Feedstocks to Biochar for the Adsorption of Organic and Inorganic Pollutants: A Review. *Journal of Cleaner Production* **2020**, 265, 121762. <https://doi.org/10.1016/j.jclepro.2020.121762>.
- (176) Chen, W.-H.; Ho, K.-Y.; Aniza, R.; Sharma, A. K.; Saravanakumar, A.; Hoang, A. T. A Review of Noncatalytic and Catalytic Pyrolysis and Co-Pyrolysis Products from Lignocellulosic and Algal Biomass Using Py-GC/MS. *Journal of Industrial and Engineering Chemistry* **2024**, 134, 51–64. <https://doi.org/10.1016/j.jiec.2024.01.020>.
- (177) Fakayode, O. A.; Aboagarib, E. A. A.; Zhou, C.; Ma, H. Co-Pyrolysis of Lignocellulosic and Macroalgae Biomasses for the Production of Biochar – A Review. *Bioresource Technology* **2020**, 297, 122408. <https://doi.org/10.1016/j.biortech.2019.122408>.
- (178) Li, Y.; Yu, H.; Liu, L.; Yu, H. Application of Co-Pyrolysis Biochar for the Adsorption and Immobilization of Heavy Metals in Contaminated Environmental Substrates. *Journal of Hazardous Materials* **2021**, 420, 126655. <https://doi.org/10.1016/j.jhazmat.2021.126655>.
- (179) Lin, B.; Huang, Q.; Chi, Y. Co-Pyrolysis of Oily Sludge and Rice Husk for Improving Pyrolysis Oil Quality. *Fuel Processing Technology* **2018**, 177, 275–282. <https://doi.org/10.1016/j.fuproc.2018.05.002>.
- (180) Zhang, J.; Jin, J.; Wang, M.; Naidu, R.; Liu, Y.; Man, Y. B.; Liang, X.; Wong, M. H.; Christie, P.; Zhang, Y.; Song, C.; Shan, S. Co-Pyrolysis of Sewage Sludge and Rice Husk/ Bamboo Sawdust for Biochar with High Aromaticity and Low Metal Mobility. *Environmental Research* **2020**, 191, 110034. <https://doi.org/10.1016/j.envres.2020.110034>.

3. Valorization of biomass via pyrolysis - 3.2 Biochar as support for heterogeneous catalysts – 3.2.4 Co-pyrolysis of LS and RH for the preparation of Pd based catalysts

- (181) Zhang, J.; Kang, G.; Yang, H.; Liu, Z.; Yu, J.; Gao, S. Co-Pyrolysis Kinetics and Pyrolysis Product Distribution of Various Tannery Wastes. *Journal of Fuel Chemistry and Technology* **2021**, *49* (11), 1638–1647. [https://doi.org/10.1016/S1872-5813\(21\)60133-0](https://doi.org/10.1016/S1872-5813(21)60133-0).
- (182) Simonov, P. A.; Romanenko, A. V.; Prosvirin, I. P.; Moroz, E. M.; Boronin, A. I.; Chuvilin, A. L.; Likhobobov, V. A. On the Nature of the Interaction of H₂PdCl₄ with the Surface of Graphite-like Carbon Materials. *Carbon* **1997**, *35* (1), 73–82. [https://doi.org/10.1016/S0008-6223\(96\)00129-7](https://doi.org/10.1016/S0008-6223(96)00129-7).
- (183) Al-Degs, Y. S.; El-Barghouthi, M. I.; El-Sheikh, A. H.; Walker, G. M. Effect of Solution pH, Ionic Strength, and Temperature on Adsorption Behavior of Reactive Dyes on Activated Carbon. *Dyes and Pigments* **2008**, *77* (1), 16–23. <https://doi.org/10.1016/j.dyepig.2007.03.001>.
- (184) Pinna, F.; Menegazzo, F.; Signoretto, M.; Canton, P.; Fagherazzi, G.; Pernicone, N. Consecutive Hydrogenation of Benzaldehyde over Pd Catalysts - Influence of Supports and Sulfur Poisoning. *Applied Catalysis A: General* **2001**, *219* (1–2), 195–200. [https://doi.org/10.1016/S0926-860X\(01\)00685-8](https://doi.org/10.1016/S0926-860X(01)00685-8).
- (185) Bergeret, G.; Gallezot, P. Particle Size and Dispersion Measurements. In *Handbook of Heterogeneous Catalysis*; Wiley-VCH, 2008; Vol. 2, pp 738–765. <https://doi.org/10.1002/9783527610044.hetcat0038>.
- (186) Liu, J.; Yang, X.; Liu, H.; Jia, X.; Bao, Y. Mixed Biochar Obtained by the Co-Pyrolysis of Shrimp Shell with Corn Straw: Co-Pyrolysis Characteristics and Its Adsorption Capability. *Chemosphere* **2021**, *282*, 131116. <https://doi.org/10.1016/j.chemosphere.2021.131116>.
- (187) Lin, X.; Guo, Y.; Tang, B.; Fu, P.; Li, H.; Zhang, J.; Li, P. Fast Co-Pyrolysis of Paper Mill Sludge and Corn Stover: Relationships between Parameters, Product Distributions, and Synergistic Interactions. *Industrial Crops and Products* **2024**, *213*, 118415. <https://doi.org/10.1016/j.indcrop.2024.118415>.
- (188) Godinho, D.; Dias, D.; Bernardo, M.; Lapa, N.; Fonseca, I.; Lopes, H.; Pinto, F. Adding Value to Gasification and Co-Pyrolysis Chars as Removal Agents of Cr³⁺. *Journal of Hazardous Materials* **2017**, *321*, 173–182. <https://doi.org/10.1016/j.jhazmat.2016.09.006>.
- (189) Xu, J.; Liu, J.; Ling, P.; Zhang, X.; Xu, K.; He, L.; Wang, Y.; Su, S.; Hu, S.; Xiang, J. Raman Spectroscopy of Biochar from the Pyrolysis of Three Typical Chinese Biomasses: A Novel Method for Rapidly Evaluating the Biochar Property. *Energy* **2020**, *202*, 117644. <https://doi.org/10.1016/j.energy.2020.117644>.
- (190) McDonald-Wharry, J. 2013–2014 Survey of Chars Using Raman Spectroscopy. *Journal of Carbon Research* **2021**, *7* (3), 63. <https://doi.org/10.3390/c7030063>.
- (191) Lampropoulos, A.; Binas, V. D.; Zouridi, L.; Athanasiou, C.; Montes-Morán, M. A.; Menéndez, J. A.; Konsolakis, M.; Marnellos, G. E. CO₂ Gasification Reactivity and Syngas Production of Greek Lignite Coal and Ex-Situ Produced Chars under Non-Isothermal and Isothermal Conditions: Structure-Performance Relationships. *Energies* **2022**, *15* (3), 679. <https://doi.org/10.3390/en15030679>.
- (192) Prakongkep, N.; Gilkes, R. J.; Wiriyakitnateekul, W.; Duangchan, A.; Darunsontaya, T. The Effects of Pyrolysis Conditions on the Chemical and Physical Properties of Rice Husk Biochar. *International Journal of Material Science* **2013**, *3* (3), 97–103.

3. Valorization of biomass via pyrolysis - 3.2 Biochar as support for heterogeneous catalysts – 3.2.4 Co-pyrolysis of LS and RH for the preparation of Pd based catalysts

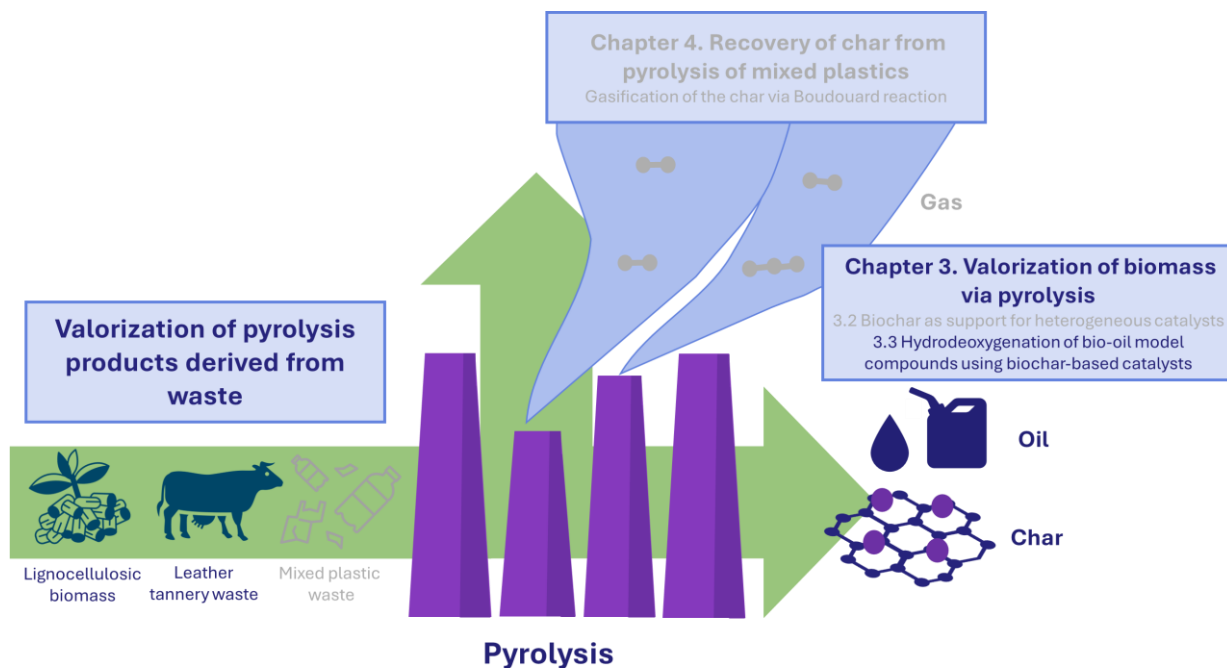
- (193) Wang, C.; Bi, H.; Lin, Q.; Jiang, X.; Jiang, C. Co-Pyrolysis of Sewage Sludge and Rice Husk by TG–FTIR–MS: Pyrolysis Behavior, Kinetics, and Condensable/Non-Condensable Gases Characteristics. *Renewable Energy* **2020**, *160*, 1048–1066. <https://doi.org/10.1016/j.renene.2020.07.046>.
- (194) Kubo, S.; White, R. J.; Yoshizawa, N.; Antonietti, M.; Titirici, M.-M. Ordered Carbohydrate-Derived Porous Carbons. *Chemistry of Materials Journal* **2011**, *23* (22), 4882–4885. <https://doi.org/10.1021/cm2020077>.
- (195) Kubo, S.; Tan, I.; White, R. J.; Antonietti, M.; Titirici, M.-M. Template Synthesis of Carbonaceous Tubular Nanostructures with Tunable Surface Properties. *Chem. Mater.* **2010**, *22* (24), 6590–6597. <https://doi.org/10.1021/cm102556h>.
- (196) Titirici, M.-M.; Thomas, A.; Antonietti, M. Aminated Hydrophilic Ordered Mesoporous Carbons. *Journal of Materials Chemistry* **2007**, *17* (32), 3412–3418. <https://doi.org/10.1039/B703569A>.
- (197) Cai, T.; Liu, X.; Zhang, J.; Tie, B.; Lei, M.; Wei, X.; Peng, O.; Du, H. Silicate-Modified Oiltea Camellia Shell-Derived Biochar: A Novel and Cost-Effective Sorbent for Cadmium Removal. *Journal of Cleaner Production* **2021**, *281*, 125390. <https://doi.org/10.1016/j.jclepro.2020.125390>.
- (198) Felten, A.; Ghijsen, J.; Pireaux, J.-J.; Drube, W.; Johnson, R. L.; Liang, D.; Hecq, M.; Van Tendeloo, G.; Bittencourt, C. Electronic Structure of Pd Nanoparticles on Carbon Nanotubes. *Micron* **2009**, *40* (1), 74–79. <https://doi.org/10.1016/j.micron.2008.01.013>.
- (199) Polidoro, D.; Chhabra, T.; Rodríguez-Castellón, E.; Perosa, A.; Luque, R.; Rodríguez-Padron, D.; Selva, M. Pd-N-Doped Carbons for Chemoselective Hydrogenation of Cinnamaldehyde: Unravelling the Influence of Particle Size and Support in Multiphase Batch and Continuous-Flow Systems. *Applied Catalysis A: General* **2024**, *685*, 119864. <https://doi.org/10.1016/j.apcata.2024.119864>.
- (200) Varodi, C.; Pogăcean, F.; Ciorîță, A.; Pană, O.; Leoștean, C.; Cozar, B.; Radu, T.; Coroș, M.; Ștefan-van Staden, R. I.; Pruneanu, S.-M. Nitrogen and Sulfur Co-Doped Graphene as Efficient Electrode Material for L-Cysteine Detection. *Chemosensors* **2021**, *9* (6), 146. <https://doi.org/10.3390/chemosensors9060146>.
- (201) Pan, X.; Bao, X. The Effects of Confinement inside Carbon Nanotubes on Catalysis. *Accounts of Chemical Research* **2011**, *44* (8), 553–562. <https://doi.org/10.1021/ar100160t>.
- (202) Hao, X.; Barnes, S.; Regalbuto, J. R. A Fundamental Study of Pt Impregnation of Carbon: Adsorption Equilibrium and Particle Synthesis. *Journal of Catalysis* **2011**, *279* (1), 48–65. <https://doi.org/10.1016/j.jcat.2010.12.021>.
- (203) Neri, G.; Musolino, M. G.; Milone, C.; Pietropaolo, D.; Galvagno, S. Particle Size Effect in the Catalytic Hydrogenation of 2,4-Dinitrotoluene over Pd/C Catalysts. *Applied Catalysis A: General* **2001**, *208* (1), 307–316. [https://doi.org/10.1016/S0926-860X\(00\)00717-1](https://doi.org/10.1016/S0926-860X(00)00717-1).
- (204) Di, L.; Zhang, J.; Craven, M.; Wang, Y.; Wang, H.; Zhang, X.; Tu, X. Dehydrogenation of Formic Acid over Pd/C Catalysts: Insight into the Cold Plasma Treatment. *Catalysis Science & Technology* **2020**, *10* (18), 6129–6138. <https://doi.org/10.1039/D0CY00055H>.
- (205) Schüth, F.; Ward, M. D.; Buriak, J. M. Common Pitfalls of Catalysis Manuscripts Submitted to Chemistry of Materials. *Chemistry of Materials Journal* **2018**, *30* (11), 3599–3600. <https://doi.org/10.1021/acs.chemmater.8b01831>.

3. Valorization of biomass via pyrolysis - 3.2 Biochar as support for heterogeneous catalysts – 3.2.4 Co-pyrolysis of LS and RH for the preparation of Pd based catalysts

(206) Stucchi, M.; Capelli, S.; Villa, A.; Vandegehuchte, B. D.; Prati, L. Effect of Carbon Oxygen Functionalization on the Activity of Pd/C Catalysts in Hydrogenation Reactions. *ChemCatChem* **2024**, *16* (12), e202301639. <https://doi.org/10.1002/cctc.202301639>.

(207) Palliyarayil, A.; Selvarajan, P.; Prakash, P. S.; Sathish, C. I.; Dasireddy, Venkata. D. B. C.; Vinu, A.; Kumar, N. S.; Sil, S. An Experimental and Theoretical Investigation on the Oxidation of CO over Pd/C Derived from the Spent Pd Catalyst. *ChemCatChem* **2021**, *13* (5), 1326–1339. <https://doi.org/10.1002/cctc.202001917>.

3.3 Hydrodeoxygenation of bio-oil model compounds using biochar-based catalysts



3.3.1 Introduction

The liquid fraction obtained from biomass pyrolysis (bio-oil) can be upgraded to biofuel, through various methods aimed to enhance its calorific value and stability, while reducing its corrosiveness and oxygen content. Finding alternatives to fossil fuels is of particular importance especially in sectors like aviation and shipping, that, differently from the road transport¹⁻³, are not easily electrifiable. In these sectors, the adoption of battery or hydrogen technologies remains limited, because it would require substantial infrastructure and aircraft design modifications, resulting in prohibitive costs, at least in the short terms. The primary challenge is related to the low energy density of batteries, compared with kerosene. Current Li-ion batteries, with a specific energy of 400 Wh/kg, fall short compared to kerosene's 12,000 Wh/kg⁴. Hydrogen fuel cell aircraft are currently limited due to hydrogen storage challenges⁵. As a result, these solutions are only used in small aircraft and short-range flights. Thus, these technologies remain long-term solutions.

Nevertheless, the transport sector accounts for 28% of global energy consumption and 23% of CO₂ emissions. In 2019, jet kerosene combustion contributed 12% of the transport industry's CO₂ emissions, reaching up to 1027 Mt. Aviation has faced increasing criticism for insufficient carbon reduction efforts.

As a result, short-term “drop-in” alternatives like *Sustainable Aviation Fuels* (SAF) have gaining importance. Aviation fuels must meet ASTM D1655 standards⁶, primarily consisting of C8-C16 alkanes and <C16 aromatics. Jet fuel typically contains 50-60% paraffins, 20-40% cycloalkanes, 5-20% aromatics, with minor components such as olefins and additives. A key requirement is a low freezing point for high-altitude flights⁷. The main difference between jet fuel, diesel, and gasoline is carbon chain length: gasoline (C4-C12), diesel (C8-C23), and jet fuel (C8-C16)⁸.

Renewable liquid fuels can be blended with conventional fuels or used as substitutes without requiring infrastructure or engine modifications. Alternative fuels include synthetic fuels (e-fuels)⁹, produced from green hydrogen and CO₂ and biofuels, derived from biological feedstocks¹⁰.

Lignocellulosic pyrolytic bio-oil is rich in phenolic compounds derived from lignin monomers (p-coumaryl alcohol, coniferyl alcohol, and sinapyl alcohol, Figure 3.3.1.1, purple). The derived compounds (Figure 3.3.1.1, black) are categorized based on their functional groups into three main types: phenol, guaiacol, and syringol (Figure 3.3.1.1, red). Some of these phenolic compounds, like isoeugenol (IE) and eugenol (EU), as well as propenyl syringol, have the right characteristics in terms of number of carbon atoms and branching, to be used as SAF, after suitable upgrading. One of the most promising approaches for the upgrading of lignocellulosic bio-oil is via hydrodeoxygenation (HDO)¹¹.

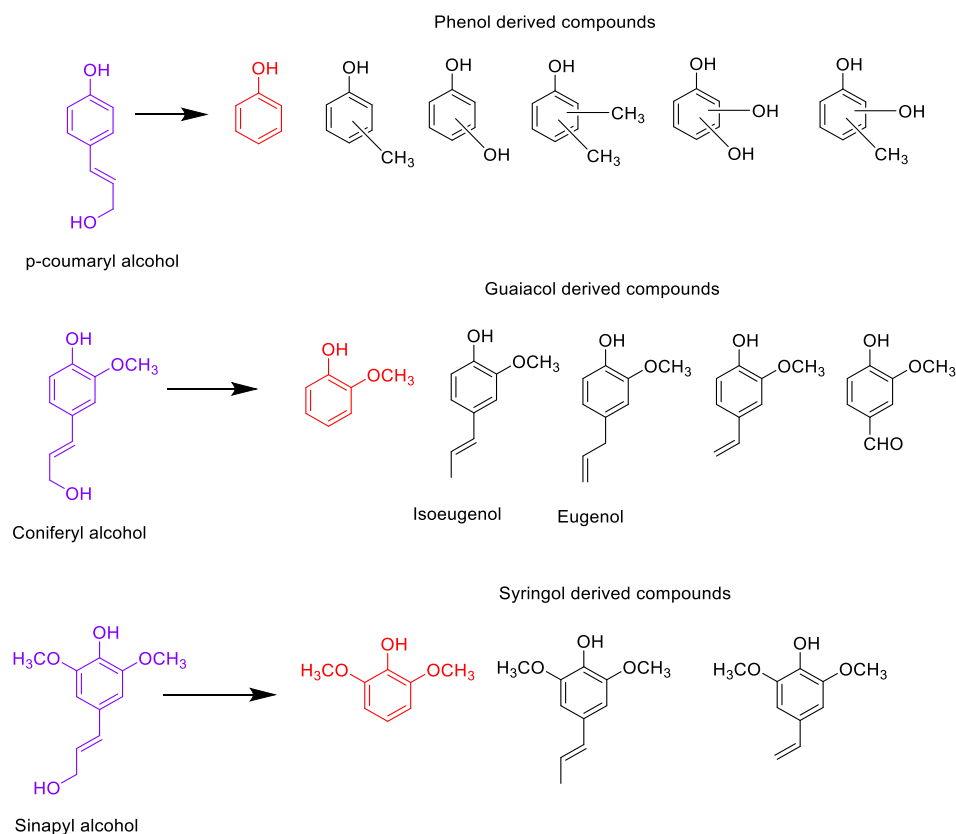


Figure 3.3.1.1. Lignin monomers and their phenolic derivatives present in bio-oil.

Apart from phenolic compounds, bio-oil consists of hundreds of different species, as widely discussed¹². Due to its complexity, model compounds are often used to study the catalytic properties of a system in HDO. In this work, the HDO of a phenolic model compound, isoeugenol, was investigated using biochar-based catalysts. The target product of complete HDO of IE, is propyl cyclohexane (PCH). PCH is a C₉ hydrocarbon with a melting point of -94 °C, a boiling point of 156-157 °C, and a flash point of 35 °C, aligning with the necessary standards for aviation fuel use. However, the selective hydrogenation of aromatic compounds to cyclohexanols (propylcyclohexanol, PCOL is produced from IE) is also valuable for the production of polymers, fragrances, and pharmaceuticals^{6,13}. Consequently, a catalyst capable of modulating its activity to achieve high yields of various target compounds would be highly advantageous.

Additionally, the possibility of co-processing isoeugenol with other bio-oil model compounds, such as furfural (FF), was evaluated. The main target products of HDO of FF are 2-methyl furan (MF)¹⁴, and cyclopentanone/cyclopentanol¹⁵. MF exhibits high energy density, a high boiling point, and a favorable octane number, along with low volatility, making it a suitable candidate for fuel replacement¹⁶. Cyclopentanone and cyclopentanol are valuable intermediates in the production of solvents, pharmaceuticals, fuel additives, and other chemicals. Further HDO of furfural can lead to linear alcohols or hydrocarbons¹⁷, although achieving such transformation remains a significant challenge^{18,19}.

Co-processing furanic and phenolic through HDO, as in real bio-oil scenarios, further presents significant challenges. Studies have shown that the presence of light oxygenates, such as FF and acetic acid, can detrimentally affect the HDO of phenolic compounds. This is primarily due to competitive adsorption phenomena on the catalyst's active sites²⁰⁻²². Therefore, the co-processing of complex bio-oil mixtures remains a challenging area of research, requiring further investigation to optimize HDO processes for future biorefineries.

The results of these investigations are presented in the following chapter. Before that, a brief overview of the HDO mechanism, reaction conditions, and catalysts used is provided.

Hydrodeoxygenation (HDO) mechanism

HDO has garnered significant attention for bio-oil upgrading over the years. The process consists in different parallel and consecutive reactions steps, involving hydrogen and a proper catalyst to remove oxygenated functionalities on the bio-oil components. The main reactions involved are outlined below¹².

- Hydrogenation: this reaction involves the addition of hydrogen to saturate the double bonds. This step is crucial for stabilizing reactive molecules in bio-oil. It is facilitated by active metal sites and H₂ high partial pressure.
- Deoxygenation (or hydrogenolysis): this reaction entails the cleavage of the C-O bond, which leads to the removal of oxygen in the form of water, or methanol (demethoxylation), depending on the functionalities of the compounds. Reducing the oxygen content improves bio-oil fuels properties and calorific value. The reaction is facilitated by Lewis's acidity and oxygen vacancies on the catalyst.
- Dehydration: it is an acid catalyzed reaction that involves the elimination of hydroxyl groups forming water and resulting in an unsaturated compound.
- Tautomerization: the enolic compound that can be formed by dehydration, fast tautomerize to the ketonic form.
- Demethylation: the C-alkyl-O cleavage occurs, leading to the formation of methane and an -OH functionality on the substrate. It is acid catalyzed.
- Methyl transfer: a methyl group of an aromatic ring gets detached and attached on the same molecule (intramolecular alkylation) or a different molecule (intermolecular alkylation). Acid catalyzed
- Hydrocracking: in the presence of hydrogen, C-C bond cleavage can also occur, reducing the size of the bio-oil components. It is promoted by acids (especially zeolites) at high temperatures.
- Decarboxylation: when carboxylic acids are present, decarboxylation reactions may occur, resulting in the removal of CO₂. This further reduces the oxygen content of bio-oil, contributing to the overall improvement in fuel quality.
- Decarbonylation: in some cases, decarbonylation can also occur, leading to the removal of carbon monoxide.

A schematic representation of the reactions involved in HDO for the main bio-oil components, namely phenols, furans, and carboxylic acids, is reported in Figure 3.3.1.2.

3. Valorization of biomass via pyrolysis - 3.3 Hydrodeoxygenation of bio-oil model compounds using biochar-based catalysts

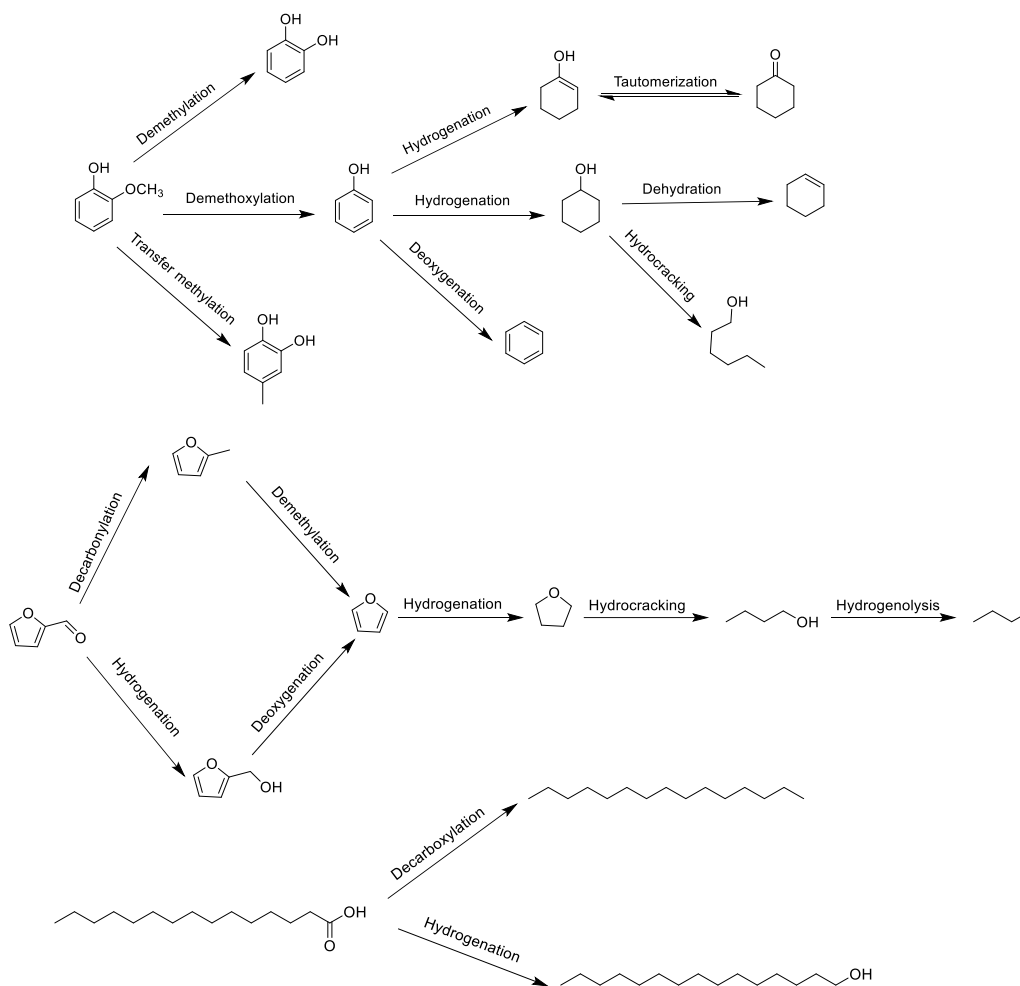


Figure 3.3.1.2. HDO reactions for phenols, furans and carboxylic acids in bio-oil.

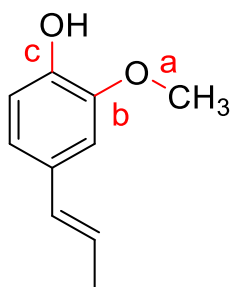
The dissociation energy of the C-O bond depends on the nature of the chemical environment. Aromatic groups have higher dissociation energies than aliphatic groups (e.g., R-OH = 385 kJ mol⁻¹ and Ar-OH = 468 kJ mol⁻¹). Therefore, hydrogenation and deoxygenation reactions in bio-oil occur at different temperatures, depending on the feedstock. At lower temperatures (under 200 °C), aldehydes and ketones can be hydrotreated, while aliphatic ethers react at temperatures above 200 °C, followed by carboxylic acids. For phenols, temperatures above 300 °C are often required, and benzofurans are among the hardest compounds to transform.

The presence of an active catalyst can lower the activation energy, enabling these reactions to occur at milder conditions. From a kinetic perspective, high temperatures are often necessary to drive reactions with high activation energy requirements. However, because many hydrogenation steps are exothermic, they become less thermodynamically favorable at higher temperatures, where entropy effects reduce the Gibbs free energy advantage. Using a catalyst therefore allows these reactions to occur at lower temperatures, where they are both thermodynamically favorable and kinetically accessible.

For example, Sulman *et al.*²³ conducted kinetic and thermodynamic analyses of guaiacol hydrodeoxygenation (HDO) and found that certain reactions, such as phenol and benzene hydrogenation, were feasible at 200 °C but became thermodynamically unfavorable at higher temperatures, such as 300 °C. However, the overall HDO process remained feasible between 200 °C and 300 °C, achieving 98% conversion of guaiacol to cyclohexanol using Pt/C as a catalyst.

HDO of Isoeugenol

IE contains three different functionalities: methoxy, hydroxyl and propenyl. The different C-O bonds possess different dissociation energies²⁴: Calkyl-O (bond “a” in Figure 3.3.1.3) exhibit the lower energy, of 200 kJ mol⁻¹; Caryl-OCH₃ (bond “b”) has an energy of 386.5 kJ mol⁻¹, and Caryl-OH (bond “c”) has the highest energy, of 542 kJ mol⁻¹.



Isoeugenol

Figure 3.3.1.3. Isoeugenol structure

IE first undergoes hydrogenation of the double bond on the propenyl chain, and it is converted into dihydroeugenol (DHE). DHE hydrodeoxygenation can occur over two pathways, called ring hydrogenation and demethoxylation pathways¹² (Figure 3.3.1.4):

- Ring hydrogenation: at low temperature the ring hydrogenation takes place, giving 2-methoxy-4-propyl cyclohexanol. As the reaction proceeds, demethylation occurs, giving 4-propyl-1,2-cyclohexanediol. Subsequently, hydrolysis occurs, forming 4-propyl-cyclohex-1-en-1ol that tautomerize to 4-propyl-cyclohexanone (PCONE). Finally, PCONE is hydrogenated to 4-propylcyclohexanol (PCOL) that is further subjected to dehydration and hydrogenation to give the completely saturated propylcyclohexane (PCH). This pathway is particularly preferred by Pd or Ru catalysts²⁵⁻²⁷, with a high hydrogenation activity.
- Demethoxylation: in this pathway, the cleavage of Caryl-OCH₃ occurs before ring hydrogenation, to give 4-propyl phenol (PPHOL). PPHOL is further hydrogenated to give PCOL and finally dehydration/hydrogenation of the hydroxy group occurs, giving PCH. This pathway is usually preferred by catalysts with higher deoxygenation activity, like Co or Mo based catalysts^{13,28}.

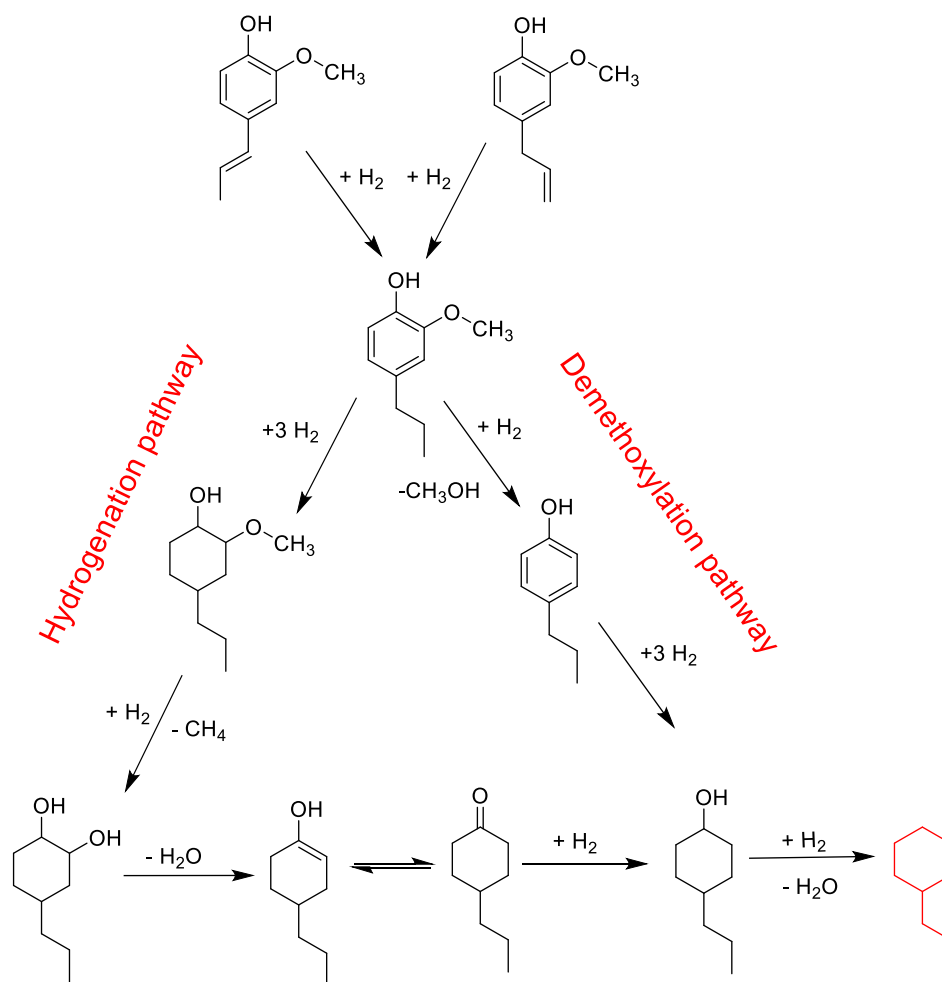


Figure 3.3.1.4. Schematic representation of DHE HDO pathways.

HDO of Furfural

The presence of furfural in bio-oil mixtures can pose significant stability issues due to its reactive carbonyl group, which is prone to oligomerization, leading to the formation of humins²⁹, therefore HDO of furfural for bio-oil upgrading is pivotal.

As illustrated in Figure 3.3.1.5, the hydrodeoxygenation (HDO) of furfural involves several reaction pathways leading to both ring-retaining and ring-opening products. Furfural initially undergoes hydrogenation of its aldehyde group, producing furfuryl alcohol. From here, the alcohol can be further hydrogenated into tetrahydrofurfuryl alcohol (FOL) or undergo ring rearrangement and hydrogenation to form cyclopentanone and cyclopentanol, valuable intermediates in the production of solvents, pharmaceuticals, fuel additives, and other chemicals¹⁵. FOL can further undergo hydrogenolysis to form 2-methylfuran (MF) or, in some cases, tetrahydro-2-methylfuran, both of which are important fuel additives^{14,16}.

Alternatively, furfural can undergo decarbonylation to form furan, which may then participate in ring-opening reactions, leading to linear-chain alkanes and alcohols¹⁷, a crucial step for biofuel production.

Further hydrogenation of furan yields saturated compounds like tetrahydrofuran (THF), which can also undergo ring-opening to produce linear alcohols or alkanes. These reactions are often catalyzed by metal-based catalysts (e.g., Pt, Ru, Ni) and occur under high-pressure hydrogen environments, driving the removal of oxygen atoms through C–O bond cleavage, facilitating the conversion of furfural into valuable fuel precursors^{18,19}.

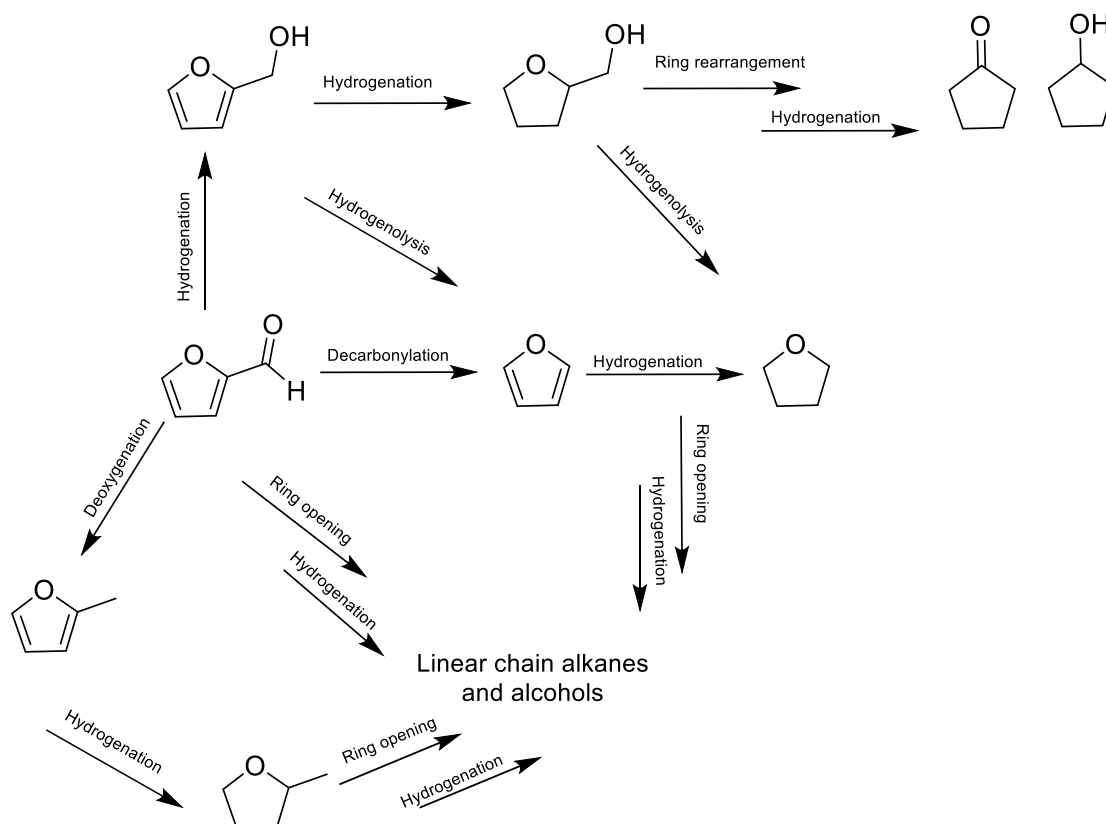


Figure 3.3.1.5 Furfural HDO reaction pathways.

HDO reaction conditions and catalysts

Batch or semi-batch HDO of bio-oil and its model compounds are commonly performed in organic solvents like methanol, acetic acid, and long-chain alkanes. However, water and biphasic water-organic solvent systems have also been investigated in literature^{12,30}. Compounds like vanillin, which are water-soluble often favor reaction environments in water or polar solvents like 2-propanol. Hydrogen-donor solvents, like methanol and 2-propanol, can reduce the need for an external hydrogen supply. Solvents influence the HDO process through various mechanisms: they can promote the formation of distinct surface intermediates and transition states, actively participate in reactions such as hydrolysis and esterification (especially in the case of water or alcohols) or compete with reactants for adsorption on the catalyst's active sites. For instance, long-chain hydrocarbons may undergo cracking and can be co-processed with bio-oil-derived compounds to produce the desired hydrocarbons^{31,32}. Additionally,

solvents can affect the diffusion of substrates, intermediates, and products, making the choice of an appropriate solvent critical for efficient HDO.

To ensure high solubility of hydrogen in the reaction media, and to have high availability of hydrogen on the catalyst's surface, relatively high pressure is required³³. Pressure has a positive effect on the reaction rate and further decreases coke formation.

The development of highly active, selective, stable and cost-effective catalysts is fundamental for bio-oil upgrading through HDO. Initially, bio-oil treatment was compared to petroleum processing, where sulfur (and to a lesser extent, nitrogen and oxygen) heteroatoms are removed through hydrotreating, using metal sulfide catalysts, or Ni-Mo, Co-Mo on Al₂O₃ supports^{34,35}. However, bio-oils lack sulfur, leading to catalyst deactivation when sulfur from the catalyst is replaced by oxygen. The addition of external sulfur sources like H₂S or CS₂ complicates the process and increases the sulfur content in the final product. Furthermore, alumina-based supports are hydrothermally unstable, deactivating rapidly in the presence of water, and their strong acidity promotes coke formation, making them not optimal for HDO³⁶.

An efficient HDO catalyst design necessitates a combination of both hydrogenation and deoxygenation sites. The metal phase is responsible for hydrogen activation and hydrogenation reactions, while acid sites or oxygen vacancies interact with oxygen functionalities to facilitate reactions such as hydrogenolysis, dehydration, and demethoxylation. In addition to the active metal, the choice of support is critical, as surface area, meso- or microporosity, acidity, and electronic interactions with the metal influence the overall performance of HDO catalysts^{26,37}. Recent research on optimal HDO catalysts has shifted toward the use of transition metals, noble metals, bimetallic systems, or metal phosphides, carbides, and nitrides, supported on materials like metal oxides, mesoporous materials, zeolites, and carbon-based supports.

Noble metals, such as Pt^{21,38}, Pd^{26,39}, Ru^{27,40}, Ir⁴¹ are well established hydrogenation catalysts, with high selectivity for double bond saturation. However, they exhibit limited C-O bond cleavage ability, with Ru displaying the highest deoxygenation activity. Nevertheless, the saturation of the aromatic ring is beneficial for the subsequent deoxygenation, as it decreases the C-O bond energy. To improve the deoxygenation capability, often noble metals are associated with oxyphilic/acidic supports or in bimetallic system with more oxophilic transition metals (Co, Fe, Re, Mo etc.)^{42,43}. However, the high cost of noble metals limits their widespread application⁴⁴ (the current cost of the main used metals is reported in Appendix, Table 3.3.5.2.).

Transition metals such as Ni⁴⁵, Co^{46,47}, Cu^{44,45}, Fe^{31,32,50}, and W⁵¹ have also shown promising HDO activity. Also in this case, often they are combined in bimetallic systems to exploit their individual strengths⁵². For instance, Ni is highly effective in hydrogenation, while Co and Fe have higher oxygen affinity, enhancing the interaction with oxygenated species^{31,53}.

Cobalt as metal active phase in HDO

Among non-noble transition metals, Ni has been the most extensively studied for HDO. However, Co exhibits promising characteristics as an active phase in HDO reactions. In comparison to Ni/Al-MCM-41, Co/Al-MCM-41 has been found more selective in cleaving C-O bonds during HDO of guaiacol. In contrast, Ni catalysts favored hydrogenolysis and ring-opening reactions, leading to notable carbon loss through methane formation⁵⁴. Co also exhibits a lower reduction temperature than Ni, making it more reactive under HDO conditions. A study comparing Co- and Ni- based catalysts for the HDO of isoeugenol reported the highest performance with Co/SBA-15. The superior deoxygenation activity of Co was attributed to its better metal dispersion, easier reducibility and interaction with the support. Ni, with its larger particle size and higher reduction temperatures, favors hydrogenation and ring-opening reactions, leading to different product distribution⁵⁵.

However, catalytic activity is strongly influenced by the interaction between the metal phase and the support, as well as the metal dispersion. For example, in the HDO of anisole, Ni-based catalysts showed higher activity than Co when supported on Al-SBA-15 and H-ZSM-5. This was attributed to the stronger interaction between Co and the acidic supports, which hindered the reduction of Co and diminished its catalytic efficiency⁵⁶.

Biochar as support

Key properties for a good catalyst's support include surface area, porosity, acidity and/or the presence of oxygen vacancies. Commonly used supports are divided into metal oxides, molecular sieves, and carbon-based materials.

Metal oxides, including Al₂O₃, TiO₂, ZrO₂, CeO₂, and SiO₂, offer mesoporosity, that enhances reactant diffusion and surface adsorption⁵⁷, and tunable acidity, that promotes HDO reactions. However, excessive acidity, as seen with Al₂O₃, can lead to strong adsorption of the reactant and coke formation. Reducible oxides like TiO₂ and CeO₂ supply oxygen vacancies, promoting deoxygenation reactions⁴⁷. Molecular sieves include highly ordered materials like zeolites⁴⁰ and mesoporous silica⁵⁸ (e. g., SBA⁵⁹). Hierarchical and mesoporous materials improve the dispersion of active sites and the diffusion high molecular weight oxygenates, that are prone to polymerize, thus moderating the coke formation⁶⁰. Zeolites, with their tunable acidity via the Si/Al ratio, and the presence of both Brønsted and Lewis acid

sites⁶¹, allow controlled catalytic activity²², on the other and, being predominantly microporous, can hinder the diffusion of large molecules like phenolic compounds.

Carbon based materials, including biochars (BCs), activated carbons (ACs), carbon nanotubes (CNT)^{62,63}, carbon black (CB), graphene have garnered significant attention over the years due to their numerous advantages²⁰. As already extensively discussed in Chapter 3.2, biochars and activated carbons, in particular, exhibit tunable pore structure, which can be readily modified to achieve specific chemical and physical properties, and high surface areas⁶⁴. The high surface area of these materials facilitates superior metal dispersion, making them highly effective as catalyst supports. Modified ACs can present a well-developed mesoporosity, that not only favors metal dispersion, but also reduce clogging by coke deposition⁶⁵. Carbon materials are inherently neutral supports⁶⁶, and compared with acidic supports, can limit undesirable side reactions such as coking and excessive hydrogenolysis that can lead to high production of gaseous byproducts like methane. Thus, they can prevent rapid deactivation of the catalyst. Echeandia *et al.* compared NiW supported on mesoporous activated carbon and on Al₂O₃, for HDO of phenol, and concluded that the formation of coke was drastically reduced when carbon was used as support. Furthermore, non-acidic supports are less prone to form metal-support strong interactions, that can lead to the formation of non-reactive species (like Co-Al spinel)⁵⁵ allowing a better reduction of metal oxide in the active form, and improving the catalytic activity. To improve the acidity, carbon surface can be modified through post-treatments with acids such as phosphoric, nitric, or sulfuric acid, introducing acidic functionalities that enhance catalytic performance. Notably, acidity can also be provided by the metallic species itself. For example, metals like Ru, Fe, Co, which have high oxophilicity, promote HDO effectively even when supported on neutral materials²⁶. Carbon-based materials, with their inherent hydrophobic nature, offer excellent hydrothermal resistance and stability in acidic environments, as bio-oil⁶⁷.

The metal/biochar interactions in biomass hydro-upgrading catalysts are reflected in several factors: geometric effects (NPs size, morphology and dispersion), electronic effects (charge transfer between metal and support), interfacial reactivity, and direct involvement of the support in the catalytic reaction⁶⁸. The high oxygen content and ideal pore structure of biochar allow to obtain non-noble metal/biochar catalyst with enhanced activity for HDO process⁶⁹. In a study by R. Shu *et al.*, the catalytic effect of Ru supported on various biochars and commercial carbons, coupled with silicotungstic acid (HSiW) was evaluated in the HDO of guaiacol. The support material played a critical role in the final catalytic performance: Ru supported on a biochar derived from bamboo exhibited higher activity due to its high mesoporosity, which promoted Ru dispersion. Additionally, Ru/C-bamboo showed enhanced H₂ adsorption, increasing the amount of hydrogen available for HDO reaction⁷⁰.

The characteristics of the support can be modulated by proper activation steps. Mudi *et al.* explored the use of chemical activation (H_2SO_4 , KOH), to modify the physicochemical properties of biochar⁷¹, to prepare Ni/biochar catalysts, compared in the catalytic HDO of vanillin.

Treatment with H_2SO_4 resulted in enhanced surface area, improved Ni NPs distribution, and overall better catalytic activity, yielding higher amount of creosol, derived by the hydrogenation and hydrogenolysis of the aldehydic group of vanillin. Santos *et al.* investigated the use of cellulose and vine shoot as precursor for biochar preparation, and subjected to a combination of physical activation (CO_2) and chemical activation (ZnCl_2)⁷². The dual activation process resulted in biochars with exceptionally high surface areas, exceeding $1000 \text{ m}^2/\text{g}$, and a well-developed pore structure comprising both micropores and mesopores.

Additionally, the biochars displayed an extensively functionalized surface, enhancing their catalytic properties. These biochars were employed as support for various noble metals (Pd, Au, Ru) and tested in HDO of vanillin. Pd/C, that displayed the best metal dispersion, resulted to have the best catalytic performances in the formation of p-creosol⁷³. These properties highlight the potential of biochar as a promising and sustainable support material for biomass hydro-upgrading processes.

The combination of carbon-based materials as catalysts support – characterized by all the advantages related on the high stability, thermal conductivity, large surface area, and well-defined porosity - with a cost-effective metal like Co, which exhibits good activity and selectivity toward deoxygenation, has proven effective for the preparation of active catalytic in HDO. For instance, reduced graphene oxide (rGO) has shown to be an efficient support for Co, facilitating the formation of single atoms of metallic Co and CoO_x NPs, providing both metallic active phase and acid sites⁷⁴. A balanced proportion of Co^0 and Co^{2+} was also achieved using a triazine-based polymer (PAF-53) as a template for the synthesis of Co/NC catalyst. It exhibited high efficiency in the HDO of eugenol, achieving 98 % yield of propyl cyclohexane^{63,75}. Furthermore, the encapsulation of Co in a carbon matrix derived from glucose carbonization, resulted in strong metal-support interaction, giving a highly stable catalyst. In this case the main active phase was found to be CoO, which selectively converted guaiacol to cyclohexanol under mild conditions⁷⁶. In addition to phenolic compounds, Co supported on carbon materials has also demonstrated catalytic activity for the hydro-upgrading of furans, such as furfural¹⁴.

Despite these advantages, the use of biochar, combined with cobalt for HDO of bio-oil compounds remains underexplored. Only a few studies have been reported in literature⁷⁷, including combinations of Co with other metals (e.g., CoMoS⁷⁸), or hybrid supports (e.g., carbon-alumina⁷⁹).

Therefore, a key focus of this thesis was to investigate the use of biochar as support and Co as the active metal phase in HDO of bio-oil model compounds. Particular attention was given to the HDO of isoeugenol. Additionally, the effect of the introduction of furfural, representative of the furanic fraction, was explored to assess the catalyst's activity and the feasibility of co-processing multiple bio-oil-derived compounds.

The use of cobalt in HDO of isoeugenol is still largely unexplored, and no examples of Co supported on biochar for this reaction have been documented in the literature. Lindfors *et al.* were the first to investigate Co supported on various oxides for the HDO of IE, comparing its performance with that of nickel (Ni) catalysts⁵⁵. Their study identified Co/SBA as the most effective catalyst. Recently, Li *et al.*⁶³ reported excellent results using Co supported on nitrogen-doped carbon (Co/NC). However, the carbon support in their study was derived from the pyrolysis of a triazine-based polymer, which is not considered environmentally sustainable. Given this context, exploring Co as a non-noble metal catalyst supported on biochar—a renewable, low-cost material derived from biomass—offers significant potential for sustainable HDO of IE, particularly for producing propyl cyclohexane, a key component for sustainable aviation fuel. This combination represents a more environmentally friendly and cost-effective alternative to conventional supports, making it a highly attractive avenue for further research.

Building on the previous investigation of the catalytic properties of various biochars (Chapter 3.2), in this Chapter, the activated biochars derived from rice husk (A-RH), chromium-free tannery byproducts, specifically leather shaving waste (A-LS), and their co-pyrolysis product (A-RL) were used for the preparation of 10 wt. % Co/biochar catalysts. The intrinsic characteristics of these carbon-based materials and their catalytic performance were explored in the hydrodeoxygenation of isoeugenol to produce propylcyclohexane as sustainable aviation fuel. For the most effective biochar-based catalysts (namely Co/A-RH), an in-depth study was conducted on the influence of reaction parameters, product distribution, and catalyst stability. A kinetic model was also developed based on the proposed reaction network. Furthermore, given that bio-oil typically consists of a diverse range of compounds, the potential for co-processing isoeugenol with a chemically distinct model compound, such as furfural, at varying concentrations was assessed.

This study aims to contribute to the development of efficient and sustainable catalysts for bio-oil upgrading. The findings from this research are expected to provide valuable insights into the broader applicability of biochar-supported catalysts in biomass conversion processes, particularly to produce SAF, a key component of the future renewable energy landscape.

3.3.2 Experimental

Catalyst preparation

10 wt. % Co/biochar were prepared by wet impregnation. Three activated biochars, derived from rice husk (A-RH), leather shaving waste (A-LS) and the co-pyrolysis of the two biomasses (A-RL), were used as support. As reference, 10 wt. % Co/AC was prepared, using a commercial activated carbon as support. The catalysts were labelled Co/A-RH, Co/A-LS, Co/A-RL, and Co/AC, respectively.

The proper amount of $\text{Co}(\text{NO}_3)_2 \cdot 6 \text{H}_2\text{O}$ (Sigma Aldrich) was dissolved in 250 mL of distilled water and placed in a round bottom flask. 0,9 g of biochar were added to the solution. The suspension was kept under stirring at 70 °C for six hours to allow adsorption of the metal in the pores of the char. After six hours, water was removed by rotary evaporation and the catalyst was dried at 110 °C overnight. After that it was subjected to calcination under inert atmosphere (argon) and reduction under H_2 .

The calcination and reduction temperatures were chosen after Temperature Programmed Desorption and Temperature Programmed Reduction analyses respectively, to evaluate the temperature of decomposition of nitrates and the reduction temperature of cobalt. Calcination was conducted at 350 °C in Ar (40 mL/min, temperature program 10 °C/min, for 2 hours). Reduction was conducted *ex-situ* prior to each reaction, at 450 °C in H_2 (5 °C/min for 2 hours).

Catalyst characterizations

The metal content was measured by MP-OES (Perkin Elmer Optima 5300 DV Optical Emission Spectrometer), after digesting the catalyst (ca 50 mg) in a mixture of aqua regia ($\text{HCl}:\text{HNO}_3$ 3:1) under microwave for one hour. The textural properties of the supports, and the fresh and spent catalysts were evaluated by N_2 physisorption at -196 °C (Micromeritics Tristar Plus II). The surface area was calculated by Langmuir and BET method⁸⁰. Temperature-programmed desorption (TPD), reduction (TPR), and NH_3 desorption (NH_3 TPD) were performed with Microtrac Belcat II equipment, coupled with mass spectrometer Pfeiffer Vacuum Omni Star. TPD was performed in He (30 mL/min) with a temperature ramp of 10 °C/min up to 100 °C for 30 minutes, 10 °C/min up to 800 °C for 20 minutes. TPR was performed using a mixture of 5% H_2 in Ar (flow 30 mL/min) with a ramp temperature of 10 °C/min from 50 °C to 800 °C, after a pre-treatment in Ar (30 mL/min) at 200 °C for 2 hours. NH_3 TPD was performed using previously a reduction step: first the sample was reduced by a 5% H_2 in Ar mixture (30 mL/min) with a temperature ramp of 10 °C/min from 50 °C to 450 °C and let at these conditions for two hours. The system was further cooled down to 100 °C, and a mixture of 5% of NH_3 in He (30 mL/min) was sent to the sample for 30 minutes, followed by a purging in He (30 mL/min) for 60 minutes. The desorption was carried out in He (30 mL/min) with a temperature ramp of 10 °C/min up to 800°C. The final

temperature was maintained for 20 minutes. Co particles size and distribution was evaluated by Transmission Electron Microscopy (TEM) using a JEM-1400 (voltage). Transmission electron microscopy (TEM) was utilized to determine the metal particle size and study the morphology and porosity. The equipment used for analysis was a Model JEM-1400Plus system (JEOL, Japan) with a maximal acceleration voltage of 120 kV. The interpretation of TEM images and determination of particle sizes of the fresh and spent catalysts were done using the ImageJ program. Prior to the TEM analysis, the samples were ground and suspended in ethanol. A drop of suspension was mounted on a copper grid coated with a carbon film and the solvent evaporated. The particle size distribution of metal particles was determined by measuring the diameter (d) of more than 300 particles visible in TEM micrographs.

The size of the metal nanoparticles was measured by ImageJ software, and the dispersion was calculated as (Eq. 3.3.2.1):

$$D_{TEM}(\%) = \frac{1 \text{ nm}}{\text{avg } d \text{ (nm)}} \times 100 \quad (\text{Eq. 3.3.2.1})$$

Powder X-ray diffraction measurements were performed by Panalytical AERIS Research Edition diffractometer in Bragg-Brentano geometry, using Cu K α radiation and equipped with PIXcel1D detector, in the diffraction angle 2θ between 5° and 85° . The samples were first ground to powder using a zero-background silicon sample holder. X-ray photoemission spectroscopy was carried out with a Thermo Scientific Nexsa XPS (ESCA) with a monochromated Al K α X-ray source. The samples were supported on a copper conductive tape compatible with UHV for charge compensation. Deconvolution of peaks was done using the XPSpeak 4.1 program. The binding energy was calibrated based on the C 1s peak at 284.6 eV.

Catalytic experiments

HDO experiments were carried out in a 300 mL semi-batch reactor (PARR Instruments), equipped with a mechanical stirrer. In a typical experiment the desired amount of pre-reduced catalyst was added to the system together with 50 mL of dodecane (Sigma Aldrich), used as solvent, and the proper amount of reactant/s. The catalyst particle size was maintained $< 63 \mu\text{m}$ and the stirring 900 rpm, to avoid mass transfer limitations. The reaction was monitored by sampling the liquid at specific time intervals. Co/ARH was also reused for three catalytic cycles. Prior to recycling, the catalyst was washed with acetone, dried in air, and reduced at the same conditions than before the first use.

The liquid samples were analyzed by a gas chromatograph using a DB-1 capillary column (Agilent 122-103e, $30 \text{ m} \times 250 \mu\text{m} \times 0.5 \mu\text{m}$). The temperature program used for GC analysis was the following: 60°C then $5^\circ\text{C}/\text{min}$ and $3^\circ\text{C}/\text{min}$ to 135°C then $15^\circ\text{C}/\text{min}$ to 300°C (1 min).

The conversion, yield and selectivity were calculated upon calibration, using isoeugenol (cis + trans) (Sigma Aldrich), dihydroeugenol ($\geq 99\%$, Sigma-Aldrich), 4-Isopropylcyclohexanol (cis + trans, $> 98\%$ TCI), 4-propylcyclohexanone ($> 98\%$ TCI), propyl cyclohexane (Sigma Aldrich).

Conversion was calculated as (Eq. 3.3.2.2):

$$\text{Conversion (\%)} = \left(\frac{\text{mol}_i \text{IE}^* - \text{mol}_t \text{IE}^*}{\text{mol}_i \text{IE}^*} \right) * 100 \quad (\text{Eq. 3.3.2.2})$$

Products yield was calculated as (Eq. 3.3.2.3):

$$\text{Yield (\%)} = \left(\frac{\text{mol}_t \text{product}}{\text{mol}_i \text{IE}} \right) * 100 \quad (\text{Eq. 3.3.2.3})$$

Mass balance was calculated as (Eq.3.3.2.4):

$$\text{Carbon balance (\%)} = \left(\frac{\text{mol}_t \text{IE} + \sum \text{mol}_t \text{products}}{\text{mol}_i \text{IE}} \right) * 10 \quad (\text{Eq. 3.3.2.4})$$

Where $\text{mol}_i \text{IE}^*$ and $\text{mol}_i \text{product}$ are the initial moles of IE or DHE, and of the products, $\text{mol}_t \text{IE}^*$ and $\text{mol}_t \text{product}$ are moles of IE or DHE, and of the products, at a certain time.

3.3.3 Results and discussion

Catalysts characterization

He-TPD analyses were performed to evaluate the decomposition temperature of $\text{Co}(\text{NO}_3)_2$. In Figure 3.3.3.1 the TPD profiles of the three biochar-based catalysts are reported.

For all samples, a primary peak centered between 225 and 230 °C is observed, along with two smaller peaks at higher temperatures (550–650 °C). Mass spectrometry analysis indicates that the first peak corresponds to the release of NO , H_2O , CO_2 , CO , N_2 , and O_2 , suggesting the decomposition of nitrates. The higher temperature peaks are associated with the release of CO and CO_2 , indicative of the decomposition of the char's functional groups. Based on these results, a calcination temperature of 350 °C was selected to ensure complete decomposition of the nitrates. For all samples, calcination was performed under an inert atmosphere (Ar flow), and the decomposition of $\text{Co}(\text{II})$ nitrate primarily yielded CoO , without a change in the oxidation state, as confirmed by XRD analyses (Figure 3.3.3.5).

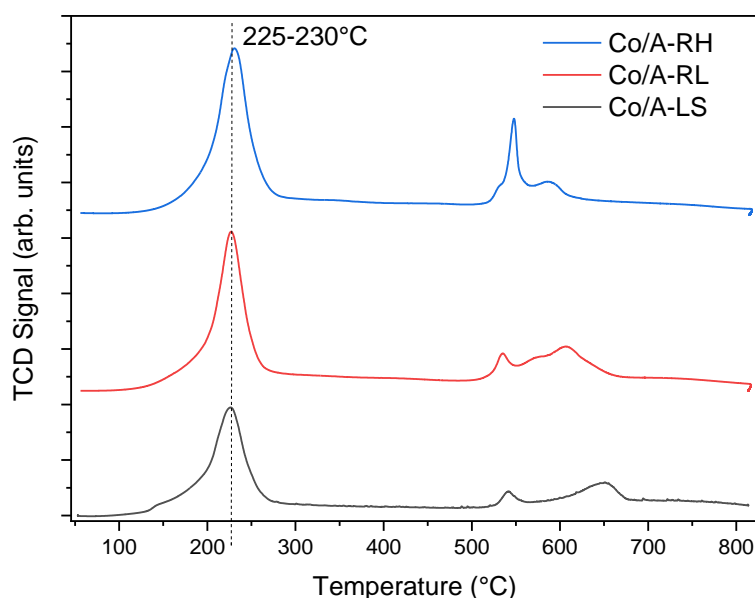


Figure 3.3.3.1. TPD profiles of Co/A-RH (blue), Co/A-RL (red), and Co/A-LS (black).

TPR was conducted to evaluate the reducibility of the cobalt species. Figure 3.3.3.2 presents the TPR profiles of the three biochar-based catalysts, and the comparison with Co/AC. The major reduction events (resumed in Table 3.3.3.1), corresponding to the reduction of cobalt oxide (CoO) to metallic cobalt (Co^0), occur between 400 °C and 600 °C across all samples. Both Co/A-LS (black curve) and Co/AC (green curve) show initial reduction peaks at 290 °C and 240 °C, respectively, which are typically attributed to the reduction of Co_3O_4 to CoO ⁶⁴, indicating a higher oxidation tendency for Co for Co/A-L

and Co/AC. In the case of Co/AC, the primary reduction event is characterized by a broad peak that begins at 330 °C and centers around 550 °C, suggesting a general strong and uniform interaction between Co and the support. In contrast, Co/A-LS, Co/A-RL (red curve), and Co/A-RH (blue curve) exhibit two sharper, partially overlapping peaks in Co/A-LS and Co/A-RL, with more distinct peaks in Co/A-RH. These peaks are centered at 405–450 °C for Co/A-LS and progressively shift to higher temperatures for Co/A-RL (430–475 °C) and Co/A-RH (410–550 °C). The differences in peak profiles and temperatures suggest that the nature of the support significantly influences the reducibility of cobalt oxides. Specifically, the distinct bimodal reduction peaks in Co/A-RH indicate dual interaction with the support, where some cobalt particles are more strongly bonded, requiring higher temperatures for reduction. The reduction temperature was set at 450 °C for all samples.

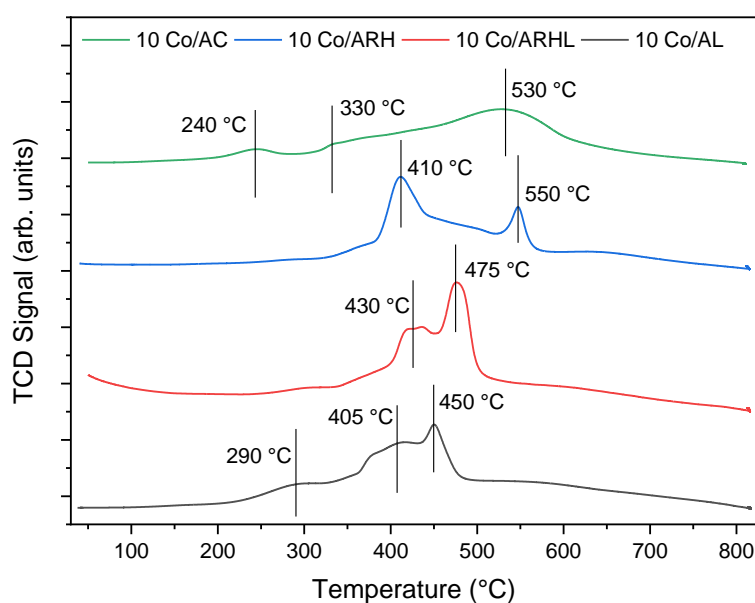


Figure 3.3.3.2. TPR profiles of Co/A-RH (blue), Co/A-RL (red), Co/A-LS (black), and Co/AC (green)

Table 3.3.3.1. TPR results of the catalysts.

Catalyst	T _{1, max} (°C)	T _{2, max} (°C)	T _{3, max} (°C)	Relative total peak area normalized by catalyst mass
10Co/AC	240	330	530	0.61
10Co/A-RH	n.a.	410	550	0.47
10Co/A-RL	n.a.	430	475	0.96
10Co/A-LS	290	405	450	1

The textural properties of the catalysts were evaluated and compared to the pristine support by N₂ physisorption analysis (Figure 3.3.3.3, Table 3.3.3.2). The results demonstrated that the porous structure of the biochars was preserved across all catalysts after impregnation. The H4 type hysteresis loop of all the samples demonstrated the presence of mesopores, with a narrow slit-like pore form typical of carbonaceous materials⁸¹. Cobalt impregnation led to a notable reduction in total surface area, likely due to pore blockage by the metal, indicating a strong interaction between the support and the active phase. The most significant surface area reduction, a 44% decrease, was observed for Co/ARH, suggesting a uniform distribution of the metal across the surface of the material.

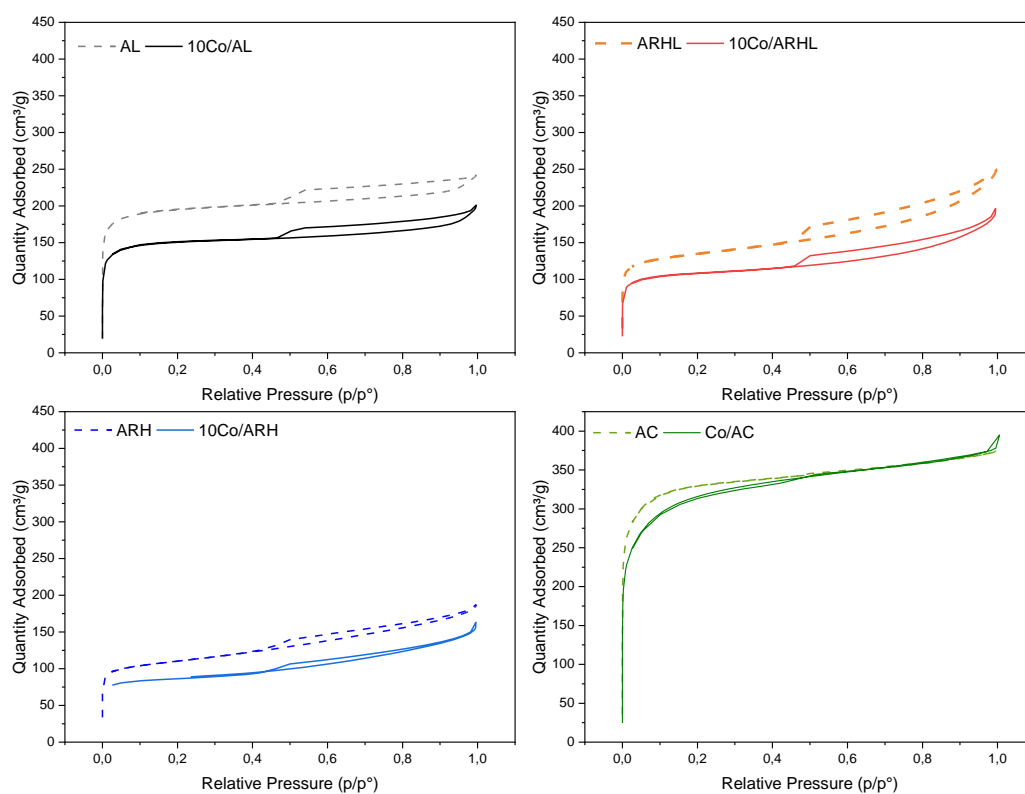


Figure 3.3.3.3. N₂ adsorption-desorption isotherms of the supports (dotted lines) and the catalysts (solid lines).

Table 3.3.3.2 Textural properties of supports and catalysts.

Sample	S_{BET} (m^2g^{-1}) ^a	S_{micro} (m^2/g) ^b	V_{tot} (cm^3/g) ^c	V_{micro} (cm^3/g) ^d
A-LS	633	789	0.25	0.23
Co/A-LS	434	528	0.19	0.15
A-RL	445	463	0.17	0.12
Co/A-RL	330	362	0.13	0.09
A-RH	367	543	0.14	0.10
Co/A-RH	214	173	0.11	0.07
AC	1113	1064	0.40	0.26
Co/AC	1010	823	0.32	0.14

^aSurface area calculated by BET method. ^bMicropore surface area calculated by t-plot method. ^cTotal pore volume calculated according to the adsorbed amount of N_2 and P/P_0 values near 0.98. ^dMicropore volume calculated by t-plot method.

MP-AES measurements (Table 3.3.3.3) indicated that Co/A-RH and Co/A-RL retained a higher metal loading (12 wt.% and 13 wt. % respectively) compared to Co/AL (8 wt.%). Notably, the amount of effective Co measured on Co/AC resulted the highest, leading to 16 wt. %. This was particularly attributed to the very high surface area of this material ($1113 \text{ m}^2/\text{g}$).

Table 3.3.3.2. Co loading determined by ICP-MS analysis, Co particle size and distribution, measured by TEM, and S_{BET} determined by N_2 physisorption.

Sample	Nominal wt. %	Effective wt. %	d_{TEM} (nm)	D_{TEM} (%)
Co/A-LS	10	8	9.6 ± 0.8	10.4
Co/A-RL	10	13	8.9 ± 0.2	11.2
Co/A-RH	10	12	8.9 ± 0.2	11.2
Co/AC	10	16	8.2 ± 0.2	12.2

The particle size and distribution of metal particles on the catalysts, as shown in Table 3.3.3.3, were determined by TEM analysis (Figure 3.3.3.4). All catalysts exhibited average particle diameters below 10 nm with a similar dispersion range (D_{TEM} 10-11 %), with the highest distribution on Co/AC, followed by Co/A-RH and Co/A-RL. Co/AL catalyst displayed a broader particle size distribution, including agglomerates larger than 50 nm, indicating poor interaction between the metal and the support. This resulted in lower metal loading and some degree of sintering during the calcination and/or reduction processes. The enhanced metal retention and better dispersion obtained on A-RH and A-RL, compared with A-LS is attributed to the intrinsic properties of the supports, particularly the morphology, microstructure, surface functionalization of Co/A-RH and Co/A-RL, as previously discussed (Chapter 3.2). Despite the lower surface area of these materials, other characteristics incurred to facilitate a more efficient cobalt deposition and interaction with the support, contributing to the higher metal loading and good dispersion, observed.

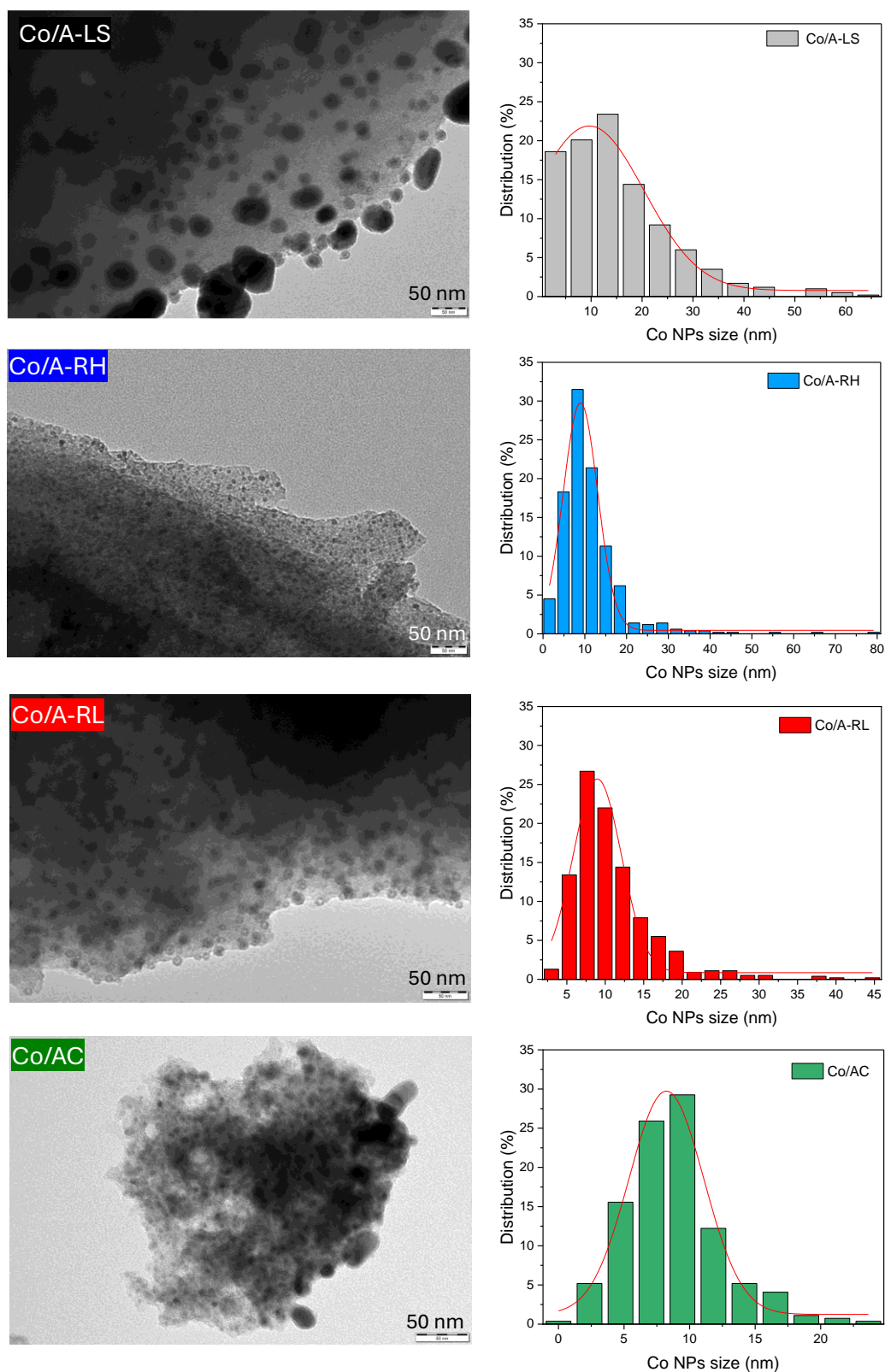
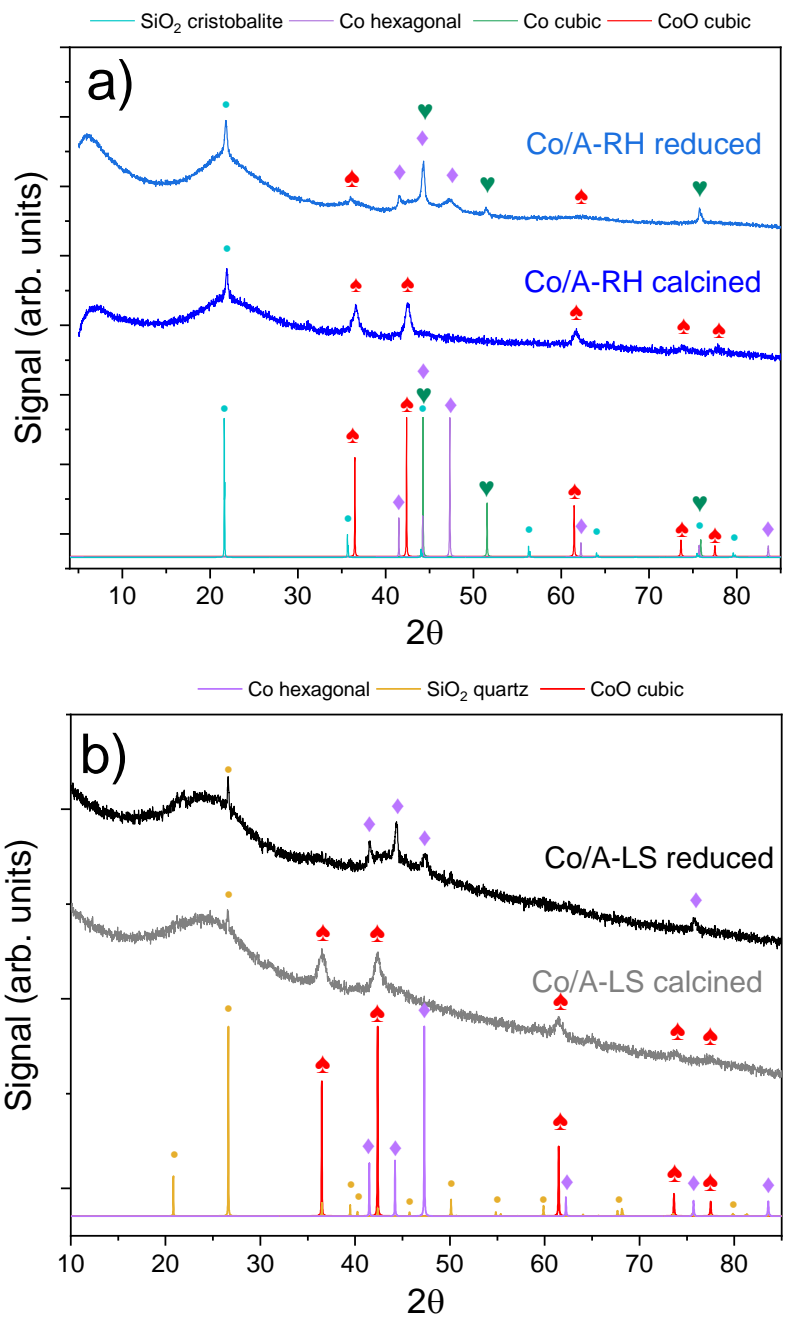


Figure 3.3.3.4. TEM microscopy and NPs size distribution of the catalysts.

XRD analyses were conducted on the catalysts before and after reduction at 450 °C to investigate the cobalt crystalline phases. The diffraction patterns are depicted in Figure 3.3.3.5 (a-d).



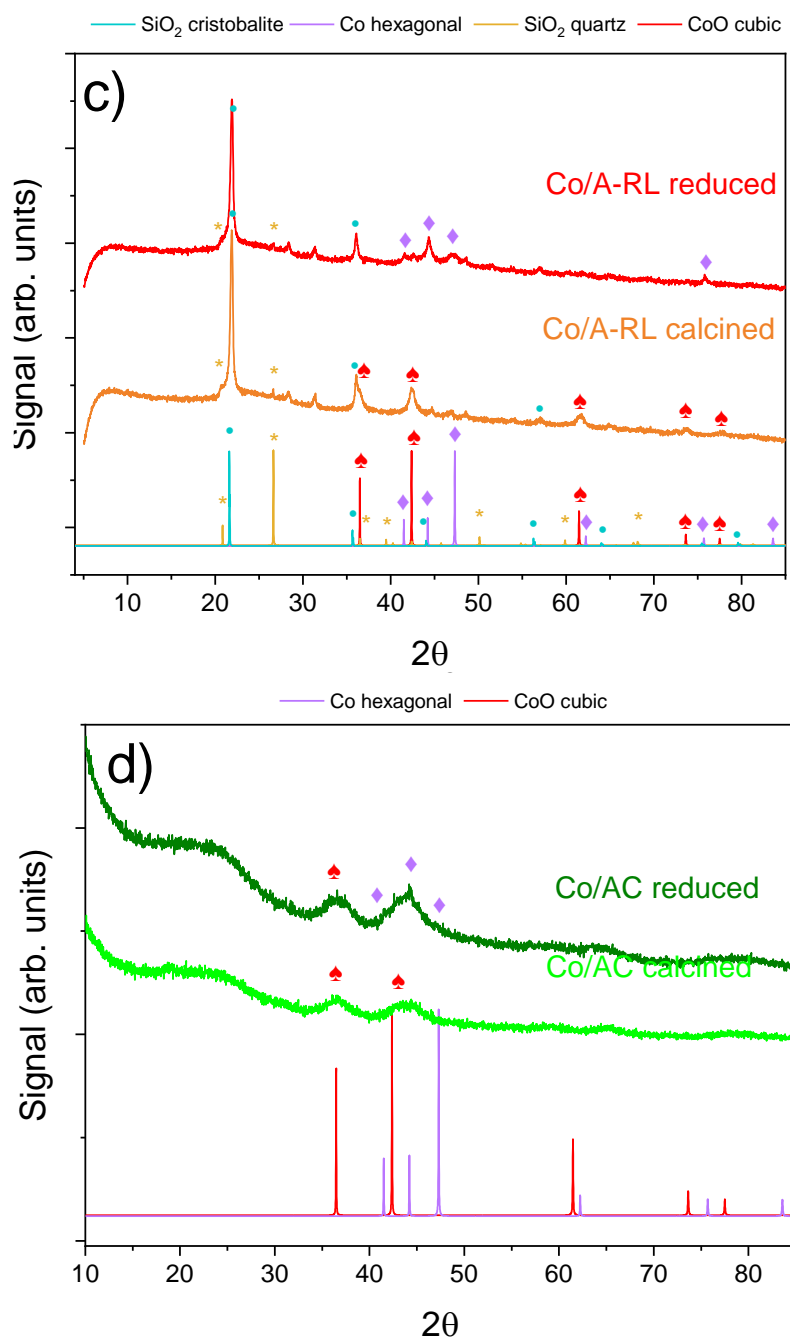


Figure 3.3.3.5. XRD patterns of the catalysts before and after reduction. b) Co/A-RH, b) Co/A-LS, c) Co/A-RL, d) Co/AC.

According to data from the Crystallography Open Database (COD) files, distinct diffraction patterns corresponding to the support and metal phases were observed. All catalysts exhibited a similar amorphous phase peak at $2\theta = 23^\circ$, which is attributed to the sp^2 -hybridized graphitic carbon (002) crystalline phase. In all samples, signals corresponding to the silica phase were clearly present. The silica derived from rice husk predominantly exists in the form of cristobalite, while the silica in AL is mainly quartz. In the ARHL samples, reflections characteristic of both cristobalite and quartz are evident.

No evidence of SiO_2 signal was detected on Co/AC, in line with the ultimate analysis (Chapter 3.2). For all the calcined catalysts (represented by the blue, orange, gray, and light green curves), the diffraction peaks associated with cobalt indicated the formation of a face-centered cubic (fcc) structure of CoO. The characteristic diffraction peaks at 36.3° , 42.3° , 61.5° , 73.4° , and 77.2° correspond to the (111), (200), (220), (311), and (222) planes of CoO, respectively^{82,83}. After reduction, the Co/A-LS and Co/A-RL catalysts showed complete reduction of Co(II) to Co(0), forming a hexagonal close-packed (hcp) structure. The characteristic diffraction peaks for the hcp phase were observed at 41.7° (100), 44.5° (002), and 47.5° (101). In contrast, the Co/A-RH catalyst exhibited the coexistence of both hcp and fcc phases of metallic cobalt, as indicated by a low-intensity diffraction peak at 51.5° , corresponding to the (111) plane of the fcc Co structure, this could be related to the hybrid nature of A-RH support, made of silica and carbon, that could have a different interaction with the metal phase. Additionally, a minor contribution from the oxide phase was detectable in this sample⁸⁴. A significant contribution from the oxide phase was observed in the reduced Co/AC sample. These findings align with TPR measurements, suggesting that for both Co/A-RH and Co/AC, the strong metal/support interaction lead to a non-complete reduction of Co at 450°C . Additionally, the signals in the Co/AC sample were broader and less defined, indicating smaller nanoparticles, consistent with the TEM results (Figure 3.3.3.4).

The acidity of the catalysts, a crucial factor in hydrodeoxygenation reactions due to its role in C–O bond cleavage, was assessed using NH_3 -TPD analysis. The desorption profiles are shown in Figure 3.3.3.6, while the results obtained by the analysis are resumed in Table 3.3.3.3.

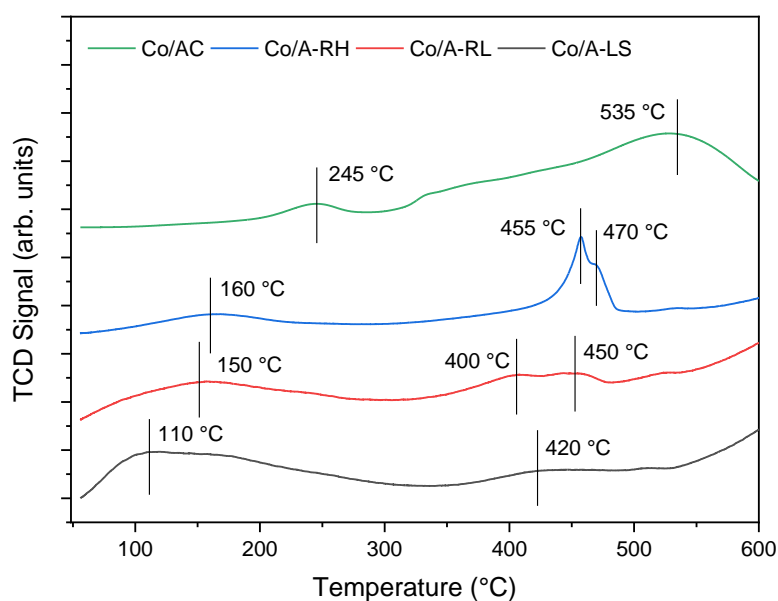


Figure 3.3.3.6. NH_3 TPD profiles of the catalysts.

Table 3.3.3.3 Results from NH_3 TPD of the catalysts

Catalyst	T _{1,max} (°C)	T _{2,max} (°C)	T _{3,max} (°C)	Relative total peak area normalized by catalyst mass
10Co/AC	245	n.a.	535	0.78
10Co/A-RH	160	455	470	1.0
10Co/A-RL	150	400	450	0.87
10Co/A-LS	110	420	n.a.	0.76

All biochar-based catalysts exhibited a broad desorption peak around 150 °C, indicative of weak acid sites. In Co/AC, this peak shifted to higher temperatures (around 245 °C). Notably, Co/A-RH (represented by the blue curve) displayed a sharp and distinct peak centered around 450 °C, which was almost absent in Co/A-LS and Co/A-RL (black and red curves respectively), that was shifted to higher temperature (565 °C) in Co/AC (green curve). This suggests the presence of medium to strong acid sites in significant concentrations. The high-temperature desorption peaks, related to strong acid sites, in Co/A-RH and Co/AC were attributed to the presence of CoO, which was absent in the other catalysts, as confirmed by XRD. The Co²⁺ species in CoO infer Lewis acidity, likely due to the electronic deficiency of the cobalt cations⁸³.

These comprehensive characterization results clearly demonstrate that the nature of the support significantly influences the metal distribution, metal-support interaction, and the oxidation state of the metal. Consequently, these factors play a pivotal role in determining the overall activity of the material.

Isoeugenol HDO

HDO experiments were conducted using different catalyst : reactant ratios to check whether experiments were performed in the kinetic regime, keeping constant the amount of IE (2 mg/mL) and changing the amount of catalyst (20, 50, 80 mg) To do so, Co/A-RH was used as catalyst. When the results from different experiments are plotted as a function of normalized abscissa, time multiplied by catalyst mass, the kinetic curves should coincide to demonstrate the absence of external mass transfer limitations. The first step of the reaction (hydrogenation of IE to DHE and formation of PCONE from DHE), the beginning of the reaction is not very well defined, some differences in concentrations are visible for example regarding PCONE, which is an intermediate in equilibrium with its enolic form that rapidly undergoes hydrogenation of the ketonic group to form PCOL (as reported in Figure 3.3.3.7). However, for PCOL the curves coincide, and it reacts further with the same rate. On the other hand, minor differences were observed in the formation rate of PCH.

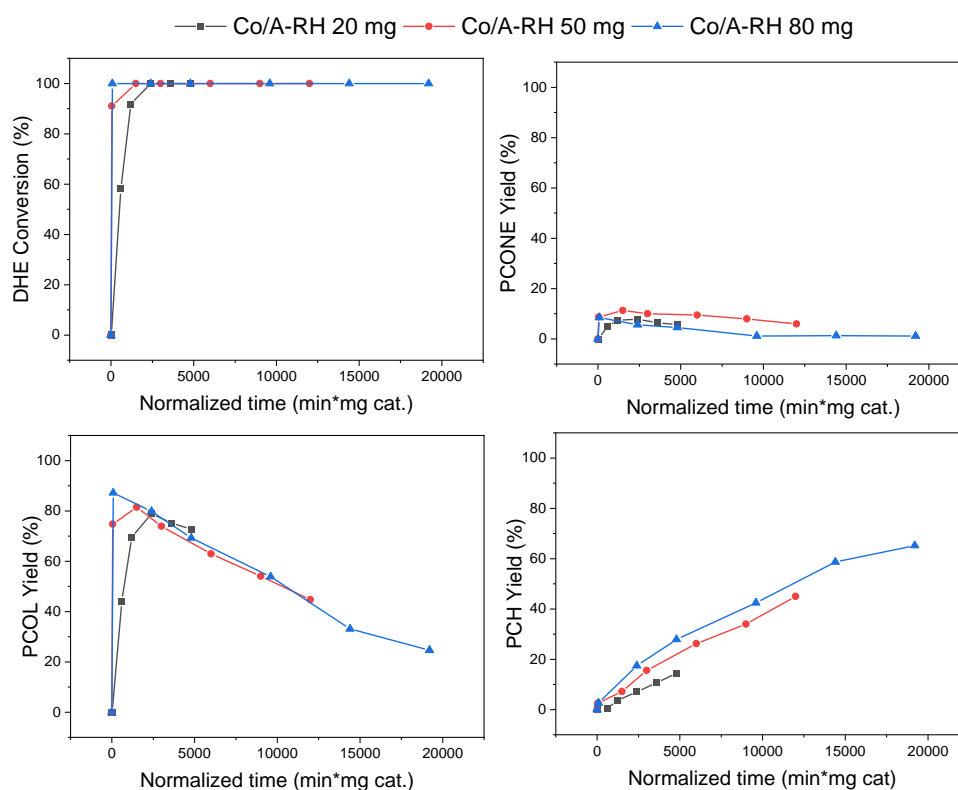


Figure 3.3.3.7. Isoeugenol HDO at different catalyst : reactant ratios. Reaction conditions: IE 2 mg/mL, dodecane 50 mL, 275 °C, 30 bar H₂, 900 rpm, 240 min. DHE: dihydroeugenol, PCONE: propylcyclohexanone, PCOL: propylcyclohexanol, PCH: propylcyclohexane.

After assessing the repeatability of the experiments using 50 mg Co/A-RH, the catalytic performance of Co/A-LS, Co/A-RH, and Co/A-RL in the hydrodeoxygenation (HDO) of isoeugenol (IE) was evaluated and compared to that of Co/AC (Table 3.3.3.4, Figure 3.3.3.8), at 300 °C, 30 bar H₂, 900 rpm for 240 min, with 50 mg of catalyst and 2 mg/mL of IE.

Over all the catalysts, the hydrogenation of the double bond in the allyl chain of IE proceeded rapidly, leading to the formation of dihydroeugenol (DHE) (Figure 3.3.3.8). Due to the fast reaction kinetics, it was not feasible to monitor the conversion of IE to DHE⁵⁵. Consequently, the study focused on tracking the conversion of DHE over time to assess the catalytic performance of the catalysts.

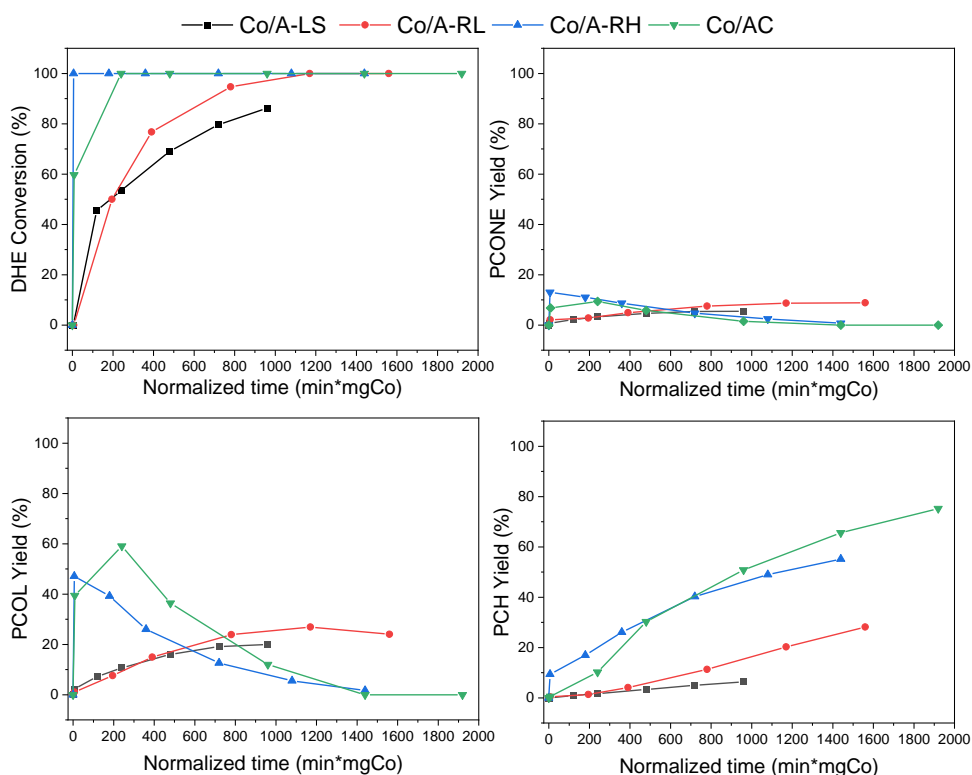


Figure 3.3.3.8. Reaction profiles of Isoeugenol HDO over different catalysts. Reaction conditions: IE 2 mg/mL, dodecane 50 mL, 50 mg cat., 300 °C, 30 bar H₂, 900 rpm, 240 min. DHE: dihydroeugenol, PCONE: propylcyclohexanone, PCOL: propylcyclohexanol, PCH: propylcyclohexane.

Table 3.3.3.4. Results of the catalyst screening. Initial rates for DHE disappearance and DHE conversion and product yields at 240 minutes.

Entry	Initial rate for DHE	DHE	PCONE	PCOL	PCH	C balance
	disappearance (mmol/min/g _{Co})					
Co/A-LS	0.89	86.2	5.5	20.0	6.3	45.4
Co/A-RL	0.79	100	8.8	24.0	28.1	60.9
Co/A-RH	Large	100	0.7	1.7	55.1	57.5
Co/AC	3.75	100	0	0	75.2	75.2

Due to the different Co loading, the conversion and yield percentages were plotted against normalized time, which was calculated by multiplying the reaction time by the mass of metal in each catalyst.

This normalization allowed for a more accurate comparison of the catalytic activity and selectivity among the tested catalysts. The initial rate for DHE transformation decreased as follows: Co/A-RH > Co/AC > Co/A-L > Co/A-RL (Table 3.3.3.4). However, the rate for DHE transformation after 30 min decreased for Co/A-LS, while the other catalysts were very active reaching 100% DHE conversion. The most active catalyst exhibited narrow particle size distribution (Figure 3.3.3.4) and medium to strong acid sites. (Figure 3.3.3.6). The second highest initial DHE rate was found for Co/AC which exhibited the highest portion of very strong acid sites. The initial DHE transformation rate did not correlate with hydrogen TPR, but more with catalyst acidity. The catalysts containing strong acid sites were also active for DHE transformation. Noteworthy is also that Co/AC exhibiting strong acid sites gave also high carbon balance, whereas in case of Pt-Beta zeolites the sum of the liquid phase products in HDO of isoeugenol decreased with increasing acidity⁸⁵. In addition, it was reported in HDO of isoeugenol over Pt-Re/carbon catalysts that liquid phase mass decreased when pH of the catalyst slurry was around 6, while those with higher pH gave nearly complete liquid phase mass balance⁸⁶.

The final yield of PCH increased in the same order as the initial DHE transformation rate indicating that the strength of acidic sites was crucial. i.e. the two catalysts exhibiting the largest amounts of strong acid sites were giving the highest yields of PCH. Among the biochar-based catalysts, Co/A-RH demonstrated the highest activity, achieving complete conversion of DHE within 1 minute and nearly complete conversion of PCOL to PCH within 240 minutes, with a maximum yield of 55%. Compared to Co/AC, Co/A-RH showed a higher initial reaction rate but lower selectivity toward the desired products (Co/AC yielded PCH at 75%). This lower selectivity was primarily due to a reduced carbon balance on Co/A-RH compared to Co/AC, likely due to hydrocracking side reactions that produced lighter compounds (e.g., methane, ethane, ethylene, propane, butane, and isobutene), which are undetectable in the liquid phase. The occurrence of hydrocracking was further confirmed by the formation of shorter-chain hydrocarbons (C₆-C₁₁) derived from the solvent dodecane, as evidenced in the GC chromatogram. The potential for co-processing fossil feedstocks with biomass-derived compounds has been previously reported³².

The slightly lower initial activity for DHE transformation for Co/AC resulted in higher selectivity and less side reactions, such as hydrocracking, leading to a carbon balance of 75%. The superior activity of Co/AC for production of PCH after prolonged times, followed by Co/A-RH, is attributed to the high metal dispersion and the coexistence of cobalt in both Co⁰ and Co²⁺ forms. This combination contributes to a higher density of acid sites⁸⁷, which promotes C–O bond cleavage. The Co²⁺ species, present as CoO nanoparticles with structural defects, play a crucial role in coordinating oxygenated compounds. These CoO nanoparticles contain oxygen vacancies that activate the C–O groups⁷⁵.

Moreover, CoO with oxygen vacancies is a highly active species for the heterolytic cleavage of H₂⁸⁸. As discussed in the introduction, the synergistic effect of metallic cobalt and CoO in HDO is well-documented. For example, Singh *et al.* highlighted that oxygen vacancies formed on Co/CoO catalysts, derived from Co₃O₄ reduction, were pivotal for the demethoxylation of guaiacol⁸³ reaching 99% conversion with 80% selectivity toward cyclohexanol, at 180 °C 20 bar H₂. achieving 99% conversion with 80% selectivity toward cyclohexanol at 180 °C and 20 bar H₂. Similar results were reported by Wen *et al.* using Co/CeO₂, leveraging the oxygen vacancies provided by the support⁴⁷. Additionally, Shen *et al.*⁷⁰, demonstrated that CoOx was the active site for the hydrogenation of furfural, yielding cyclopentanone and cyclopentanol as the main products with a total yield of 82%. In bimetallic CoNi, the presence of CoOx species lead to the formation of oxygen vacancies, improving catalytic performance on HDO of vanillin, yielding 100% methyl cyclohexanol at mild conditions (200 °C, 1.0 MPa H₂)⁸⁹. Similar synergy was found in CuCoOx catalysts for the HDO of 5-hydroxymethyl furfural to dimethylfuran⁴⁸.

Further evidence of the synergistic effect between the two cobalt oxidation states was obtained by comparing the catalytic activity of Co/A-RH in its reduced form with that of Co/A-RH in its calcined form, without an additional reduction step (Figure 3.3.3.9). At 250 °C and 30 bar, the reaction proceeded at a slower rate with the calcined Co/ARH catalyst. This resulted in a decrease in DHE conversion from 100% to 72%, as well as a reduction in the yields of PCOL (from 79% to 50%) and PCH (from 5.3% to 2.0%) as the main products.

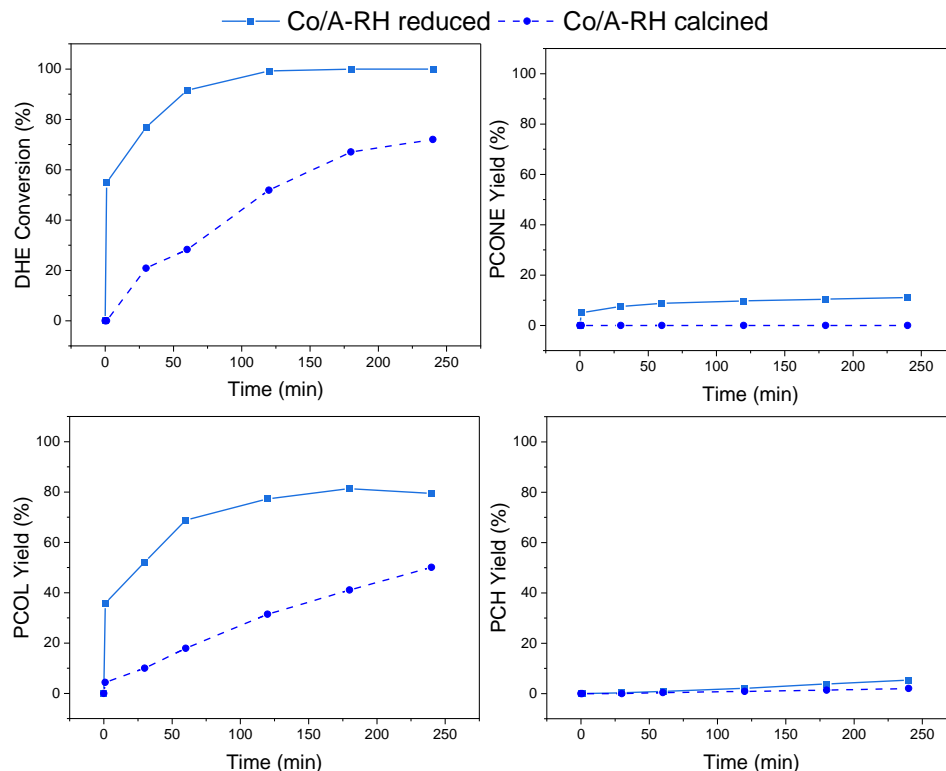


Figure 3.3.3.9. Comparison of IE HDO over Co/A-RH calcined (blue dotted line) and reduced (light blue solid line). Reaction conditions: IE 2 mg/mL, dodecane 50 mL, 50 mg cat., 250 °C, 30 bar H₂, 900 rpm, 240 min. DHE: dihydroeugenol, PCONE: propylcyclohexanone, PCOL: propylcyclohexanol, PCH: propylcyclohexane.

However, a balanced ratio of metallic Co and CoO species and an appropriate number of acid sites are necessary to prevent over-reactions, such as cracking⁹⁰, as observed for Co/A-RH. The higher concentration of acid sites on Co/A-RH was responsible for the lower carbon balance and the occurrence of acid-catalyzed side reactions.

From the mechanistic point of view, it is important to investigate the reaction network. Multiple consecutive reactions were observed: demethoxylation of the -OCH₃ group and hydrogenation of the aromatic occurred rapidly, with 4-propylcyclohexanol (PCOL) emerging as the main product within the first hour of reaction. The detection of 4-propyl cyclohexanone (PCONE) could suggest two different pathways: on one case, the hydrogenation of the aromatic ring occurred, followed by the cleavage of the O-CH₃ bond to form 4-propyl-1,2-cyclohexanediol (represented by the letter D in the reaction scheme reported in Figure 3.3.3.10), and by the dehydration of the hydroxylic group to form 4-propyl-cyclohex-1-en-1ol (E), which rapidly tautomerized to PCONE³⁸. On the second case, the demethoxylation occurred first, leading to the formation of propylphenol (I), and further hydrogenation of the aromatic ring occurred, to form the enol, that was stabilized in the ketonic form by tautomerization, and further hydrogenated to PCOL.

Several intermediates were formed and consumed rapidly and it was not possible to detect them, however, considering the dissociation energies reported in literature for different C-O bonds, ($C_{\text{alkyl-O}} 200 \text{ kJ mol}^{-1}$; $C_{\text{aryl-OCH}_3} 386.5 \text{ kJ mol}^{-1}$, and $C_{\text{aryl-OH}} 542 \text{ kJ mol}^{-1}$)²⁴ both pathways could be feasible.

A general reaction scheme based on the products detected is reported in the scheme in Figure 3.3.3.10.

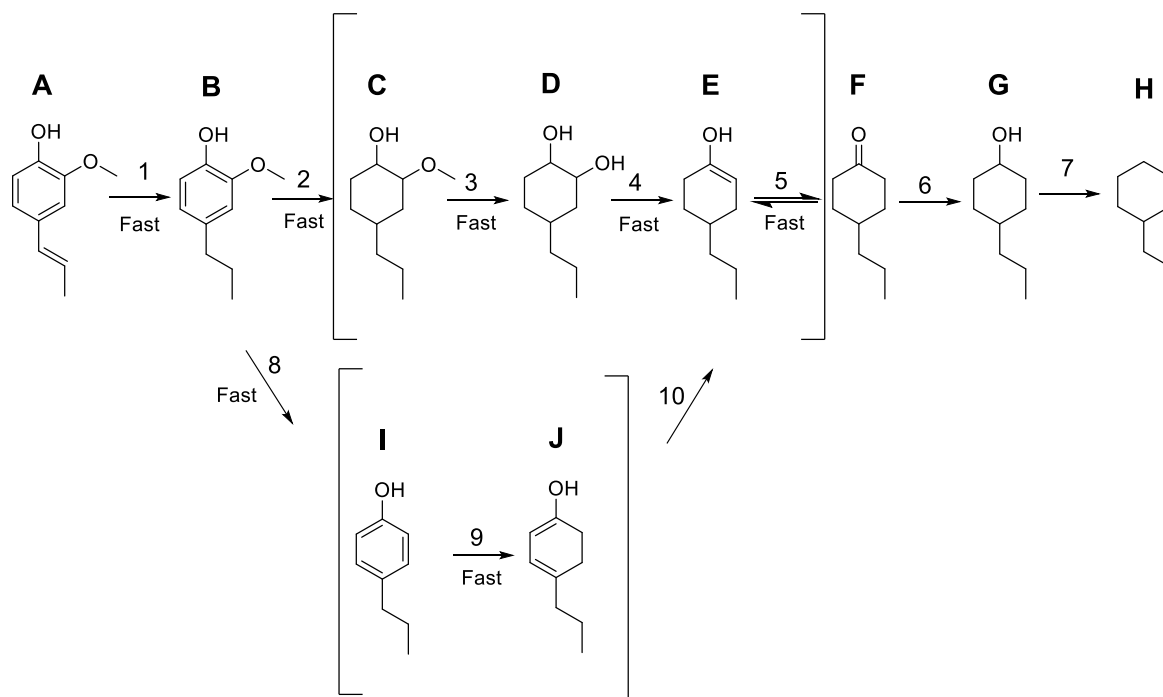


Figure 3.3.3.10. Proposed reaction network for HDO of Isoeugenol.

In parentheses the products that were not detected by GC analyses.

The catalytic performance of the two best-performing catalysts from this study was compared with results reported in the literature. Numerous studies have investigated the HDO of various phenolic compounds, such as guaiacol, phenol, and anisole, utilizing both noble and non-noble metal catalysts supported on various oxides, zeolites, and carbon materials. However, the focus of this work was primarily on the use of carbon-based supports and non-noble metals for the complete HDO of eugenol or IE to PCH. A comprehensive overview of relevant literature data, particularly on carbon-supported and non-noble metal catalysts for HDO reactions, is provided in Table 3.3.3.5.

Table 3.3.3.5. Comparison of results obtained with different reported heterogeneous catalysts

Entry	Carbon based catalyst	Solvent	Reaction conditions	PCH yield (%)	Ref
1	Pt/AC ^a	n-decane	2 h, 280 °C, 30 bar	44.3	[21]
2	PtRe/C ^a	dodecane	4 h, 300 °C, 30 bar	91	[43]
3	Ni/graphite ^a	dodecane	4 h, 300 °C, 30 bar	60	[55]
4	RuRe/MWCNT ^b	heptane	1 h, 200 °C, 30 bar	62.6	[67]
5	Ru/C + Nb ₂ O ₅ ^c	H ₂ O + MeOH	12 h, 250 °C, 11 bar	74	[36]
6	Ru/CNT ^b	H ₂ O + dodecane	3 h, 220 °C, 50 bar	94	[27]
7	Pd/C + HZSM-5 ^b	H ₂ O	0.5h, 240 °C, 20 bar	64	[91]
8	Co/NC-T ^b	n-heptane	LHSV 12 h ⁻¹ , 300 °C, 30 bar	98.4	[63]
Entry	Non noble metal-based catalyst	Solvent	Reaction conditions	PCH yield (%)	Ref
9	Ni/SBA ^a	dodecane	4 h, 300 °C, 30 bar	75	[59]
10	Co/SBA ^a	dodecane	4 h, 300 °C, 30 bar	63	[55]
11	Ni/HZSM-5 ^b	hexane	2 h, 250 °C, 30 bar	80	[30]
12	Ni/Al-SBA-15-HZSM-5 ^b	dodecane	2 h 260 °C, 30 bar	68	[45]
13	Ni/Al-SBA-15 ^b	dodecane	2 h 240 °C, 20 bar	85	[45]
14	Co/A-RH	dodecane	4 h, 300 °C, 30 bar	55	this work
15	Co/AC	dodecane	4 h, 300 °C, 30 bar	75	this work

^aIE, ^bEU, ^cIE+DHE+4-allyl-syringol

The PCH yields obtained using Co/A-RH and Co/AC catalysts in this study (55% and 75%, entry 14,15 respectively) are competitive with other non-noble metal systems, such as Ni/graphite (60%, entry 3) and Co/SBA (63%, entry 10)⁵⁵. These yields are also comparable to those achieved with some noble metal catalysts, including Pd/C + HZSM-5 (64 %, entry 7)⁹¹, Ru/C + Nb₂O₅ (74 %, entry 5)³⁶, RuRe/MWCNT (62.6% , entry 4)⁶⁷. Notably, the Pt/AC catalyst exhibits a relatively low yield of 44.3% (entry 1)²¹, suggesting that noble metals often require the addition of oxophilic sites to enhance their performance in HDO reactions. Some noble metal systems, such as Ru/CNT, achieved a high PCH yield of 94% (entry 6)²⁷ likely due to the combination of well-dispersed Ru on supports with high surface area, mechanical strength, and good chemical stability, resulting in enhanced metal-support interactions and a higher density of active sites. Despite their high activity, noble metal catalysts like Pt, Pd, and Ru are generally not economically viable for large-scale applications due to their high cost. Among cobalt-based catalysts, the study by Murzin *et al.* showed that Co/SBA was the most efficient catalyst producing PCH, while other supports like Co/SiO₂, Co/TiO₂, and Co/Al₂O₃ achieved yields of less than 10%, which was attributed to the high dispersion of the cobalt phase on the highly ordered mesoporous structure of SBA-15. One of the best results in the literature was reported for a Co/NC-T catalyst with a PCH yield of 98.4% (entry 8)⁶³. However, comparing this to our results is challenging, as the reaction conditions differed, with their study not being conducted in a batch system. Nonetheless, the crucial role of nitrogen-doping in enhancing catalytic activity was highlighted as a key factor in achieving these results.

In this context, the use of biochar as support for cobalt-based catalysts offers several potential advantages, including lower costs, simplified preparation procedures, and reduced environmental impact. Biochar, being a sustainable and low-cost material derived from biomass, provides an eco-friendly alternative to synthetic carbon supports, aligning with the goals of green chemistry and sustainable catalysis. Therefore, Co/A-RH was chosen to investigate the reaction at different conditions, to get better insights on its performance, reaction network and activation energy of each step. In particular, the effect of temperature, H₂ pressure, catalyst amount and IE concentration were evaluated, and the results are listed in Table 3.3.3.6.

Table 3.3.3.6. Results from HDO of Isoeugenol using Co/A-RH under different conditions.

Entry	T (°C)	P (bar)	[IE] mg/mL	Cat. (mg)	DHE Conversion (%)	PCONE Yield ^{a,b} (%)	PCOL Yield ^{a,b} (%)	PCH Yield ^{a,b} (%)	C balance (%)
1	200	30	2	50	100	0	79 (84)	0 (0.5)	84.5
2	250	30	2	50	100	8 (11)	67 (79.4)	1 (5.3)	95.8
3	275	30	2	50	100	0 (5.9)	73 (44.7)	3.7 (45.0)	95.6
4	300	30	2	50	100	n.a. (0.7)	n.a. (1.7)	n.a. (55.1)	57.5
5	200	20	2	50	79.4	n.a. (0)	n.a. (55.5)	n.a. (0)	75.8
6	200	40	2	50	100	0	83 (96.5)	0	96.5
7	275	10	2	50	100	13 (6.5)	60 (65.7)	0 (16.8)	88.9
8	275	20	2	50	100	12 (9.1)	69 (55.8)	0 (25.6)	90.5
9	275	30	3.5	50	100	10 (8.3)	90 (59.4)	3 (27.4)	95.2
10	275	30	6.5	50	100	3 (5.2)	65 (62.2)	1 (20.5)	87.8
11	275	30	2	20	100	8 (5.6)	68 (72.7)	3 (14.5)	92.9
12	275	30	2	80	100	n.a. (1.5)	n.a. (24.7)	n.a. (65.2)	91.0
13	275 (II)	30	2	50	100	4.5	43.2	42.7	90.5
14	275 (III)	30	2	50	100	8.4	58.6	34.6	99.0

^a at DHE conversion level of 90%, ^b in parenthesis after 240 min.

Effect of temperature

The effect of temperature was clearly visible in the conversion rate, when it increased with increasing temperature from 200 °C to 300 °C. As detailed in Table 3.3.3.6 (entries 1-4) and illustrated in Figure 3.3.3.11, the product distribution was notably temperature dependent. At 200 °C, the predominant product was PCOL, with a yield of 84%, while only 0.5% of PCH was produced. As the temperature increased, the cleavage of the hydroxyl group's carbon-oxygen bond became more favorable, leading to a PCH yield of 55% at 300 °C. This shift can be attributed to the differing temperature dependencies of the hydrogenation and deoxygenation steps; hydrogenation, characterized by a lower activation energy, was favored at lower temperatures, whereas deoxygenation, which has a higher activation energy, became more favorable at elevated temperatures²⁶.

Notably, at 275 °C 45.0 % yield of PCH, and 44.7 % yield of PCOL were obtained, corresponding to a carbon balance of 95.6 %. At this temperature, side reactions like hydrocracking were limited, consequently, 275 °C was selected as the optimal temperature for further investigations. Activation energies and rate constants are given in the kinetic modelling section, reported in Appendix.

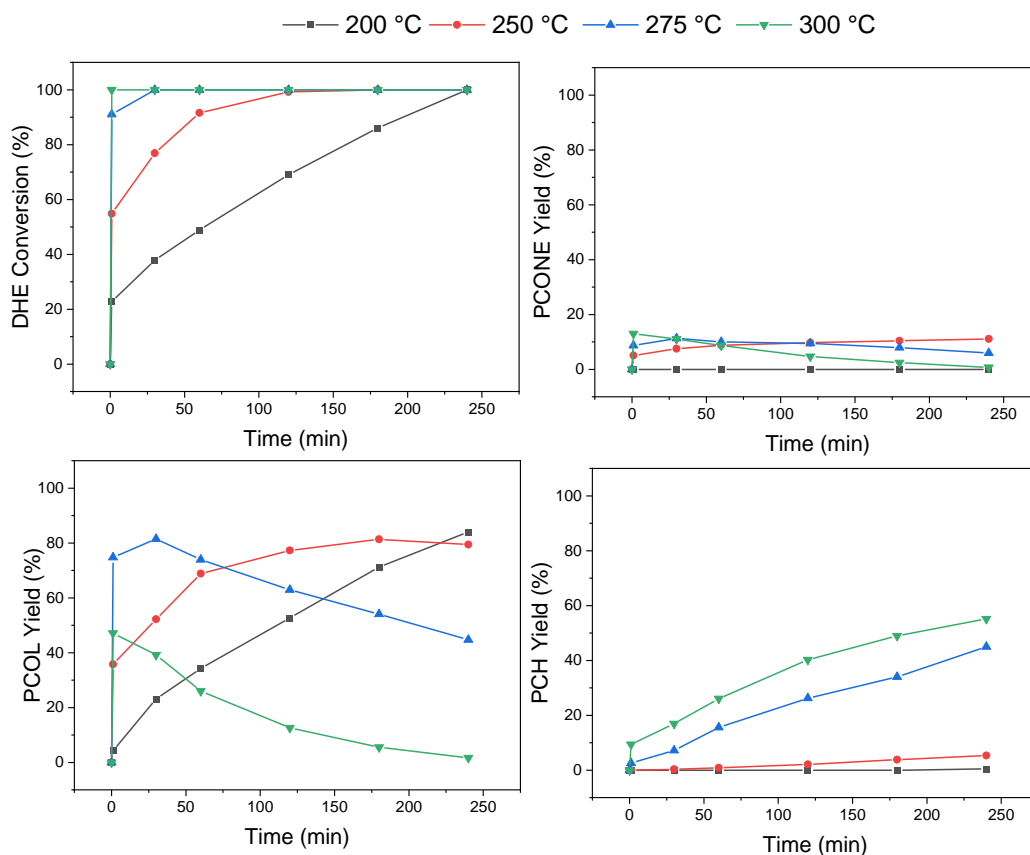


Figure 3.3.3.11. IE HDO over Co/A-RH at different reaction temperatures. Reaction conditions: 50 mg Co/A-RH (< 63 μm), IE 2 mg/mL, dodecane 50 mL, 30 bar H_2 , 900 rpm, 240 min. DHE: dihydroeugenol, PCONE: propylcyclohexanone, PCOL: propylcyclohexanol, PCH: propylcyclohexane.

Effect of pressure

The effect of H_2 pressure (between 10 and 40 bar) was investigated, both at low temperature (200 °C) (Figure 3.3.3.12, Table 3.3.3.6, entries 1, 5, 6) and at high temperature (275 °C). (Figures 3.3.3.13 and Table 3.3.6, entries 3, 7, 8).

3. Valorization of biomass via pyrolysis - 3.3 Hydrodeoxygenation of bio-oil model compounds using biochar-based catalysts

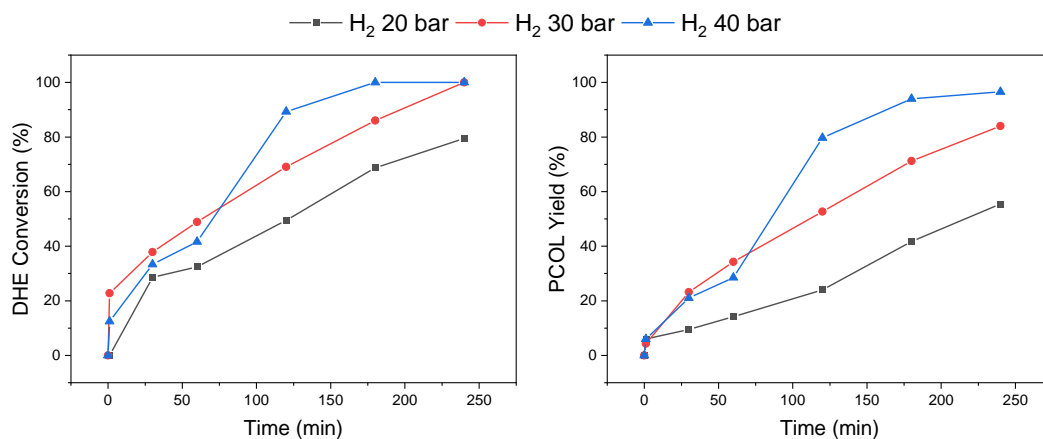


Figure 3.3.3.12. IE HDO at different pressures, 200 °C. Reaction conditions: 50 mg Co/A-RH (< 63 μm), IE 2 mg/mL, dodecane 50 mL, 200 °C, 900 rpm, 240 min. DHE: dihydroeugenol, PCOL: propylcyclohexanol.

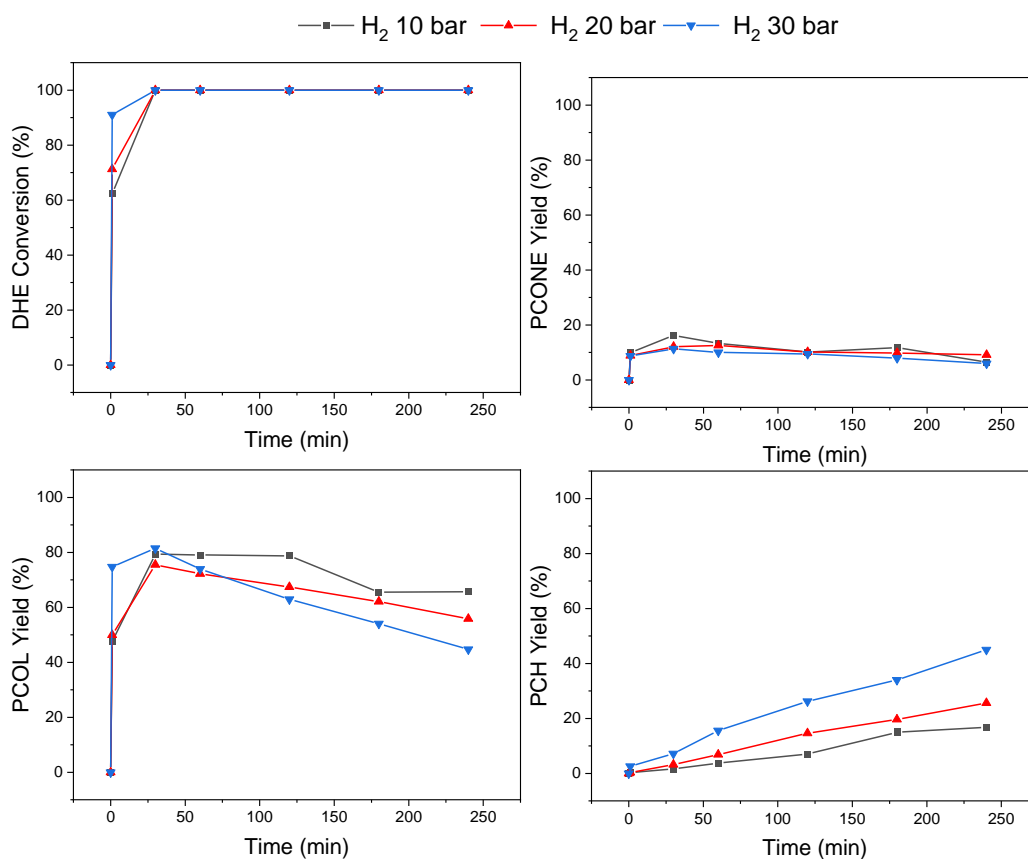


Figure 3.3.3.13. IE HDO at different pressures, 275 °C. Reaction conditions: 50 mg Co/A-RH (< 63 μm), IE 2 mg/mL, dodecane 50 mL, 275 °C, 900 rpm, 240 min. DHE: dihydroeugenol, PCONE: propylcyclohexanone, PCOL: propylcyclohexanol, PCH: propylcyclohexane.

In both cases, the increasing of H₂ pressure had a positive effect on the reaction rate. Higher pressure increases the solubility of hydrogen in the reaction medium, and the diffusion of hydrogen to the active sites, promoting hydrogenation steps. At 200 °C, the reaction occurred selectively only toward the formation of PCOL, and the final yield rose from 55.0 % to 96.5 % as the pressure increased from 20 to 40 bar.

These results are in line with the study of Zhang *et al.*, who investigated different Co based catalysts (TiO₂, HZM-5, ZrO₂, CeO₂, SiO₂) on the selective HDO of phenols to cyclohexanols at relatively mild conditions⁹². At 275 °C the C-O cleavage of the PCOL hydroxy group was favored, and initial PCH formation rate increased as follows: 0.003 mmol/min/g_{cat} at 10 bar, followed by 0.008 mmol/min/g_{cat} at 20 bar and 0.013 mmol/min/g_{cat} at 30 bar, respectively. The influence of pressure was less remarkable at higher temperature, however, PCH yield, at 90% DHE conversion increased from zero at 10 bar and 20 bar to 37% at 30 bar indicating that the consecutive reactions are slow under low hydrogen pressures. The final yields of PCH increased from 16.8% < 25.6% < 45% when applying 10, 20 or 30 bar total pressure. The increase of pressure had also a positive effect on carbon balance, both at 200 °C and 275 °C, suggesting that the high H₂ pressure suppressed side reactions like polymerization, and avoided a strong adsorption of the reactant on the catalyst surface. This effect is more marked at low temperature, where the reaction rate for HDO is lower and therefore side reactions are more likely to occur. This result is in line with Alda-Onggar *et al.*⁴¹, reporting that the liquid phase mass balance closure was also the highest in HDO of isoeugenol using Ir-Re/Al₂O₃ catalyst under the highest applied pressure, 40 bar.

Effect of IE concentration

The effect of the initial reactant concentration was evaluated, increasing IE concentration from 2 mg/mL up to 6.5 mg/mL, using 50 mg Co/A-RH, at 275 °C, 30 bar H₂, in dodecane (50 mL) (Table 3.3.3.6, entries 3,9,10, Figure 3.3.3.14).

The initial rates for DHE transformation with 2 mg/ml and 6.5 mg/ml of IE decreased were 0.26 mol/min/g_{cat}, and 1.05 mmol/min/g_{cat}, respectively showing that 3.3-fold higher initial IE concentration enhanced the rate by factor 4. This result indicates that the reaction order with respect to IE amount is close to unity, being in line with the results reported in Alda-Onggar *et al.*⁴¹. The conversion of DHE, as shown in Figure 3.3.14a, occurs quickly at every concentration, reaching total conversion after 60 minutes for the highest value. The formation of PCONE enhanced also with increasing initial IE concentration as visible in Fig. 3.3.14b. However, after reaching the maximum concentration the further transformation rate for PCONE decreased especially after 120 min reaction time. An interesting result is shown for PCH formation (Fig. 3.3.3.14d).

Initially, at all initial IE concentrations, the same transformation rate for PCH was observed (Fig. 3.3.3.14d). However, after 120 min PCH transformation rate increased. This shows that initially PCH transformation is limited due to slow hydrogenolysis of PCOL to PCH after 50 min (Fig. 3.3.3.14c), which is the rate limiting step.

The final yields of PCH for 2 mg/ml, 3.5 mg/ml and 6.5 mg/ml initial IE concentration, were 45%, 27% and 20%, respectively indicating that at higher initial IE concentration the consecutive reaction steps were rather slow.

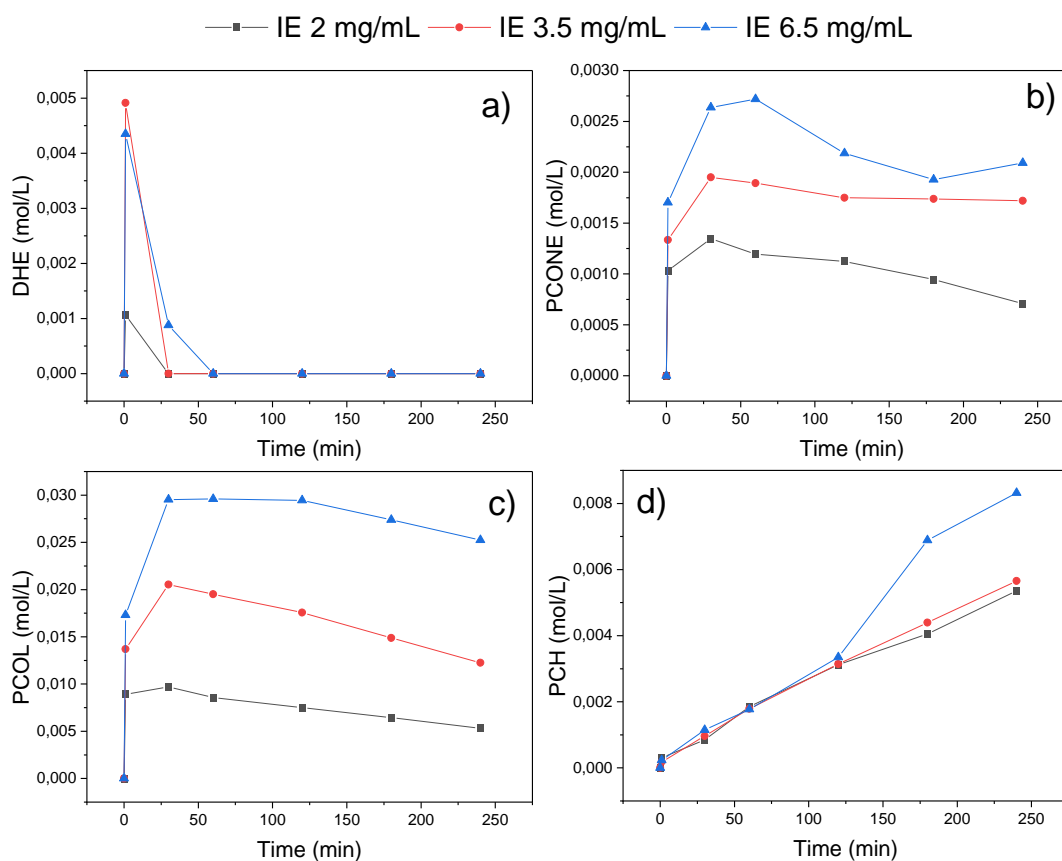


Figure 3.3.3.14. IE HDO at different IE concentrations. Reaction conditions: 50 mg Co/A-RH (< 63 μm), dodecane 50 mL, 275 $^{\circ}\text{C}$, 30 bar H_2 900 rpm, 240 min. DHE: dihydroeugenol, PCONE: propylcyclohexanone, PCOL: propylcyclohexanol, PCH: propylcyclohexane.

Kinetic modeling

For the investigated reaction, a kinetic modelling was proposed. It was based on the reaction network that considered the formation of propyl phenol as intermediate, as reported in Figure 3.3.3.15.

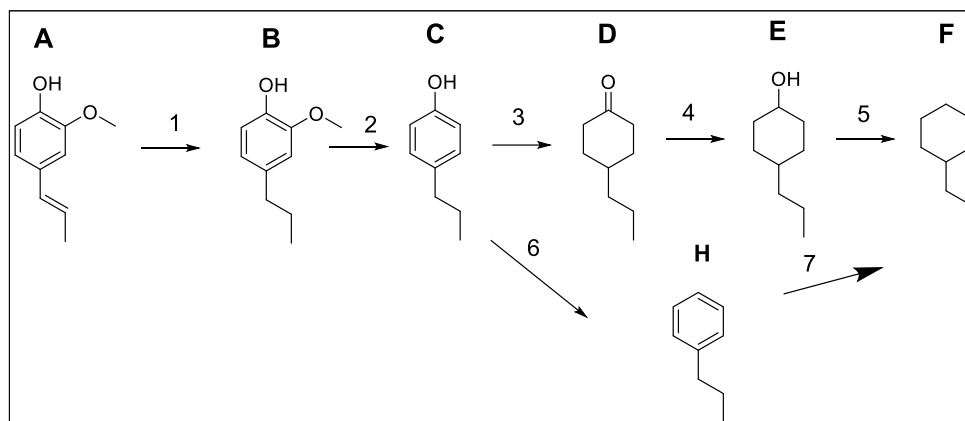
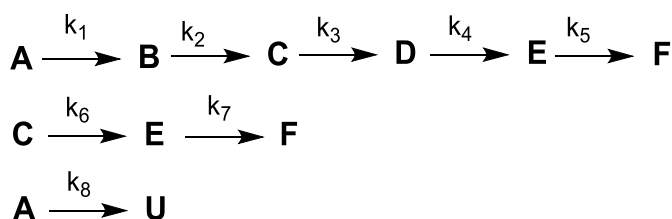


Figure 3.3.3.15 Proposed reaction network for HDO of Isoeugenol.



In which A, B, C, D, E, F denote IE, DHE, 4-PPHOL, PCONE, PCOL and PCH, respectively. The reaction network also takes into account a parallel reaction route where 4-PPHOL reacts directly to PCH via propylbenzene (H) and IE to unknown compounds (U), because the carbon balance was not 100%.

Kinetic modelling was performed using MODEST software¹⁰² by solving the differential equations 3.3.5.1 and 3.3.5.2 reported in the Appendix, with backward difference method.

Some model fits are shown in Figure 3.3.3.16 and others are reported in the Appendix (Figure 3.3.5.1) as well as the parameter values in Table 3.3.5.2 (Appendix). The degree of explanation was 94.05%. It can be seen that in some cases model fits well with the experimental data (Figure 3.3.3.16) while, especially at 200°C under 40 bar deviation is relatively large.

3. Valorization of biomass via pyrolysis - 3.3 Hydrodeoxygenation of bio-oil model compounds using biochar-based catalysts

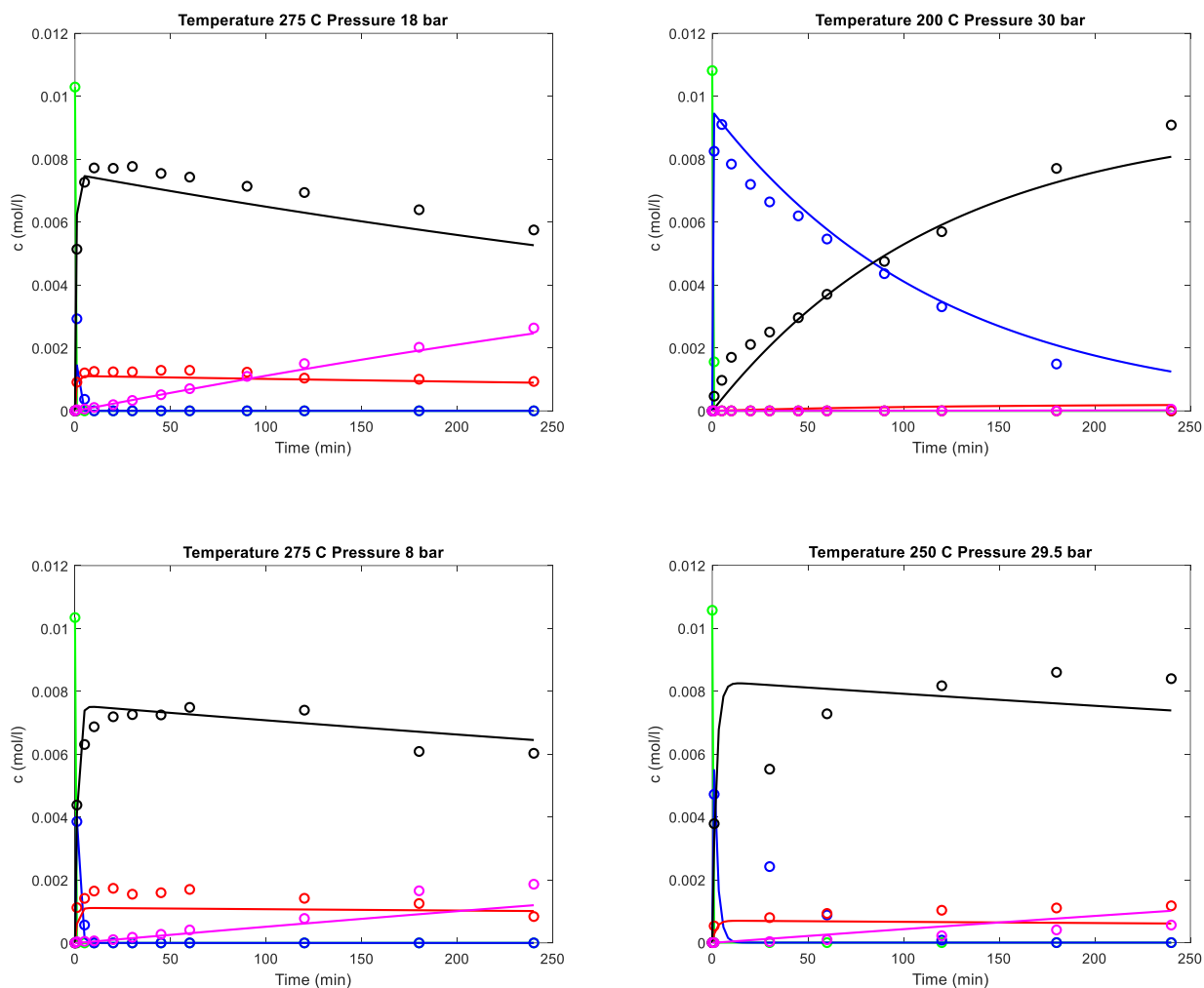


Figure 3.3.3.16. Experimental kinetic results and model fit for IE transformation at different reaction conditions. IE : Isoeugenol (green), DHE : dihydroeugenol (blue), PCOL : propylcyclohexanol (black), PCONE : propylcyclohexanone (red), PCH : propylcyclohexane (pink).

The estimated parameters, such as reaction rate and activation energies, indicated that the activation energy for the formation of PCH is 151 kJ/mol with a small error. In addition, transformation of PPHOL directly to PCOL is also considered and it exhibits low activation energy, confirming that this could be the preferential pathway.

Catalyst recyclability

The stability and recyclability of Co/A-RH was assessed by performing three consecutive reaction cycles at 275 °C and 30 bars. As reported in Figure 3.3.3.17, the catalyst demonstrated good stability in the first 2 cycles, and a slow decrease in activity at the third cycle, losing around 10 % of PCH final yield.

3. Valorization of biomass via pyrolysis - 3.3 Hydrodeoxygenation of bio-oil model compounds using biochar-based catalysts

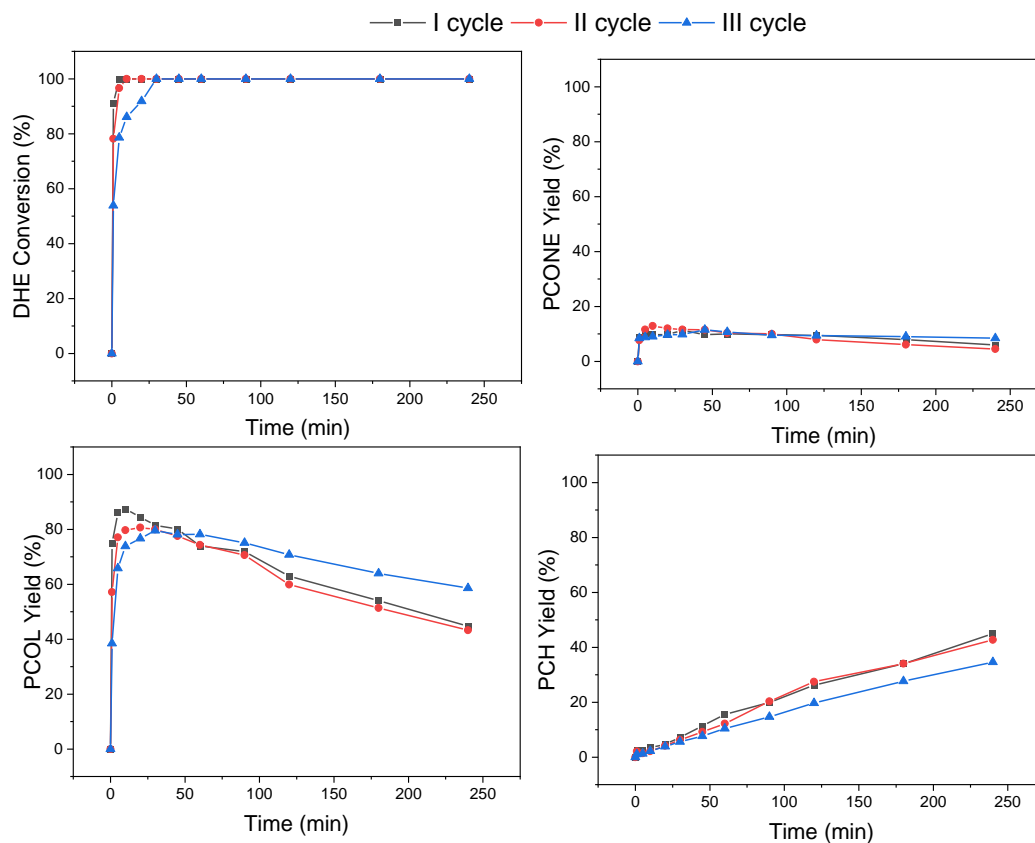


Figure 3.3.3.17. Catalyst recyclability. Reaction conditions: 50 mg Co/A-RH (< 63 μm), dodecane 50 mL, IE 2 mg/mL, 275 $^{\circ}\text{C}$, 30 bar H_2 900 rpm, 240 min. DHE: dihydroeugenol, PCONE: propylcyclohexanone, PCOL: propylcyclohexanol, PCH: propylcyclohexane.

TEM microscopy and ICP analyses of the spent catalyst demonstrated that no leaching or sintering of the Co nanoparticles occurred. Although the nanoparticles showed a slightly broader size distribution compared to the fresh catalyst (Figure 3.3.3.18), the average diameter was smaller (7.7 nm vs 8.9 nm, Table 3.3.3.7). This reduction in size could be attributed to the partial reduction of Co in the reaction environment, leading to shrinkage of the nanoparticles due to the loss of the external oxide layer. XPS analyses confirmed this, showing a higher contribution from the Co^0 signal in the spent Co/A-RH catalyst (ca. 20% vs 12%). CHNS analyses revealed a slight increase in carbon content on the spent catalyst, likely due to organic deposition on the surface. This organic deposition, along with the partial reduction of the metal phase, contributed to the minor deactivation of Co/A-RH after three reaction cycles. However, the absence of leaching and sintering is a highly positive outcome for this biochar-based catalyst, highlighting its potential stability and resilience in repeated use. Further optimization of reduction conditions and surface cleaning strategies could help mitigate deactivation, enhancing the catalyst's longevity and performance.

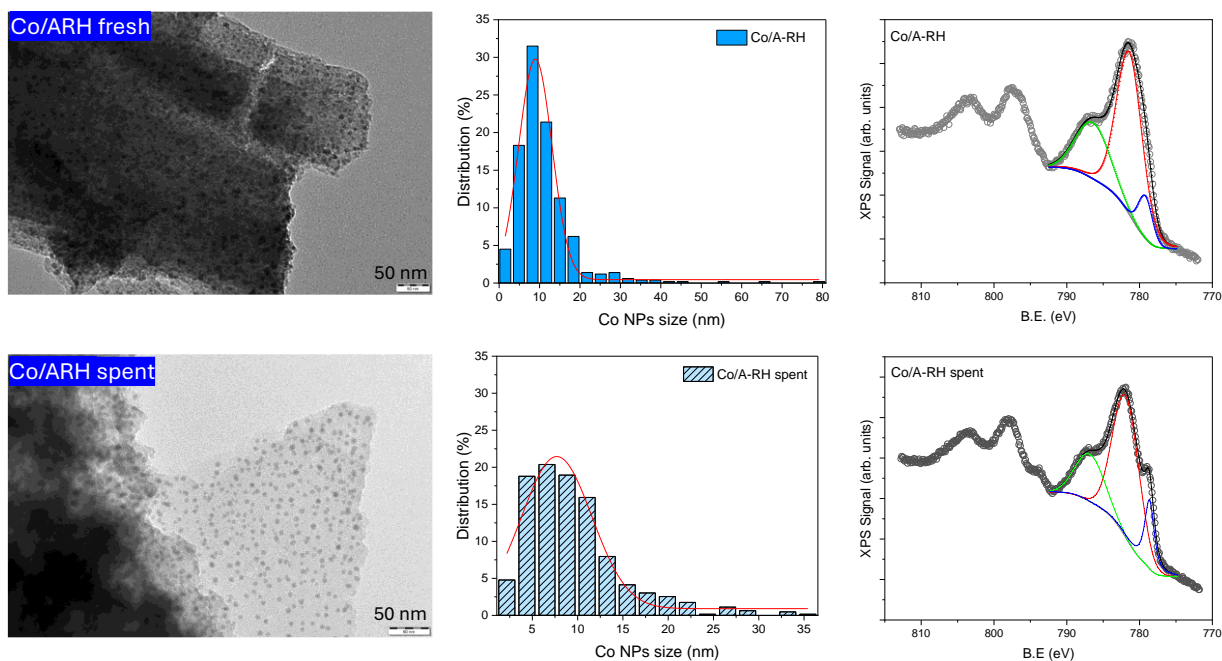


Figure 3.3.3.18. TEM microscopy, CO NPs size distribution, and Co2p XPS spectra of Co/A-RH fresh, and Co/A-RH spent, after 3 reaction cycles.

Table 3.3.3.7. Characterizations of fresh and spent Co/A-RH: CHNS, ICP, TEM and XPS.

Sample	C (%)	H (%)	N (%)	S (%)	Co wt. %	D _{TEM} (nm)	Co 2p (eV) (atomic %)	
							Co ⁰	Co ²⁺
Co/A-RH fresh	31.99	0.98	0.39	0.06	12	9.8	779.21 (12.1)	781.40 (87.9)
Co/A-RH spent	34.99	0.95	0.39	0.06	12	7.7	778.64 (19.4)	781.89 (80.6)

Effect of Furfural addition

Furfural (FF) is one of the most abundant furanic compounds found in lignocellulosic-derived bio-oil, origination from the decomposition of hemicellulose⁹³. It is recognized as one of the “Top 10” bio-derived platform molecules⁹⁴, and has been extensively studied for upgrading through both by oxidation and hydrogenation processes, to obtain valuable products for various industrial applications^{95–97}. However, due to its carbonyl group, it tends to destabilize bio-oil by undergoing polymerization and forming humins. Therefore, it must be processed to ensure the stability of the mixture. The possibility of co-processing IE and FF was therefore investigated. The reaction was conducted at the optimized conditions for IE HDO (275 °C, 30 bar H₂, 50 mg Co/A-RH, IE 2 mg/mL, 900 rpm, 240 min) and with different IE:FF ratios (1:0, 1:1, 1:2). The effect of FF addition on IE reaction rate and product distribution is reported in Figure 3.3.3.19.

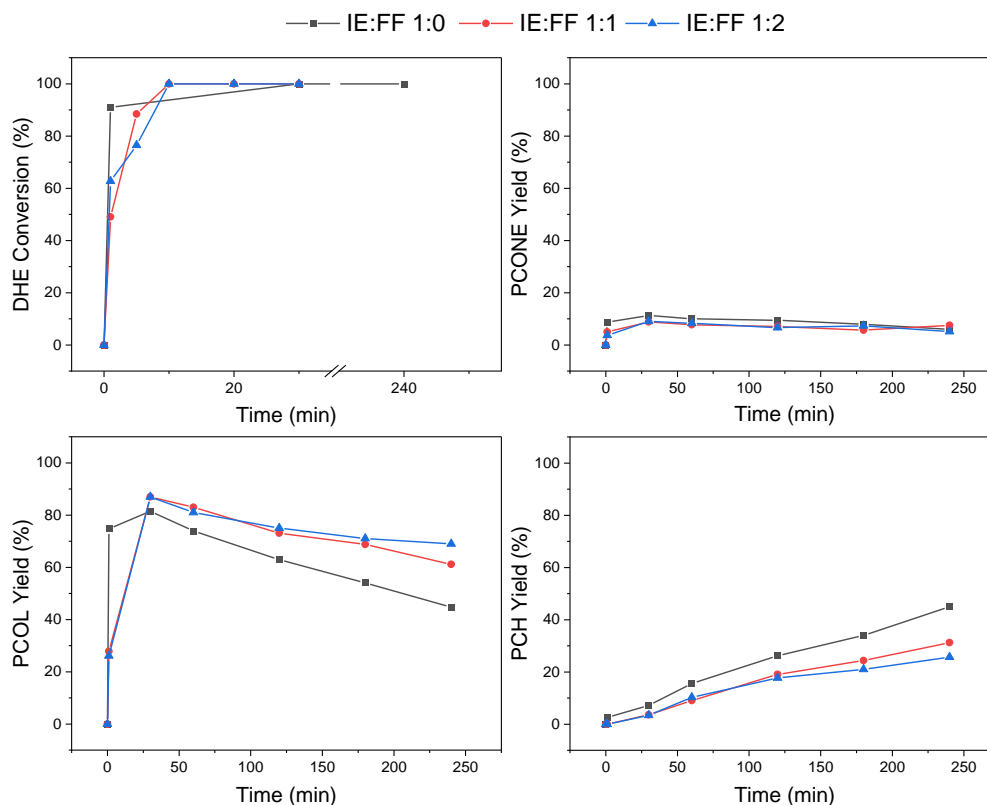


Figure 3.3.3.19. Effect of FF addition of IE HDO. Reaction conditions: 275 °C, 30 bar H₂, 50 mg Co/A-RH, IE 2 mg/mL, 900 rpm, 240 min. DHE: dihydroeugenol, PCONE: propylcyclohexanone, PCOL: propylcyclohexanol, PCH: propylcyclohexane.

The presence of FF caused a slight reduction in the reaction rate and a corresponding decrease in the final yield of PCH. Remarkably, the differences between IE ratios of 1:1 and 1:2 were less significant, with the PCH yield dropping from 45% without FF, to 31% at a 1:1 ratio, and 25% at a 1:2 ratio. Despite this, the reaction did not exhibit a sharp decline, and in all cases, complete conversion of dihydroeugenol (DHE) was achieved within a maximum of 10 minutes. This result stands out positively compared to existing literature on co-processing phenolic compounds in the presence of furfural or other bio-oil components, such as acetic acid or glycerol. For instance, Li *et al.* demonstrated that the addition of furfural during the hydrodeoxygenation (HDO) of eugenol (EU) over a Ni/Al-SBA-HZSM-5 catalyst significantly reduced catalytic activity. When furfural concentration increased from 0 to 3%, PCH selectivity dropped drastically from 98% to 17%, with furfural being converted into tetrahydrofurfuryl alcohol and methyl tetrahydrofuran⁹⁸. Similarly, Wang *et al.* found that in a model bio-oil mixture (acetic acid, phenol, furfural, 4-ethylguaiacol, and water) using a Ni₂P/HZSM-5 catalyst, smaller molecules like acetic acid and furfural outcompeted phenol for active sites, impeding its conversion²². Other studies corroborate this competitive inhibition effect, such as Chen *et al.*, who reported a drop in guaiacol conversion from 98% to 62% in the presence of acetic acid over Ru/C⁹⁹, and Dwiatmoko *et al.* who observed a more pronounced decrease from 98% to 28% with furfural using

Ru/AC¹⁰⁰. Density functional theory (DFT) studies indicate that the higher adsorption energies of furfural and its derivatives on the Ru surface are responsible for their preferential adsorption. Vinu *et al.* also noted a dramatic decline in PCH yield from 35.5% to 1.2% when co-processing isoeugenol with acetic acid and furfural over a Pt/C + HZSM-5 catalyst mixture²¹. Smaller, more reactive molecules like furfural and acetic pose a significant barrier to the efficient HDO of phenolic compounds in bio-oil mixtures, however, our results demonstrate a notably better performance, as we achieved complete conversion of DHE within 10 minutes, even in the presence of furfural, making this a highly favorable outcome compared to previously reported findings.

The conversion of FF and product distribution in the presence of IE was also evaluated, and reported in Figure 3.3.3.20.

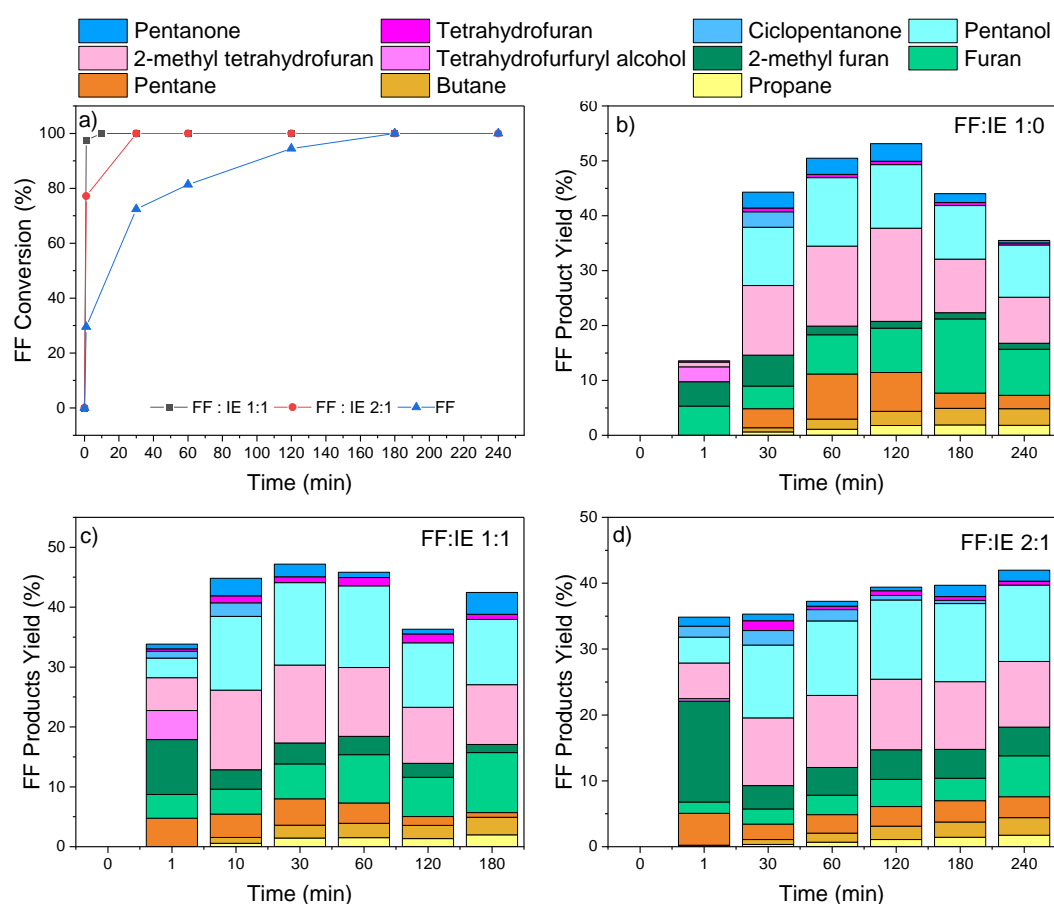


Figure 3.3.3.20. Influence of IE on Furfural conversion (a) and products yield (b,c,d). Reaction conditions: 275 °C, 30 bar H₂, 50 mg Co/A-RH, 900 rpm, 240 min.

As shown in Figure 3.3.3.20, the reaction rate of furfural (FF) significantly increased with the addition of isoeugenol (IE) to the reaction mixture. Complete FF conversion was achieved within 1 minute in the presence of IE at a 1:1 ratio, compared to nearly 200 minutes required for total FF conversion in absence of IE. While further addition of IE slightly decreased the reaction rate, it still led to complete conversion in 30 minutes.

This synergistic effect has been observed in literature. Schiesser and colleagues²⁰ reported a similar enhancement in the FF reaction rate when co-processed with phenolic compounds like guaiacol or anisole. Furfural resulted in being absorbed more efficiently on the catalyst surface in presence of guaiacol than alone. Since this effect was pronounced with guaiacol, and not with anisole, the explanation, supported also by DFT study, was found in the hydrogen atom of the phenolic hydroxyl group could act as a hydrogen bond donor for the carbonyl group in FF, stabilizing the reactant and reducing coke formation. The same effect could plausibly occur in the presence of IE or its derivatives like DHE and PCOL, having a hydroxyl group capable to form H bonding.

Escalona *et al.* furthermore noticed that the presence of guaiacol slightly generates a change in the selectivity of furfural products. This was also attributed to its hydroxyl group, as such a change was not observed with anisole. Indeed, also in our case a slight difference in product distribution was observed (Figures 3.3.3.20 b,c,d). Notably, the presence of IE increased the total yield of the products that could be detected in the liquid phase, that passed from 35 % to 42 % after 240 minutes. However, product yields resulted quite low, likely due to the formation of substantial amounts of gas products from furfural hydrocracking, or possibly solid residues due to the polymerization of furfural. The formation of light compounds was evidenced by the detection of light hydrocarbons, such as pentane, butane, and propane, also in the liquid mixture which were partially solubilized in the reaction mixture. A qualitative analysis of the gas phase was carried out with a MicroGC and it evidenced the presence of hydrocarbons, as well as CO and CH₄, however due to the high concentration of H₂ in the gas phase, a quantitative analysis could not be performed.

Although FF hydrodeoxygenation (HDO) did not show selectivity towards a single target product under the reaction conditions, as shown in Figure 3.3.3.20, FF could be converted in less oxygenated compounds, with the main products in the liquid phase being pentanol (10-11 % Figure 3.3.3.20c,d respectively), methyl tetrahydrofuran (ca. 9 %), and furan (6-10 % Figure 3.3.3.20c,d respectively), in line with the results reported in literature regarding the co-processing of FF and phenolics^{21,101}. These products can be employed as additives for fuels or even as fuels themselves, due to their favorable properties such as higher energy density and compatibility with existing fuel infrastructures.

Although these were only preliminary and exploratory results regarding the feasibility of co-processing phenolics like IE with other bio-oil model compounds such as FF, the findings were positive and open the door to further investigation. Future studies can focus on optimizing the carbon balance of FF transformation and increasing selectivity under the best conditions.

3.3.4. Conclusions

In this work, the use of biochar-based catalysts was investigated for the hydrodeoxygenation (HDO) of bio-oil model compounds. In the context of a circular economy, biomass-derived waste was utilized and transformed into higher-value products. Through pyrolysis, the solid fraction, biochar, was activated and used as a support for the preparation of heterogeneous catalysts. Meanwhile, compounds from the liquid fraction, bio-oil, were converted into potential biofuels by leveraging the catalytic activity of biochar itself, thus creating a closed and virtuous cycle of waste valorization.

Cobalt was selected as the active phase due to its affordability and status as a non-noble metal, which enhances the economic viability of the process. Two different types of biomass (rice husk and leather shaving waste) were chosen for the preparation of activated biochars. A third activated biochar was obtained through the co-pyrolysis of these two biomasses. The catalytic activity was evaluated for the HDO of isoeugenol (IE). Among the biochar-based catalysts, Co/A-RH (rice husk biochar) demonstrated the best performance. Co/A-RH was able to fully convert IE within a few minutes, achieving a 55% yield of propylcyclohexane after 240 minutes at 300°C and 30 bar H₂, compared to a commercial carbon-derived catalyst that achieved a 75% yield under the same conditions.

The superior performance of these two catalysts was attributed to the strong metal-support interaction, which not only facilitated good anchoring and dispersion but also prevented the complete reduction of the cobalt phase under reduction conditions. This resulted in a synergy between the Co⁰ and Co²⁺ phases, where Co⁰ acted as a hydrogenating active site and Co²⁺ as a Lewis acid site, promoting oxygen-cleavage. The balance between acid sites and metallic sites proved crucial for achieving high yields of the desired products while avoiding acid-catalyzed side reactions like hydrocracking. Co/A-RH, with more pronounced acid sites, achieved a carbon balance of 57.5% at 300°C and 30 bar H₂, but a reduction in reaction temperature by just 25°C drastically improved the carbon balance to 96.5% by suppressing cracking reactions.

Co/A-RH showed stability in recycling, with no observed metal leaching or sintering. A slight reduction in reaction rate was attributed to an increase of Co in the reduced state, compared to the fresh catalyst, and by some organic residue covering the active sites. From the screening of various reaction parameters (temperature, pressure, IE concentration), a reaction network was proposed, and kinetic modeling allowed for the calculation of rate constants and activation energy for each reaction step. Additionally, Co/A-RH exhibited activity in the co-processing of IE with varying amounts of furfural, suggesting further potential for this catalyst in upgrading more complex mixtures or even real bio-oils, and envisioning new opportunities for future investigations.

3.3.5 Appendix

Table 3.5.1. XPS results of C 1s, O 1s, and Co 2p signals of the biochar-based catalysts.

	Co/A-LS		Co/A-RL		Co/A-RH	
	BE (eV)	AC (at. %)	BE (eV)	AC (at. %)	BE (eV)	AC (at. %)
C 1s	284.80	86.2	284.80	86.0	284.80	88
	289.81	13.8	289.90	14.0	289.26	12.0
O 1s	532.56	91.9	533.83	91.1	533.88	95.8
	529.72	8.1	531.00	8.9	530.85	4.2
Co 2p	781.01	96.8	781.13	93.2	781.40	87.9
	778,50	3.2	778.84	6.8	779.21	12.1

Kinetic modelling

The following rate equations were proposed:

$$r_1 = k_1 \cdot c_A \cdot p_{H_2} / D \quad (x)$$

$$r_2 = k_2 \cdot c_A \cdot p_{H_2} / D \quad (x)$$

$$r_3 = k_3 \cdot c_A \cdot p_{H_2} / D$$

$$r_4 = k_4 \cdot c_A \cdot p_{H_2} / D$$

$$r_5 = k_5 \cdot c_A \cdot p_{H_2} / D$$

$$r_6 = k_6 \cdot c_A \cdot p_{H_2} / D$$

$$r_7 = k_7 \cdot c_A \cdot p_{H_2} / D$$

and $D=1$.

The mass balances for each compound are given as:

$$dc_A/dt = -(r_1 + r_8) \cdot \rho_B$$

$$dc_B/dt = (r_1 - r_2) \cdot \rho_B$$

$$dc_C/dt = (r_2 - r_3 - r_7) \cdot \rho_B$$

$$dc_D/dt = (r_3 - r_6) \cdot \rho_B$$

$$dc_E/dt = (r_4 + r_6 - r_5) \cdot \rho_B$$

$$dc_F/dt = r_5 \cdot \rho_B$$

$$dc_U/dt = r_7 \cdot \rho_B$$

Kinetic modelling was performed using MODEST software¹⁰² by solving the differential equations 3.3.5.1 and 3.3.5.2 with backward difference method. For parameter estimation simplex and Levenberg-Marquardt methods were applied. The objective function θ and the degree of explanations were defined as:

$$\theta = \sum_i^n (y_i - \hat{y}_i)^2 \tag{Eq. 3.3.5.1}$$

$$R^2 = 1 - \frac{(y_i - \hat{y}_i)^2}{(y_i - \bar{y}_i)^2} \tag{Eq. 3.3.5.2}$$

In which \hat{y}_i denotes the estimated value and \bar{y}_i the mean value of observations.

Table 3.3.5.2. Estimated parameters from the kinetic modelling

Parameter	Estimated	Standard error (%)	Standard error
k₁	58.5 too large	43.4	2.3
k₂	0.09	8.3	12.1
k₃	2.15	91.4	1.1
k₄	15.0	90.6	1.1
k₅	0.81·10 ⁻⁴	6.0	16.8
k₆	0.44·10 ⁻⁴	48.3	2.1
k₇	11.5	40.8	2.5
	kJ/mol		
E_{A1}	59.2	179.3	0.6
E_{A2}	169	1.5	65.7
E_{A3}	84.0	38.4	2.6
E_{A4}	30.6	112.1	0.9
E_{A5}	151	5.51	18.2
E_{A6}	85.6	69.6	1.4
E_{A7}	69.6	153	0.7

The correlation matrix of the parameters is the following:

k1 1.000

k2 0.133 1.000

k3 0.019 0.099 1.000

k4 -0.008 0.086 0.986 1.000

k5 0.059 -0.033 -0.154 -0.123 1.000

k6 0.115 0.068 0.344 0.312 -0.313 1.000

k8 0.977 0.160 -0.013 -0.021 0.048 0.070 1.000

Ea1 -0.027 -0.004 -0.035 -0.027 0.005 -0.044 -0.009 1.000

Ea2 0.145 0.934 0.073 0.069 -0.027 0.080 0.179 -0.023 1.000

3. Valorization of biomass via pyrolysis - 3.3 Hydrodeoxygenation of bio-oil model compounds using biochar-based catalysts

Ea3 0.714 0.068 0.356 0.361 -0.124 0.405 0.740 -0.237 0.093 1.000

Ea4 0.686 0.081 0.398 0.395 -0.141 0.391 0.702 -0.212 0.087 0.983 1.000

Ea5 -0.490 -0.046 -0.020 -0.017 -0.577 -0.110 -0.475 0.065 -0.063 -0.353 -0.318 1.000

Ea6 0.361 -0.034 -0.244 -0.263 0.153 -0.408 0.396 -0.234 -0.022 -0.049 -0.092 -0.280 1.000

Ea8 0.112 0.043 -0.021 0.005 -0.002 -0.110 0.182 0.900 0.029 0.010 0.037 -0.001 -0.131 1.000

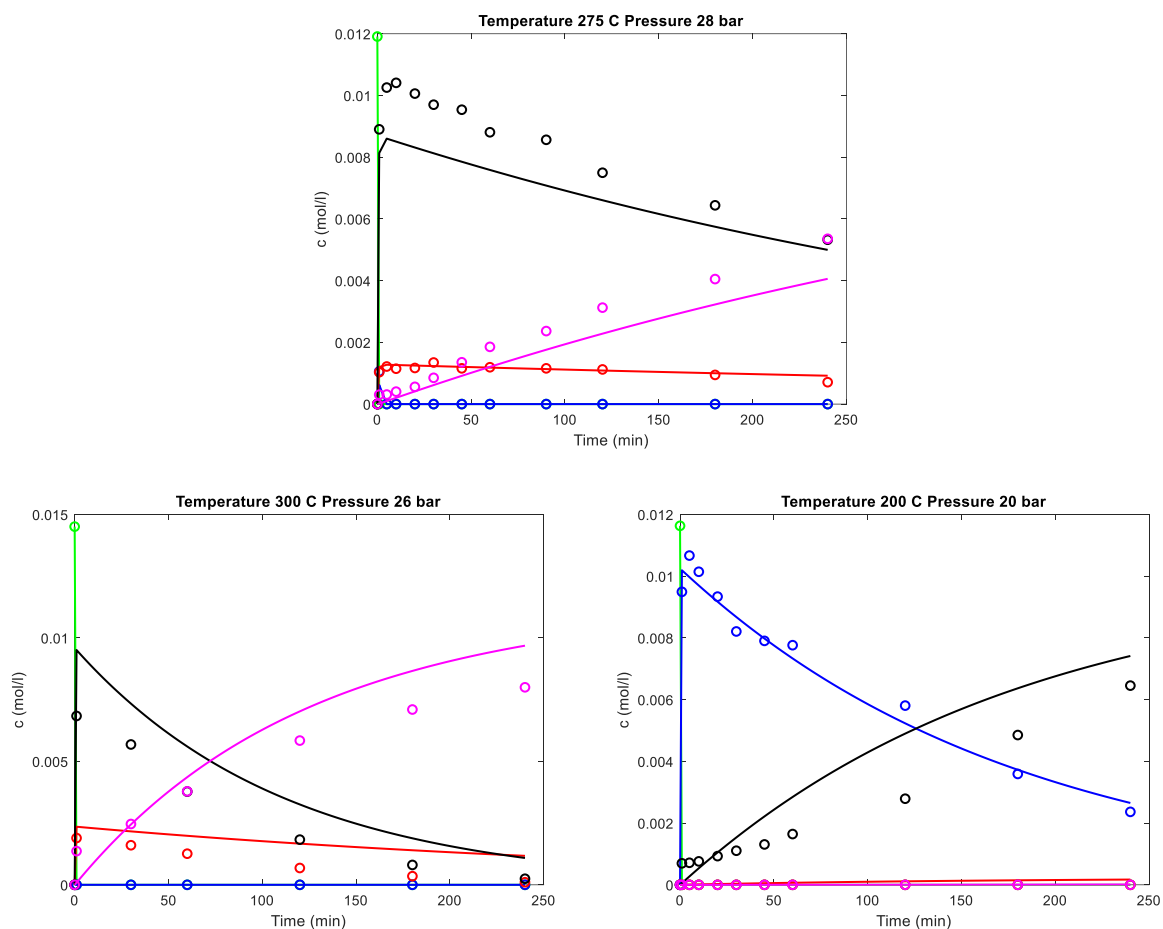


Figure 3.3.5.1 Experimental kinetic results and model fit for IE transformation at different reaction conditions. IE (green), DHE (blue), PCOL (black), PCONE (red), PCH (pink).

Table 3.3.5.3 Current metals price (October 2024). Source: <https://www.dailymetalprice.com/metalprices.php>¹⁰³

Metal	Price (\$/kg)
Cu	9.5
Co	24.3
Ir	149500
Fe	0.1
Mo	67.4
Ni	16.1

3. Valorization of biomass via pyrolysis - 3.3 Hydrodeoxygenation of bio-oil model compounds using biochar-based catalysts

Pd	37809
Pt	32761
Rh	151912
Ru	15593

3.3.3 References

- (1) Cheng, H.; Shapter, J. G.; Li, Y.; Gao, G. Recent Progress of Advanced Anode Materials of Lithium-Ion Batteries. *Journal of Energy Chemistry* **2021**, *57*, 451–468. <https://doi.org/10.1016/j.jechem.2020.08.056>.
- (2) Schmuch, R.; Wagner, R.; Hörpel, G.; Placke, T.; Winter, M. Performance and Cost of Materials for Lithium-Based Rechargeable Automotive Batteries. *Nature Energy* **2018**, *3* (4), 267–278. <https://doi.org/10.1038/s41560-018-0107-2>.
- (3) Rabaia, M. K. H.; Abdelkareem, M. A.; Sayed, E. T.; Elsaid, K.; Chae, K.-J.; Wilberforce, T.; Olabi, A. G. Environmental Impacts of Solar Energy Systems: A Review. *Science of The Total Environment* **2021**, *754*, 141989. <https://doi.org/10.1016/j.scitotenv.2020.141989>.
- (4) Su-ungkavatin, P.; Tiruta-Barna, L.; Hamelin, L. Biofuels, Electrofuels, Electric or Hydrogen?: A Review of Current and Emerging Sustainable Aviation Systems. *Progress in Energy and Combustion Science* **2023**, *96*, 101073. <https://doi.org/10.1016/j.pecs.2023.101073>.
- (5) Sahoo, S.; Zhao, X.; Kyprianidis, K. A Review of Concepts, Benefits, and Challenges for Future Electrical Propulsion-Based Aircraft. *Aerospace* **2020**, *7* (4), 44. <https://doi.org/10.3390/aerospace7040044>.
- (6) Cabrera, E.; de Sousa, J. M. M. Use of Sustainable Fuels in Aviation—A Review. *Energies* **2022**, *15* (7), 2440. <https://doi.org/10.3390/en15072440>.
- (7) Li, P.; Pan, H.; Wan, K.; Zhou, S.; Zhang, Z.; Hong, D.; Zhang, Y. Jet Fuel-Range Hydrocarbon Production from Catalytic Pyrolysis of Low-Density Polyethylene by Metal-Loaded Activated Carbon. *Sustainable Energy Fuels* **2022**, *6* (9), 2289–2305. <https://doi.org/10.1039/D2SE00129B>.
- (8) Mancio, A. A.; da Mota, S. A. P.; Ferreira, C. C.; Carvalho, T. U. S.; Neto, O. S.; Zamian, J. R.; Araújo, M. E.; Borges, L. E. P.; Machado, N. T. Separation and Characterization of Biofuels in the Jet Fuel and Diesel Fuel Ranges by Fractional Distillation of Organic Liquid Products. *Fuel* **2018**, *215*, 212–225. <https://doi.org/10.1016/j.fuel.2017.11.029>.
- (9) Schmidt, P.; Batteiger, V.; Roth, A.; Weindorf, W.; Raksha, T. Power-to-Liquids as Renewable Fuel Option for Aviation: A Review. *Chemie Ingenieur Technik* **2018**, *90* (1–2), 127–140. <https://doi.org/10.1002/cite.201700129>.
- (10) Doliente, S. S.; Narayan, A.; Tapia, J. F. D.; Samsatli, N. J.; Zhao, Y.; Samsatli, S. Bio-Aviation Fuel: A Comprehensive Review and Analysis of the Supply Chain Components. *Frontiers in Energy Research* **2020**, *8*. <https://doi.org/10.3389/fenrg.2020.00110>.
- (11) Gea, S.; Hutapea, Y. A.; Piliang, A. F. R.; Pulungan, A. N.; Rahayu, R.; Layla, J.; Tikoalu, A. D.; Wijaya, K.; Saputri, W. D. A Comprehensive Review of Experimental Parameters in Bio-Oil Upgrading from Pyrolysis of Biomass to Biofuel Through Catalytic Hydrodeoxygenation. *Bioenergy Research* **2023**, *16* (1), 325–347. <https://doi.org/10.1007/s12155-022-10438-w>.
- (12) Prabhudesai, V. S.; Gurrata, L.; Vinu, R. Catalytic Hydrodeoxygenation of Lignin-Derived Oxygenates: Catalysis, Mechanism, and Effect of Process Conditions. *Energy Fuels* **2022**, *36* (3), 1155–1188. <https://doi.org/10.1021/acs.energyfuels.1c02640>.
- (13) Liu, X.; Xu, L.; Xu, G.; Jia, W.; Ma, Y.; Zhang, Y. Selective Hydrodeoxygenation of Lignin-Derived Phenols to Cyclohexanols or Cyclohexanes over Magnetic CoNx@NC Catalysts under Mild Conditions. *ACS Catalysis* **2016**, *6* (11), 7611–7620. <https://doi.org/10.1021/acscatal.6b01785>.
- (14) Yang, H.; Chen, H.; Zhou, W.; Fan, H.; Chen, C.; Sun, Y.; Zhang, J.; Wang, S.; Guo, T.; Fu, J. Construction of N, O Co-Doped Carbon Anchored with Co Nanoparticles as Efficient Catalyst for Furfural Hydrodeoxygenation in Ethanol. *Journal of Energy Chemistry* **2023**, *78*, 195–202. <https://doi.org/10.1016/j.jechem.2022.11.037>.
- (15) Wang, C.; Luo, J.; Liao, V.; Lee, J. D.; Onn, T. M.; Murray, C. B.; Gorte, R. J. A Comparison of Furfural Hydrodeoxygenation over Pt-Co and Ni-Fe Catalysts at High and Low H₂ Pressures. *Catalysis Today* **2018**, *302*, 73–79. <https://doi.org/10.1016/j.cattod.2017.06.042>.

3. Valorization of biomass via pyrolysis - 3.3 Hydrodeoxygenation of bio-oil model compounds using biochar-based catalysts

- (16) Fang, W.; Riisager, A. Recent Advances in Heterogeneous Catalytic Transfer Hydrogenation/Hydrogenolysis for Valorization of Biomass-Derived Furanic Compounds. *Green Chemistry* **2021**, *23* (2), 670–688. <https://doi.org/10.1039/D0GC03931D>.
- (17) Lachos-Perez, D.; Martins-Vieira, J. C.; Missau, J.; Anshu, K.; Siakpebru, O. K.; Thengane, S. K.; Morais, A. R. C.; Tanabe, E. H.; Bertuol, D. A. Review on Biomass Pyrolysis with a Focus on Bio-Oil Upgrading Techniques. *Analytica* **2023**, *4* (2), 182–205. <https://doi.org/10.3390/analytica4020015>.
- (18) Bohre, A.; Dutta, S.; Saha, B.; Abu-Omar, M. M. Upgrading Furfurals to Drop-in Biofuels: An Overview. *ACS Sustainable Chemistry & Engineering Journal* **2015**, *3* (7), 1263–1277. <https://doi.org/10.1021/acssuschemeng.5b00271>.
- (19) Banerjee, A.; Mushrif, S. H. Investigating Reaction Mechanisms for Furfural Hydrodeoxygenation on Ni and the Effect of Boron Doping on the Activity and Selectivity of the Catalyst. *The Journal of Physical Chemistry C* **2018**, *122* (32), 18383–18394. <https://doi.org/10.1021/acs.jpcc.8b01301>.
- (20) Schiesser, E. C.; Blanco, E.; Dongil, A. B.; Zarate, X.; Saavedra-Torres, M.; Schott, E.; Canales, R. I.; Escalona, N. Insights into Hydrodeoxygenation of Furfural and Guaiacol Mixture: Experimental and Theoretical Studies. *The Journal of Physical Chemistry C* **2021**, *125* (14), 7647–7657. <https://doi.org/10.1021/acs.jpcc.0c11415>.
- (21) Prabhudesai, V. S.; Vinu, R. Hydrodeoxygenation of Biomass-Derived Oxygenate Mixtures Over Pt/C and HZSM-5 Mixed Catalysts. *Topics in Catalysis* **2023**, *66* (5), 405–419. <https://doi.org/10.1007/s11244-023-01782-y>.
- (22) Wang, J.; Abdelouahed, L.; Xu, J.; Brodu, N.; Taouk, B. Catalytic Hydrodeoxygenation of Model Bio-Oils Using HZSM-5 and Ni₂P/HZM-5 Catalysts: Comprehension of Interaction. *Chemical Engineering & Technology* **2021**, *44* (11), 2126–2138. <https://doi.org/10.1002/ceat.202100239>.
- (23) Sulman, A.; Mäki-Arvela, P.; Bomont, L.; Alda-Onggar, M.; Fedorov, V.; Russo, V.; Eränen, K.; Peurla, M.; Akhmetzyanova, U.; Skuhrovcová, L.; Tišler, Z.; Grénman, H.; Wärnå, J.; Murzin, D. Yu. Kinetic and Thermodynamic Analysis of Guaiacol Hydrodeoxygenation. *Catalysis Letters* **2019**, *149* (9), 2453–2467. <https://doi.org/10.1007/s10562-019-02856-x>.
- (24) Verma, A. M.; Kishore, N. Gas Phase Conversion of Eugenol into Various Hydrocarbons and Platform Chemicals. *RSC Adv.* **2017**, *7* (5), 2527–2543. <https://doi.org/10.1039/C6RA26357G>.
- (25) Xing, J.; Song, L.; Zhang, C.; Zhou, M.; Yue, L.; Li, X. Effect of Acidity and Porosity of Alkali-Treated ZSM-5 Zeolite on Eugenol Hydrodeoxygenation. *Catalysis Today* **2015**, *258*, 90–95. <https://doi.org/10.1016/j.cattod.2015.04.014>.
- (26) Bjelić, A.; Grilc, M.; Likozar, B. Bifunctional Metallic-Acidic Mechanisms of Hydrodeoxygenation of Eugenol as Lignin Model Compound over Supported Cu, Ni, Pd, Pt, Rh and Ru Catalyst Materials. *Chemical Engineering Journal* **2020**, *394*, 124914. <https://doi.org/10.1016/j.cej.2020.124914>.
- (27) Chen, M.-Y.; Huang, Y.-B.; Pang, H.; Liu, X.-X.; Fu, Y. Hydrodeoxygenation of Lignin-Derived Phenols into Alkanes over Carbon Nanotube Supported Ru Catalysts in Biphasic Systems. *Green Chemistry* **2015**, *17* (3), 1710–1717. <https://doi.org/10.1039/C4GC01992J>.
- (28) Diao, X.; Ji, N.; Zheng, M.; Liu, Q.; Song, C.; Huang, Y.; Zhang, Q.; Alemayehu, A.; Zhang, L.; Liang, C. MgFe Hydrotalcites-Derived Layered Structure Iron Molybdenum Sulfide Catalysts for Eugenol Hydrodeoxygenation to Produce Phenolic Chemicals. *Journal of Energy Chemistry* **2018**, *27* (2), 600–610. <https://doi.org/10.1016/j.jechem.2017.07.008>.
- (29) Tian, Y.; Chen, B.; Yu, Z.; Huang, R.; Yan, G.; Li, Z.; Sun, Y.; Yang, S.; Tang, X.; Lin, L.; Zeng, X. Efficient Catalytic Hydrogenation of Furfural over Cobalt-Based Catalysts with Adjustable Acidity. *Chemical Engineering Science* **2023**, *270*, 118527. <https://doi.org/10.1016/j.ces.2023.118527>.
- (30) Qi, J.; Sun, X.; Tang, S.-F.; Sun, Y.; Xu, C.; Li, X.; Li, X. Integrated Study on the Role of Solvent, Catalyst and Reactant in the Hydrodeoxygenation of Eugenol over Nickel-Based Catalysts. *Applied Catalysis A: General* **2017**, *535*, 24–31. <https://doi.org/10.1016/j.apcata.2017.01.020>.
- (31) Vajglová, Z.; Gauli, B.; Mäki-Arvela, P.; Kumar, N.; Eränen, K.; Wärnå, J.; Lassfolk, R.; Simakova, I. L.; Prosvirin, I. P.; Peurla, M.; Lindén, J. K. M.; Huhtinen, H.; Paturi, P.; Doronkin, D. E.; Murzin, D. Yu. Interactions between Iron and Nickel in Fe-

3. Valorization of biomass via pyrolysis - 3.3 Hydrodeoxygenation of bio-oil model compounds using biochar-based catalysts

Ni Nanoparticles on Y Zeolite for Co-Processing of Fossil Feedstock with Lignin-Derived Isoeugenol. *ACS Applied Nano Materials* **2023**, 6 (12), 10064–10077. <https://doi.org/10.1021/acsnm.3c00620>.

(32) Vajglová, Z.; Gauli, B.; Mäki-Arvela, P.; Simakova, I. L.; Kumar, N.; Eränen, K.; Tirri, T.; Lassfolk, R.; Peurla, M.; Doronkin, D. E.; Murzin, D. Yu. Co-Processing of Fossil Feedstock with Lignin-Derived Model Compound Isoeugenol over Fe-Ni/H-Y-5.1 Catalysts. *Journal of Catalysis* **2023**, 421, 101–116. <https://doi.org/10.1016/j.jcat.2023.03.016>.

(33) Mortensen, P. M.; Grunwaldt, J.-D.; Jensen, P. A.; Jensen, A. D. Screening of Catalysts for Hydrodeoxygenation of Phenol as a Model Compound for Bio-Oil. *ACS Catalysis* **2013**, 3 (8), 1774–1785. <https://doi.org/10.1021/cs400266e>.

(34) Auersvald, M.; Shumeiko, B.; Staš, M.; Kubička, D.; Chudoba, J.; Šimáček, P. Quantitative Study of Straw Bio-Oil Hydrodeoxygenation over a Sulfided NiMo Catalyst. *ACS Sustainable Chemistry & Engineering Journal* **2019**, 7 (7), 7080–7093. <https://doi.org/10.1021/acssuschemeng.8b06860>.

(35) Nikulshin, P. A.; Salnikov, V. A.; Varakin, A. N.; Kogan, V. M. The Use of CoMoS Catalysts Supported on Carbon-Coated Alumina for Hydrodeoxygenation of Guaiacol and Oleic Acid. *Catalysis Today* **2016**, 271, 45–55. <https://doi.org/10.1016/j.cattod.2015.07.032>.

(36) Li, S.; Liu, B.; Truong, J.; Luo, Z.; C. Ford, P.; M. Abu-Omar, M. One-Pot Hydrodeoxygenation (HDO) of Lignin Monomers to C9 Hydrocarbons Co-Catalysed by Ru/C and Nb 2 O 5. *Green Chemistry* **2020**, 22 (21), 7406–7416. <https://doi.org/10.1039/D0GC01692F>.

(37) Song, W.; Liu, Y.; Baráth, E.; Zhao, C.; Lercher, J. A. Synergistic Effects of Ni and Acid Sites for Hydrogenation and C–O Bond Cleavage of Substituted Phenols. *Green Chemistry* **2015**, 17 (2), 1204–1218. <https://doi.org/10.1039/C4GC01798F>.

(38) Prabhudesai, V. S.; Yerrayya, A.; Gurralla, L.; Castaño, P.; Vinu, R. Hydrodeoxygenation of Mixtures of Biomass-Derived Model Compound Oxygenates over Pt/HY Catalysts. *Chemical Engineering Science* **2024**, 288, 119800. <https://doi.org/10.1016/j.ces.2024.119800>.

(39) Simakova, I.; Simakova, O.; Mäki-Arvela, P.; Simakov, A.; Estrada, M.; Murzin, D. Yu. Deoxygenation of Palmitic and Stearic Acid over Supported Pd Catalysts: Effect of Metal Dispersion. *Applied Catalysis A: General* **2009**, 355 (1), 100–108. <https://doi.org/10.1016/j.apcata.2008.12.001>.

(40) Luo, Z.; Zheng, Z.; Wang, Y.; Sun, G.; Jiang, H.; Zhao, C. Hydrothermally Stable Ru/HZSM-5-Catalyzed Selective Hydrogenolysis of Lignin-Derived Substituted Phenols to Bio-Arenes in Water. *Green Chemistry* **2016**, 18 (21), 5845–5858. <https://doi.org/10.1039/C6GC01971D>.

(41) Alda-Onggar, M.; Mäki-Arvela, P.; Eränen, K.; Aho, A.; Hemming, J.; Paturi, P.; Peurla, M.; Lindblad, M.; Simakova, I. L.; Murzin, D. Yu. Hydrodeoxygenation of Isoeugenol over Alumina-Supported Ir, Pt, and Re Catalysts. *ACS Sustainable Chemistry & Engineering Journal* **2018**, 6 (12), 16205–16218. <https://doi.org/10.1021/acssuschemeng.8b03035>.

(42) Sirous-Rezaei, P.; Jae, J.; Cho, K.; Ko, C. H.; Jung, S.-C.; Park, Y.-K. Insight into the Effect of Metal and Support for Mild Hydrodeoxygenation of Lignin-Derived Phenolics to BTX Aromatics. *Chemical Engineering Journal* **2019**, 377, 120121. <https://doi.org/10.1016/j.cej.2018.10.058>.

(43) Martínez-Klimov, M. E.; Mäki-Arvela, P.; Vajglova, Z.; Alda-Onggar, M.; Angervo, I.; Kumar, N.; Eränen, K.; Peurla, M.; Calimli, M. H.; Muller, J.; Shchukarev, A.; Simakova, I. L.; Murzin, D. Yu. Hydrodeoxygenation of Isoeugenol over Carbon-Supported Pt and Pt–Re Catalysts for Production of Renewable Jet Fuel. *Energy Fuels* **2021**, 35 (21), 17755–17768. <https://doi.org/10.1021/acs.energyfuels.1c02656>.

(44) Zhao, M.; Hu, J.; Wu, S.; Yang, L.; An, X.; Yuan, P.; Lu, P. Hydrodeoxygenation of Lignin-Derived Phenolics over Facile Prepared Bimetallic RuCoNx/NC. *Fuel* **2022**, 308, 121979. <https://doi.org/10.1016/j.fuel.2021.121979>.

(45) Li, X.; Chen, L.; Chen, G.; Zhang, J.; Liu, J. The Relationship between Acidity, Dispersion of Nickel, and Performance of Ni/Al-SBA-15 Catalyst on Eugenol Hydrodeoxygenation. *Renewable Energy* **2020**, 149, 609–616. <https://doi.org/10.1016/j.renene.2019.12.094>.

3. Valorization of biomass via pyrolysis - 3.3 Hydrodeoxygenation of bio-oil model compounds using biochar-based catalysts

- (46) Yang, H.; Nie, R.; Xia, W.; Yu, X.; Jin, D.; Lu, X.; Zhou, D.; Xia, Q. Co Embedded within Biomass-Derived Mesoporous N-Doped Carbon as an Acid-Resistant and Chemoselective Catalyst for Transfer Hydrodeoxygenation of Biomass with Formic Acid. *Green Chem.* **2017**, *19* (23), 5714–5722. <https://doi.org/10.1039/C7GC02648J>.
- (47) Wen, C.; Lu, M.; Zhao, M.; Zhu, J.; Li, M.; Shang, J.; Shan, Y.; Song, C. Co-Based Catalysts Supported on Ceria with Different Shape Structures for Hydrodeoxygenation of Guaiacol. *Energy Fuels* **2022**, *36* (24), 14986–14993. <https://doi.org/10.1021/acs.energyfuels.2c02913>.
- (48) Wang, X.; Zhang, Z.; Yan, Z.; Li, Q.; Zhang, C.; Liang, X. Synergistic Contribution of Metal–Acid Sites in Selective Hydrodeoxygenation of Biomass Derivatives over Cu/CoO_x Catalysts. *Journal of Colloid and Interface Science* **2023**, *648*, 1–11. <https://doi.org/10.1016/j.jcis.2023.05.207>.
- (49) Sangnikul, P.; Phanpa, C.; Xiao, R.; Zhang, H.; Reubroycharoen, P.; Kuchonthara, P.; Vitidsant, T.; Pattiya, A.; Hinchiranan, N. Role of Copper- or Cerium-Promoters on NiMo/γ-Al₂O₃ Catalysts in Hydrodeoxygenation of Guaiacol and Bio-Oil. *Applied Catalysis A: General* **2019**, *574*, 151–160. <https://doi.org/10.1016/j.apcata.2019.02.004>.
- (50) Vajglová, Z.; Yevdokimova, O.; Medina, A.; Eränen, K.; Tirri, T.; Hemming, J.; Lindén, J.; Angervo, I.; Damlin, P.; Doronkin, D. E.; Mäki-Arvela, P.; Murzin, D. Y. Solventless Hydrodeoxygenation of Isoeugenol and Dihydroeugenol in Batch and Continuous Modes over a Zeolite-Supported FeNi Catalyst. *Sustainable Energy Fuels* **2023**, *7* (18), 4486–4504. <https://doi.org/10.1039/D3SE00371J>.
- (51) Fang, H.; Wu, L.; Chen, W.; Yuan, Y. Synergy of Carbon Defect and Transition Metal on Tungsten Carbides for Boosting the Selective Cleavage of Aryl Ether CO Bond. *Applied Catalysis A: General* **2021**, *613*, 118023. <https://doi.org/10.1016/j.apcata.2021.118023>.
- (52) Ferrari, M.; Delmon, B.; Grange, P. Influence of the Impregnation Order of Molybdenum and Cobalt in Carbon-Supported Catalysts for Hydrodeoxygenation Reactions. *Carbon* **2002**, *40* (4), 497–511. [https://doi.org/10.1016/S0008-6223\(01\)00128-2](https://doi.org/10.1016/S0008-6223(01)00128-2).
- (53) Blanco, E.; Carrales-Alvarado, D.; Belen Dongil, A.; Escalona, N. Effect of the Support Functionalization of Mono- and Bimetallic Ni/Co Supported on Graphene in Hydrodeoxygenation of Guaiacol. *Industrial & Engineering Chemistry Research* **2021**, *60* (51), 18870–18879. <https://doi.org/10.1021/acs.iecr.1c03073>.
- (54) Tran, N. T. T.; Uemura, Y.; Ramli, A.; Trinh, T. H. Vapor-Phase Hydrodeoxygenation of Lignin-Derived Bio-Oil over Al-MCM-41 Supported Pd-Co and Pd-Fe Catalysts. *Molecular Catalysis* **2022**, *523*, 111435. <https://doi.org/10.1016/j.mcat.2021.111435>.
- (55) Lindfors, C.; Mäki-Arvela, P.; Paturi, P.; Aho, A.; Eränen, K.; Hemming, J.; Peurla, M.; Kubička, D.; Simakova, I. L.; Murzin, D. Yu. Hydrodeoxygenation of Isoeugenol over Ni- and Co-Supported Catalysts. *ACS Sustainable Chemistry & Engineering Journal* **2019**, *7* (17), 14545–14560. <https://doi.org/10.1021/acssuschemeng.9b02108>.
- (56) Sankaranarayanan, T. M.; Berenguer, A.; Ochoa-Hernández, C.; Moreno, I.; Jana, P.; Coronado, J. M.; Serrano, D. P.; Pizarro, P. Hydrodeoxygenation of Anisole as Bio-Oil Model Compound over Supported Ni and Co Catalysts: Effect of Metal and Support Properties. *Catalysis Today* **2015**, *243*, 163–172. <https://doi.org/10.1016/j.cattod.2014.09.004>.
- (57) Cheng, S.; Wei, L.; Julson, J.; Rabnawaz, M. Upgrading Pyrolysis Bio-Oil through Hydrodeoxygenation (HDO) Using Non-Sulfided Fe-Co/SiO₂ Catalyst. *Energy Conversion and Management* **2017**, *150*, 331–342. <https://doi.org/10.1016/j.enconman.2017.08.024>.
- (58) Nava, R.; Pawelec, B.; Castaño, P.; Álvarez-Galván, M. C.; Loricera, C. V.; Fierro, J. L. G. Upgrading of Bio-Liquids on Different Mesoporous Silica-Supported CoMo Catalysts. *Applied Catalysis B: Environmental* **2009**, *92* (1), 154–167. <https://doi.org/10.1016/j.apcatb.2009.07.014>.
- (59) Tieuli, S.; Mäki-Arvela, P.; Peurla, M.; Eränen, K.; Wärnå, J.; Cruciani, G.; Menegazzo, F.; Murzin, D. Yu.; Signoretto, M. Hydrodeoxygenation of Isoeugenol over Ni-SBA-15: Kinetics and Modelling. *Applied Catalysis A: General* **2019**, *580*, 1–10. <https://doi.org/10.1016/j.apcata.2019.04.028>.

3. Valorization of biomass via pyrolysis - 3.3 Hydrodeoxygenation of bio-oil model compounds using biochar-based catalysts

- (60) Cordero-Lanzac, T.; Rodríguez-Mirasol, J.; Cordero, T.; Bilbao, J. Advances and Challenges in the Valorization of Bio-Oil: Hydrodeoxygenation Using Carbon-Supported Catalysts. *Energy Fuels* **2021**, *35* (21), 17008–17031. <https://doi.org/10.1021/acs.energyfuels.1c01700>.
- (61) Zhang, J.; Fidalgo, B.; Shen, D.; Zhang, X.; Gu, S. Mechanism of Hydrodeoxygenation (HDO) in Anisole Decomposition over Metal Loaded Brønsted Acid Sites: Density Functional Theory (DFT) Study. *Molecular Catalysis* **2018**, *454*, 30–37. <https://doi.org/10.1016/j.mcat.2018.05.015>.
- (62) Ranaware, V.; Verma, D.; Insyani, R.; Riaz, A.; Kim, S. M.; Kim, J. Highly-Efficient and Magnetically-Separable ZnO/Co@N-CNTs Catalyst for Hydrodeoxygenation of Lignin and Its Derived Species under Mild Conditions. *Green Chemistry* **2019**, *21* (5), 1021–1042. <https://doi.org/10.1039/C8GC03623C>.
- (63) Li, Z.; Li, Z.; Wu, M.; Qiu, Z.; Zhu, Y.; Zhang, R. Selective Hydrodeoxygenation of Lignin-Derived Eugenol to Propylcyclohexane over Triazine Polymer Derived Co/NC-T Catalyst. *Molecular Catalysis* **2024**, *557*, 113987. <https://doi.org/10.1016/j.mcat.2024.113987>.
- (64) Espinosa, J. C.; Manickam-Periyaraman, P.; Bernat-Quesada, F.; Sivanesan, S.; Álvaro, M.; García, H.; Navalón, S. Engineering of Activated Carbon Surface to Enhance the Catalytic Activity of Supported Cobalt Oxide Nanoparticles in Peroxymonosulfate Activation. *Applied Catalysis B: Environmental* **2019**, *249*, 42–53. <https://doi.org/10.1016/j.apcatb.2019.02.043>.
- (65) Echeandia, S.; Arias, P. L.; Barrio, V. L.; Pawelec, B.; Fierro, J. L. G. Synergy Effect in the HDO of Phenol over Ni–W Catalysts Supported on Active Carbon: Effect of Tungsten Precursors. *Applied Catalysis B: Environmental* **2010**, *101* (1), 1–12. <https://doi.org/10.1016/j.apcatb.2010.08.018>.
- (66) Deepa, A. K.; Dhepe, P. L. Function of Metals and Supports on the Hydrodeoxygenation of Phenolic Compounds. *ChemPlusChem* **2014**, *79* (11), 1573–1583. <https://doi.org/10.1002/cplu.201402145>.
- (67) Jung, K. B.; Lee, J.; Ha, J.-M.; Lee, H.; Suh, D. J.; Jun, C.-H.; Jae, J. Effective Hydrodeoxygenation of Lignin-Derived Phenols Using Bimetallic RuRe Catalysts: Effect of Carbon Supports. *Catalysis Today* **2018**, *303*, 191–199. <https://doi.org/10.1016/j.cattod.2017.07.027>.
- (68) Wang, S.; Li, H.; Wu, M. Advances in Metal/ Biochar Catalysts for Biomass Hydro-Upgrading: A Review. *Journal of Cleaner Production* **2021**, *303*, 126825. <https://doi.org/10.1016/j.jclepro.2021.126825>.
- (69) Shen, Y.; Yoshikawa, K. Tar Conversion and Vapor Upgrading via in Situ Catalysis Using Silica-Based Nickel Nanoparticles Embedded in Rice Husk Char for Biomass Pyrolysis/Gasification. *Industrial & Engineering Chemistry Research* **2014**, *53* (27), 10929–10942. <https://doi.org/10.1021/ie501843y>.
- (70) Shu, R.; Jiang, H.; Xie, L.; Liu, X.; Yin, T.; Tian, Z.; Wang, C.; Chen, Y. Efficient Hydrodeoxygenation of Lignin-Derived Phenolic Compounds by Using Ru-Based Biochar Catalyst Coupled with Silicotungstic Acid. *Renewable Energy* **2023**, *202*, 1160–1168. <https://doi.org/10.1016/j.renene.2022.11.092>.
- (71) Mudi, I.; Hart, A.; Ingram, A.; Wood, J. Catalytic Hydrodeoxygenation of Vanillin, a Bio-Oil Model Compound over Renewable Ni/Biochar Catalyst. *Catalysts* **2023**, *13* (1), 171. <https://doi.org/10.3390/catal13010171>.
- (72) Santos, J. L.; Mäki-Arvela, P.; Monzón, A.; Murzin, D. Y.; Centeno, M. Á. Metal Catalysts Supported on Biochars: Part I Synthesis and Characterization. *Applied Catalysis B: Environmental* **2020**, *268*, 118423. <https://doi.org/10.1016/j.apcatb.2019.118423>.
- (73) Santos, J. L.; Mäki-Arvela, P.; Wärnå, J.; Monzón, A.; Centeno, M. A.; Murzin, D. Yu. Hydrodeoxygenation of Vanillin over Noble Metal Catalyst Supported on Biochars: Part II: Catalytic Behaviour. *Applied Catalysis B: Environmental* **2020**, *268*, 118425. <https://doi.org/10.1016/j.apcatb.2019.118425>.
- (74) Guo, Q.; Mao, J.; Li, S.; Yin, J.; Lv, Y.; Zhou, J. Cobalt–Graphene Catalyst for Selective Hydrodeoxygenation of Guaiacol to Cyclohexanol. *Nanomaterials* **2022**, *12* (19), 3388. <https://doi.org/10.3390/nano12193388>.

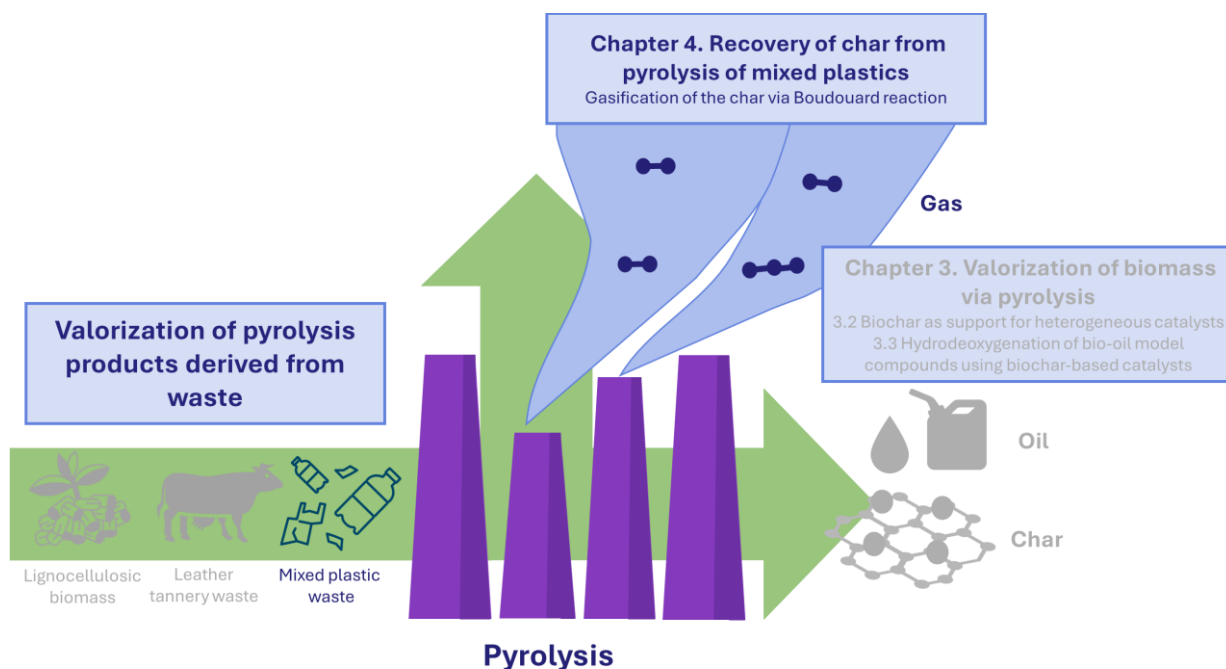
3. Valorization of biomass via pyrolysis - 3.3 Hydrodeoxygenation of bio-oil model compounds using biochar-based catalysts

- (75) Qu, X.; Zhang, S.; Mao, J.; Lv, H.; Zhou, J. Core-Shell Structured Cobalt Oxide Nanoparticles and Single Co Atoms Supported on Graphene for Selective Hydrodeoxygenation of Syringol to Cyclohexanol. *Catalysis Science & Technology* **2024**, *14* (12), 3382–3395. <https://doi.org/10.1039/D4CY00295D>.
- (76) Jiang, D.; Lin, M.; Yan, Y.; Zhan, L.; Li, R.; Wu, Y. Highly Selective Hydrogenation of Guaiacol to Cyclohexanol over Carbon-Encapsulated Highly Dispersed Cobalt Catalyst. *Chemical Engineering Science* **2024**, *290*, 119779. <https://doi.org/10.1016/j.ces.2024.119779>.
- (77) Khanh Tran, Q.; Vu Ly, H.; Anh Vo, T.; Tae Hwang, H.; Kim, J.; Kim, S.-S. Highly Selective Hydrodeoxygenation of Wood Pallet Sawdust Pyrolysis Oil to Methyl Phenol Derivatives Using Cobalt and Iron on Activated Carbon Supported Catalysts. *Energy Conversion and Management: X* **2022**, *14*, 100184. <https://doi.org/10.1016/j.ecmx.2022.100184>.
- (78) Roy, P.; Jahromi, H.; Rahman, T.; Adhikari, S.; Feyzbar-Khalkhali-Nejad, F.; Barbary Hassan, E.; Oh, T.-S. Understanding the Effects of Feedstock Blending and Catalyst Support on Hydrotreatment of Algae HTL Biocrude with Non-Edible Vegetable Oil. *Energy Conversion and Management* **2022**, *268*, 115998. <https://doi.org/10.1016/j.enconman.2022.115998>.
- (79) Peng, Q.; Jiang, X.; Cao, G.; Xie, T.; Jin, Z.; Xie, L.; Gan, F.; Ma, S.; Peng, M. Selective Production of High-Value Fuel via Catalytic Upgrading of Bio-Oil over Nitrogen-Doped Carbon-Alumina Hybrid Supported Cobalt Catalysts. *Bioresource Technology* **2024**, *406*, 131059. <https://doi.org/10.1016/j.biortech.2024.131059>.
- (80) Fagerlund, G. Determination of Specific Surface by the BET Method. *Mat. Constr.* **1973**, *6* (3), 239–245. <https://doi.org/10.1007/BF02479039>.
- (81) Tang, X.; Jiang, Z.; Li, Z.; Gao, Z.; Bai, Y.; Zhao, S.; Feng, J. The Effect of the Variation in Material Composition on the Heterogeneous Pore Structure of High-Maturity Shale of the Silurian Longmaxi Formation in the Southeastern Sichuan Basin, China. *Journal of Natural Gas Science and Engineering* **2015**, *23*, 464–473. <https://doi.org/10.1016/j.jngse.2015.02.031>.
- (82) Purkayastha, D. D.; Sarma, B.; Bhattacharjee, C. R. Surfactant-Assisted Low-Temperature Synthesis of Monodispersed Phase Pure Cubic CoO Solid Nanoparallelepiped via Thermal Decomposition of Cobalt(II) Acetylacetonate. *Materials Letters* **2013**, *107*, 71–74. <https://doi.org/10.1016/j.matlet.2013.05.122>.
- (83) Singh, B. P.; More, G. S.; Bal, R.; Srivastava, R. The Cooperative Effect of Co and CoO in Co/CoO Enabled Efficient Catalytic Hydrogenation and Demethoxylation of Guaiacol to Cyclohexanol. *Sustainable Energy Fuels* **2024**, *8* (10), 2153–2166. <https://doi.org/10.1039/D4SE00183D>.
- (84) de la Peña O'Shea, V. A.; de la Piscina, P. R.; Homs, N.; Aromí, G.; Fierro, J. L. G. Development of Hexagonal Closed-Packed Cobalt Nanoparticles Stable at High Temperature. *Chemistry of Materials Journal* **2009**, *21* (23), 5637–5643. <https://doi.org/10.1021/cm900845h>.
- (85) Bomont, L.; Alda-Onggar, M.; Fedorov, V.; Aho, A.; Peltonen, J.; Eränen, K.; Peurla, M.; Kumar, N.; Wärnå, J.; Russo, V.; Mäki-Arvela, P.; Grénman, H.; Lindblad, M.; Murzin, D. Yu. Production of Cycloalkanes in Hydrodeoxygenation of Isoeugenol Over Pt- and Ir-Modified Bifunctional Catalysts. *European Journal of Inorganic Chemistry* **2018**, *2018* (24), 2841–2854. <https://doi.org/10.1002/ejic.201800391>.
- (86) Martinez-Klimov, M.; Mäki-Arvela, P.; Çiftçi, A.; Kumar, N.; Eränen, K.; Peurla, M.; Hensen, E. J. M.; Murzin, D. Yu. Bifunctional Pt-Re Catalysts in Hydrodeoxygenation of Isoeugenol as a Model Compound for Renewable Jet Fuel Production. *ACS Engineering Au Journal* **2022**, *2* (5), 436–449. <https://doi.org/10.1021/acsengineeringau.2c00015>.
- (87) Si, M.; Wang, S.; Gou, X.; Song, H. Co Doping Induces Co_xP-Ni₂P Bimetallic Site and Acid Synergistic Effect to Achieve Efficient Hydrodeoxygenation. *Journal of Fuel Chemistry and Technology* **2024**, *52* (9), 1327–1335. [https://doi.org/10.1016/S1872-5813\(24\)60477-9](https://doi.org/10.1016/S1872-5813(24)60477-9).
- (88) Xiang, S.; Dong, L.; Wang, Z.-Q.; Han, X.; Daemen, L. L.; Li, J.; Cheng, Y.; Guo, Y.; Liu, X.; Hu, Y.; Ramirez-Cuesta, A. J.; Yang, S.; Gong, X.-Q.; Wang, Y. A Unique Co@CoO Catalyst for Hydrogenolysis of Biomass-Derived 5-Hydroxymethylfurfural to 2,5-Dimethylfuran. *Nature Communications* **2022**, *13* (1), 3657. <https://doi.org/10.1038/s41467-022-31362-9>.

3. Valorization of biomass via pyrolysis - 3.3 Hydrodeoxygenation of bio-oil model compounds using biochar-based catalysts

- (89) Liu, M.; Zhang, J.; Zheng, L.; Fan, G.; Yang, L.; Li, F. Significant Promotion of Surface Oxygen Vacancies on Bimetallic CoNi Nanocatalysts for Hydrodeoxygenation of Biomass-Derived Vanillin to Produce Methylcyclohexanol. *ACS Sustainable Chemistry & Engineering Journal* **2020**, *8* (15), 6075–6089. <https://doi.org/10.1021/acssuschemeng.0c01015>.
- (90) Leite, D. S.; Strapasson, G. B.; Zanchet, D. Unveiling the Effect of Metallic and Oxidized Phases of Cobalt on Acetone Hydrodeoxygenation. *Molecular Catalysis* **2022**, *530*, 112623. <https://doi.org/10.1016/j.mcat.2022.112623>.
- (91) Zhao, C.; He, J.; Lemonidou, A. A.; Li, X.; Lercher, J. A. Aqueous-Phase Hydrodeoxygenation of Bio-Derived Phenols to Cycloalkanes. *Journal of Catalysis* **2011**, *280* (1), 8–16. <https://doi.org/10.1016/j.jcat.2011.02.001>.
- (92) Liu, X.; Jia, W.; Xu, G.; Zhang, Y.; Fu, Y. Selective Hydrodeoxygenation of Lignin-Derived Phenols to Cyclohexanols over Co-Based Catalysts. *ACS Sustainable Chemistry & Engineering Journal* **2017**, *5* (10), 8594–8601. <https://doi.org/10.1021/acssuschemeng.7b01047>.
- (93) Lyu, G.; Wu, S.; Zhang, H. Estimation and Comparison of Bio-Oil Components from Different Pyrolysis Conditions. *Frontiers in Energy Research* **2015**, *3*. <https://doi.org/10.3389/fenrg.2015.00028>.
- (94) J. Bozell, J.; R. Petersen, G. Technology Development for the Production of Biobased Products from Biorefinery Carbohydrates—the US Department of Energy’s “Top 10” Revisited. *Green Chemistry* **2010**, *12* (4), 539–554. <https://doi.org/10.1039/B922014C>.
- (95) Climent, M. J.; Corma, A.; Iborra, S. Conversion of Biomass Platform Molecules into Fuel Additives and Liquid Hydrocarbon Fuels. *Green Chemistry* **2014**, *16* (2), 516–547. <https://doi.org/10.1039/C3GC41492B>.
- (96) Dawes, G. J. S.; Scott, E. L.; Nôtre, J. L.; Sanders, J. P. M.; Bitter, J. H. Deoxygenation of Biobased Molecules by Decarboxylation and Decarbonylation – a Review on the Role of Heterogeneous, Homogeneous and Bio-Catalysis. *Green Chemistry*. **2015**, *17* (6), 3231–3250. <https://doi.org/10.1039/C5GC00023H>.
- (97) Carlos Serrano-Ruiz, J.; Luque, R.; Sepúlveda-Escribano, A. Transformations of Biomass-Derived Platform Molecules: From High Added-Value Chemicals to Fuels via Aqueous-Phase Processing. *Chemical Society Reviews* **2011**, *40* (11), 5266–5281. <https://doi.org/10.1039/C1CS15131B>.
- (98) Wang, C.; Bi, H.; Lin, Q.; Jiang, X.; Jiang, C. Co-Pyrolysis of Sewage Sludge and Rice Husk by TG–FTIR–MS: Pyrolysis Behavior, Kinetics, and Condensable/Non-Condensable Gases Characteristics. *Renewable Energy* **2020**, *160*, 1048–1066. <https://doi.org/10.1016/j.renene.2020.07.046>.
- (99) Chen, W.; Luo, Z.; Yu, C.; Yang, Y.; Li, G.; Zhang, J. Catalytic Conversion of Guaiacol in Ethanol for Bio-Oil Upgrading to Stable Oxygenated Organics. *Fuel Processing Technology* **2014**, *126*, 420–428. <https://doi.org/10.1016/j.fuproc.2014.05.022>.
- (100) Dwiatmoko, A. A.; Lee, S.; Ham, H. C.; Choi, J.-W.; Suh, D. J.; Ha, J.-M. Effects of Carbohydrates on the Hydrodeoxygenation of Lignin-Derived Phenolic Compounds. *ACS Catalysis* **2015**, *5* (1), 433–437. <https://doi.org/10.1021/cs501567x>.
- (101) Luo, Z.; Wang, S.; Liao, Y.; Zhou, J.; Gu, Y.; Cen, K. Research on Biomass Fast Pyrolysis for Liquid Fuel. *Biomass and Bioenergy* **2004**, *26* (5), 455–462. <https://doi.org/10.1016/j.biombioe.2003.04.001>.
- (102) Murzin, D. Yu.; Wärmå, J.; Haario, H.; Salmi, T. Parameter Estimation in Kinetic Models of Complex Heterogeneous Catalytic Reactions Using Bayesian Statistics. *Reaction Kinetics Mechanisms and Catalysis* **2021**, *133* (1), 1–15. <https://doi.org/10.1007/s11144-021-01974-1>.
- (103) *Daily Metal Price: Lead Price (USD / Kilogram) for the Last Month*. <https://www.dailymetalprice.com/metalprices.php> (accessed 2024-10-27).

4. Recovery of char from pyrolysis of mixed plastics



4.1 Introduction

4.1.1 Plastic pyrolysis

Among the chemical recycling methods for plastics, pyrolysis and gasification are the most widely utilized due to their versatility and robustness in handling heterogeneous and contaminated plastics. In contrast, chemical recycling like solvolysis is limited to specific plastics such as polyethylene terephthalate (PET), poly lactic acid (PLA) or polycarbonate (PC) and it is ineffective for polyolefins, which are the most commonly used plastics^{1,2}. Plastic pyrolysis is typically carried out in inert atmosphere at temperatures between 400 to 600 °C, causing the degradation of the polymeric structure³.

The thermal degradation of polymers consists of two distinct reactions, that can occur simultaneously⁴. The random scission (Eq. 4.1.1, 4.1.2) breaks down the polymer in a causal position of the chain, causing a reduction of the molecular weight. The random degradation is typical of polyolefins (PP, PE), PET etc.

The second mechanism, the end chain scission (Eq. 4.1.3) occurs at the end of the polymer chain, forming the monomers. It is favored on polymethyl methacrylate (PPMA), polystyrene (PS) etc.



As for biomass, also from plastic pyrolysis the three fractions are obtained⁵ (oil, gas, and char) (Figure 4.1.1), in variable proportion depending by the operational parameters (such as reactor type, temperature, residence time, heating rate, and the eventual use of a catalyst) and type of plastics treated. Plastics with a high percentage of volatile matter tend to favor liquid oil production, whereas higher ash content leads to increased yields of gas and char⁶.

The liquid fraction primarily consists in aliphatic, monoaromatic and polyaromatic compounds within the C₅-C₁₆ range⁵. In general, compared to biomass, plastics exhibit a higher percentage of volatile matter and lower ash content, making them particularly suitable for conversion into liquid oil, via pyrolysis.

Typically, high liquid yields are favored at controlled temperatures, between 300-500°C, while higher yield of gas and solid fraction are obtained at higher temperature^{5,7}. The product distribution (typically in size of hydrocarbon chain) is strongly affected also by the pyrolysis temperature: the higher the temperature the higher the light fraction C₂-C₄. Apart from temperature, residence time influences the product distribution⁸. As for biomass pyrolysis, low residence time enhance liquid yield⁹, while longer residence time increases the conversion of primary products, forming lighter hydrocarbons and non-condensable gases¹⁰. The thermal pyrolysis suffers from some limitations related to endothermic cracking, scarce selectivity, low thermal conductivity of plastics, low quality of the products that require further upgrading and purification steps. To improve economic feasibility and selectivity, catalytic pyrolysis has been often employed for plastic treatment. The addition of catalysts allows to decrease the activation energy of the process, thus, to carry on pyrolysis at lower temperatures and shorter reaction times¹¹. The catalysts can improve the selectivity of the cracking of the polymer chains, obtaining higher quality products, and improving the physical properties of the liquid obtained^{12,13}. The mechanism occurring during catalytic pyrolysis is mostly through carbocation formation, by protonation on Brønsted acid sites or by hydride abstraction by a Lewis acid site, forming the carbonium ion¹⁴. This process is then followed by acid catalyzed processes such as cracking, aromatization, cyclization, isomerization etc. With respect to thermal pyrolysis, catalytic pyrolysis leads to a higher yield of gaseous products, favoring the decarboxylation approach and forming CO₂, together with CO, CH₄, H₂¹².

4. Recovery of char from pyrolysis of mixed plastics

The type of feedstock significantly affects the final oil yield, quality and composition. For example, PE, PP and PS have volatile matter content around 98-99 wt.%, yielding liquid outputs of 70-80% for PP and HDPE¹⁵, up to 95% for LDPE^{16,17}, and 97% for PS¹⁸.

Oil

The oil derived from these plastics has a high calorific value (40-45 MJ/kg), and characteristics similar to diesel, gasoline or kerosene in terms of density, octane number, flash point etc. making it suitable for direct use as an alternative fuel¹⁹⁻²³. On the other hand, PET and polyvinyl chloride (PVC), with volatile matter contents of 86% and 93% respectively⁶⁻⁸, result in lower liquid yields (below 80% for PET, and less than 15% for PVC). The pyrolysis of PET and PVC also presents specific challenges. Cepeliogullar *et al.*²⁴ reported that half of the oil produced from PET pyrolysis consists of benzoic acid, which can cause corrosion and clogging in the plant's piping. PVC, which is made for the 57 wt.% of chlorine, primarily generates HCl, posing significant toxicity and corrosion risks to the operators and the equipment²⁵. This leads also to oils with lower calorific values, below 30 MJ/kg¹⁸. These differences underscore the challenges associated with the pyrolysis of mixed plastic waste, such as that found in municipal solid waste (MSW). Pyrolysis of mixed plastics typically results in lower liquid yields, with literature reporting values not exceeding 50 %²⁶⁻²⁸. It is also crucial to control the composition of the feedstock; for instance, PVC must be kept below 1% to avoid negatively impacting the quality of the resulting oil²⁸. The pyrolysis oil is suitable to undergo further upgrading, for example through steam or catalytic cracking^{29,30} reduce the size of the hydrocarbons obtained, and to produce C₂-C₄ olefins, valuable platform chemicals that can be used as building blocks of many plastic products. By this process it is possible to obtain new virgin polymers with the same properties as those derived from fossil sources, making them suitable for all applications, including food-related uses, due to their high purity and lack of contamination.

Gas

The gas phase is mainly composed by hydrogen, and light hydrocarbons C₁-C₄³¹. However, when oxygenated plastics, like PET, are involved, also CO and CO₂ are produced, while when PVC is pyrolyzed the main product is HCl. Nevertheless, the main gases produced have significant calorific value and they can be used as heating source in pyrolysis industrial plants, self-sustaining the entire process³², or they can be transformed into syngas via dry reforming⁹⁸⁻⁹⁹.

Char

During the pyrolysis process, condensation reactions contribute to char formation³³. The latter is typically favored at slow pyrolysis conditions, which involve a slow heating rate and long residence times. However, even under optimized conditions for maximum oil yield, some char is inevitably generated. The quantity and quality of this byproduct depend heavily on the feedstock. In certain cases, such as when char is derived from single-component plastics like high density polyethylene (HDPE), it features a low ash and sulfur content with a high calorific value (18.84 MJ/kg), making it suitable for use as a solid fuel³⁴. Literature also reports several other applications for plastic-derived chars, akin to those of activated carbon, coal, and biochar, including soil amendment, pollutant adsorption, electrode materials, and catalysis. However, the viability of these applications depends on key properties of the char, such as ash content, fixed carbon, surface area, and pore structure. When mixed plastics from solid wastes are processed, the resulting char generally deviates from the desired characteristics, limiting its applicability⁸. The char typically appears as a fine black powder composed of both carbon and inorganic substances (ranging from 30 to 98 wt. %), such as carbonates, chlorides, and oxides of metals like calcium, sodium, and iron, which originate from the additives and fillers in the plastics. These additives fulfill essential roles, such as providing antioxidant properties, enhancing stability, acting as fillers, imparting color, improving flame resistance, or serving as barriers against specific gases like oxygen and CO₂³⁵. The additives used can be either organic, including compounds like phenols and aromatic amines for antioxidation and UV protection, or inorganic, such as metal complexes for photostabilization, pigments like titanium dioxide (TiO₂) and iron oxide (Fe₃O₄), cobalt for green and blue pigmentation, and borates for flame retardancy. The proportions of carbon and inorganic components vary depending on the plastic feedstock and pyrolysis conditions. Additionally, the fine particulate nature of char can make it difficult to handle, as it may exhibit pyrophoric properties.

Currently, the primary use of char from plastic pyrolysis is in the cement and steel industries, owing to its variable composition and high inorganic content. However, in many cases, this char is treated as waste, which reduces the overall efficiency of carbon recycling and limits the production of new polymers from recycled materials. Recently, a novel application for plastic-derived char as carbon black has been patented³⁶.

To achieve high carbon purity and a high percentage of carbon content, though, the char must undergo intense and harsh washing processes to remove inorganic contaminants. This raises concerns about the sustainability of the approach. Thus, this chapter has been devoted to the valorization of the char deriving from the pyrolysis of mixed plastic waste.

4. Recovery of char from pyrolysis of mixed plastics

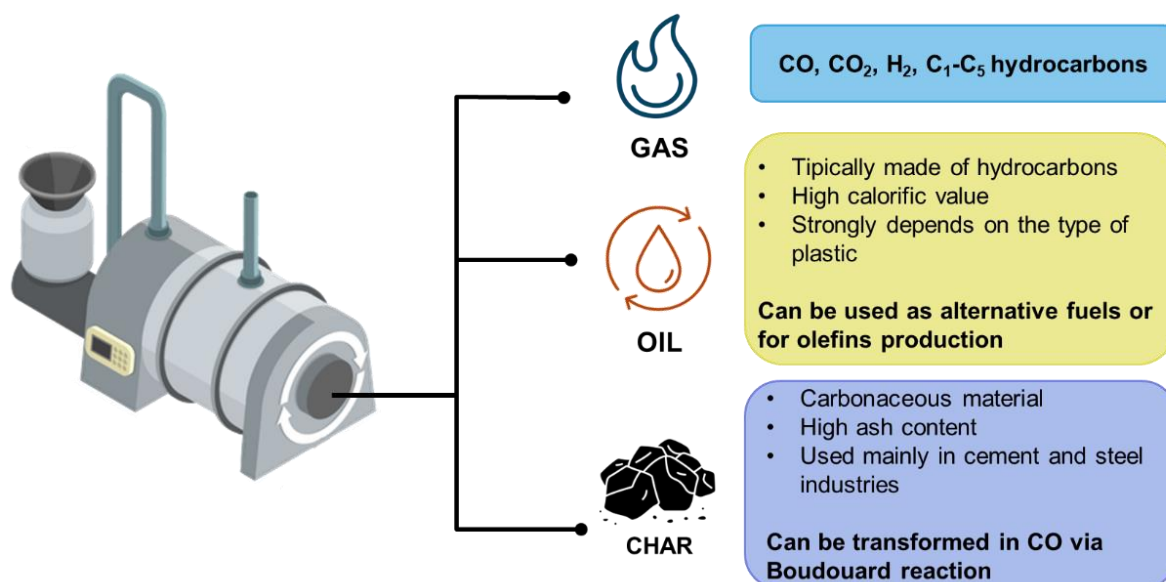


Figure 4.1.3. The products obtained by pyrolysis of plastics

4.1.2 Plastic recycling and industries: an overview

Up to days, chemical recycling is still not commercially fully in operation, and the first pilot and industrial plants are now under construction. Nevertheless, the possibility to obtain the monomers that can be further repolymerized to obtain virgin polymers, could lower the price of the raw materials, and contributes greatly to the circular economy of the process. This is pushing companies and research through the development of this strategy².

Pyrolysis of plastics is therefore resulting in the most promising technology for the treatment of mixed plastic that cannot undergo to mechanical recycling. Indeed, several companies are moving toward the building of pilot plants for pyrolysis. The pyrolysis plant market is expected to grow considerably between 2023 and 2030, as reported in the **Global Waste Plastic Pyrolysis Plant Market** report³⁷. In 2008 the ISO 15270:2008 standard, titled "Plastics – Guidelines for the recovery and recycling of plastics waste," was introduced to support the plastics recovery and recycling industry, promoting sector growth and facilitating international trade. Since its publication, numerous companies have made significant advancements in chemical recycling technologies³⁸. However, almost 10 years were necessary to see the first signs of an industrial commitment. Even if some plants are planned to be built in USA, and Asian countries like China, South Korea, Malaysia, India etc., Europe remains the leader in investing in plastic recycling. PlasticEurope³⁹ members are planning to invest in Europe for chemical recycling more than 8 billion euros, to pass from a production of 0.9 Mt forecast for 2025 to produce 2.8 MT of recycled plastic by 2030. The investment involves 13 countries and 44 plants. Most of them are located between the Netherlands, Belgium, Germany and France.

4. Recovery of char from pyrolysis of mixed plastics

Ineos has been at the forefront of these developments, starting with the chemical recycling of polystyrene in 2017 in collaboration with the University of Aachen. By 2020 Ineos joined Plastic Energy to establish a chemical recycling plant in Germany, in operation since 2023. Additionally, it has taken part in a joint project together with Styrolution and Agilyx to build a polystyrene plant in Illinois. Sabic has also played a pivotal role in advancing recycling technologies. In 2018 the company announced a partnership with Plastic Energy to build a thermochemical plant in the Netherlands, which became operational in 2021. SABIC expanded its efforts globally, collaborating with an Indian group, Pashupati, and planning a facility in Malaysia with Petronas, expected to process 33,000 tons annually by 2026. In 2023, SABIC, alongside Aramco and TotalEnergies, launched the first chemical recycling project in the Middle East at Jubail. Besides its partnership with Ineos and Sabic, Plastic Energy, leader in the expertise of chemical recycling, has operated two plants in Spain between 2014 and 2017. The company has also partnered with ExxonMobil in 2021 to build a new plant in France with an initial capacity of 25.000 tons annually. ExxonMobil in the same year launched a chemical recycling plant in Baytown, Texas, with a capacity of 30.000 tons annually. LyondellBasell has made significant strides in chemical recycling as well, developing technologies for catalytic pyrolysis (named MoReTec) in the R&D center of Ferrara, Italy, where a pilot plant is active since 2020, and in collaboration with the Karlsruhe Institute of Technology (KIT). The company invested in the building of a plant in Wesseling, Germany that will be operational by 2025 with a capacity of 50.000 tons annual. The company has recently started also a partnership with a Chinese company, Genox Recycling, to manage a plant in Zhaoqing. Dow has also made advancements in chemical recycling. In 2019, Dow collaborated with Fuenix Ecology to produce products from the pyrolysis of mixed plastic waste in the Netherlands. Additionally, Dow and Mura Technology introduced HydroPRS technology in the UK in 2021, with a facility capable of processing 20,000 tons annually. The same technology is projected to be exploited in Böhlen, Germany.

Versalis, plastic recycling and Hoop technology

In Italy, Versalis SpA, Eni's chemical company that operates in the basic chemicals, intermediates for plastic and rubber, is also active in the context of circularity and sustainability. Indeed, Versalis developed different technologies for recycling solutions of plastics and rubbers. Versalis Revive® is a line of plastic products made of different polymers, containing mechanically recycled plastics. The Revive® technology is not only applicable to styrene and polyethylene materials, but also elastomeric materials, like tires.

In 2020, Versalis patented a new technology for the chemical recycling of *plasmix*, defined by the Italian law as “the set of heterogeneous plastics included in post-consumer packaging and not recovered as single polymers”⁴⁰.

4. Recovery of char from pyrolysis of mixed plastics

The project, named Hoop[®], was developed in collaboration with the Italian engineering company *Servizi di Ricerche e Sviluppo* (S.R.S), owner of a pyrolysis technology^{41,42}. The first demo plant with a capacity of 6000 tons annually was inaugurated in October 2023, it is now under construction and will be operational by 2025.

The novelty of Hoop[®] technology is related to the processing of plastics materials of variable composition, as it could be the composition of municipal plastic wastes. This technology is able to treat not only mixed plastic with a variable composition, but also with the presence of other substances such as inorganics derived from additives, (like silica, titanium dioxide, talc, coke, graphite, carbon black, calcium carbonate, tricalcium phosphate, zeolites, aluminum silicates, titanates, organo-brominated or organo-chlorinated additives, perovskites or packaging, like aluminum), and paper. The target feedstock is the fraction of plastic waste that remains after the process of selection and extraction of individual polymers that can be mechanically recycled. Hoop technology is able to treat mixed plastics made of vinyl polymers such as PE and PP, polyvinyl aromatic polymers like PS, oxygenated polymers like PET and cellulose, and halogenated polymers like PVC, or polymers containing halogenated compounds like flame retardants. The co-processing of halogenated plastics, such as PVC, is facilitated by the addition of dehalogenating agents like CaCO₃. During pyrolysis, CaCO₃ reacts with the HCl and Cl₂ produced, forming CaCl₂, thereby effectively sequestering these toxic and corrosive gases. This process helps to prevent damage to equipment, protect operators, and minimize environmental impact^{43,44}. By adjusting the reaction conditions, and particularly the pressure, according to the composition of the material to be processed, Hoop[®] technology is able to successfully transform the *plasmix* into hydrocarbons, achieving more than 90% of the liquid fraction.

The pilot plant consists of a semi-continuous vertical reactor, operating between 300 and 600 °C, that exploits molten salts as heat transfer. The operational pressure goes between atmospheric pressure to 13 bar(a), and it can be regulated according to the starting composition of the feedstock. The plastic material will be fed into the reactor already in the molten state, and in the reactor, it will be treated at a temperature higher than 300 °C in absence of oxygen, under a specific pressure, and under stirring for a variable time between 30 and 240 minutes. The volatile fractions are continuously removed from the reactor when formed, and the liquid fraction is separated by a distillation column, to maintain a high temperature of the effluent out of the reactor, and to recycle the gas formed with a lower loss of thermal energy. Indeed, the gaseous fraction, mainly made of light hydrocarbons, syngas and methane, obtained by the pyrolysis can be remitted into the reactor as auxiliary gaseous fluid to regulate the pressure of the system. The obtained liquid fraction is mainly made of C₅-C₁₂ hydrocarbons, with a small % of tetrahydrofuran and a content of benzoic acid lower than 2%.

4. Recovery of char from pyrolysis of mixed plastics

At the conditions described, a solid residue is formed, and the wt. % ranges between 5 to 20 wt.% of the starting feed, depending on the feedstock composition. The reactor is projected to work continuously between 2 to 10 days before it is necessary to remove the solid fraction that remains inside the reactor. With a plant capacity of 6,000 tons, this results in the production of approximately 300 to 1200 tons of char annually. Therefore, recovering this byproduct in a form of higher added value is crucial to enhancing the overall feasibility of the process. This approach supports the implementation of circular economy principles and improves the overall sustainability of the system.

In addition to char, pyrolysis of plastics also produces a certain percentage of CO₂ as a byproduct, deriving from the decomposition of a fraction of PET that can be found in the *plasmix*. However, in a more generic optic of decarbonization, the objective of this work is to explore the combined utilization of the char with the CO₂ emitted by industrial processes, by exploiting the Boudouard reaction, to convert both into a more valuable chemical, namely carbon monoxide. The Boudouard reaction is indeed the disproportion between CO₂ and C to give CO⁴⁵. The gasification of the char by CO₂ offers not only the potential to convert char into higher value-added products, thereby improving the carbon balance within the plastic recycling process, but also provides a viable application for one of the most problematic greenhouse gases. This approach aligns with the carbon capture and utilization (CCU) strategies promoted under the European Green Deal, contributing to global decarbonization efforts⁴⁶. The resulting product, carbon monoxide (CO), can be effectively reintegrated into the chemical industry, where it serves as a fundamental building block for the synthesis of essential chemicals. CO can be converted into hydrogen via the water-gas shift reaction⁴⁷, and the resulting syngas can be employed in the synthesis of methanol and Fischer-Tropsch hydrocarbons⁴⁸. Alternatively, CO can be utilized as a carbonylation reagent in the synthesis of various chemicals⁴⁹. The mix of CO and CO₂ can be employed in the synthesis of methanol and further transformation of it to olefins (methanol to olefin process, MTO), thereby remitted these components in the plastic production chain, increasing the overall production of recycled virgin plastic.

4.1.3 Boudouard Equilibrium

The Boudouard equilibrium is the disproportionation of 3 oxidation states of carbon, as in Eq. 4.1.3.1 follows:



This equilibrium was first studied by the French chemist Octave Leopold Boudouard in 1905. The large positive enthalpy (at 298K $\Delta H = 172$ kJ/mol), makes it highly endothermic reaction, causing the equilibrium to favor the formation of CO_2 and coke. Consequently, this reaction is often an undesired pathway in various industrial processes, like steam reforming⁵⁰, dry reforming⁵¹, methanol synthesis⁵², and Fisher-Tropsch synthesis⁵³, where it leads to coke formation and catalyst deactivation.

At high temperatures (typically > 700 °C) the entropic contribution ($T\Delta S$) becomes sufficiently large to yield a negative free Gibbs energy (ΔG), making the formation of CO thermodynamically favorable⁴⁵. Nevertheless, the reaction is typically very slow, and it becomes significant at temperatures > 900 °C. Alternatively, a catalyst is required to lower the activation energy of the system and to increase the reaction rate.

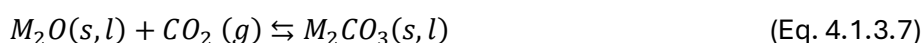
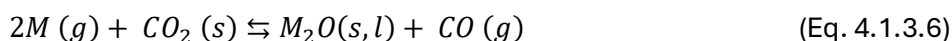
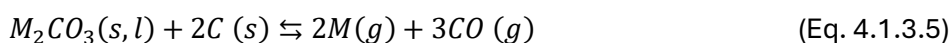
The Boudouard reaction has been exploited by different researchers for the gasification of different types of carbonaceous materials. For instance, Fermoso et al.¹⁰⁰ investigated the gasification of bituminous coal and algae with CO_2 ; the Italian National Agency for New Technologies, Energy and Sustainable Economic Development (ENEA) studied the gasification with CO_2 of various mineral coals, deriving from the mining basin of Sulcis (Italy) and South Africa⁵⁴. The reactivity of the chars was assessed through thermogravimetric analysis, correlating weight loss with the conversion of carbon into CO. The study found that the chars exhibited significant reactivity at temperatures above 900 °C. Similarly, Chun *et al.*⁵⁵ reported a gasification temperature of 900 °C for biochars derived from various biomass sources. Another study⁵⁶ demonstrated that 85% of char produced from waste tire pyrolysis could be converted via the Boudouard reaction at temperatures exceeding 900 °C. Additionally, research on char derived from PET⁵⁷ showed that partial CO_2 gasification occurred at temperatures between 925 °C and 1125 °C, resulting in a porous material due to incomplete gasification.

Although numerous studies on char gasification are reported in the literature, there are limited examples focused on chars derived from the pyrolysis of plastics⁵⁸. Furthermore, there are no documented examples of utilizing the Boudouard reaction to recover carbon from chars produced as byproducts of *plasmix* recycling.

The reactivity of char during the gasification process is significantly influenced by its thermal history, including the various parameters involved in the pyrolysis of the precursor carbonaceous material. The key factors that impact the thermal history of char include pyrolysis temperature, heating rate, residence time, atmosphere during pyrolysis, as well as the feedstock composition⁵⁹. These factors collectively define the morphological characteristics of the char, such as porosity and particle size, as well as the chemical features, such as fixed carbon, presence of heteroatoms, amount and type of ash, which in turn govern its reactivity during gasification^{60,61}. For example, heteroatoms present within the polynuclear aromatic structure of carbon, such as oxygen, nitrogen, or sulfur, can act as active sites and therefore significantly enhance the reactivity. Carbon atoms bonded to heteroatoms exhibit reactivity an order of magnitude greater than those bonded exclusively to other carbon atoms⁶². This phenomenon can occur by the oxygen-exchange reaction mechanism proposed by Ergun (Eq. 4.1.3.2, 4.1.3.3)⁶³.



Where C_f represents a free active carbon site free carbon active site and $C(O)$ refers to an occupied surface complex formed by the dissociation of CO_2 at the active site, producing CO . Subsequently, the complex decomposes to give an additional molecule of CO and another C_f , effectively transferring carbon from the solid phase to the gas phase. Also the mineral content of char plays a crucial role in influencing the reaction kinetics of the Boudouard reaction^{55,64}. Alkali metals (K, Na), alkaline earth metals (Ca, Mg), and transition metals (Fe), can act as catalysts in this process^{61,65}. The catalytic activity of these metals typically follows the order: $K > Na > Ca > Fe > Mg$. These metals are often added as catalysts in the form of carbonates, and extensive research has been conducted to elucidate the reaction mechanisms between carbon and these catalytic species. For instance, Rao *et al.*⁶⁵ proposed that the catalytic mechanism for the Boudouard reaction involving these metals may proceed via gaseous intermediates such as $M(g)$, $CO(g)$ and $CO_2(g)$, where M represents metals like K, Li, Na, and others. The process involves reactions such as in Eq. 4.1.3.4, 4.1.3.5, 4.1.3.6:



Additionally, elements such as Si and Al, present in the ash, can inhibit the reaction by forming inert silicates or aluminates, reducing the catalytic efficiency of alkali metals⁶⁶.

To quantify the catalytic effect of minerals in the ash, the Alkali Index (Eq. 4.1.3.8) is often employed⁶⁷:

$$\text{Alkali index} = \text{ash content (wt. \%)} \frac{\text{Fe}_2\text{O}_3 + \text{CaO} + \text{MgO} + \text{Na}_2\text{O} + \text{K}_2\text{O}}{\text{SiO}_2 + \text{Al}_2\text{O}_3} \quad (\text{Eq. 4.1.3.8})$$

Several studies have demonstrated a positive correlation between an increased Alkali Index and enhanced gasification reactivity^{68,69}. Floess *et al.*⁷⁰ conducted a kinetic study on microporous carbon gasification with and without the addition of Ca as catalyst, demonstrating that dispersed calcium significantly lowered the activation energy, from 2953.9 kcal/mol for non-catalyzed chars to 2430.9 kcal/mol for catalyzed char. Sadhwani *et al.*⁷¹ investigated the influence of K, Ca, Na, and Mg on the gasification of the southern pine char, showing that the activation energy decreased from 219 kJ/mol for bare char to as low as 104.2 kJ/mol upon metal addition. Similarly, Duman *et al.*⁷² compared the gasification reactivity of raw and acid-washed biomass chars, finding that the removal of K and Ca via acid washing led to a marked decrease in reactivity.

Apart from the intrinsic characteristics of the char, the gasification conditions play a central role in the reaction rate, especially the gasification temperature. At relatively low temperatures (depending on the char it is reported below 900 °C or up to 1200 °C), the reaction is governed by chemical reaction rate, while at higher temperatures pore diffusion mechanism becomes dominant⁶⁹. For this range of temperatures, the reaction rate has a linear correlation with the inverse temperature, following the Arrhenius plot. Gas diffusion in the pores and on the surface of the char is another important factor that controls the conversion rate. There are several diffusion events occurring during the reaction: a) diffusion of CO₂ from the bulk phase gas to the surface of the char (film diffusion), b) diffusion of CO₂ into the porous structure of the char (pore diffusion), c) outward diffusion of CO from the pores of the char (pore diffusion), d) transfer of CO from the surface to the bulk gas phase (film diffusion). Total pressure has an important influence on the diffusion of the gases. Studies have shown that CO₂ partial pressure generally increases the reaction rate, as it increases the number of occupied active sites of the char surface⁷³. However, the effect of total and partial CO₂ pressure is complex and depends on several factors, like the diffusion mechanism, char structure, temperature etc.

It is worth mentioning that many of these factors have a complex effect on the reactivity of the char in the CO₂ gasification process. Indeed, it is not always straightforward to distinguish between the promoting and hindering effects contributing to the overall char reactivity, as some of these parameters might change during char gasification, like surface area. The ultimate achievable conversion of char through the gasification might be a combination of several influential parameters rather than being simply inferred from individual factors.

Kinetic model and data analysis

The Boudouard reaction being a gas-solid reaction, it is characterized by a series of sequential steps, with different rates:

1. The gas is chemisorbed on the surface of the solid with a diffusive phenomenon
2. Oxidation of C occurs
3. The produced gas is desorbed from the surface of the solid with a diffusive phenomenon

Depending on the reaction conditions, the slowest step is the rate determining step. It is reported that, for temperatures below 1000 °C, the rate determining step is the chemical reaction⁶⁹.

The gasification kinetic of chars has been matter of several studies. The thermogravimetry resulted a powerful tool to evaluate the kinetics of the process, evaluating several parameters such as temperature, CO₂ partial pressure, effect of metals, etc.⁶⁴. The study of gasification kinetics is important to determine the reaction rate, mass transfer, and for the design of a reaction plant, and for the optimization of the production process. There are several models reported in literature to describe and simulate the gasification of carbonaceous materials^{74,75}. In the kinetic modeling of carbon gasification, carbon conversion ratio, x , is defined as follows (Eq.4.1.3.9):

$$x = \frac{m_0 - m}{m_0} \quad (\text{Eq.4.1.3.9})$$

where m_0 is the initial mass of the char, and m is the mass of the char at a time t , on a dry, ash-free basis. The rate of conversion is expressed as (Eq.4.1.3.10):

$$\frac{dx}{dt} = k(T, p_{CO_2})f(x) \quad (\text{Eq. 4.1.3.10})$$

Where k is the rate constant based on the reaction temperature (T), p_{CO_2} is the CO₂ partial pressure, and $f(x)$ is a kinetic model-dependent function. Assuming constant p_{CO_2} during the reaction, the rate can be expressed by the Arrhenius equation (Eq. 4.1.3.11):

$$k = A \exp\left(-\frac{E}{RT}\right) \quad (\text{Eq. 4.1.3.11})$$

Where A is the pre-exponential factor (1/min), R is the universal gas constant (8.314 J/molK) and E is the activation energy (kJ/mol).

Different models have been suggested to describe char gasification. The most studied are the volume reaction model (VRM), the shrinking core model (SCM), and the random pore model (RPM)^{76,77}.

The volume reaction model (VRM) assumes that the reaction proceeds homogeneously throughout the solid particles, resulting in linear variation of the reaction rate with respect to the conversion. Consequently, the reaction occurs at all active sites, which are hypothesized to be uniformly distributed⁶⁹.

4. Recovery of char from pyrolysis of mixed plastics

The equations that describe the reaction rate are the following (Eq. 4.1.3.12, 4.1.3.13):

$$\frac{dx}{dt} = k(1-x) \quad (\text{Eq. 4.1.3.12})$$

$$x = 1 - e^{-kt} \quad (\text{Eq. 4.1.3.13})$$

Where k is the kinetic constant and x the conversion.

The shrinking core model (SCM) assumes that the reaction occurs on the external surface of each grain, considered spherical in shape. The volume of the solid reactant decreases as the reaction progresses, leaving behind an ash layer through which the reacting gas diffuses. Consequently, the overall size of the particle remains constant over time. The reaction rate decreases over time, because of the decreasing of the active surface (Eq. 4.1.3.14, 4.1.3.15).

$$\frac{dx}{dt} = k(1-x)^{\frac{2}{3}} \quad (\text{Eq. 4.1.3.14})$$

$$x = 1 - (1-kt)^3 \quad (\text{Eq. 4.1.3.15})$$

The random pore model (RPM) assumes that during the gasification, the pores of the char are destroyed by competing pore growth and coalescing with neighboring pores. RPM is classified as one of the most realistic and acceptable approaches to predict gasification kinetics of char, where RPM can estimate maximum reactivity as the reaction proceeds in consideration with overlapping of pore surfaces of grains (Eq. 4.1.3.16, 4.1.3.17).

$$\frac{dx}{dt} = k(1-x)\sqrt{1-\psi \ln(1-x)} \quad (\text{Eq. 4.1.3.16})$$

$$\psi = \frac{4\pi L_0(1-\varepsilon_0)}{S_0^2} \quad (\text{Eq. 4.1.3.17})$$

Where L_0 , ε_0 and S_0 are the pores length, porosity and surface area of the solid at the beginning of the reaction.

The aim of this work was to explore the potential for valorizing char, by-produced from the pyrolysis of *plasmix*, through gasification via the Boudouard reaction, converting it into CO for use in syngas production. This approach could reintegrate this fraction of C into the plastic production chain, enhancing the overall carbon efficiency of the plastic recycling process. Valorizing the char through gasification could also streamline pyrolysis operations by eliminating the need to pelletize the char powder for alternative applications. Additionally, by utilizing CO₂ in the gasification process, this method could facilitate the recovery of this secondary byproduct, contributing to carbon capture and utilization strategies. To achieve this, four distinct chars were studied. The reference char, labelled VerChar, was obtained by Versalis SpA from the pyrolysis of different *plasmix* materials.

4. Recovery of char from pyrolysis of mixed plastics

Two chars were derived from VerChar with specific modifications: one involved adding PET to the *plasmix* to assess the influence of a more oxygenated plastic on the final char properties (labelled VerOx), and the other involved the addition of K_2CO_3 as a dehalogenating agent to evaluate the catalytic properties of ash enriched with potassium (VerK). The fourth char was a commercial char obtained by an external company (the name is omitted for confidentiality reason), and it was labelled CommChar. The chars were characterized through proximate and ultimate analyses, N_2 physisorption, and metal content evaluation to identify the key factors affecting reactivity. The gasification reactions were initially investigated using thermogravimetric analysis (TGA) under CO_2 at different temperatures, from which a kinetic model was developed for each sample. Kinetic constants and activation energies were subsequently calculated. The gasification experiments were further conducted in a semi-batch system to assess char conversion and CO production.

4.2 Experimental

Preparation of char samples

The plastic waste considered for the chemical recycling through pyrolysis, defined *plasmix*, complies with the UNI 2066-18 as secondary raw plastic materials by the definition “mixture of heterogeneous plastics based on polyolefins from industrial residues and/or post-consumer materials intended for the conversion into mixture of solid, liquid or gaseous hydrocarbons to be used as liquid and/or gaseous fuels or for further industrial chemical processes”⁷⁸.

The composition of this waste is variable by its nature, and the compositional range, including the average values, is indicated in Table 4.2.1.

Table 4.2.2. Average composition of plasmix.

Component	Wt. %		
	Min.	Max.	Average
PE	46.9	55.7	52.0
PP	23.1	27.4	24.0
PS	4.3	7.1	6.0
PET	4.0	8.5	6.5
PVC	0.7	1.6	1.0
PA	1.4	1.7	1.5
Paper pulp	3.5	6.8	5.0
Inerts (ash)	2.9	4.4	4.0

VerChar was obtained as a by-product of the pyrolysis process performed on the previously described *plasmix* in the laboratories of Versalis, following the procedure outlined in WO 2024/141843⁷⁹.

In brief, 25 g of ground *plasmix* were mixed with an appropriate amount of CaCO₃, employed as a dehalogenating agent. This mixture was introduced into a tubular reactor ($\varnothing = 19$ mm, $l = 30$ cm), equipped with a nitrogen flow meter at the bottom and a pressure-regulating valve at the top, and positioned within an electric furnace. The reactor was initially subjected to a nitrogen flow of 60 mL/min and heated to 240 °C. Once the temperature of 240 °C was reached, the nitrogen flow was halted, and heating continued to 380 °C at a pressure of 1 bar gauge. The reactor was maintained under these conditions for 3 hours. The temperature was then increased to 430 °C and held for an additional 3 hours. Finally, the temperature was raised to 480 °C and maintained until volatile production ceased, typically after 3 hours. VerOx was produced using the same pyrolysis procedure as VerChar, but with the *plasmix* containing an additional 20 wt. % of PET. VerK was obtained by pyrolyzing the same *plasmix* as VerChar, with the addition of 7 wt. % of K₂CO₃ as a dehalogenating agent. CommChar, a commercial char derived from the pyrolysis of a different *plasmix*.

4. Recovery of char from pyrolysis of mixed plastics

VerChar exhibited a particle size distribution with 50% of the particles below 10 μm , 30% within the 10–50 μm range, 10% between 50 and 100 μm , and the remaining 10% ranging from 100 to 500 μm . To ensure consistency across all samples, the other chars were sieved to match this distribution profile.

Characterizations of the chars

All chars were subjected to the following characterizations to evaluate the morphological and structural properties, as well as the chemical composition.

Proximate analysis, for the determination of volatiles, fixed carbon, and ash content, was conducted following the ASTM method D5142/02⁵⁴. The temperature program and the reaction gases used are reported in Table 4.2.2.

The analyses were performed using a thermogravimeter (TGA 550 Discovery TA Instruments).

Table 4.2.3. Temperature program for proximate analyses conducted in TGA.

T [°C]	Temperature ramp [°C/min]	N ₂ [mL/min]	Air [mL/min]
40-850	10	150	-
850	Isotherm – 10 min	150	-
850-400	20	150	-
400	Isotherm – 5 min	150	-
400-500	20	-	150
850	Isotherm - 10	-	150

Ultimate analysis was carried out with the UNICUBE Organic Elemental Analyzer (Elementar). The oxygen content was calculated by difference as follows (Eq. 4.2.1):

$$O\% = 100 - (\%C + \%H + \%N + \%S + \%ash) \quad (\text{Eq. 4.2.1})$$

The chemical composition and quantification of the ash was characterized using Microwave Plasma Optical Emission Spectroscopy (MP-OES) after the demineralization of the samples. The samples were digested using a solution consisting of aqua regia (HCl 3:1), hydrogen peroxide, and hydrofluoric acid in an Ethos UP Microwave digester at a power of 1800 W, a temperature of 210°C, for 35 minutes. The textural properties were evaluated through N₂ physisorption. The measurement was performed using a Tristar II Plus Micromeritics instrument at -196°C. Prior to the analysis, the sample was pretreated at 200°C under vacuum for 2 hours. The specific surface area was calculated using the Brunauer Emmett Teller (BET) equation.

Additionally, VerChar, that was considered the reference sample, was subjected to the following characterizations. Particle size distribution was determined using the Mastersizer 2000 Laser Diffraction instrument, with the carbonaceous material being assigned a refractive index of 2.42.

4. Recovery of char from pyrolysis of mixed plastics

Temperature Programmed Desorption (TPD) analysis was conducted using a custom lab-made instrument, with the effluent gases analyzed by a Micromeritics TPDTPR 2900 equipped with a TCD detector (Gow-Mac 24-550 TCD, Bethlehem, PA, USA). The char was subjected to heating from 25 to 1000 °C at a ramp rate of 10 °C/min under He, at a flow rate of 40 mL/min. The pH of the char was measured following the ASTM D3838-80 protocol. Fourier Transformed Infra-Red Spectroscopy (FT-IR) analysis was performed using a Perkin Elmer Spectrum One spectrometer over the range of 400 to 4000 cm^{-1} with a resolution of 4 cm^{-1} . The sample was analyzed in the solid state, with KBr used to prepare the pellet. Char morphology was assessed using Scanning Electron Microscopy (SEM) coupled with Energy-Dispersive X-ray Spectroscopy (EDX), which provides information on the chemical composition and element distribution within the sample. Analyses were conducted using a FE-SEM LEO 1525 ZEISS (Jena, DE). The acceleration voltage was maintained at 15 keV, and measurements were performed using both the AsB and In-lens detectors. The samples were mounted on conductive carbon adhesive and coated with a chromium sputter coating. Elemental composition and chemical mapping were determined using the Bruker Quantax EDX detector.

CO₂ reactivity tests

Preliminary reactivity tests were conducted in a thermogravimetric instrument (TGA 550 Discovery TA Instruments) at atmospheric pressure on VerChar, VerOx, VerK and CommChar. Approximately 10 mg of char were used for each experiment. CO₂ was used as carrier gas, at a flow rate of 40 mL/min. The temperature ramp was composed of an isotherm step at 40 °C for 5 minutes to equilibrate the system, a ramp of 10 °C/min up to the desired temperature (between 700 °C and 850 °C), followed by an isotherm step with variable time (between 240 to 360 min, depending on the temperature).

The char conversion was calculated as (Eq. 4.2.2):

$$X_{daf} = \frac{m_0 - m_t}{m_0 - m_{ash}} \quad (\text{Eq. 4.2.2})$$

Where X_{daf} = conversion on a dry ash free basis, m_0 in the initial mass of the char, m_t the mass of the char at time t , and m_{ash} the mass of the ashes, calculated by the proximate analysis.

The VRM model was used to determine the reactive behavior of the chars. Reaction rate is expressed as Eq. 4.1.3.13. The apparent reaction rate k can be expressed as Eq. 4.1.3.12.

The chars were subjected to reaction with CO₂ in a semibatch system, in a small laboratory set-up, as described below. A schematic representation of the semi-batch system is reported in Figure 4.2.1.

4. Recovery of char from pyrolysis of mixed plastics

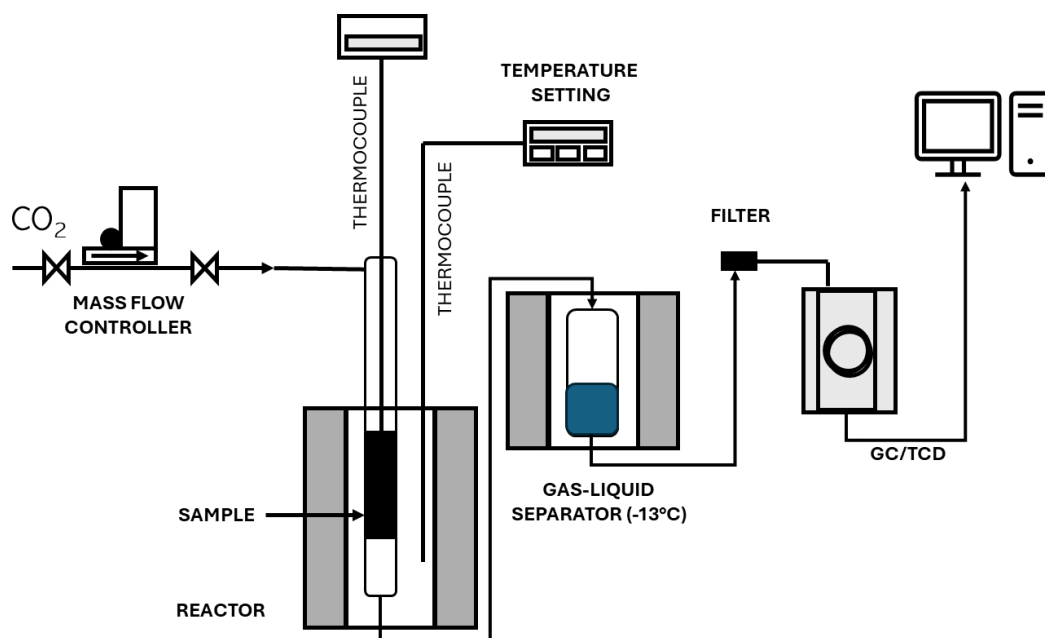


Figure 4.2.1. Semi-batch system for gasification of chars via Boudouard reaction.

In each experiment, approximately 100 mg of char were placed in a tubular quartz reactor with an inner diameter of 10 mm and a length of 200 mm, equipped with a quartz wool septum, positioned midway through the tube. The reactor was placed inside an electric furnace (Micromeritics), equipped with control thermocouples, and connected at the inlet to mass-flow controllers (Brooks 5859) to regulate the supply of gases (He degree of purity 4.8, CO₂ degree of purity 5.5. or the mixture 16 % CO/CO₂ degree of purity 5.5, purchased by SIAD). At the reactor outlet, a cold trap filled with 2-propanol at – 13 °C was installed to capture the condensable fraction, followed by an anhydrous trap to remove water, and finally to a gas chromatograph (GC) (Agilent Technologies, model GC1540A) coupled with a thermal conductivity (TCD) detector, for gas analysis. The GC was equipped with two columns, a Porapak B column (2.5 m long) for CO₂ analysis, and a molecular sieve column (5 m long) for CO, H₂, CH₄ analysis. The gas analysis conditions were as follows: carrier gas carrier He, pressure: 63 psi, temperature ramp: 35 °C x 0.7 min, increased to 75 °C in 1 min, followed by an isothermal hold at 75 °C for 4 minutes, cooled to 35 °C, and held isothermally 35 °C for 2.2 minutes. Gas sampling occurred continuously, with an interval between samples of approximately 18 minutes, allowing for complete analysis. In a typical experiment, the reactor was purged with He until all air signals disappeared. The reactor was then heated from room temperature to 50 °C below the target reaction temperature under a flow of CO₂ at a rate of 10 °C/min, followed by a slower ramp of 5 °C/min to the reaction temperature. The reactor was maintained at the desired temperature for 260 minutes before being cooled under He flow.

4.3 Results and discussion

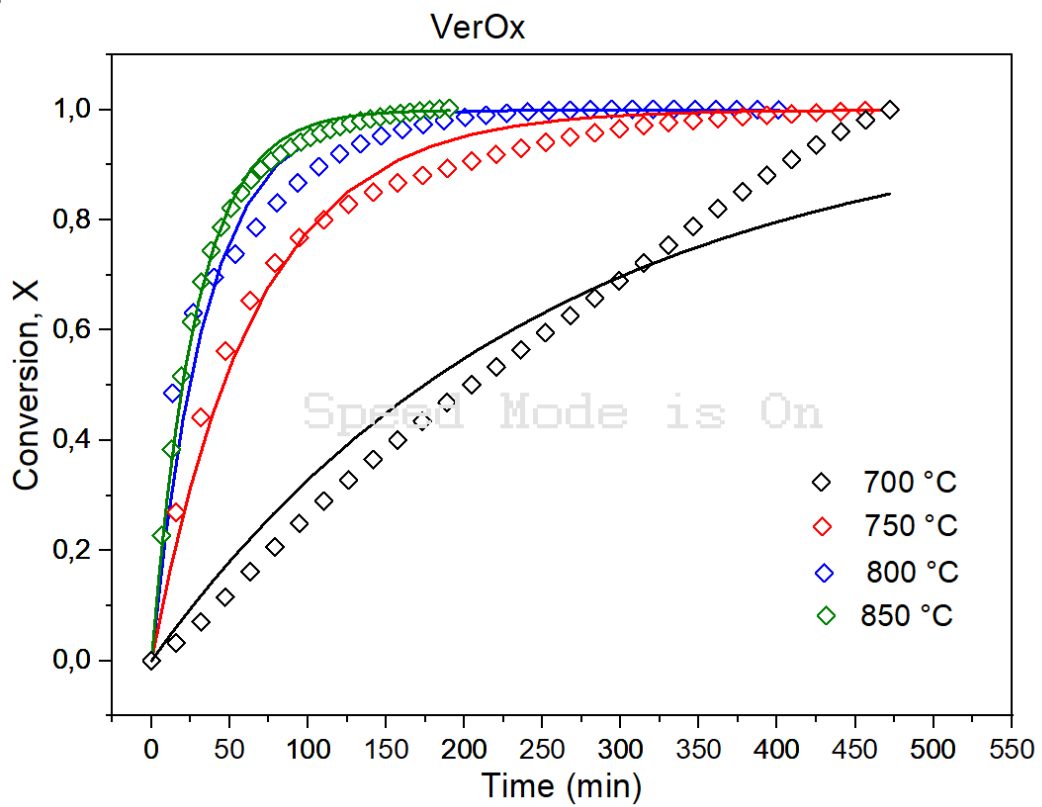
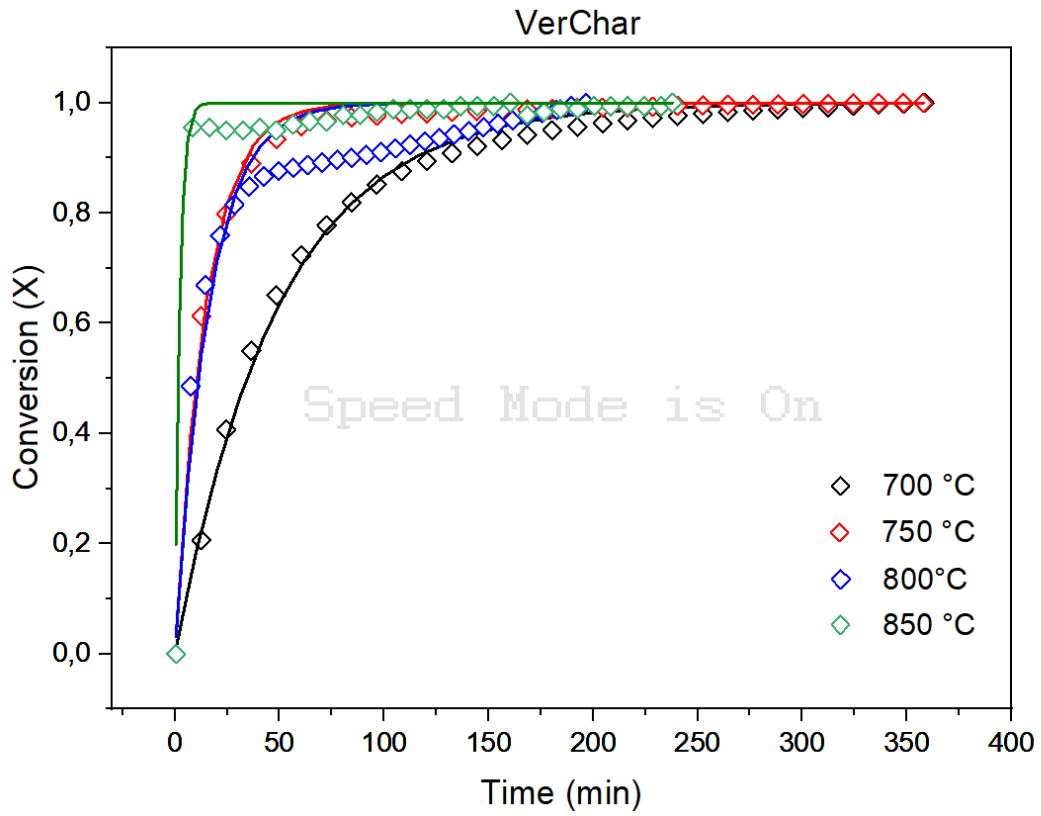
Chars characterizations and kinetic investigation via TGA

The VerChar, CommChar, VerOx and VerK were subjected to gasification in presence of CO₂ at varying temperatures ranging from 700 to 850 °C. The reaction was monitored by TGA, and when possible, it was carried out until the complete conversion.

Figure 4.3.1 shows the experimental conversion (X) versus time (t) profiles, calculated as in Eq. 4.2.2 (expressed by symbols) along with fitted curves obtained using the VRM kinetic model (solid lines) of each char at 700, 750, 800, and 850 °C. VRM was used to calculate the kinetic constants and activation energies of the processes, and to compare the results with the literature data. Molina *et al.*⁷⁴ reported that the efficiency of kinetic model to predict the reaction rate depends on the char characteristics, and on the experimental conditions. Most of the studies reported the RPM as the most suitable model for describing the gasification of chars both in presence or absence of a catalyst⁵⁷. VM and the SCM do not take into account structural changes of char during the gasification, and they consider the process to be controlled by the chemical reaction. In this work the reactions are carried out at low temperatures (under 900 °C), therefore reaction rate can be considered controlled by the chemical reaction step. The goal of the work is to describe the relation between time and conversion, therefore VRM was preferred for their mathematical simplicity^{80,81}. In general, VRM provided a good fit for the gasification behavior of the chars, with high correlation coefficients.

From the results obtained it is clear that conversion is strongly influenced by temperature. As the temperature increases, the reaction rate accelerates for all samples, with a notable increase in reactivity between 700°C and 750°C. However, the total reaction time required to achieve complete conversion varies significantly among the different chars. This was attributed to the different characteristics of the chars.

4. Recovery of char from pyrolysis of mixed plastics



4. Recovery of char from pyrolysis of mixed plastics

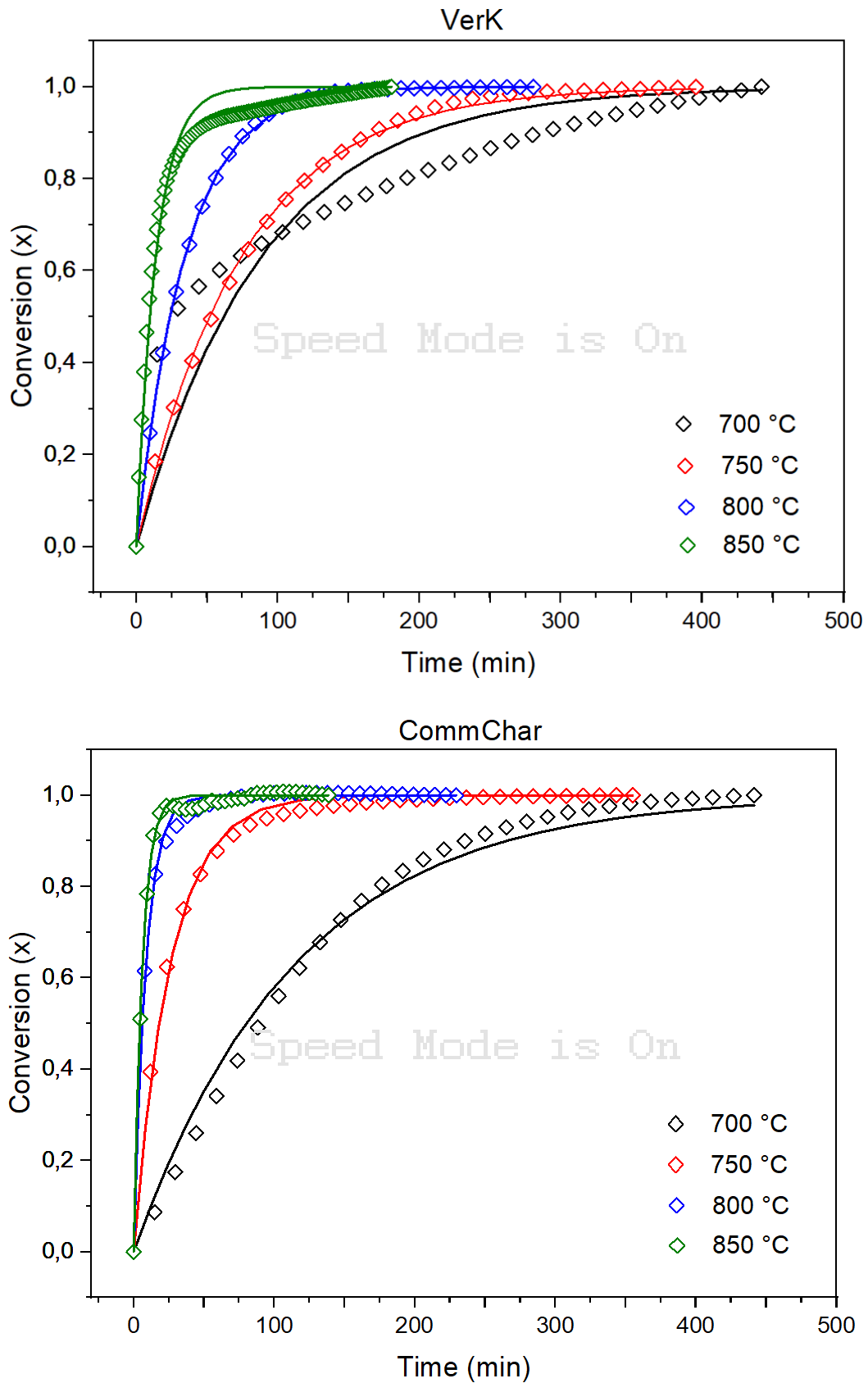


Figure 4.3.1. Experimental conversion of the chars over time at different temperatures (symbols) and fitting of the curves obtained by the VRM model. In order: VarChar, VerOx, VerK, and CommChar. Black= 700 °C, red = 750 °C, blue = 800 °C, green = 850 °C.

4. Recovery of char from pyrolysis of mixed plastics

Figure 4.3.2 shows the Arrhenius plots for the four chars, used to derive the kinetic parameters of the reaction rate constants. The linear relationship between $\ln(k)$ and $1/T$ confirms that the reactions follow Arrhenius behavior. The corresponding activation energies (E_a) and pre-exponential factors (A) are presented in Table 4.3.1. VerK and VerOx exhibit lower activation energies (130 and 160 kJ/mol respectively) compared to VerChar and CommChar, which have similar E_a values (180 kJ/mol).

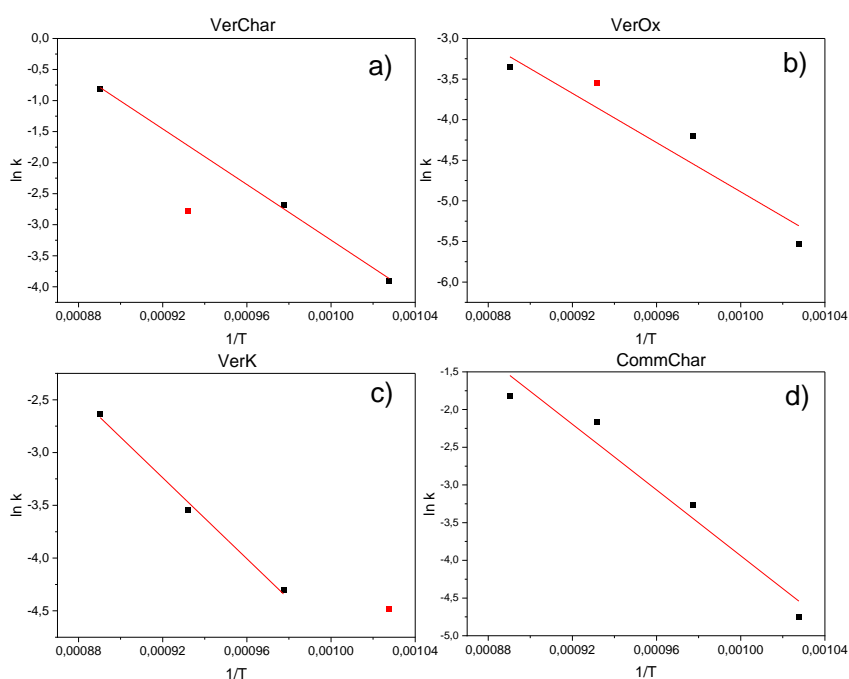


Figure 4.3.2. Arrhenius plots for the four chars a) VerChar, b) VerOx, d) VerK, e) CommChar.

Table 4.3.1. Pre-exponential factors and activation energies of VerChar, VerOx, VerK, and CommChar gasification with CO_2

Char	A	E_a (kJ/mol)
VerChar	$1.4 \cdot 10^7$	186 ± 6
VerOx	$6.3 \cdot 10^4$	130 ± 36
VerK	$1.1 \cdot 10^4$	160 ± 12
CommChar	$5.8 \cdot 10^7$	180 ± 27

In all cases, the results are in line with the activation energies reported in literature for the gasification of various coals⁴⁵. For instance, Kim *et al.*⁶⁹ examined 12 different coals, calculating activation energies at both high reaction temperatures (> 1150 °C) and lower temperatures. They found distinct values for E_a depending on whether the reaction was controlled by chemical kinetics or by pore diffusion, the latter becoming the rate-limiting step at higher temperatures. In the chemical regime, the E_a ranged from 126.9 to 207.6 kJ/mol, with pre-exponential factors between 4.1×10^4 and 1.4×10^7 , values consistent with those obtained in this study. Similarly, Zhang *et al.* investigated the gasification of 6 anthracite chars between 920 and 1050 °C, reporting activation energies between 140 to 202 kJ/mol⁸¹. Ahn *et al.* reported

4. Recovery of char from pyrolysis of mixed plastics

values of 144 kJ/mol for a subbituminous coal char gasified at 900-1000 °C⁷⁵. Similar values were found by Jansen *et al.* and Zhang *et al.*, for the gasification of waste tires derived chars^{56,82}.

Notably, compared to other coals investigated in literature for the gasification via Boudouard reaction, the considered chars derived from *plasmix* achieved extremely high conversions at lower temperatures. For example, the ENEA Report assessed that a minimum temperature of 900 °C was necessary to achieve good conversions of the considered coals⁵⁴, and Jansen *et al.* reported similar temperature ranges for the gasification of waste tires derived chars, to achieve around 85 % conversion⁵⁶. These findings are highly promising, as achieving high conversion rates at lower temperatures translates to reduced energy demands and, consequently, lower operational costs, including savings on plant construction materials. Operating at approximately 800 °C allows for the use of more cost-effective materials than those required for higher-temperature applications, while also enabling the adoption of simplified technological solutions.

As already mentioned, the reaction rate of char is affected by its intrinsic characteristics such as particle size and surface area, VM, FC, and chemical composition, as well as alkali content⁵⁵. Therefore, the chars were subjected to different characterizations to highlight the main features influencing the reactivity. Surface areas, proximate and ultimate analyses, as well as mineral content and alkali index of the chars are reported in Table 4.3.2.

The textural properties of the materials, evaluated through N₂ physisorption (isotherms reported in Appendix, Figure 4.5.1), suggest that all materials are essentially non-porous, as indicated by the low BET surface area values. While it is generally understood that in gas-solid reactions, porosity affects the accessibility of gas to the reactive surface, there is ongoing debate regarding the specific influence of microstructural properties for this specific reaction. For example, Scott *et al.*, demonstrated that the micropores, which constitute most of the surface area of activated carbon, are largely unreactive during gasification⁸³. However, for coals with low surface area⁶⁹, particle granulometry is a critical factor affecting the progression of Boudouard reaction. Adequately small particles are required to mitigate limitations associated with heat transfer and CO₂ diffusion within the particles. Moreover, in large particles, at high conversion levels, the CO concentration inside the particles may inhibit further reaction progress⁸⁴. Mani *et al.*⁸⁵ investigated the influence of particle size (ranging from 60 to 925 μm) on the gasification reactivity of wheat straw biochar and demonstrated that the reactivity increases as particle size decreased.

However, for chars in which the pore surface is much higher than the external surface area, this effect becomes less pronounced, as the number of active sites is independent from the particle size⁶³. Given

4. Recovery of char from pyrolysis of mixed plastics

the low surface areas of all the chars studied this parameter was excluded from considerations in explaining reactivity differences. Instead, emphasis was placed on the other characteristics.

Table 4.3.2. Chars surface areas, proximate and ultimate analysis, metal content and alkali index.

	VerChar	VerOx	VerK	CommChar
Surface area (m²/g)	8	8	9	n.d.
Proximate analysis (wt. %)				
Moisture	4.2	3.7	10.8	3.2
Volatile Matter	22.8	23.0	35.8	43.8
Fixed Carbon	40.9	46.2	26.3	25.6
Ash	32.1	27.1	27.1	27.4
Ultimate analysis (wt. %)				
Carbon	55	65.4	35.4	52.4
Hydrogen	2.6	2.2	1.8	3.7
Nitrogen	0.8	0.9	0.7	2.6
Sulfur	0.4	0.4	0.4	0.4
Oxygen	9.1	4.0	2.4	6.4
H/C	0.047	0.034	0.051	0.071
O/C				
Mineral content (mg/g)				
Si	110.42	106.50	91.09	119.57
Ca	77.80	77.20	42.10	90.60
Ti	31.90	26.60	15.80	14.50
Al	14.70	11.00	6.10	11.90
Na	11.50	12.70	6.20	9.30
Mg	4.36	3.80	2.23	5.10
Fe	4.33	3.80	1.99	30.20
K	3.54	5.10	235.80	6.70
Mo	0.26	0.23	0.18	0.15
Zr	0.16	0.05	0.03	0.44
Cr	0.11	0.05	0.10	0.36
Cu	0.06	0.34	>0.05	>0.05
Ni	0.05	0.05	>0.05	0.20
Mn	0.05	0.03	>0.05	0.23
Alkali index	18.3	15.6	100.1	24.7

For all the chars, proximate analysis indicated a volatile content of between 23 and 43 %, attributable to tarry compounds that were not devolatilized during pyrolysis. The volatile % is relatively high if compared to biochars derived from the pyrolysis of biomasses⁸⁶, probably due to the lower pyrolysis temperature used for plastic feedstocks (400-500 °C), in order to maximize the amount and quality of the oil fraction. Indeed, the pyrolysis conditions for the pyrolysis of these *plasmix* are optimized for oil production, and not all the volatile fraction is removed from the char, thus remaining in the solid fraction. The VM % is also correlated with the H/C ratio; H/C ranges between 0.034 and 0.071, values almost double the one of the lignocellulosic biochars, that are obtained at high temperatures (700°C) and low heating rate (5°C/min). In particular, a higher amount of volatiles was found in CommChar (VM = 43.8 wt. %, H/C = 0.071), that was prepared at unknown conditions, being a commercial sample. VerChar and VerOx displayed almost the same amount of volatiles (~23 wt. %), that instead resulted higher in VerK (35.8 %).

4. Recovery of char from pyrolysis of mixed plastics

This difference can be attributed also to the high amount of K present in VerK, as demonstrated by the ICP analyses of the ashes, that could catalyze the char decomposition. Anyways, the volatile content resulted similar or lower than values reported for other plastic-derived chars^{87,88}. For instance, Jamradloedluk *et al.*³⁴ reported a VM content of 51.40 % in a char obtained by the fast pyrolysis of HDPE plastic wastes. Yousef *et al.*⁶⁴ reported a volatile content of 41.5% in char derived from metallized food packaging, which decreased to 18% following treatment with H₂SO₄ at 150 °C to remove metals. As an example, anthracite, that is the coal with the lower volatile matter content, ranges between 2 to 12%, bituminous and lignite coals range between 15-45% and 24-32 % respectively^{89,90}. The % of VM and fixed carbon (FC) are directly correlated to the coalification ranking, that is an important parameter to determine char reactivity towards gasification. High-rank coals corresponds to char with high % of FC and result in elevated thermal stability, and therefore lower reactivity than low-rank coals⁶⁰. On the other hand, chars with higher VM tend to be more reactive, likely due to the development of a porous structure during devolatilization, which enhances the concentration of active sites, as C atoms at the edges⁶⁹. As shown in the CO₂ TGA curves (Appendix, Figure 4.5.2), volatile matter is predominantly released between 570 and 650 °C, prior to the onset of CO₂-char reactions. During this devolatilization step the structure of the char could undergo to textural modifications, with an enhancement of the surface area and a increase of active sites for the gasification reaction to occur^{45,91}.

However, Lampropoulos *et al.*⁹² conducted the pyrolysis of a Greek lignite at different temperatures (300, 500 and 800 °C) to modify the coalification ranking, enhancing the fixed carbon content. These chars, along with the raw lignite were subjected to gasification, and the char produced at 800 °C exhibited superior gasification performance. This was attributed to a more disordered surface, that provided more active sites for the reaction to occur.

Ultimate analysis revealed that the samples are primarily composed of carbon (between 35 to 65 %), with smaller but notable amounts of heteroatoms, especially O (from 2 to 9 %). The presence of oxygen is attributed to the depolymerization of oxygenated polymers such as PET, or contaminants like cellulose from paper pulp. CommChar exhibited the highest nitrogen content, likely due to a higher proportion of nitrogen-containing plastics, such as polyamide (PA), in the *plasmix*. The low sulfur content (0.4%) in all samples is favorable for gasification, as it reduces the potential for toxic emissions like SO₂⁶⁴. The presence of heteroatoms into the char structure enhances surface chemistry, catalytic behavior, and gasification kinetics by creating highly reactive sites, particularly in aromatic clusters, which serve as initiation points for the Boudouard reaction and significantly increase reactivity compared to regular carbon atoms⁴⁵.

4. Recovery of char from pyrolysis of mixed plastics

The overall gasification process can be viewed as a combination of non-catalytic and catalytic reactions, influenced by both the physicochemical properties of the char and its mineral content. Non-catalytic gasification is primarily governed by char properties, while catalytic gasification is strongly influenced by alkali and alkaline earth metals, which are abundant in low-rank coal and biomass chars. The addition of elements such as K and Ca has been shown to significantly increase CO₂ uptake, indicating that alkali metals contribute to the concentration of active sites on the char surface⁵⁹. Interestingly, all chars displayed high ash content, around 30 wt. %. The ICP analyses demonstrated in all chars high % of alkali metals, especially Ca (and K in the case of VerK), added during the pyrolysis as dehalogenating agents, but also Na, Mg, and Fe, deriving from pigments, additives, or contaminants found in plastic wastes. Notably, the ashes presented also high % of Si and Al, that are detrimental for the catalytic activity of the alkali metals, because they can form inactive aluminate and silicate species, reducing the availability of the alkali for the Boudouard reaction^{93,94}. Therefore, the alkali index was calculated as proposed by Sakawa *et al.*⁶⁷, to quantify and compare the catalytic abilities of the minerals present in the ashes. The results reported in Table 4.3.2 showed comparable index values for VerChar, VerOx and CommChar, between 15 to 25. VerK demonstrated a much higher value, due to the presence of a high amount of K. Nevertheless, compared to results reported in literature, the alkali index of these chars resulted quite high. For example, Kim *et al.*⁶⁹ reported the alkali index of 12 different bituminous coals, that never exceeded 5. The alkali index of various lignocellulosic biochars, reported by Duman *et al.*⁷², assessed around 1, and the values reported for three South Africa coals by Hatting *et al.*⁶⁸ were between 4.2 and 6.5.

Despite the significantly higher alkali index of VerK, its kinetic parameters do not differ substantially from the other samples. While K and Na are known to enhance catalytic activity, Ca provides advantages such as lower volatility and reduced risk of agglomeration during gasification^{95,96}. K species present during gasification, such as K₂CO₃, K₂O, or metallic K, have lower melting points compared to their calcium counterparts (m.p. K₂CO₃: 891 °C, CaCO₃: 825 °C, K₂O: 740 °C, CaO: 2613 °C, K: 63.5 °C, Ca: 842 °C), which could result in the formation of a resistant layer in VerK, that hinders gas diffusion⁹⁷.

However, as displayed in Figure 4.3.3, plotting the rate kinetic constants (at 750 °C) of each char vs key characteristics of the chars, such as VM, Al, C% and heteroatoms %, did not reveal a clear linear correlation. This suggests that the overall gasification process is governed by a complex interplay of multiple char properties rather than by any single factor alone.

4. Recovery of char from pyrolysis of mixed plastics

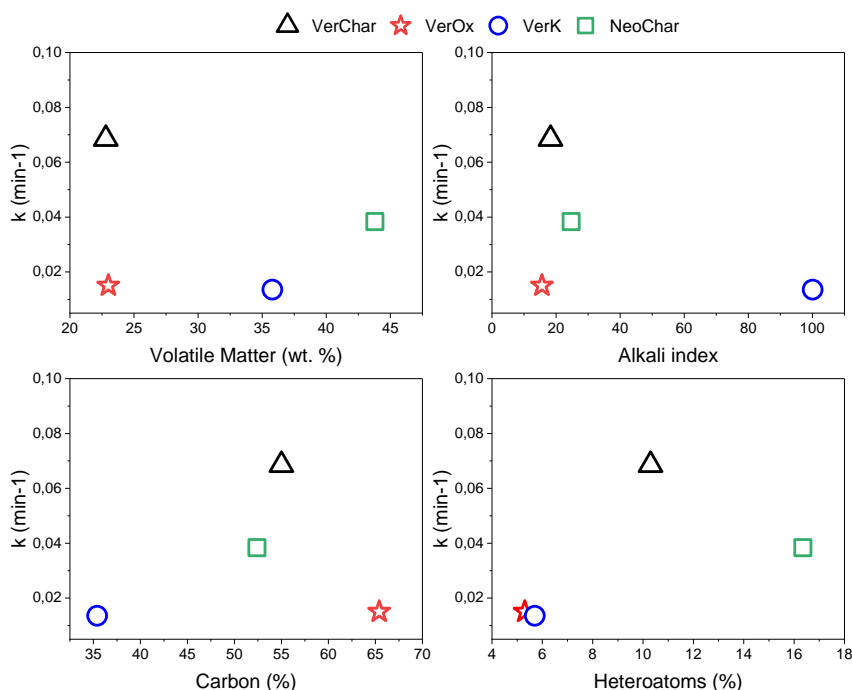


Figure 4.3.3. Correlation between the kinetic constant of each char at 750 °C) to its main chemical physical characteristics (VM, FC, %C, AI).

Anyways, compared to other gasification processes reported in the literature, the results obtained from these plastic-derived chars were promising. Preliminary TGA screening demonstrated that all chars could be quantitatively converted at lower temperatures than those typically reported. Notably, efficient conversion was achieved at 750°C, indicating that these chars perform well under milder conditions than commonly seen in similar studies.

Given the promising results, semi-batch experiments were conducted at varying temperatures and CO₂ flow rates to maximize the CO concentration in the outlet gas mixture. These experiments aimed to further explore the potential of the plastic-derived chars under controlled conditions, building on the insights gained from the TGA screening.

Semi-batch gasification experiments

Most of the experiments were conducted on the reference char, VerChar, with comparative analysis conducted on VerOx, VerK, and ComChar. VerChar was subjected to gasification in the semi-batch system, investigating the effect of temperature and CO₂ flow rate in the production of CO.

As shown in Figure 4.3.5a, the temperature was varied from 700 to 850 °C, with a constant CO₂ flow rate of 20 mL/min.

4. Recovery of char from pyrolysis of mixed plastics

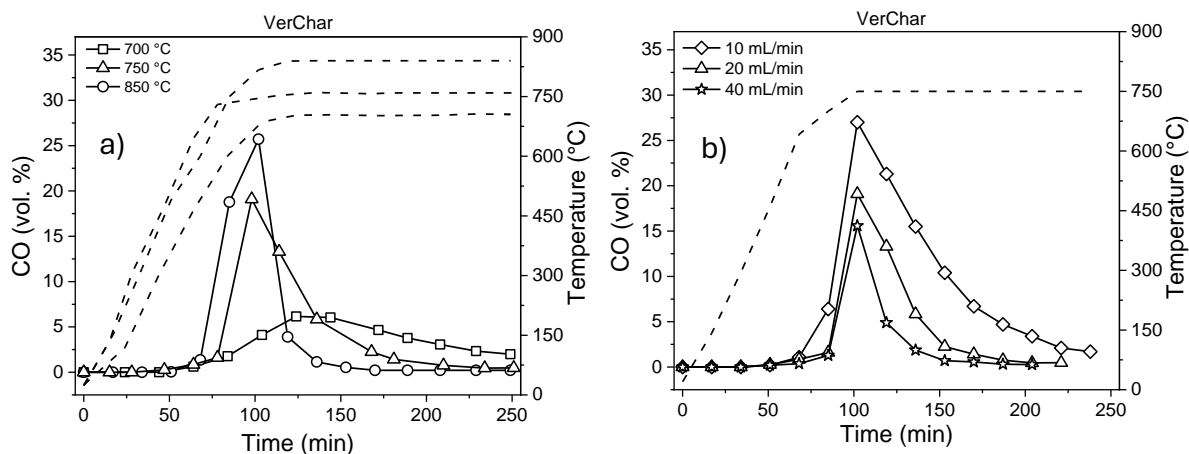


Figure 4.3.5. CO evolution profiles during VerChar gasification under different conditions. a) 100 mg char, CO₂ flow rate: 20 mL/min, variable temperature. b) 100 mg char, fixed temperature: 750 °C, variable CO₂ flow rate. The dashed lines indicate the temperature ramps.

The reaction rate showed a positive correlation with temperature, consistent with TGA analyses. At 700 °C, the CO maximum volume was registered at approximately 130 minutes, while by increasing the temperature, the CO max. peak was shifted at shorter times (around 100 minutes). Another indication of an increased reaction rate with the increase of temperature was associated with the CO max. vol. % value, that was higher at 850 °C, passing from 6 % at 700 °C, to 19 % at 750 °C, up to 26 % at 850 °C (Table 4.3.3, entries 1,2,3). After reaching the maximum, CO concentration declined as char consumption progressed, with a sharper decline observed at higher temperatures, indicating faster char consumption.

The overall char conversion was calculated at the end of the reaction using Eq.4.2.2. Conversion rates followed the same trend, increasing from 76% at 700°C to 93% at 750 °C, and nearly complete (>99%) conversion at 850°C, as summarized in Table 4.3.3, entries 1,2,3. Thus, 750 °C was considered the minimum temperature required to achieve high conversion rates and significant CO concentrations.

The effect of CO₂ flow rate on CO production was evaluated to optimize CO yield at a moderate reaction temperature. Therefore, experiments were conducted at 750 °C with CO₂ flow rates of 10, 20, and 40 mL/min, as shown in Figure 4.3.5b. The CO₂ flow rate significantly affected maximum CO concentration, with 27% CO achieved at 10 mL/min, but only 16% at 40 mL/min. While higher flow rates led to faster CO removal, they also resulted in lower overall conversion (85% at 40 mL/min) (Table 4.3.3, entries 2,4,5). This suggests limited CO₂ diffusion at higher flow rates, impeding complete gasification.

Gasification experiments at 750°C and 20 mL/min were conducted on VerOx, VerK, and CommChar (Figure 4.3.6). VerOx and CommChar displayed similar trends to VerChar, with maximum CO concentrations of 15% and 13%, respectively, both peaking at around 100 minutes (Table 4.3.3, entries

4. Recovery of char from pyrolysis of mixed plastics

6,8). VerK, however, exhibited a different behavior, with a faster reaction rate and a peak CO concentration of 20% at 85 minutes (Table 4.3.3, entry 7). This different trend was attributed to its high alkali index and K content, which enhances catalytic activity. Indeed, preliminary TGA analyses confirmed that VerK had the lowest activation energy, likely due to the catalytic effect of the ashes. However, this pronounced difference was not fully reflected in the TGA results, possibly due to interference from a mineral layer limiting CO₂ diffusion during gasification in the TGA setup. This issue seemed less significant in the semi-batch system, where a larger reactor allowed for better gas interaction. To verify VerK superior reactivity, additional experiments were conducted at 700°C and 650°C. VerK achieved over 90% conversion at 700°C, with CO volumes comparable to other chars at 750°C. However, at 650°C, the reaction slowed significantly, reaching only 75% conversion with a peak CO concentration of 11% (Table 4.3.3 entries 7,9,10). These results confirmed the beneficial effect of K in gasification, allowing lower temperature operation, which could lead to energy savings and reduced equipment costs.

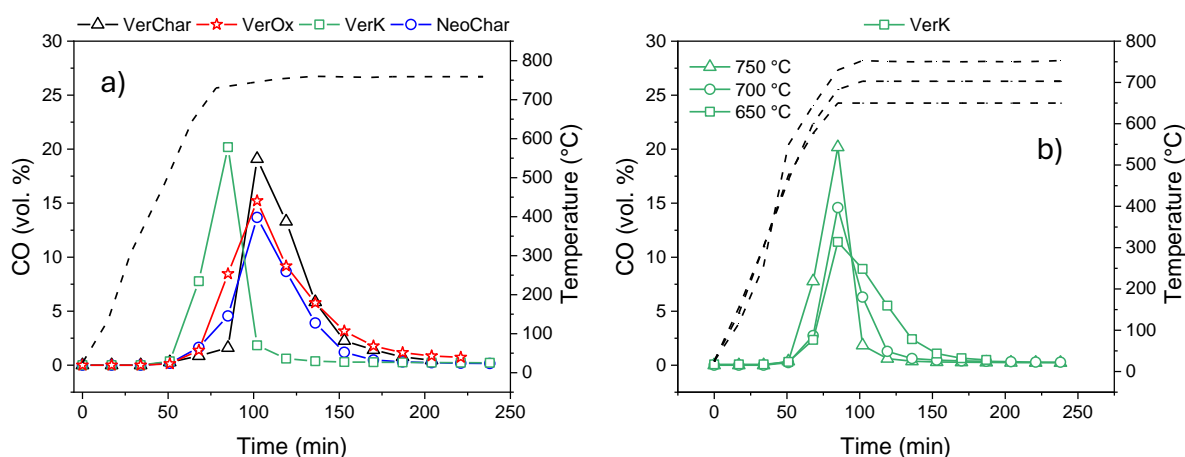


Figure 4.3.6. a) CO evolution profiles during different chars gasification. Reaction conditions: 100 mg char, 750 °C, CO₂ flow rate 20 mL/min. b) CO evolution profiles of VerK gasification at different temperatures. Reaction conditions: 100 mg char, CO₂ flow rate 20 mL/min. The dashed lines indicate the temperature ramps.

To assess the potential for scaling up to industrial levels, the possibility of recycling the outlet gases to increase CO concentration was evaluated. A simulation was performed by feeding the reactor with a gas mixture of 15% CO in CO₂ and conducting the reaction under the same conditions (750°C, 20 mL/min, 240 min). The results (Figure 4.3.7a, entry 11 in Table 4.3.3) showed that the conditions employed were still far from equilibrium, and 90% conversion of VerChar was achieved, increasing the maximum CO concentration to 32%. This suggests that recycling the outlet gas could significantly increase CO production, improving the CO/CO₂ separation step in an industrial process, as schematized in Figure 4.3.7b.

4. Recovery of char from pyrolysis of mixed plastics

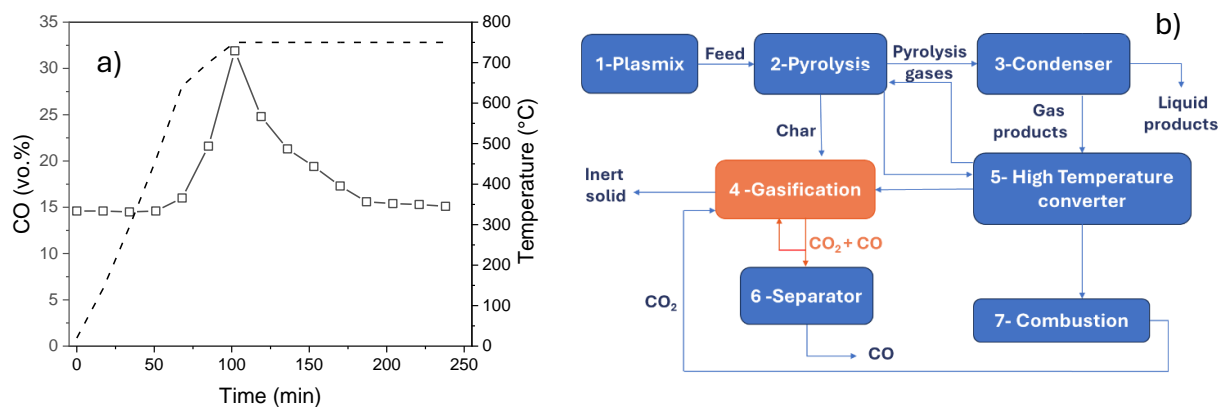


Figure 4.3.7. a) CO evolution profile during VerChar gasification, Reaction conditions: 100 mg char, 750 °C, 16% CO in CO₂ total flow rate: 20 mL/min, b) scheme of a plant of plasmix pyrolysis coupled with the gasification of the char, with the recycling of the gas.

Table 4.3.3. Summary of temperature and flow rate effects on conversion and CO production on the gasification of VerChar, VerOx, VerK, and CommChar.

Entry	Char	T (°C)	CO ₂ flow rate (mL/min)	Conversion (%)	CO(max) (vol. %)
1	VerChar	700	20	76	6
2	VerChar	750	20	93	19
3	VerChar	850	20	>99	26
4	VerChar	750	10	>99	27
5	VerChar	750	40	85	16
6	VerOx	750	20	90	15
7	VerK	750	20	>99	20
8	CommChar	750	20	90	13
9	VerK	700	20	93	15
10	VerK	650	20	75	11
11	VerChar	750	20 ^a	90	32

^a 15 % CO in CO₂

4.4 Conclusions

This chapter presents an innovative approach to char gasification via Boudouard reaction, exploring for the first time the use of chars derived from the pyrolysis of mixed plastic waste, and giving a significant contribution to the field of sustainable plastic recycling. Through a series of thermogravimetric and semi-batch experiments, it was demonstrated that these plastic-derived chars can achieve high conversion rates at relatively low temperatures, significantly lower than those required for other types of chars such as those derived from coal or biomass. This lower operational temperature not only reduces the energy input and costs associated with the process but also enhances sustainability by lessening the need for high-temperature-resistant equipment.

The experimental results show that at 750 °C, over 90% of all the char tested was successfully converted via the Boudouard reaction, with the generation of carbon monoxide (CO) as a valuable product. Comparative tests among different chars confirmed that the addition of Ca_2CO_3 had the double positive effect to avoid the releasing of chlorinated toxic gases during pyrolysis, and to catalyze the Boudouard reaction. The addition of K_2CO_3 further improved gasification efficiency and facilitated higher reactivity at even lower temperatures, underscoring the potential for energy savings and optimized process performance. Furthermore, variations in CO_2 flow rates revealed an ability to optimize CO production, which holds promise for scalable CO capture and utilization strategies in industrial settings.

In addition to the technical findings, this research has culminated in a patent filing (WO2024/141843), recognizing the originality and industrial relevance of this approach to char valorization. This patent formalizes a process that not only addresses a pressing environmental need for effective plastic waste management but also aligns with circular economy principles by reintegrating recovered carbon into chemical and fuel production chains.

This work laid the foundation for a new and feasible pathway in chemical recycling that is both sustainable and industrially applicable, with promising economic and environmental benefits for the future.

4.5 Appendix

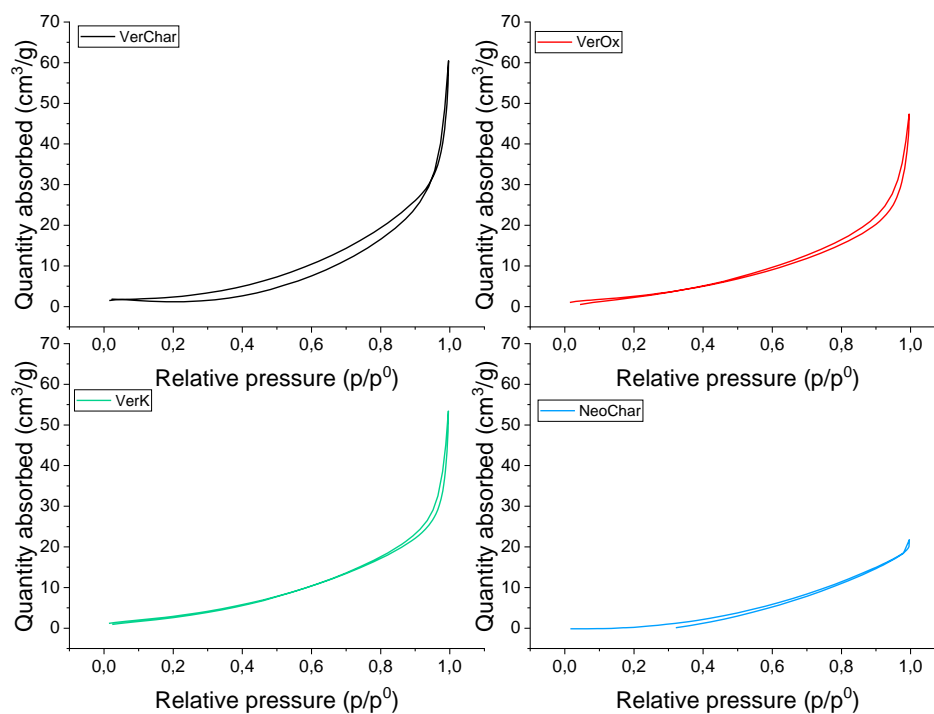


Figure 4.5.1. N₂ adsorption-desorption isotherms of the chars.

Proximate analysis

The proximate analysis provides a standardized procedure to determine moisture content, volatile matter, fixed carbon, and ash using thermogravimetric analysis (Figure SXX). In the first stage, the sample is heated to 850 °C under an inert nitrogen atmosphere, during which moisture and volatile matter are released. In the second stage, the char is cooled and reheated from 400 to 850 °C under air, promoting total combustion. The inorganic residue remaining after combustion constitutes the ash content, while the fixed carbon is calculated by weight difference. Ultimate analysis complements this by providing the elemental composition in terms of carbon, hydrogen, nitrogen, sulfur, and oxygen. Together, the volatile matter, fixed carbon, and the hydrogen-to-carbon (H/C) ratio provide insights into the coalification rank of the chars, indicating their level of carbonization and potential reactivity.

4. Recovery of char from pyrolysis of mixed plastics

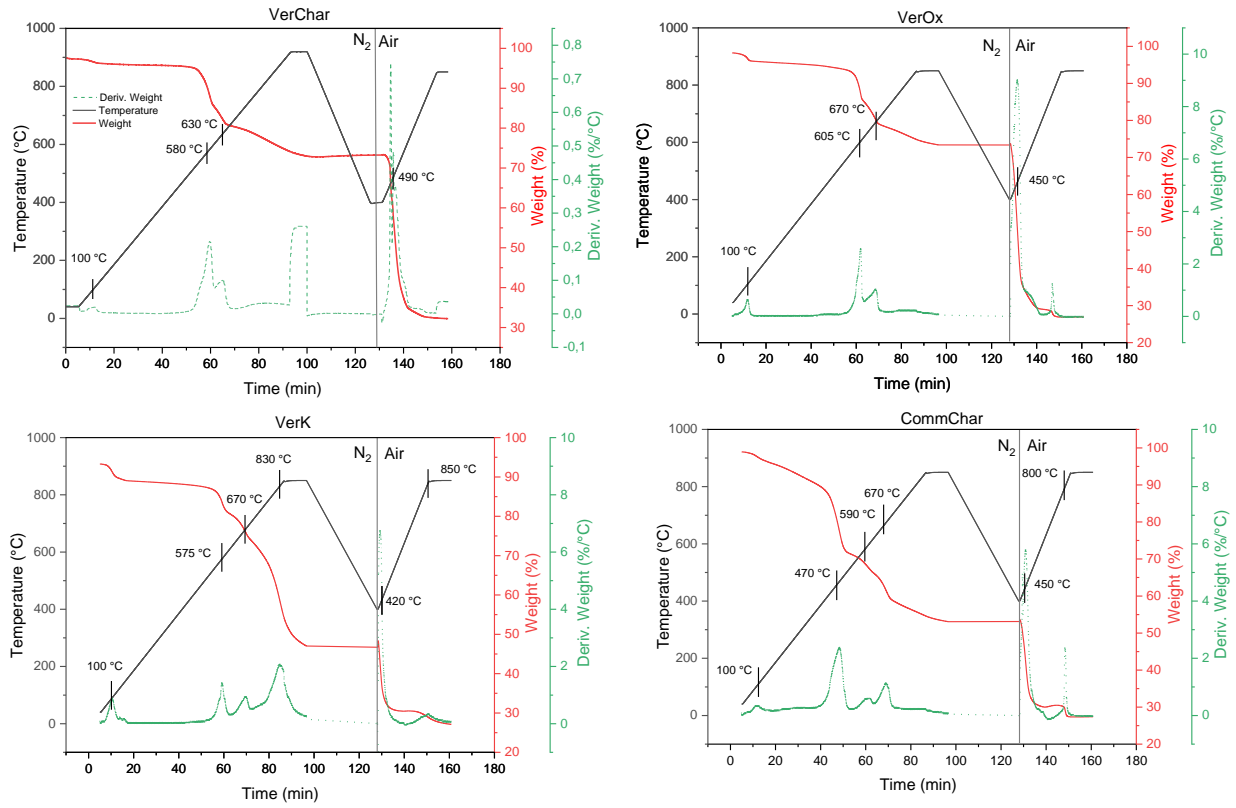


Figure 3.5.2. TGA analyses in N₂ and air to determine the moisture content, volatile matter, fixed carbon and ash in the chars.

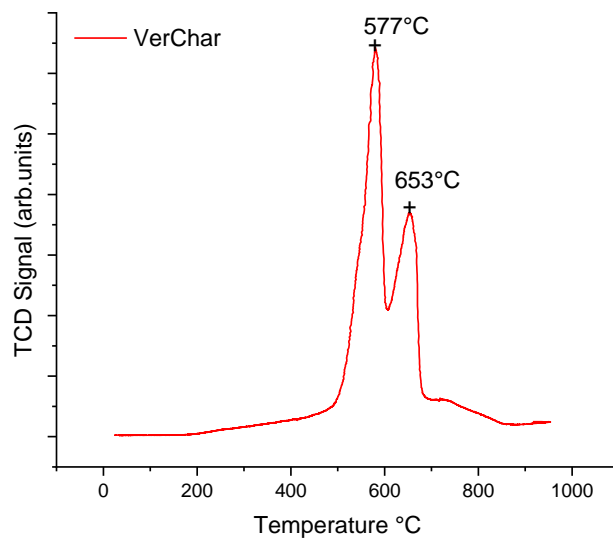


Figure 3.5.3. TPD analysis of VerChar

4. Recovery of char from pyrolysis of mixed plastics

pH

The pH of VerChar resulted 7.8

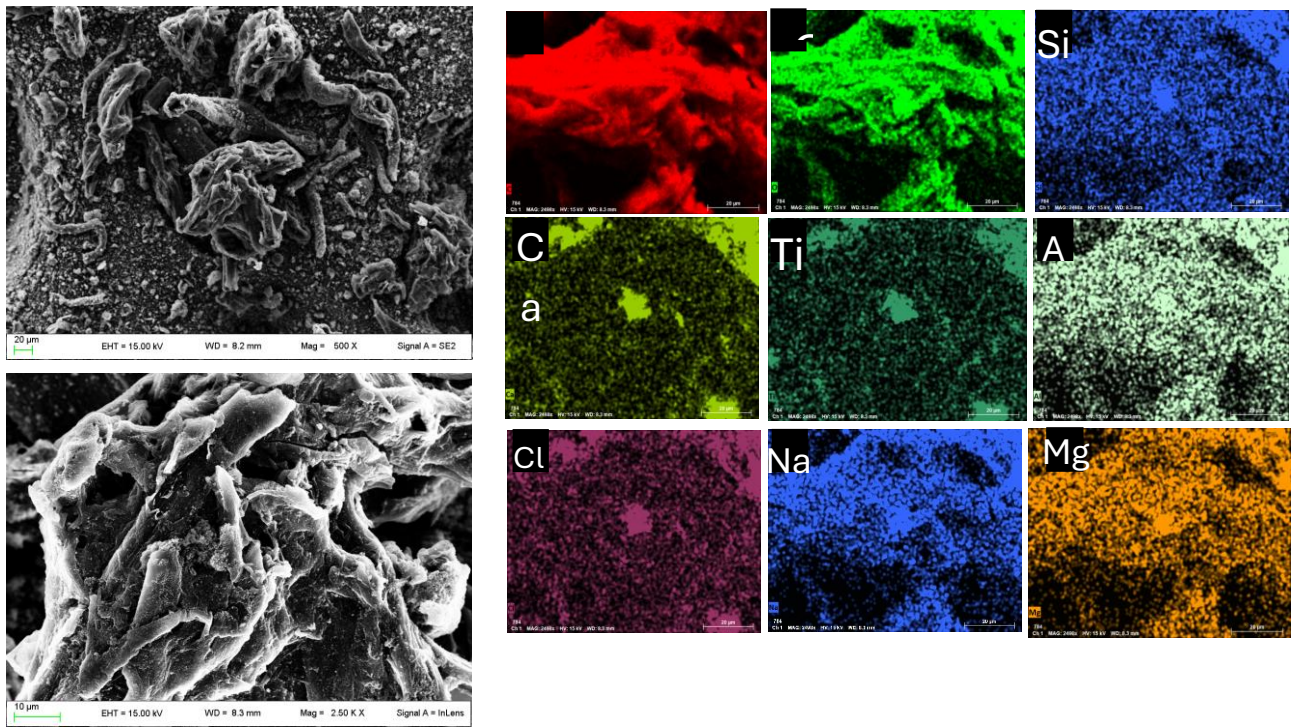
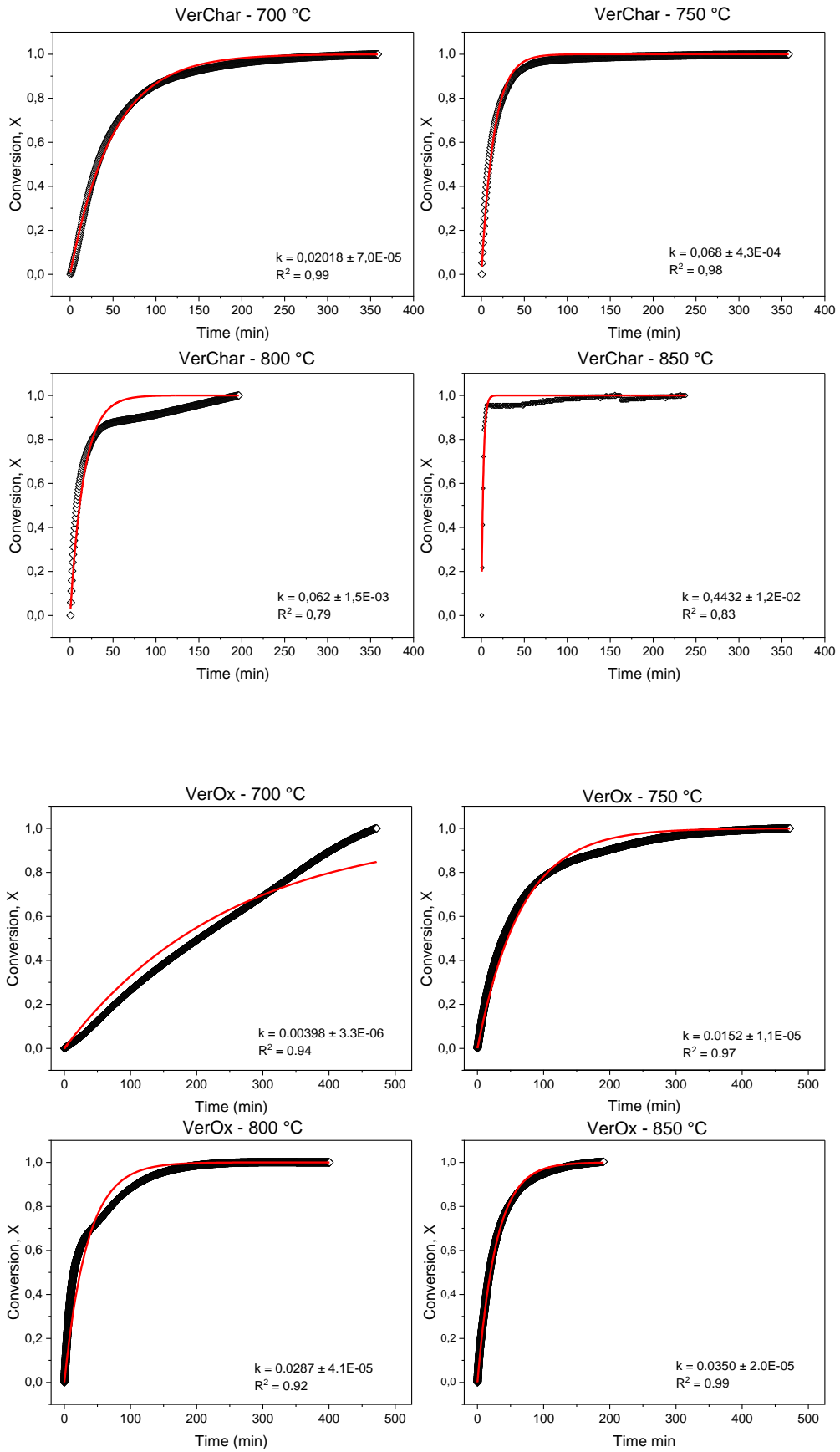


Figure 3.5.4. SEM-EDX microscopy of VerChar

4. Recovery of char from pyrolysis of mixed plastics



4. Recovery of char from pyrolysis of mixed plastics

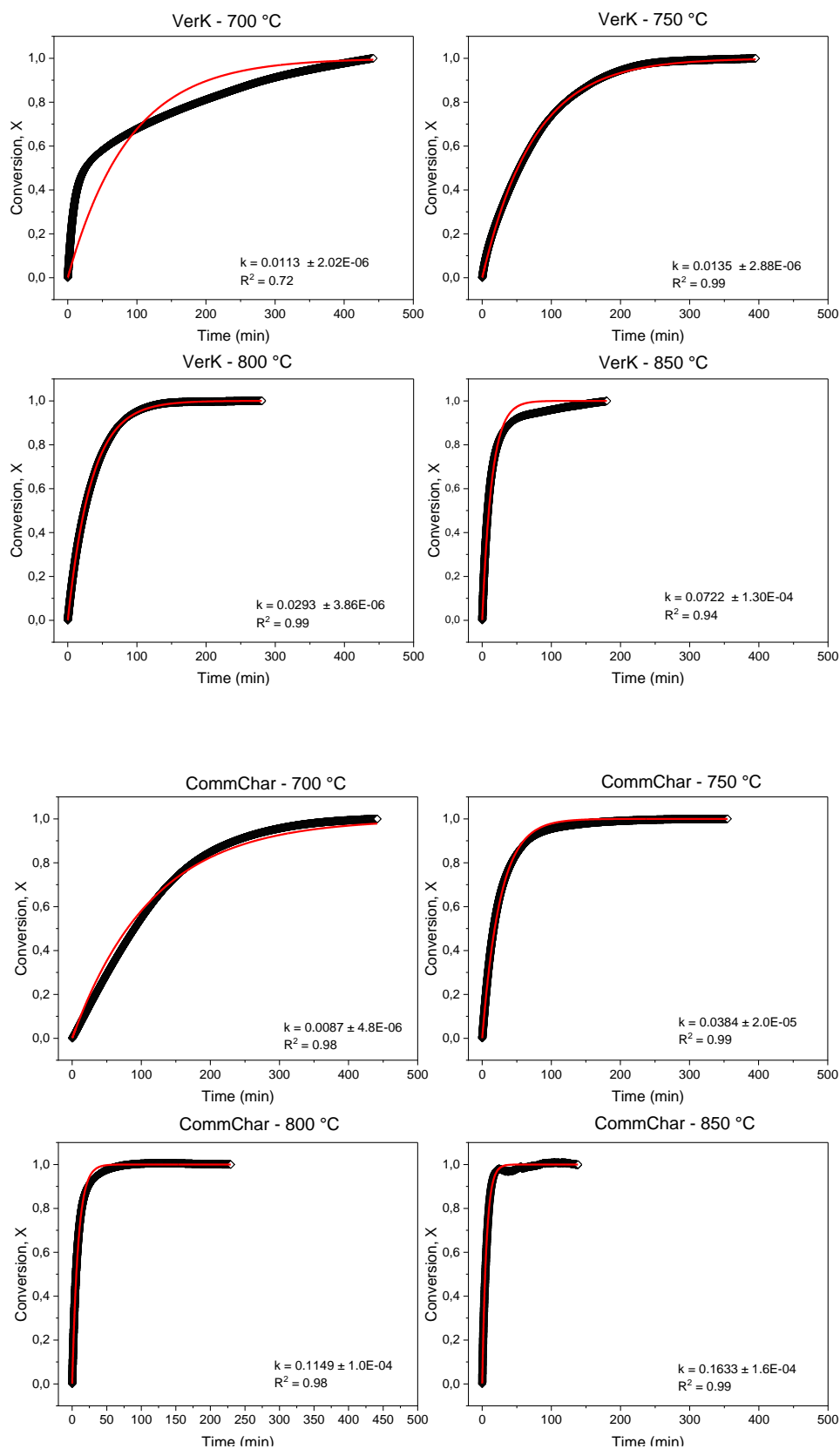


Figure 4 Conversion profiles obtained by TGA in CO₂ at 700, 750, 800 and 850 °C for all chars, fitting of the experimental data with the VRM model, and obtained kinetic constants.

4.6 References

- (1) Bai, B.; Wang, W.; Jin, H. Experimental Study on Gasification Performance of Polypropylene (PP) Plastics in Supercritical Water. *Energy* **2020**, *191*, 116527. <https://doi.org/10.1016/j.energy.2019.116527>.
- (2) Rahimi, A.; García, J. M. Chemical Recycling of Waste Plastics for New Materials Production. *Nat Rev Chem* **2017**, *1* (6), 1–11. <https://doi.org/10.1038/s41570-017-0046>.
- (3) Jiang, J.; Shi, K.; Zhang, X.; Yu, K.; Zhang, H.; He, J.; Ju, Y.; Liu, J. From Plastic Waste to Wealth Using Chemical Recycling: A Review. *Journal of Environmental Chemical Engineering* **2022**, *10* (1), 106867. <https://doi.org/10.1016/j.jece.2021.106867>.
- (4) Sath, P. K.; Chawla, P.; Kumar, S.; Das, A.; Kumar, R.; Bains, A.; Sridhar, K.; Duhan, J. S.; Sharma, M. Recovery of Agricultural Waste Biomass: A Path for Circular Bioeconomy. *Science of The Total Environment* **2023**, *870*, 161904. <https://doi.org/10.1016/j.scitotenv.2023.161904>.
- (5) Anuar Sharuddin, S. D.; Abnisa, F.; Wan Daud, W. M. A.; Aroua, M. K. A Review on Pyrolysis of Plastic Wastes. *Energy Conversion and Management* **2016**, *115*, 308–326. <https://doi.org/10.1016/j.enconman.2016.02.037>.
- (6) Abnisa, F.; Wan Daud, W. M. A. A Review on Co-Pyrolysis of Biomass: An Optional Technique to Obtain a High-Grade Pyrolysis Oil. *Energy Conversion and Management* **2014**, *87*, 71–85. <https://doi.org/10.1016/j.enconman.2014.07.007>.
- (7) Yansaneh, O. Y.; Zein, S. H. Recent Advances on Waste Plastic Thermal Pyrolysis: A Critical Overview. *Processes* **2022**, *10* (2), 332. <https://doi.org/10.3390/pr10020332>.
- (8) Jung, S.-H.; Cho, M.-H.; Kang, B.-S.; Kim, J.-S. Pyrolysis of a Fraction of Waste Polypropylene and Polyethylene for the Recovery of BTX Aromatics Using a Fluidized Bed Reactor. *Fuel Processing Technology* **2010**, *91* (3), 277–284. <https://doi.org/10.1016/j.fuproc.2009.10.009>.
- (9) Mastral, F. J.; Esperanza, E.; García, P.; Juste, M. Pyrolysis of High-Density Polyethylene in a Fluidised Bed Reactor. Influence of the Temperature and Residence Time. *Journal of Analytical and Applied Pyrolysis* **2002**, *63* (1), 1–15. [https://doi.org/10.1016/S0165-2370\(01\)00137-1](https://doi.org/10.1016/S0165-2370(01)00137-1).
- (10) Ludlow-Palafox, C.; Chase, H. A. Microwave-Induced Pyrolysis of Plastic Wastes. *Industrial Engineering and Chemistry Research* **2001**, *40* (22), 4749–4756. <https://doi.org/10.1021/ie010202j>.
- (11) Thiounn, T.; Smith, R. C. Advances and Approaches for Chemical Recycling of Plastic Waste. *Journal of Polymer Science* **2020**, *58* (10), 1347–1364. <https://doi.org/10.1002/pol.20190261>.
- (12) Whyte, H. E.; Loubar, K.; Awad, S.; Tazerout, M. Pyrolytic Oil Production by Catalytic Pyrolysis of Refuse-Derived Fuels: Investigation of Low Cost Catalysts. *Fuel Processing Technology* **2015**, *140*, 32–38. <https://doi.org/10.1016/j.fuproc.2015.08.022>.
- (13) Stelmachowski, M. Thermal Conversion of Waste Polyolefins to the Mixture of Hydrocarbons in the Reactor with Molten Metal Bed. *Energy Conversion and Management* **2010**, *51* (10), 2016–2024. <https://doi.org/10.1016/j.enconman.2010.02.035>.
- (14) Corma, A. Inorganic Solid Acids and Their Use in Acid-Catalyzed Hydrocarbon Reactions. *Chem. Rev.* **1995**, *95* (3), 559–614. <https://doi.org/10.1021/cr00035a006>.
- (15) FakhrHoseini, S. M.; Dastanian, M. Predicting Pyrolysis Products of PE, PP, and PET Using NRTL Activity Coefficient Model. *Journal of Chemistry* **2013**, *2013* (1), 487676. <https://doi.org/10.1155/2013/487676>.
- (16) Bagri, R.; Williams, P. T. Catalytic Pyrolysis of Polyethylene. *Journal of Analytical and Applied Pyrolysis* **2002**, *63* (1), 29–41. [https://doi.org/10.1016/S0165-2370\(01\)00139-5](https://doi.org/10.1016/S0165-2370(01)00139-5).

4. Recovery of char from pyrolysis of mixed plastics

- (17) Marcilla, A.; Beltrán, M. I.; Navarro, R. Thermal and Catalytic Pyrolysis of Polyethylene over HZSM5 and HUSY Zeolites in a Batch Reactor under Dynamic Conditions. *Applied Catalysis B: Environmental* **2009**, *86* (1), 78–86. <https://doi.org/10.1016/j.apcatb.2008.07.026>.
- (18) Onwudili, J. A.; Insura, N.; Williams, P. T. Composition of Products from the Pyrolysis of Polyethylene and Polystyrene in a Closed Batch Reactor: Effects of Temperature and Residence Time. *Journal of Analytical and Applied Pyrolysis* **2009**, *86* (2), 293–303. <https://doi.org/10.1016/j.jaap.2009.07.008>.
- (19) Sarker, M.; Kabir, A.; Rashid, M. M.; Molla, M.; Din Mohammad, A. S. M. Waste Polyethylene Terephthalate (PETE-1) Conversion into Liquid Fuel. *Journal of Fundamentals of Renewable Energy and Applications* **2011**, *1*, 1–5. <https://doi.org/10.4303/jfrea/R101202>.
- (20) Ahmad, I.; Khan, M. I.; Khan, H.; Ishaq, M.; Tariq, R.; Gul, K.; Ahmad, W. Pyrolysis Study of Polypropylene and Polyethylene Into Premium Oil Products. *International Journal of Green Energy* **2015**, *12* (7), 663–671. <https://doi.org/10.1080/15435075.2014.880146>.
- (21) Desai, M. S. B. Production and Analysis of Pyrolysis Oil from Waste Plastic in Kolhapur City. **2015**, *International Journal of Engineering Research and General Science* **2015** *3* (1). ISSN 2091-2730.
- (22) Kumar Jha, K.; Kannan, T. T. M. Recycling of Plastic Waste into Fuel by Pyrolysis - a Review. *Materials Today: Proceedings* **2021**, *37*, 3718–3720. <https://doi.org/10.1016/j.matpr.2020.10.181>.
- (23) Li, P.; Pan, H.; Wan, K.; Zhou, S.; Zhang, Z.; Hong, D.; Zhang, Y. Jet Fuel-Range Hydrocarbon Production from Catalytic Pyrolysis of Low-Density Polyethylene by Metal-Loaded Activated Carbon. *Sustainable Energy Fuels* **2022**, *6* (9), 2289–2305. <https://doi.org/10.1039/D2SE00129B>.
- (24) Çepelioğullar, Ö.; Pütün, A. E. Utilization of Two Different Types of Plastic Wastes from Daily and Industrial Life. Digital Proceeding Of THE ICOEST'2013.
- (25) Miranda, R.; Yang, J.; Roy, C.; Vasile, C. Vacuum Pyrolysis of PVC I. Kinetic Study. *Polymer Degradation and Stability* **1999**, *64* (1), 127–144. [https://doi.org/10.1016/S0141-3910\(98\)00186-4](https://doi.org/10.1016/S0141-3910(98)00186-4).
- (26) Kaminsky, W.; Schlesselmann, B.; Simon, C. M. Thermal Degradation of Mixed Plastic Waste to Aromatics and Gas. *Polymer Degradation and Stability* **1996**, *53* (2), 189–197. [https://doi.org/10.1016/0141-3910\(96\)00087-0](https://doi.org/10.1016/0141-3910(96)00087-0).
- (27) Demirbas, A. Hydrogen from Mosses and Algae via Pyrolysis and Steam Gasification. *Energy Sources, Part A: Recovery, Utilization, and Environmental Effects* **2009**, *32* (2), 172–179. <https://doi.org/10.1080/15567030802464388>.
- (28) Donaj, P. J.; Kaminsky, W.; Buzeto, F.; Yang, W. Pyrolysis of Polyolefins for Increasing the Yield of Monomers' Recovery. *Waste Management* **2012**, *32* (5), 840–846. <https://doi.org/10.1016/j.wasman.2011.10.009>.
- (29) Akin, O.; Varghese, R. J.; Eschenbacher, A.; Oenema, J.; Abbas-Abadi, M. S.; Stefanidis, G. D.; Van Geem, K. M. Chemical Recycling of Plastic Waste to Monomers: Effect of Catalyst Contact Time, Acidity and Pore Size on Olefin Recovery in Ex-Situ Catalytic Pyrolysis of Polyolefin Waste. *Journal of Analytical and Applied Pyrolysis* **2023**, *172*, 106036. <https://doi.org/10.1016/j.jaap.2023.106036>.
- (30) Kusenberg, M.; Eschenbacher, A.; Djokic, M. R.; Zayoud, A.; Ragaert, K.; De Meester, S.; Van Geem, K. M. Opportunities and Challenges for the Application of Post-Consumer Plastic Waste Pyrolysis Oils as Steam Cracker Feedstocks: To Decontaminate or Not to Decontaminate? *Waste Management* **2022**, *138*, 83–115. <https://doi.org/10.1016/j.wasman.2021.11.009>.
- (31) Williams, P. T.; Williams, E. A. Interaction of Plastics in Mixed-Plastics Pyrolysis. *Energy Fuels* **1999**, *13* (1), 188–196. <https://doi.org/10.1021/ef980163x>.
- (32) Koderá, Y.; Yamamoto, T.; Ishikawa, E. Energy- and Economic-Balance Estimation of Pyrolysis Plant for Fuel-Gas Production from Plastic Waste Based on Bench-Scale Plant Operations. *Fuel Communications* **2021**, *7*, 100016. <https://doi.org/10.1016/j.fueco.2021.100016>.

4. Recovery of char from pyrolysis of mixed plastics

- (33) Miskolczi, N.; Ateş, F.; Borsodi, N. Comparison of Real Waste (MSW and MPW) Pyrolysis in Batch Reactor over Different Catalysts. Part II: Contaminants, Char and Pyrolysis Oil Properties. *Bioresource Technology* **2013**, *144*, 370–379. <https://doi.org/10.1016/j.biortech.2013.06.109>.
- (34) Jamradloedluk, J.; Lertsatitthanakorn, C. Characterization and Utilization of Char Derived from Fast Pyrolysis of Plastic Wastes. *Procedia Engineering* **2014**, *69*, 1437–1442. <https://doi.org/10.1016/j.proeng.2014.03.139>.
- (35) Al-Malaika, S.; Axtell, F.; Rothon, R.; Gilbert, M. Chapter 7 - Additives for Plastics. In *Brydson's Plastics Materials (Eighth Edition)*; Gilbert, M., Ed.; Butterworth-Heinemann, 2017; pp 127–168. <https://doi.org/10.1016/B978-0-323-35824-8.00007-4>.
- (36) Atkins, M. Production of Carbon Black. WO2022144440A1, July 7, 2022.
- (37) (22) *Waste Plastic Pyrolysis Plant Market Insights Research Report [2024-2032] | 113 Pages | LinkedIn*. <https://www.linkedin.com/pulse/waste-plastic-pyrolysis-plant-market-insights-research-pbobj/> (accessed 2024-10-25).
- (38) Polimerica.it. *Polimerica - notizie aggiornate su plastica e gomma*. Polimerica.it. <https://www.polimerica.it/index.asp> (accessed 2024-10-26).
- (39) *Plastics Europe • Enabling a sustainable future*. Plastics Europe. <https://plasticseurope.org/> (accessed 2024-10-25).
- (40) *XVII Legislatura - XVII Legislatura - Lavori - Progetti di legge - Scheda del progetto di legge*. <https://www.camera.it/leg17/126?leg=17&idDocumento=4502> (accessed 2024-10-26).
- (41) *Il Progetto SC-HOOP | Versalis*. <https://versalis.eni.com/it-IT/sostenibilita/economia-circolare/sc-hoop.html> (accessed 2024-10-25).
- (42) Polimerica.it. *Polimerica > Cerca nel sito > riciclo chimico pirolisi*. Polimerica.it. https://www.polimerica.it/cerca.asp?page_number=14&tool_input_ricerca=riciclo+chimico+pirolisi (accessed 2024-10-26).
- (43) Snow, J.; Lederer, J.; Kuráň, P.; Koutník, P. Dechlorination during Pyrolysis of Plastics: Effect of Municipal Plastic Waste Composition. *Fuel Processing Technology* **2023**, *248*, 107823. <https://doi.org/10.1016/j.fuproc.2023.107823>.
- (44) Felisari, R.; Galeotti, A.; Nodari, M.; Bonacini, F. Pyrolysis Process for the Production of a Pyrolysis Oil Suitable for Closed Loop Recycling, Related Apparatus, Product and Use Thereof. CA3240315A1, July 6, 2023.
- (45) Lahijani, P.; Zainal, Z. A.; Mohammadi, M.; Mohamed, A. R. Conversion of the Greenhouse Gas CO₂ to the Fuel Gas CO via the Boudouard Reaction: A Review. *Renewable and Sustainable Energy Reviews* **2015**, *41*, 615–632. <https://doi.org/10.1016/j.rser.2014.08.034>.
- (46) *Il Green Deal europeo - Commissione europea*. https://commission.europa.eu/strategy-and-policy/priorities-2019-2024/european-green-deal_it (accessed 2024-10-26).
- (47) Ratnasamy, C.; Wagner, J. P. Water Gas Shift Catalysis. *Catalysis Reviews* **2009**, *51* (3), 325–440. <https://doi.org/10.1080/01614940903048661>.
- (48) Dry, M. E. The Fischer–Tropsch Process: 1950–2000. *Catalysis Today* **2002**, *71* (3), 227–241. [https://doi.org/10.1016/S0920-5861\(01\)00453-9](https://doi.org/10.1016/S0920-5861(01)00453-9).
- (49) Beller, M.; Cornils, B.; Frohning, C. D.; Kohlpaintner, C. W. Progress in Hydroformylation and Carbonylation. *Journal of Molecular Catalysis A: Chemical* **1995**, *104* (1), 17–85. [https://doi.org/10.1016/1381-1169\(95\)00130-1](https://doi.org/10.1016/1381-1169(95)00130-1).
- (50) Megía, P. J.; Vizcaíno, A. J.; Ruiz-Abad, M.; Calles, J. A.; Carrero, A. Coke Evolution in Simulated Bio-Oil Aqueous Fraction Steam Reforming Using Co/SBA-15. *Catalysis Today* **2021**, *367*, 145–152. <https://doi.org/10.1016/j.cattod.2020.04.069>.
- (51) Sasson Bitters, J.; He, T.; Nestler, E.; Senanayake, S. D.; Chen, J. G.; Zhang, C. Utilizing Bimetallic Catalysts to Mitigate Coke Formation in Dry Reforming of Methane. *Journal of Energy Chemistry* **2022**, *68*, 124–142. <https://doi.org/10.1016/j.jechem.2021.11.041>.

4. Recovery of char from pyrolysis of mixed plastics

- (52) Entesari, N.; Goeppert, A.; Prakash, G. K. S. Renewable Methanol Synthesis through Single Step Bi-Reforming of Biogas. *Industrial Engineering and Chemistry Research* **2020**, *59* (22), 10542–10551. <https://doi.org/10.1021/acs.iecr.0c00755>.
- (53) Hazemann, P.; Decottignies, D.; Maury, S.; Humbert, S.; Meunier, F. C.; Schuurman, Y. Selectivity Loss in Fischer-Tropsch Synthesis: The Effect of Cobalt Carbide Formation. *Journal of Catalysis* **2021**, *397*, 1–12. <https://doi.org/10.1016/j.jcat.2021.03.005>.
- (54) Bassano, C.; Deiana, P.; Ricci, G.; Veca, E. Analisi termogravimetrica su campioni di carbone.
- (55) Chun, D. D.; Ni, D.; Simson, A. The Effect of Inherent Inorganics and CO₂ Co-Pyrolysis on Biochar Production from Biowastes and Their Gasification Reactivity. *Biomass and Bioenergy* **2022**, *158*, 106361. <https://doi.org/10.1016/j.biombioe.2022.106361>.
- (56) Jansen, A. A.; van der Walt, I. J.; Crouse, P. L. Waste-Tyre Pyrolysis and Gasification via the Reverse Boudouard Reaction: Derivation of Empirical Kinetics from TGA Data. *Thermochimica Acta* **2022**, *708*, 179104. <https://doi.org/10.1016/j.tca.2021.179104>.
- (57) Gil, M. V.; Feroso, J.; Pevida, C.; Pis, J. J.; Rubiera, F. Intrinsic Char Reactivity of Plastic Waste (PET) during CO₂ Gasification. *Fuel Processing Technology* **2010**, *91* (11), 1776–1781. <https://doi.org/10.1016/j.fuproc.2010.07.019>.
- (58) Trapp, W.; Bitting, D.; Slivensky, D.; Wu, X.; Debruin, B. Treatment of Heavy Pyrolysis Products by Partial Oxidation Gasification. WO2021163110A1, August 19, 2021.
- (59) Miura, K.; Hashimoto, K.; Silveston, P. L. Factors Affecting the Reactivity of Coal Chars during Gasification, and Indices Representing Reactivity. *Fuel* **1989**, *68* (11), 1461–1475. [https://doi.org/10.1016/0016-2361\(89\)90046-X](https://doi.org/10.1016/0016-2361(89)90046-X).
- (60) Jing, X.; Wang, Z.; Zhang, Q.; Yu, Z.; Li, C.; Huang, J.; Fang, Y. Evaluation of CO₂ Gasification Reactivity of Different Coal Rank Chars by Physicochemical Properties. *Energy Fuels* **2013**, *27* (12), 7287–7293. <https://doi.org/10.1021/ef401639v>.
- (61) Huang, Y.; Yin, X.; Wu, C.; Wang, C.; Xie, J.; Zhou, Z.; Ma, L.; Li, H. Effects of Metal Catalysts on CO₂ Gasification Reactivity of Biomass Char. *Biotechnology Advances* **2009**, *27* (5), 568–572. <https://doi.org/10.1016/j.biotechadv.2009.04.013>.
- (62) Xu, K.; Hu, S.; Su, S.; Xu, C.; Sun, L.; Shuai, C.; Jiang, L.; Xiang, J. Study on Char Surface Active Sites and Their Relationship to Gasification Reactivity. *Energy Fuels* **2013**, *27* (1), 118–125. <https://doi.org/10.1021/ef301455x>.
- (63) Ergun, S. Kinetics of the Reaction of Carbon with Carbon Dioxide. *Journal of Physical Chemistry* **1956**, *60* (4), 480–485. <https://doi.org/10.1021/j150538a022>.
- (64) Yousef, S.; Eimontas, J.; Striūgas, N.; Abdelnaby, M. A. Gasification Kinetics of Char Derived from Metallised Food Packaging Plastics Waste Pyrolysis. *Energy* **2022**, *239*, 122070. <https://doi.org/10.1016/j.energy.2021.122070>.
- (65) Rao, Y. K.; Adjorlolo, A.; Haberman, J. H. On the Mechanism of Catalysis of the Boudouard Reaction by Alkali-Metal Compounds. *Carbon* **1982**, *20* (3), 207–212. [https://doi.org/10.1016/0008-6223\(82\)90022-7](https://doi.org/10.1016/0008-6223(82)90022-7).
- (66) Aho, A.; DeMartini, N.; Pranovich, A.; Krogell, J.; Kumar, N.; Eränen, K.; Holmbom, B.; Salmi, T.; Hupa, M.; Murzin, D. Yu. Pyrolysis of Pine and Gasification of Pine Chars – Influence of Organically Bound Metals. *Bioresource Technology* **2013**, *128*, 22–29. <https://doi.org/10.1016/j.biortech.2012.10.093>.
- (67) Sakawa, M.; Sakurai, Y.; Hara, Y. Influence of Coal Characteristics on CO₂ Gasification. *Fuel* **1982**, *61* (8), 717–720. [https://doi.org/10.1016/0016-2361\(82\)90245-9](https://doi.org/10.1016/0016-2361(82)90245-9).
- (68) Hattingh, B. B.; Everson, R. C.; Neomagus, H. W. J. P.; Bunt, J. R. Assessing the Catalytic Effect of Coal Ash Constituents on the CO₂ Gasification Rate of High Ash, South African Coal. *Fuel Processing Technology* **2011**, *92* (10), 2048–2054. <https://doi.org/10.1016/j.fuproc.2011.06.003>.
- (69) Kim, Y. T.; Seo, D. K.; Hwang, J. Study of the Effect of Coal Type and Particle Size on Char–CO₂ Gasification via Gas Analysis. *Energy Fuels* **2011**, *25* (11), 5044–5054. <https://doi.org/10.1021/ef200745x>.

4. Recovery of char from pyrolysis of mixed plastics

- (70) Floess, J. K.; Longwell, J. P.; Sarofim, A. F. Intrinsic Reaction Kinetics of Microporous Carbons. 1. Noncatalyzed Chars. *Energy Fuels* **1988**, *2* (1), 18–26. <https://doi.org/10.1021/ef00007a004>.
- (71) Sadhwani, N.; Adhikari, S.; Eden, M. R.; Wang, Z.; Baker, R. Southern Pines Char Gasification with CO₂—Kinetics and Effect of Alkali and Alkaline Earth Metals. *Fuel Processing Technology* **2016**, *150*, 64–70. <https://doi.org/10.1016/j.fuproc.2016.04.037>.
- (72) Duman, G.; Uddin, M. A.; Yanik, J. The Effect of Char Properties on Gasification Reactivity. *Fuel Processing Technology* **2014**, *118*, 75–81. <https://doi.org/10.1016/J.FUPROC.2013.08.006>.
- (73) Roberts, D. G.; Harris, D. J. A Kinetic Analysis of Coal Char Gasification Reactions at High Pressures. *Energy Fuels* **2006**, *20* (6), 2314–2320. <https://doi.org/10.1021/ef060270o>.
- (74) Molina, A.; Mondragón, F. Reactivity of Coal Gasification with Steam and CO₂. *Fuel* **1998**, *77* (15), 1831–1839. [https://doi.org/10.1016/S0016-2361\(98\)00123-9](https://doi.org/10.1016/S0016-2361(98)00123-9).
- (75) Ahn, D. H.; Gibbs, B. M.; Ko, K. H.; Kim, J. J. Gasification Kinetics of an Indonesian Sub-Bituminous Coal-Char with CO₂ at Elevated Pressure. *Fuel* **2001**, *80* (11), 1651–1658. [https://doi.org/10.1016/S0016-2361\(01\)00024-2](https://doi.org/10.1016/S0016-2361(01)00024-2).
- (76) Wang, G.; Zhang, J.; Chang, W.; Li, R.; Li, Y.; Wang, C. Structural Features and Gasification Reactivity of Biomass Chars Pyrolyzed in Different Atmospheres at High Temperature. *Energy* **2018**, *147*, 25–35. <https://doi.org/10.1016/j.energy.2018.01.025>.
- (77) Zaini, I. N.; García López, C.; Pretz, T.; Yang, W.; Jönsson, P. G. Characterization of Pyrolysis Products of High-Ash Excavated-Waste and Its Char Gasification Reactivity and Kinetics under a Steam Atmosphere. *Waste Management* **2019**, *97*, 149–163. <https://doi.org/10.1016/j.wasman.2019.08.001>.
- (78) Wen, X.; Wang, H.; Luo, Y.; Luo, K.; Fan, J. Numerical Investigation of the Effects of Volatile Matter Composition and Chemical Reaction Mechanism on Pulverized Coal Combustion Characteristics. *Fuel* **2017**, *210*, 695–704. <https://doi.org/10.1016/j.fuel.2017.08.115>.
- (79) Vecchini, N.; Galeotti, A.; Gradella, C.; Signoretto, M.; Longo, L. Process for Treating Char from Recycled Plastics. WO2024141843A1, July 4, 2024.
- (80) Wang, G.; Ren, S.; Zhang, J.; Ning, X.; Liang, W.; Zhang, N.; Wang, C. Influence Mechanism of Alkali Metals on CO₂ Gasification Properties of Metallurgical Coke. *Chemical Engineering Journal* **2020**, *387*, 124093. <https://doi.org/10.1016/j.cej.2020.124093>.
- (81) Zhang, L.; Huang, J.; Fang, Y.; Wang, Y. Gasification Reactivity and Kinetics of Typical Chinese Anthracite Chars with Steam and CO₂. *Energy Fuels* **2006**, *20* (3), 1201–1210. <https://doi.org/10.1021/ef050343o>.
- (82) Issac, M.; Dai, B.; Zhang, L. Kinetics Underpinning the C-CO₂ Gasification of Waste Tyre Char and Its Interaction with Coal Char upon Co-Gasification. *Fuel* **2019**, *256*, 115991. <https://doi.org/10.1016/j.fuel.2019.115991>.
- (83) Scott, S. A.; Davidson, J. F.; Dennis, J. S.; Fennell, P. S.; Hayhurst, A. N. The Rate of Gasification by CO₂ of Chars from Waste. *Proceedings of the Combustion Institute* **2005**, *30* (2), 2151–2159. <https://doi.org/10.1016/j.proci.2004.08.061>.
- (84) Gómez-Barea, A.; Ollero, P.; Fernández-Baco, C. Diffusional Effects in CO₂ Gasification Experiments with Single Biomass Char Particles. 1. Experimental Investigation. *Energy Fuels* **2006**, *20* (5), 2202–2210. <https://doi.org/10.1021/ef050365a>.
- (85) Mani, T.; Mahinpey, N.; Murugan, P. Reaction Kinetics and Mass Transfer Studies of Biomass Char Gasification with CO₂. *Chemical Engineering Science* **2011**, *66* (1), 36–41. <https://doi.org/10.1016/j.ces.2010.09.033>.
- (86) Enders, A.; Hanley, K.; Whitman, T.; Joseph, S.; Lehmann, J. Characterization of Biochars to Evaluate Recalcitrance and Agronomic Performance. *Bioresource Technology* **2012**, *114*, 644–653. <https://doi.org/10.1016/j.biortech.2012.03.022>.
- (87) Martín-Lara, M. A.; Piñar, A.; Ligeró, A.; Blázquez, G.; Calero, M. Characterization and Use of Char Produced from Pyrolysis of Post-Consumer Mixed Plastic Waste. *Water* **2021**, *13* (9), 1188. <https://doi.org/10.3390/w13091188>.

4. Recovery of char from pyrolysis of mixed plastics

- (88) López, A.; de Marco, I.; Caballero, B. M.; Laresgoiti, M. F.; Adrados, A.; Torres, A. Pyrolysis of Municipal Plastic Wastes II: Influence of Raw Material Composition under Catalytic Conditions. *Waste Management* **2011**, *31* (9), 1973–1983. <https://doi.org/10.1016/j.wasman.2011.05.021>.
- (89) Gonzalo-Tirado, C.; Jiménez, S.; Ballester, J. Kinetics of CO₂ Gasification for Coals of Different Ranks under Oxy-Combustion Conditions. *Combustion and Flame* **2013**, *160* (2), 411–416. <https://doi.org/10.1016/j.combustflame.2012.10.020>.
- (90) Donahue, C. J.; Rais, E. A. Proximate Analysis of Coal. *Journal of Chemical Education* **2009**, *86* (2), 222. <https://doi.org/10.1021/ed086p222>.
- (91) Jamil, K.; Hayashi, J.; Li, C.-Z. Pyrolysis of a Victorian Brown Coal and Gasification of Nascent Char in CO₂ Atmosphere in a Wire-Mesh Reactor. *Fuel* **2004**, *83* (7), 833–843. <https://doi.org/10.1016/j.fuel.2003.09.017>.
- (92) Lampropoulos, A.; Binas, V. D.; Zouridi, L.; Athanasiou, C.; Montes-Morán, M. A.; Menéndez, J. A.; Konsolakis, M.; Marnellos, G. E. CO₂ Gasification Reactivity and Syngas Production of Greek Lignite Coal and Ex-Situ Produced Chars under Non-Isothermal and Isothermal Conditions: Structure-Performance Relationships. *Energies* **2022**, *15* (3), 679. <https://doi.org/10.3390/en15030679>.
- (93) Gul-e-Rana, J.; Zhang, J. Catalytic Activity of the Black Liquor and Calcium Mixture in CO₂ Gasification of Fujian Anthracite*. *Chinese Journal of Chemical Engineering* **2007**, *15* (5), 670–679. [https://doi.org/10.1016/S1004-9541\(07\)60144-X](https://doi.org/10.1016/S1004-9541(07)60144-X).
- (94) de Lasa, H.; Salaices, E.; Mazumder, J.; Lucky, R. Catalytic Steam Gasification of Biomass: Catalysts, Thermodynamics and Kinetics. *Chemical Reviews* **2011**, *111* (9), 5404–5433. <https://doi.org/10.1021/cr200024w>.
- (95) Risnes, H.; Fjellerup, J.; Henriksen, U.; Moilanen, A.; Norby, P.; Papadakis, K.; Posselt, D.; Sørensen, L. H. Calcium Addition in Straw Gasification. *Fuel* **2003**, *82* (6), 641–651. [https://doi.org/10.1016/S0016-2361\(02\)00337-X](https://doi.org/10.1016/S0016-2361(02)00337-X).
- (96) Keown, D. M.; Favas, G.; Hayashi, J.; Li, C.-Z. Volatilisation of Alkali and Alkaline Earth Metallic Species during the Pyrolysis of Biomass: Differences between Sugar Cane Bagasse and Cane Trash. *Bioresource Technology* **2005**, *96* (14), 1570–1577. <https://doi.org/10.1016/j.biortech.2004.12.014>.
- (97) Dai, B.; Hoadley, A.; Zhang, L. Characteristics of High Temperature C-CO₂ Gasification Reactivity of Victorian Brown Coal Char and Its Blends with High Ash Fusion Temperature Bituminous Coal. *Fuel* **2017**, *202*, 352–365. <https://doi.org/10.1016/j.fuel.2017.04.044>.
- (98) Saad, J. M.; Williams, P. T.; Pyrolysis-catalytic-dry-reforming of waste plastics and mixed waste plastics for syngas production, *Energy & Fuel* **2016**, *30*, 3198-3204. [10.1021/acs.energyfuels.5b02508](https://doi.org/10.1021/acs.energyfuels.5b02508)
- (99) Saad, J. M.; Williams, P. T.; Manipulating the H₂/CO ratio from dry reforming of simulated mixed waste plastics by the addition of steam, *Fuel Processing Technology* **2017**, *156*, 331-338. <https://doi.org/10.1016/j.fuproc.2016.09.016>
- (100) Fermoso, J.; Corbet, T.; Ferrara, F.; Pettinau, A.; Maggio, E.; Sanna, A.; Synergistic effects during the co-pyrolysis and co-gasification of high volatile bituminous coal with microalgae, *Energy Conversion and Management* **2018**, *164*, 399-409. <https://doi.org/10.1016/j.enconman.2018.03.023>

5. Concluding remarks

This thesis addresses the challenges associated with fossil fuel reliance and waste management, as discussed in Chapter 1. It aims to demonstrate how pyrolysis can effectively transform various byproducts into valuable sources for new materials, biofuels, and chemicals. Overall, this research has made significant advancements in the valorization of waste through pyrolysis, aligning with the principles of a sustainable circular economy.

Chapter 3 presents findings on the potential of activated biochars derived from diverse biomass sources as effective support for palladium and cobalt-based catalysts. Notably, rice husk emerged as a promising biomass for producing activated biochar with optimal characteristics for catalytic applications, including desirable morphology and surface functionalities. The Pd/A-RH catalyst achieved nearly complete benzaldehyde conversion under mild conditions, showcasing not only high selectivity towards desired products but also the critical role of biochar properties in enhancing catalytic performance. These findings are documented in the publication: Longo et al., “Waste Biomasses as Precursors of Catalytic Supports in Benzaldehyde Hydrogenation,” *Catalysis Today*, 2023, 1140381.

The study of co-pyrolysis further underscored the feasibility of tailoring biochar properties to enhance catalyst efficiency, demonstrating the versatility of waste-derived materials in catalysis. A paper regarding these findings is currently in preparation.

Co/A-RH has demonstrated significant potential for the hydrodeoxygenation of bio-oil model compounds such as isoeugenol. The results underline the importance of strong metal-support interactions and the synergy between metallic and acid sites in promoting selective reactions while minimizing undesirable side reactions, such as hydrocracking. Moreover, the observed stability and recyclability of Co/A-RH, along with its performance in co-processing with furfural, positions it as a promising candidate for future applications in bio-oil upgrading. These results are currently being drafted into a manuscript.

Chapter 4 introduced an innovative approach to the valorization of char obtained from mixed plastic waste through gasification via the Boudouard reaction. This research illustrated that these plastic-derived chars could achieve over 90% conversion at significantly lower temperatures than traditional feedstocks, thereby reducing energy consumption and operational costs. The incorporation of additives like CaCO_3 and K_2CO_3 not only enhanced gasification efficiency but also mitigated the release of toxic byproducts, demonstrating a practical solution to the pressing issue of plastic waste management.

5. Concluding remarks

The results obtained allowed the filing of a patent application, that is now accessible as WO2024141843A1.

Together, these findings not only enrich our understanding of biomass and plastic waste valorization but also establish a comprehensive framework for developing novel catalytic systems and recycling technologies. The implications of this research extend beyond theoretical knowledge, offering practical pathways for integrating recovered carbon into chemical and fuel production chains. This work culminates in the potential for impactful environmental and economic benefits, addressing critical challenges in waste management and resource recovery.

Overall, this thesis underscores the vital importance of innovative approaches to waste valorization and highlights the role of pyrolysis as a transformative strategy for sustainable resource utilization. Future research directions will build upon these findings, exploring additional feedstocks and refining catalytic processes to further enhance the efficiency and sustainability of waste-to-resource pathways.

Curriculum Vitae

I am Lilia Longo, born in 1994, Venice, Italy. I pursued the bachelor's degree in Chemistry and Sustainable Technology in 2017 at Ca' Foscari University of Venice with the thesis titled "Phosphonium salts for the synthesis of cyclic carbonates from carbon dioxide" under the supervision of Professor Alvise Perosa. In the same University I took my master's degree in Chemistry and Sustainable Technology with the thesis titled "Hydrogenation/hydrogenolysis of 5-(hydroxymethyl) furfural (HMF) catalyzed by Ru/C under multiphase and continuous flow conditions" under the supervision of Professor Maurizio Selva. Part of the research related to my master thesis was performed abroad, at Universidad de Cordoba, Spain, under the supervision of Professor Rafael Luque. I pursued my degree cum laude. After my master's degree I joined Professor Signoretto's group, CATMAT, with a research grant funded by the European Social Fund titled "HAIR: hair and agrifood, innovating by recycling", with the aim of valorizing agrifood waste (like artichoke waste) for the extraction of functional compounds to be used in cosmetic. In 2021 I started my PhD joint program between Ca' Foscari University and Trieste University, under the supervision of Professor Michela Signoretto and the co-supervision of Dr. Nicola Vecchini, from Versalis S.p.A. Part of my research was carried abroad, at Åbo Akademi University, under the supervision of Professor Dmitry Murzin.

My entire research route has been devoted to the valorization of byproducts, waste materials, and bio-derived compounds with a multidisciplinary approach, ranging from the organic chemistry to the industrial chemistry, approaching the chemical reaction engineering.

The results of my research have been disseminated by some publications, and participation of several national and international congresses.

Chapter 3.2

Publications

- Longo, L.; Taghavi, S.; Riello, M.; Ghedini, E.; Menegazzo, F.; Di Michele, A.; Cruciani, G.; Signoretto, M. Waste Biomasses as Precursors of Catalytic Supports in Benzaldehyde Hydrogenation. *Catalysis Today* **2023**, *420*, 114038.
<https://doi.org/10.1016/j.cattod.2023.02.015>.
- Menegazzo, F.; Ghedini, E.; Longo, L.; Baldassin, D.; Taghavi, S.; Signoretto, M. On the Applications as Catalytic Support of Biochars Obtained by Pyrolysis of Waste Biomasses. *Chemical Engineering Transactions* 2024, *109*, 367–372.
<https://doi.org/10.3303/CET24109062>.

Conference presentations

- Lilia Longo, Sebastiano Tieuli, Federica Menegazzo, Elena Ghedini, Michela Signoretto, “*Biochar-based catalysts for biomass valorization*”, Merck Young Chemist’s Symposium, Rimini, Italy, November 22-24 2021. – Poster presentation
- Lilia Longo, Somayeh Taghavi, Margherita Riello, Alessandro Di Michele, Michela Signoretto, “*Novel applications of biomass waste derived biochars: catalysts for hydrogenation reactions*” Merck Young Chemist’s Symposium, Rimini, Italy, November 21-23, 2022. – Poster presentation.
- Lilia Longo, Michela Signoretto, Federica Menegazzo, Alessandro Di Michele “*Influence of the starting biomass on the starting biomass in the Pd-biochar catalyst properties*”, EUROPACAT2023, Prague, Czech Republic, August 27 – September 1 2023. – Poster presentation.
- Lilia Longo, Davide Baldassin, Elena Ghedini, Alessandro Di Michele, Federica Menegazzo, Michela Signoretto “*A road from non-conventional biomass to innovative metal-based catalysts*”, X Workshop GC-CS – Industrial Chemistry – Green Chemistry, Firenze, Italy, October 6, 2023. – Oral presentation
- Lilia Longo, Davide Baldassin, Federica Menegazzo, Carla Bittencourt, Michela Signoretto, “*Co-pyrolysis as an efficient way to transform wastes in heterogeneous catalysts*”, International Congress on Catalysts (ICC2024), Lyon, France, 14-19 July 2024. – Oral presentation.

Chapter 3.3

Conference presentations

- Lilia Longo, “*Hydrodeoxygenation of model bio-oil compounds by biochar based catalyst*” Young Scientific Forum, Espoo, Finland, April 12 2024. – Oral presentation.
- Lilia Longo, Davide Baldassin, Päivi Mäki-Arvela, Joan Wärnå, Mark E. Martinez Klimov, Olha Yevdokimova, Kari Eränen, Dmitry Y. Murzin, Michela Signoretto, “*Hydrodeoxygenation of Isoeugenol catalyzed by Co/biochar: reaction network analysis*”, International Symposium on Chemical Reaction Engineering (ISCRE28), Turku, Finland, June 16-19 2024. – Poster presentation.

Chapter 4

Publications

- Vecchini, N.; Galeotti, A.; Gradella, C.; Signoretto, M.; Longo, L. Process for Treating Char from Recycled Plastics. WO2024141843A1, July 4, 2024.

Conference presentations

- Lilia Longo, Michela Signoretto, Nicola Vecchini, Armando Galeotti, Cecilia Gradella, “*Valorization of char from chemical recycling of plastics*” National Congress of the Italian Chemical Society (SCI 2024), August 26-30 2024. – Oral presentation.

Other publications

- Ghedini, E.; Pizzolato, M.; Longo, L.; Menegazzo, F.; Zanardo, D.; Signoretto, M. Which Are the Main Surface Disinfection Approaches at the Time of SARS-CoV-2? *Front. Chem. Eng.* 2021, 2. <https://doi.org/10.3389/fceng.2020.589202>.
- Rodríguez-Padrón, D.; Perosa, A.; Longo, L.; Luque, R.; Selva, M. Tuning the Selectivity of the Hydrogenation/Hydrogenolysis of 5-Hydroxymethylfurfural under Batch Multiphase and Continuous-Flow Conditions. *ChemSusChem* 2022, 15 (13), e202200503. <https://doi.org/10.1002/cssc.202200503>.
- Longo, L.; Taghavi, S.; Ghedini, E.; Menegazzo, F.; Di Michele, A.; Cruciani, G.; Signoretto, M. Selective Hydrogenation of 5-Hydroxymethylfurfural to 1-Hydroxy-2,5-Hexanedione by Biochar-Supported Ru Catalysts. *ChemSusChem* **2022**, 15 (13), e202200437. <https://doi.org/10.1002/cssc.202200437>.